

Die approbierte Originalversion dieser Diplom-/Masterarbeit ist an der Hauptbibliothek der Technischen Universität Wien aufgestellt (<http://www.ub.tuwien.ac.at>).

The approved original version of this diploma or master thesis is available at the main library of the Vienna University of Technology (<http://www.ub.tuwien.ac.at/englweb/>).



TECHNISCHE  
UNIVERSITÄT  
WIEN

VIENNA  
UNIVERSITY OF  
TECHNOLOGY

D I P L O M A R B E I T

# Investigations on high pressure direct current glow-discharges

ausgeführt am

Institut für Allgemeine Physik, TU Wien

Wiedner Hauptstrasse 8-10

A-1040 Wien

unter Anleitung von

Ao.Univ-Prof. Dipl.-Ing. Dr.techn. Johann Laimer

durch

Christian Maszl

Joseph Haydn Gasse 1a/7/1

A-7111 Parndorf

Parndorf, 10. Jänner 2007



*Must I praise the leaves where no fruit I find?*  
John Dowland (1563 - 1626)



Erstellt auf einem Mac



# Contents

<b>Acknowledgements</b>	<b>iii</b>
<b>Abstract</b>	<b>v</b>
<b>Introduction</b>	<b>vii</b>
<b>1 Theoretical Background</b>	<b>1</b>
1.1 Definition of Plasma . . . . .	1
1.2 Ignition of a DC glow discharge . . . . .	1
1.3 Townsend's 1 <sup>st</sup> and 2 <sup>nd</sup> ionization coefficients . . . . .	2
1.4 Condition for initialising a self-sustaining discharge . . . . .	3
1.5 General structure and observable features of a stable DC glow discharge . . . . .	4
1.6 Similarity relations . . . . .	7
1.7 Scope of the similarity laws . . . . .	9
1.7.1 Density correction for the similarity laws. . . . .	9
1.8 Determination of gas temperatures via optical spectroscopy . . . . .	11
<b>2 Experimental details</b>	<b>13</b>
2.1 Used equipment and experimental setup . . . . .	13
2.1.1 Measurement system . . . . .	14
2.1.2 A brief manual . . . . .	18
2.2 Difficulties and imperfectness of the experiment . . . . .	19
2.2.1 Contamination of the plasma due to Teflon-shieldings . . . . .	19
2.2.2 Increased ignition and discharge voltages due to contaminated helium . . . . .	22
2.3 Recommendations for improvements . . . . .	23
2.3.1 Improvement of breakdown voltage determination . . . . .	23
2.3.2 Methods to monitor and improve the gas quality . . . . .	24
<b>3 Results &amp; Discussion</b>	<b>27</b>
3.1 Investigations on breakdown voltages . . . . .	28
3.1.1 Paschen curves with fixed inter-electrode gaps and variable pressures . . . . .	29
3.1.2 Paschen curves with fixed pressures and variable inter-electrode gaps . . . . .	29
3.1.3 Discussion . . . . .	31
3.2 Determination of the reduced normal current density . . . . .	34
3.2.1 Discussion . . . . .	37
3.3 On the pressure dependence of the positive column cross section . . . . .	38
3.3.1 On the temperature in the cathode fall region . . . . .	41

3.3.2	Discussion . . . . .	42
3.4	I-V characterisation of similar glow discharges . . . . .	44
3.4.1	Measurement series with scaling factors $a=2$ and $1.4$ . . . . .	44
3.4.2	Discussion . . . . .	45
3.5	Reduced field strength in the positive column . . . . .	49
3.5.1	Measurement series with scaling factors $a=2$ and $1.4$ . . . . .	49
3.5.2	Discussion . . . . .	50
3.6	Sheath measurements of the cathode dark-space . . . . .	52
3.6.1	Discussion . . . . .	54
3.7	Anode light spots & anode glow . . . . .	55
3.7.1	Anode spots at large electrode surfaces . . . . .	55
3.7.2	Anode spots at small electrode surfaces . . . . .	57
3.7.3	Relation between anode spots and voltage drop in the high pressure case . . . . .	58
3.7.4	Time evolution from anodic glow to anodic light spots . . . . .	60
3.7.5	Discussion . . . . .	63
<b>4</b>	<b>Conclusion and Outlook</b>	<b>67</b>
<b>5</b>	<b>References</b>	<b>69</b>
<b>A</b>	<b>Measured raw-data</b>	<b>73</b>
A.1	Reduced field strength in the positive column . . . . .	74
A.1.1	Measurement series with scaling factors $a=2$ and $1.4$ . . . . .	75
A.2	I-V characterisation of similar glow discharges . . . . .	102
A.2.1	Measurement series with scaling factors $a=2$ and $1.4$ . . . . .	103
A.2.2	Comparison of similar DC glow discharges (I-V) . . . . .	130
A.3	Measurement-tables for Sec.3.1, Sec.A.1 and Sec.A.2 . . . . .	135
A.3.1	Tables for Sec.3.1 - Investigations on breakdown voltages . . . . .	135
A.3.2	Tables for Sec.A.1 - Reduced field strength in the positive column . . . . .	143
A.3.3	Tables for Sec.A.2 - I-V characterisation of similar glow discharges . . . . .	157
<b>B</b>	<b>Construction</b>	<b>171</b>
B.1	Guidelines . . . . .	171
B.2	Production drawings & parts list . . . . .	174
B.3	List of suppliers . . . . .	176
<b>C</b>	<b>Production drawings</b>	<b>177</b>
C.1	Catalogue of production drawings . . . . .	177
	<b>List of figures and tables</b>	<b>191</b>

# Acknowledgements

Diese Diplomarbeit und die Arbeit am Institut für Allgemeine Physik wird mir immer in schöner Erinnerung bleiben. Rückblickend kann ich sagen, dass es eine lehrreiche und wertvolle Zeit gewesen ist. Diese Arbeit wäre ohne Unterstützung von vielen Menschen nicht möglich gewesen. Zuallererst möchte ich mich bei Prof. Herbert Störi und Prof. Johann Laimer bedanken. Schon bei der ersten Besprechung, bei der wir mögliche Diplomarbeitsthemen diskutiert haben, war ich von ihrer Begeisterung für Physik und ihrer Kreativität angetan. Auch in schwierigen Zeiten haben sie immer ein offenes Ohr, Geduld und viel Verständnis gezeigt.

Besonders möchte ich mich bei Prof. Johann Laimer, meinem Betreuer, bedanken. Zum ersten Mal in meinem Leben habe ich ein Lehrer- Schüler-Verhältnis erlebt, wie man es sonst nur in Erzählungen von Hermann Hesse findet. Gerne denke ich an die unzähligen Stunden zurück, in denen ich an seiner Erfahrung teilhaben durfte. Sein tiefes Verständnis der Dinge und seine Art sich Problemen zu nähern, wird mir immer Vorbild sein.

Bedanken möchte ich mich auch bei Ralph Kolm und Christian Tomastik für die Messungen in Sec.2.2.1. Stefan Haslinger danke ich für viele interessante Diskussionen und die gute Zeit in Prag und Graz wo wir unsere Arbeiten präsentieren durften. Ing. Franz Meyer danke ich für die vielen wertvollen Anregungen während der Konstruktion des Experimentes. Selten habe ich einen Ingenieur mit solch einem Hang zur Perfektion und einer eleganten Klarheit und Einfachheit in seinen Entwürfen erlebt. Dank gilt auch Ing. Wolfgang Beck und seinem Team in der Werkstätte, die die Hochdruck-Entladungszelle gebaut haben und maßgeblich an der Konstruktion beteiligt waren.

Ganz besonders möchte ich mich bei meinen Eltern Anneliese und Johann bedanken, die mir das Studium ermöglicht und mich stets unterstützt haben. Meinem Bruder danke ich für seine fröhliche Art, sein offenes, heiteres Wesen und seinen Gesang, mit dem er mir viel Freude bereitet, seiner Freundin Livia, weil sie ihn in richtige Bahnen lenkt wenn es nötig ist. Nicht vergessen möchte ich meine Großmutter Maria, meinen Firmpaten Werner, meine Taufpatin Brigitte, meine Onkeln Stefan, Joschko und Berti, meine Tanten Dani, Eva und Helene die mich ebenfalls immer sehr großzügig unterstützt haben. Die lauten und hektischen Kartenpartien am Freitag und die gemütlichen Sonntag-Nachmittage bei Oma haben mir über so manch schwierige Zeit hinweg geholfen.



# Abstract

Direct current (DC) glow-discharges are well known today and in widespread use. However, there is less known about DC glow-discharges at high pressures. High pressure glow-discharges are interesting because expensive and maintenance-intensive vacuum equipment is not required. This fact allows minituarization of discharges for various applications. Main goal of this study was to investigate similarity (“scaling”) laws for high pressure DC glow-discharges. Therefore, a high pressure chamber was constructed in order to observe glow discharges in a pressure range from 200 to 2000 *hPa* with inter-electrode gaps between 0.1 and 7 mm. Distances are adjusted with a micrometer-head. Both electrodes are water cooled to allow measurements at higher powers. The electrodes are replaceable to permit experiments with various electrode materials. Electrical characterisation of the discharge is accomplished by the determination of current-voltage (I-V) curves. Optical analyses are done with microscopes and spectrometers.

Investigations on breakdown voltages were performed. It turned out that neither of the established formulas for the ignition potential is capable to fit the experimental data. The reduced normal current density for helium and copper was measured for the first time. Investigations on the pressure dependence of the positive column cross section and the temperature in the cathode fall region took place. I-V characterisation and measurements of the reduced field strength in the positive column of mathematically similar discharges were performed. The reduced thickness of a normal cathode sheath was measured for the first time for helium and tungsten. Finally, investigations on anode light spots and anode glows took place. Two different types of anode spots, ring-like structures and self-organised hexagonal structures were observed.

Violations of the similarity laws are presented and the influence of gas heating on the discharge parameters in the high pressure case is demonstrated. Glow-discharges with operating voltages below the normal cathode fall voltage are presented. This work provides a broad overview of a variety of phenomena and a solid base for future research.



# Introduction

Since the first definition of *Plasma* by Langmuir [9] in 1928 generations of scientists and engineers worked and enlarged this interesting and comprehensive field. Nowadays, the scope of plasma physics ranges from the cold plasmas of glow discharges to the elemental forces of future fusion reactors.

Industrial plasma are used to modify and to coat surfaces, to cut and weld, as illuminants, ... to mention a few examples. In the last couple of years an increasing general interest in high pressure glow discharges is observable. The advantages are at hand. With a good understanding of high pressure glow discharges it is possible to miniaturise devices and save expensive and maintenance-intensive vacuum equipment. New applications like micro-analysis systems are possible with simple instrumentation, small detector sizes and good sensitivity [5].

Therefore it is interesting and important to revisit theories and ideas developed for low pressure discharges in the past. Another reason is that

*Partially ionized plasmas used in industry have been considered "dirty science" or a "black art" because they were developed empirically, without an understanding of the underlying physics.* Francis F. Chen, UCLA

In the beginning the main objective of this thesis was to investigate similarity laws of DC glow discharges in the high pressure case. After first measurements it soon become evident that a strict compliance to the initial setting of tasks would skip a couple of interesting observations. Therefore a broader approach was chosen and seven areas of interest turned out.

- Ignition behaviour
- Determination of reduced normal current densities
- Pressure dependence of the positive column cross section
- I-V characterisation of similar discharges
- Field strength in the positive column of similar discharges
- Sheath measurements of the cathode dark-space
- Characterisation and behaviour of anode spots

The extension of the project definition was possible because of the use of a simple but flexible discharge chamber developed during a foregoing project work. Due to the broad approach it was not possible to study all encountered phenomena in detail. Anyway discrepancies with the classic theories are revealed and explanations are given as good as possible in the limited framework of a diploma thesis. The intention of this text is to point out interesting fields of activity and provide a base for future research.



# Chapter 1

## Theoretical Background

### 1.1 Definition of Plasma

A useful but simple definition of a Plasma is given by Chen [3].

*A plasma is a quasineutral gas of charged and neutral particles which exhibits collective behaviour.*

The postulation of quasineutrality requires that the Debye length  $\lambda_D$  is much smaller than the dimensions  $L$  of a system.  $\lambda_D$  is a measure of the shielding distance of the sheath. In addition to  $\lambda_D \ll L$  the number  $N_D$  of particles in a Debye sphere must be much greater than 1 to satisfy the claim for collective behaviour. The third criterion necessary is that the motion of charged particles is controlled by electromagnetic and not by hydrodynamic forces. This implies that the mean time  $\tau$  between collisions with neutral atoms is much greater than the reciprocal of the frequency of typical plasma oscillations  $\omega$ . The three conditions a plasma must satisfy are therefore:

$$\lambda_D \ll L$$

$$N_D \gg 1$$

$$\omega\tau > 1$$

### 1.2 Ignition of a DC glow discharge

The glow discharge is a *self-sustaining* discharge with a *cold* cathode. For ignition a few "seed" electrons are necessary. These may be generated due to cosmic radiation or by radioactive isotopes. After applying a voltage high enough to satisfy the condition for initiating a self-sustaining discharge ignition occurs. Due to a potential difference electrons become accelerated towards the anode. On their way these electrons ionize some atoms of the neutral gas. These heavy and slow ions are accelerated towards the cathode. Due to the ion bombardment on the cathode, secondary electrons are emitted. Every electron causes an avalanche of secondary electrons which sustain the discharge.

After a few  $\mu s$  a positive space charge layer develops at the cathode. The potential drop is called *cathode fall*. If the inter-electrode separation is large enough, an electrical neutral plasma region is formed between the cathode layer and the anode. The relatively homogenous middle part is called the *positive column*. The plasma in this region is described as *weakly ionized nonequilibrium plasma* [19] sustained by an electric field.

### 1.3 Townsend's 1<sup>st</sup> and 2<sup>nd</sup> ionization coefficients

As explained in Sec.1.2 single seed electrons create electron avalanches [19]. These avalanches evolve in time and space. Therefore it is convenient to characterize the *ionization coefficient*  $\alpha$  as a number of ionization events per unit distance per electron.  $\alpha$  is obviously given by

$$\alpha = \nu_i/v_d \quad (1.1)$$

where  $v_d$  is the drift velocity and  $\nu_i$  is the ionization frequency. Note that the primary and complete characteristic of the rate of ionization is the frequency  $\nu_i$ !

Theoretical and numerical analysis often use the empirical formula suggested by Townsend Eq.[1.2].  $E$  is the electric field,  $p$  the pressure and  $N$  the number density.

$$\alpha = Ap \cdot e^{-\left(\frac{Bp}{E}\right)} \quad \text{or} \quad \frac{\alpha}{N} = A_1 \cdot \exp\left(-\frac{B_1}{E/N}\right). \quad (1.2)$$

$A$ ,  $B$ ,  $A_1$  and  $B_1$  are determined from the experiment.

Yuri Raizer [19] suggested Eq.[1.3] for inert gases like helium which leads to better results.

$$\alpha = Cp \cdot e^{-D\sqrt{\frac{p}{E}}} \quad \text{or} \quad \frac{\alpha}{N} = A_1 \cdot e^{-B_1\sqrt{\frac{N}{E}}}. \quad (1.3)$$

More recent works of Marić et al. [14] show that Eq.[1.2] and Eq.[1.3] are only valid for small  $E/N$  regions. Fits for the electron ionization coefficient  $\alpha/N$  with Eq.[1.4] give better results in a larger range of the reduced field strength  $E/N$ .

$$\frac{\alpha}{N} = \sum_i A_i \cdot \exp\left(-\frac{B_i}{E/N}\right) \quad (1.4)$$

The  $B_i$  value gives an  $E/N$  range where the term  $i$  is significant. At the same time  $A_i$  provides an insight of the maximum contribution of the term [14]. Tab.1.1 shows the

Table 1.1: Constants  $A_i$  and  $B_i$  from Eq.[1.2], Eq.[1.3] and Eq.[1.4] for helium.

Eq.	Author	$A_1$ $10^{-21} m^2$	$B_1$ in Td	$A_2$ $10^{-21} m^2$	$B_2$ in Td	range of $E/N$ in Td
Eq.[1.2]	Raizer [19]	12	136	-	-	60 – 455
Eq.[1.3]	Raizer [19]	17.6	28	-	-	300
Eq.[1.4]	Marić et al. [14]	1.7	75	8	350	10 – 900

constants for the presented equations.  $E/N$  and  $B_i$  are given in units of Townsend (Td) -  $1Td = 10^{-21} m^2$ ,  $1V/cmTorr = 3.034 Td$  at 293 K. The constants for Eq.[1.2] and Eq.[1.3] are transformed from CGS to SI units. The pressure  $p$  is replaced by the number density using the gas equation  $p = N \cdot k \cdot T$ . The temperature  $T$  is set to 293 K.

## 1.4 Condition for initialising a self-sustaining discharge

The current at the cathode in stationary state [19] can be written as

$$i = i_{e^-} + i_{i^+} = i_0 \exp(\alpha d) / \{1 - \gamma[\exp(\alpha d) - 1]\}. \quad (1.5)$$

$\gamma$  is the effective *secondary emission coefficient* for the cathode. The emission is mainly caused by ions (photons, metastable atoms, ...). As long as the denominator is positive the current remains not-self-sustained.

$$\gamma[e^{\alpha d} - 1] = 1 \quad (1.6)$$

Eq.[1.6] represents a *steady self-sustained current* in a homogenous field  $E_i = V_i/d$ . Townsend's law implies no space charge. Ignition occurs if the *ignition condition* is fulfilled

$$\gamma[e^{\alpha d} - 1] > 1. \quad (1.7)$$

Substituting Eq.[1.2] into Eq.[1.7] with  $E_i = V_i/d$  gives the well known formula for the *ignition potential*  $V_i$

$$V_i = \frac{B_1 \cdot (pN)}{C + \ln(pN)} \quad (1.8)$$

with  $C = \ln[A_1/\ln(1/\gamma + 1)]$ . The experimental curves  $V_i(pd)$  are called *Paschen curves* (Fig.1.1). Note that  $V_i$  depends also on  $\gamma$ . The ignition potential therefore is not independent from the cathode material [8].

Using Eq.[1.3] gives a different expression of  $V_i$  for inert gases. Eq.[1.9] was used for the analysis in Sec.1.2.

$$V_i = \frac{B_1^2 \cdot (pd)}{\ln^2\left(\frac{\ln(\frac{1}{\gamma}+1)}{A_1 \cdot (pd)}\right)} \quad (1.9)$$

Eq.[1.4] substituted into Eq.[1.7] was not used to fit the data in Sec.1.2. The fit is not significant better than Eq.[1.9] but needs more computational effort. The equation can only be solved numerically.

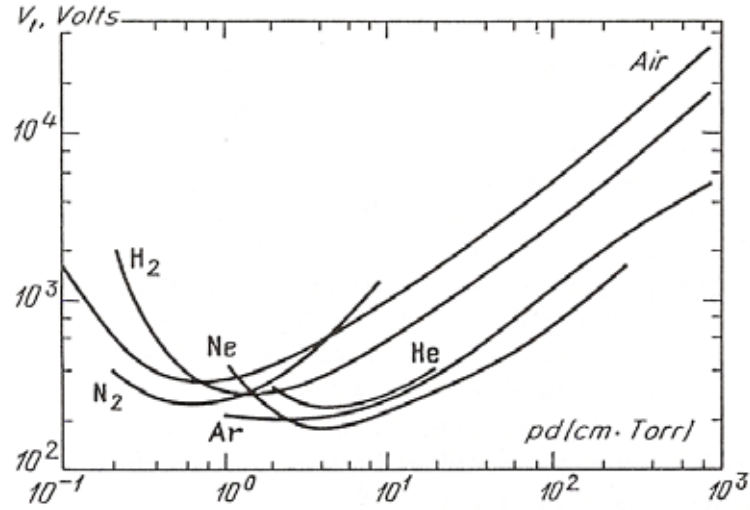


Figure 1.1: Breakdown potentials in various gases over a wide range of  $pd$  values on the basis of data given in [19] (p. 134)

## 1.5 General structure and observable features of a stable DC glow discharge

The pattern of light emission pictured in Fig.1.2 is typical for DC glow discharges. A qualitative interpretation of the light emission pattern is given by Raizer [19]. Please refer to the book for a more detailed description. At higher pressures all the layers become thinner and shift closer to the cathode. The only features that are visible at atmospheric pressures are the cathode dark space, the negative glow, the Faraday dark space, the positive column and the anode glow (Fig.1.2).

Fig.1.2 gives also a simplified presentation of the basic parameters and structure of a glow discharge like glow intensity, potential  $\varphi$ , longitudinal field  $E$ , current densities  $j_e$  and  $j_+$ , charge densities  $n_e$  and  $n_+$  and the space charge  $\rho = e(n_+ - n_e)$ .

Fig.1.3 depicts the  $V - I$  characteristic of a DC discharge between electrodes for a wide range of currents.  $V_t$  is the ignition potential. This voltage ensures the stationary reproduction of electrons ejected from the cathode and pulled to the anode. As long no space charge develops  $V_t$  remains constant (region BC). This self-sustaining discharge mode is observed at currents of  $i \sim 10^{-10} - 10^{-5}$  A. This mode is called Townsend dark discharge. Ionization is so small that no light emission is visible [19].

The region DE corresponds to the normal glow discharge. The remarkable property is that the current density at the cathode remains unchanged. The luminous spot at the cathode, the negative glow (Fig.1.2) expands with increasing current. When no more free surface is left, the current is increased by increasing the voltage hence, extracting more electrons by unit surface area. This is the region of abnormal glow EF.

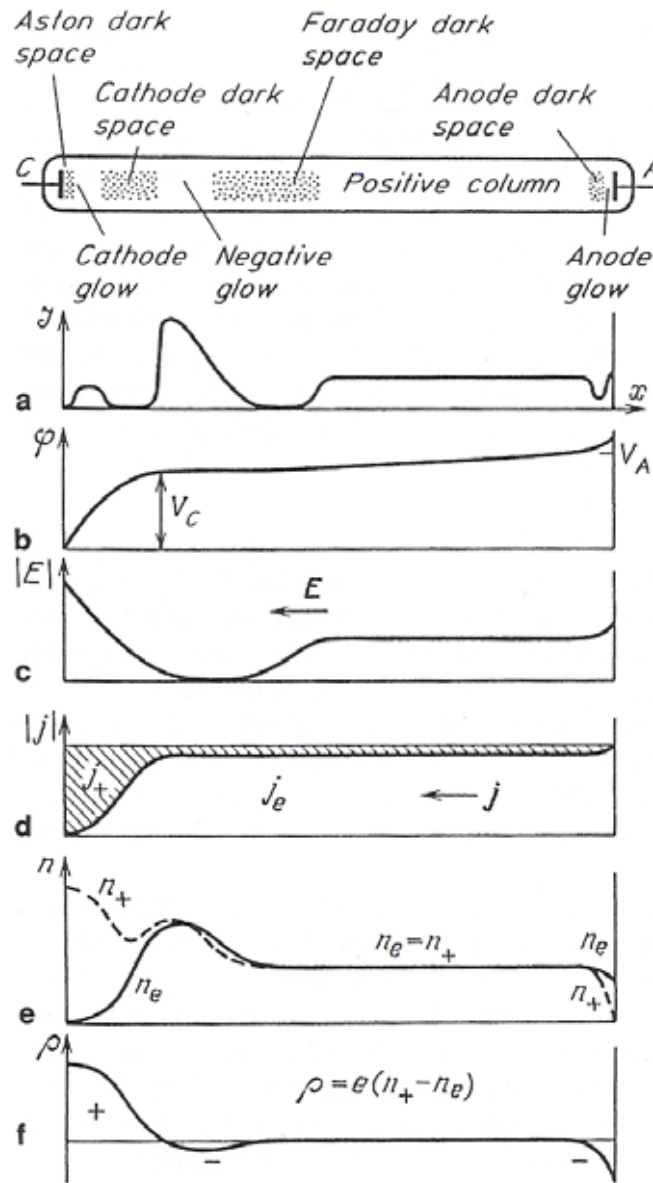


Figure 1.2: Glow discharge in a tube and the distribution of: (a) glow intensity, (b) potential  $\varphi$ , (c) longitudinal field  $E$ , (d) electronic and ionic current densities  $j_e$  and  $j_+$ , (e) charge densities  $n_e$  and  $n_+$  and (f) space charge  $\rho = e(n_+ - n_e)$  from [19] (p. 169)

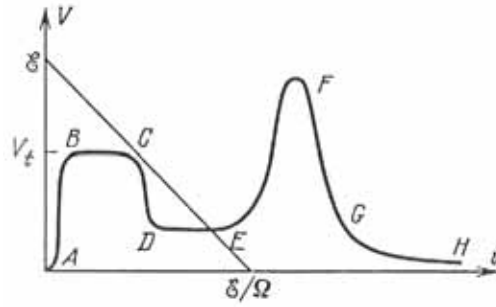


Figure 1.3:  $I - V$  characteristic of discharge between electrodes for a wide range of currents and the loading line: (A) region of non-self-sustaining discharge, (BC) Townsend dark discharge, (DE) normal glow discharge, (EF) abnormal glow discharge, (FG) transition to arcing, (GH) arc [19] (p. 173)

GH represents the arc discharge. In this mode the cathode is so hot that thermal electron emission is predominant over secondary electron emission. The discharge is very hot and strongly contracted. The discharge voltage is very low.

The operation mode is set via the load line Eq.[1.10]. The line is the steeper, the larger the external resistance.

$$\varepsilon = V + i\Omega \quad (1.10)$$

The ohmic resistance  $\Omega$  sets the absolute limit to the current. This resistance is either specially introduced or the resistance of the lead wires and power supply.

## 1.6 Similarity relations

The variation of some of the parameters e.g. the pressure, inter-electrode separation has a direct influence on the pattern of light emission. An increase in pressure leads to thinner layers, shifted towards the cathode [19]. An elevated pressure also causes the column to contract to the axis.

If the electrodes are moved closer at constant pressure, the positive column is shortened. If the inter-electrode distance is thinner than the cathode layer, the glow discharge cannot be sustained.

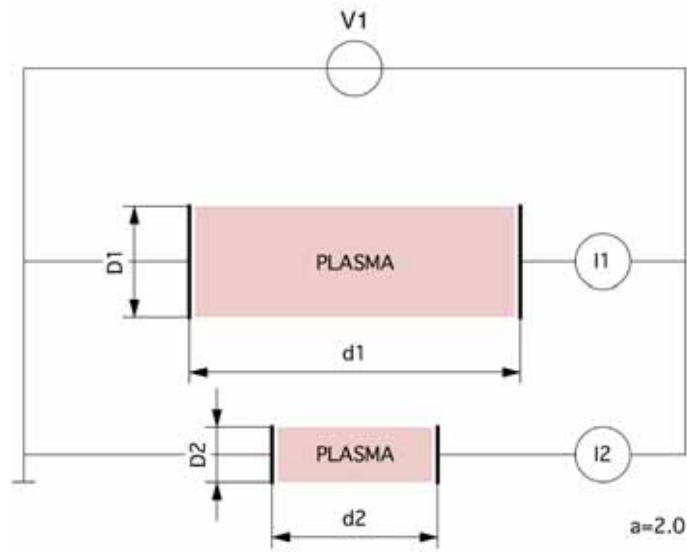


Figure 1.4: Similar discharges  $p_1 d_1 = p_2 d_2 = const$  ( $I_1 = I_2$ )

Therefore, it is interesting to ask if it is possible to find similarity laws to scale e.g. a very well understood discharge to smaller or bigger geometries (Fig.1.4). As described in [21] two glow discharges with the same voltage drop  $V_1$ , and drawing the same current  $I$  are said to be similar if their electrodes separation is

$$d_1 = a \cdot d_2 \quad (1.11)$$

and the electrodes diameters are given by

$$D_1 = a \cdot D_2. \quad (1.12)$$

In addition, also the scaling of the pressures

$$p_2 = a \cdot p_1 \quad (1.13)$$

the mean free paths

$$\lambda_1 = a \cdot \lambda_2 \quad (1.14)$$

the electric fields

$$E_2 = a \cdot E_1 \quad (1.15)$$

the current densities

$$J_2 = a^2 \cdot J_1 \quad (1.16)$$

and the scaling of the electron number densities in the two discharges

$$n_{e2} = a^2 \cdot n_{e1} \quad (1.17)$$

are given by the same factor  $a$ . Using this relations we get the result that the breakdown parameter  $pd$  is the same in similar discharges

$$p_1 d_1 = p_2 d_2 = \text{const.} \quad (1.18)$$

Further we get results for the ratio of the electric field to pressure

$$\frac{E_1}{p_1} = \frac{E_2}{p_2} = \text{const.} \quad (1.19)$$

for the reduced current density

$$\frac{j_1}{p_1^2} = \frac{j_2}{p_2^2} = \text{const.} \quad (1.20)$$

and for the paramter  $\alpha/p$

$$\frac{\alpha_1}{p_1} = \frac{\alpha_2}{p_2} = \text{const} \quad (1.21)$$

where  $\alpha$  is Townsend's first ionization coefficient.

## 1.7 Scope of the similarity laws

A. von Engel summarises processes which violate the similarity rules in his book "Ionized gases" [28] in Appendix 1. In order to show that in similar discharges only certain fundamental processes are allowed, it is necessary to test whether the rate processes transform according to the rules in Sec.1.6, i.e.

$$\left(\frac{\partial N}{\partial t}\right)_1 = \frac{1}{n^3} \left(\frac{\partial N}{\partial t}\right)_2. \quad (1.22)$$

The results of this considerations is presented in Tab.1.2. The similarity rules serve a dual

Table 1.2: Validity of the similarity laws

Permissible	Forbidden
Ionization by single collision	Stepwise ionization
Ambipolar diffusion	Photoelectric emission
Electron attachment and detachment	Field emission
Neutralization charge transfer	Ionization charge transfer
Ion-ion recombination at high $p$	Ion-ion recombination at low $p$

purpose: they predict the behaviour of a discharge when its parameters are changed and they facilitate sometimes discrimination between fundamental processes.

### 1.7.1 Density correction for the similarity laws.

As in Sec.1.6 described, two discharges are to be said similar if they draw the same current  $I$  and have the same voltage drop. An increased pressure therefore leads to an increased power density and therefore to higher gas temperatures and decreased gas densities.

Therefore measured current densities for example at higher temperatures are too low [27]. A. v. Engel et al. introduced a mathematical method to correct the error due to gas heating.

The derivation is based on three assumptions:

- The problem is linear.
- The gas is heated by friction of ions and neutral gas atoms.
- The cathode fall is linear.

The assumption of a linear cathode fall leads to a simple equation for the field strength  $E(x)$  and the current density  $j_0^+(x)$  in the cathode fall region

$$E(x) = E_0 \cdot \left(1 - \frac{x}{d}\right) \quad (1.23)$$

$$j^+(x) = j_0^+ \cdot \left(1 - \frac{x}{d}\right) \quad (1.24)$$

where  $E_0$  is the field strength on the cathode's surface and  $j_0^+$  the positive ion current density. The electron current density is neglected (Sec.1.5). The generated heat per area unit and

sheath thickness  $dx$  is given by

$$dQ = j_0 E_0 \cdot \left(1 - \frac{x}{d}\right)^2 dx. \quad (1.25)$$

In stationary state the heat must be absorbed by the cold cathode (cooled) which yields a temperature  $T_k$  on the cathode's surface. In thermodynamical equilibrium the equation of thermal conduction is given by

$$E(x)j^+(x) + \lambda(T)\frac{d^2T}{dx^2} + \frac{d\lambda}{dT}\left(\frac{dT}{dx}\right)^2 = 0 \quad (1.26)$$

where  $\lambda$  is the thermal conductivity of the gas ( $\lambda(T) = \alpha \cdot T$ ).  $\alpha$  denotes a gas specific coefficient. As a first approximation for  $\alpha$ ,  $\lambda$  is divided by  $T = 286 \text{ K}$ . The boundaries for Eq.[1.26] are

$$\frac{dT}{dx} = 0 \quad \text{for } x = d \quad \text{and} \quad T = T_k \quad \text{for } x = 0 \quad (1.27)$$

giving the solution

$$T_x - T_k = d \cdot \left(\frac{2x}{d} - \frac{x^2}{d^2}\right) \sqrt{\frac{E_0 j_0}{6\alpha}}. \quad (1.28)$$

The average Temperature in the cathode fall region is given by

$$\bar{T} = \int_0^d T_x dx = T_k + \frac{2}{3}d \sqrt{\frac{E_0 j_0}{6\alpha}}. \quad (1.29)$$

The similarity relations for  $j_0$ ,  $E_0$  and  $d_0$  are given by

$$j_0 = j_1 \left(\frac{pT_1}{\bar{T}}\right)^2 \quad E_0 = E_1 \left(\frac{pT_1}{\bar{T}}\right) \quad d_0 = d_1 \left(\frac{\bar{T}}{pT_1}\right). \quad (1.30)$$

$j_1$ ,  $E_1$  and  $d_1$  are the parameters for a normal glow discharge at  $p=1$  and a temperature  $T_1$  (room temperature). Substituting  $j_0$  in Eq.[1.29] with Eq.[1.30] and assuming a linear electric field  $E_0 = 2V_k/d$  leads to an expression for the average temperature  $\bar{T}$  in the cathode fall region depending on the pressure  $p$ .

$$\bar{T} - T_k = \frac{2}{3} \sqrt{\frac{V_k j_1 d_1}{3\alpha}} \sqrt{\frac{pT_1}{\bar{T}}} \quad (1.31)$$

Substituting  $\bar{T}$  by the current current density  $j_0$  (Eq.[1.30]) on the cathode's surface gives an equation for  $p$  depending on the current density  $j_0$ .

$$p = \frac{T_k}{T_1} \sqrt{\frac{j_0}{j_1}} + \frac{2}{3T_1} \sqrt{\frac{V_k j_1 d_1}{3\alpha}} \sqrt[4]{\left(\frac{j_0}{j_1}\right)^3} \quad (1.32)$$

## 1.8 Determination of gas temperatures via optical spectroscopy

The rotational spectra of diatomic molecules like  $OH$  can be used to determine gas kinetic temperatures. The line intensities of absorption or emission are proportional to the population densities. In thermodynamical equilibrium the population density for an initial state with the energy  $E_j$  is given by the Boltzmann equation [13]. The population therefore is

$$\frac{N(E_j)}{N} \propto (2j + 1) \cdot e^{-\frac{E_j}{kT}}. \quad (1.33)$$

$k$  is the Boltzmann constant,  $T$  the temperature and  $N$  the population densities. Therefore, it is possible to determine the absolute temperatures of a gas by comparison of the relative line intensities.



## Chapter 2

# Experimental details

### 2.1 Used equipment and experimental setup

The experiment was designed during a project-work in preparation for this diploma thesis. Discussions with Prof. Laimer, Prof. Störi and Ing. Beck resulted in guidelines for the construction. The high pressure chamber (Fig.2.1) was manufactured in the workshop of the "Institut für Allgemeine Physik, TU Wien". All experiments took place in the "Plasma chemistry" laboratory.

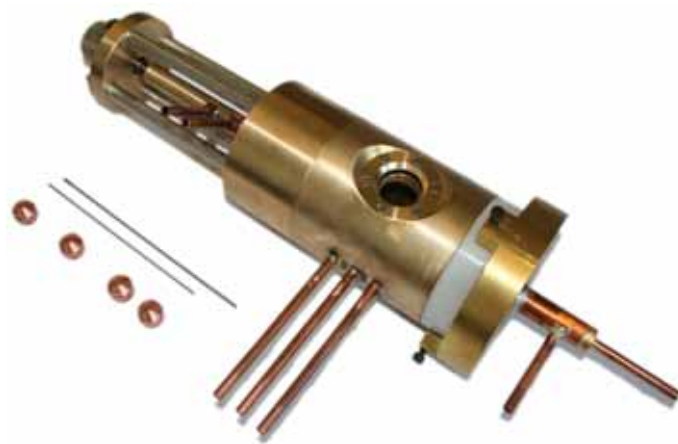


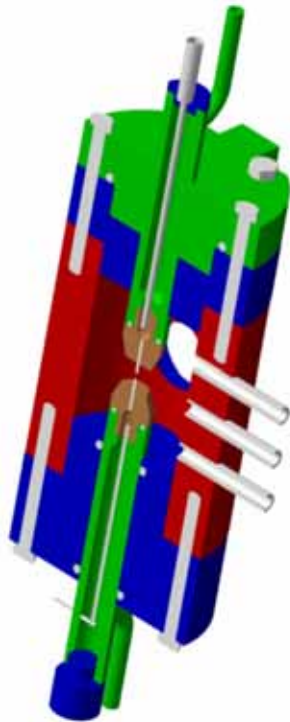
Figure 2.1: The high pressure chamber

The whole set of production drawings, the parts list, used materials ... and a few comments concerning the construction can be found in the appendix (Sec.B and Sec.C). During operation minor changes took place which are not documented in this text. The following chapter provides an overview about the measurement system and a brief manual. Furthermore, there are recommendations for improvements.

In the last part of this chapter problems, difficulties and imperfections will be presented and some recommendations how to enhance the high pressure chamber.

### 2.1.1 Measurement system

As mentioned in Sec.1.7.1 variable electrode diameters, variable inter-electrode gaps and proper cooling conditions are required in order to investigate similarity laws in the high pressure case. These requirements built the foundation for the construction. Fig.2.2 shows a cross section of the device. Another requirement was simplicity and variability to allow a big spectrum of measurements because of little knowledge in this new field of interest. Last but not least it was decided to build the whole experiment "in-house" to reduce costs and to have the possibility to carry out modifications faster and easier.



- Maximum voltage:  $2.0 \text{ kV}$
- Maximum pressure:  $2000 \text{ hPa}$
- Electrode diameters:  $1.6 - 15 \text{ mm}$
- Max. inter-electrode gap:  $7.0 \text{ mm}$

Figure 2.2: Cross-section of the high pressure discharge chamber

The core of the system consists of two electrode copper-heads (brown, Sec.C.1, PL1). These electrodes are replaceable in order to change the electrode diameters. The discharge is located between the two white pins and can be observed through a quartz window. In the case of pure copper electrodes the whole part is manufactured in one piece (brown+white). Otherwise the pin becomes pressed into the copper body. The pins are shielded with  $Al_2O_3$  or Teflon tubes (Sec.C.1, PL1). These tubes prevent that the negative glow can grow backwards on the electrodes surface (Sec.2.2.1). These cylinders ensure well defined conditions (two parallel circular surfaces). Both electrode-heads are screwed into two water-cooled electrode carriers (green, Sec.C.1, PL8 and PL9). For this high pressure chamber a pipe in pipe cooling system is used. The water stream points directly towards the back of the electrode. The lower electrode carrier is the anode and on earth potential. Therefore no insulation to the main body (red, Sec.C.1, PL2) is necessary. This part is moveable and is guided with two o-rings in the brass-body (blue). The upper electrode is the cathode. This electrode is insulated from

the brass-body (red) with a Teflon part (blue) and lies on a negative potential. The screws are also insulated with Teflon-tubes. This part is shielded with a grounded cage for safety reasons (Fig.2.5).

Fig.2.3 depicts the equivalent circuit and Fig.2.4 the gas-flow diagram of the setup. Tab.2.1 gives an overview of the used equipment. The distance of the electrodes is adjustable with a micrometer head with a thread pitch of  $0.75\text{ mm}$  ( $1' \equiv 0.05\text{ mm}$ ).

The pressure is controlled with two valves (Fig.2.4). One controls the gas-flow from the gas cylinder (5) and the second one regulates the effective pumping speed of the *Alcatel* backing pump (6). The pressure is measured with a *MKS Baratron* capacitance manometer and a *WIKA EN837-1* bourdon tube pressure gauge for pressures above  $1000\text{ hPa}$ .

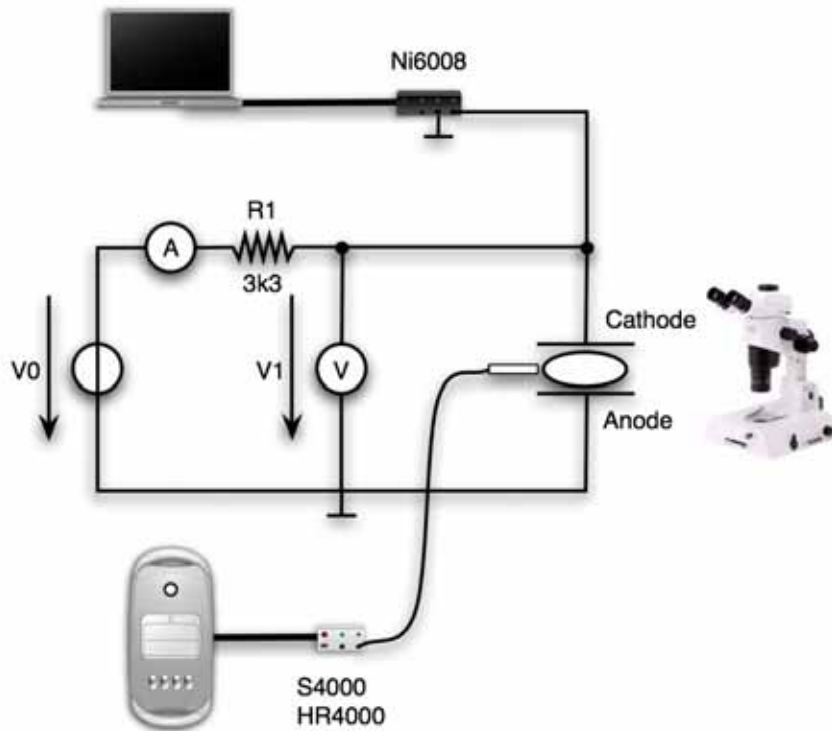


Figure 2.3: Equivalent circuit of the setup

The power supply unit is a *Fug MCN350-2000* with a maximum voltage of  $2000\text{ V}$  and a maximum current of  $150\text{ mA}$ . The current is measured with a *Voltcraft VC160* and the voltage with a *Fluke75 Serie II* multi-meter. Long-time measurements are performed with a *Ni6008* ADC-USB card and a *Powerbook G4 12"* with  $1.5\text{ GHz}$ .

For optical investigations an *Olympus SZX12* stereo microscope is used. Related equipment is an *Olympus 3100* highlight and an *Olympus 330e* consumer camera. Optical spectroscopy is done with an *Ocean Optics optical spectrometer S4000* and a *HR4000* ADC. The data is read by a *Hewlett Packard* PC with a Pentium 4 ( $3.4\text{ GHz}$ ) processor. Fig.2.5 and Fig.2.6 give an impression of the whole setup in the "Plasma chemistry" laboratory.

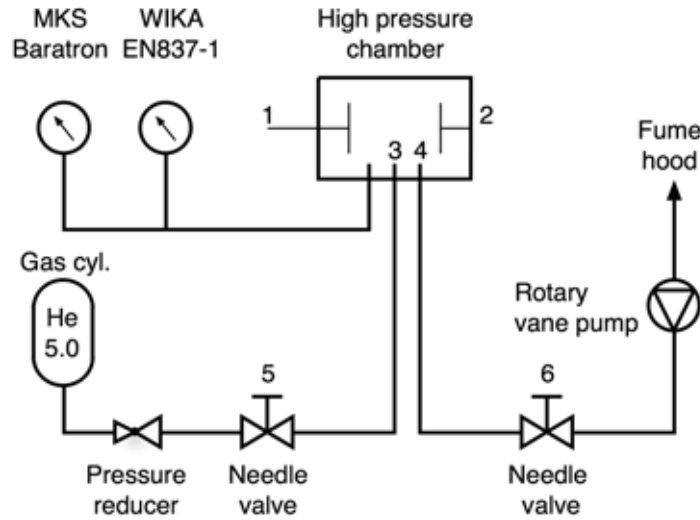


Figure 2.4: Gas-flow diagram of the laboratory setup, 1...moveable anode, 2...fixed cathode, 3...gas inlet, 4...gas outlet, 5...inlet valve, 6...outlet valve

Table 2.1: Parts list

Device	Range	Type
Backing pump		Alcatel
Pressure gauge	0 – 1.0 bar, 0 – 10 V	MKS Baratron
Pressure gauge	0 – 1.5 bar	WIKA EN837-1
Power supply unit	0 – 2000 V, 0 – 150 mA	Fug MCN350-2000
Voltmeter	0 – 1000 V	Fluke75 Serie II
Amperemeter	0 – 400 mA	Voltcraft VC160
ADC-USB card	0 – 10 V	Ni6008
Microscope		Olympus SZX12
Highlight		Olympus 3100
Camera		Olympus E-330
Spectrometer	S4000, ADC HR4000	Ocean Optics
Computer	G4 1.5G Hz, 1.25 GB RAM	Powerbook G4
Computer	P4 3.4 GHz, 1.00 GB RAM	Hewlett Packard

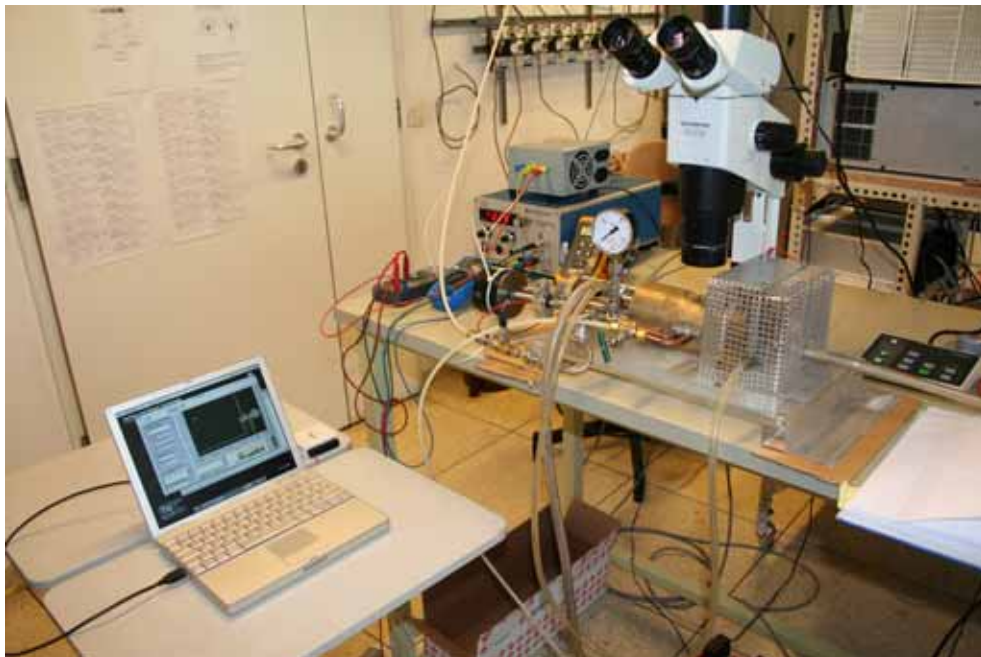


Figure 2.5: Photograph of the lab setup

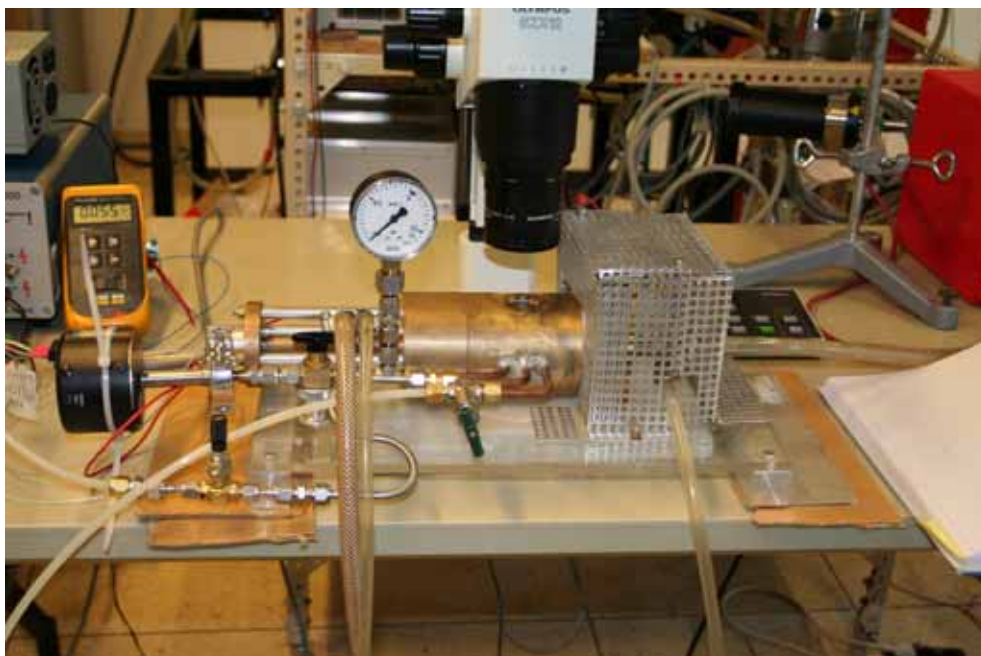


Figure 2.6: Close view of the high pressure chamber

## 2.1.2 A brief manual

### Preparation of the electrodes

In order to provide reproducible conditions a few proceedings turned out be useful. Before use the electrodes became grinded and cleaned. For this task a *Struers LaboPol-4* and waterproof silicon carbide abrasive papers (FEPA *P500 – P4000*) were used. After that the electrodes became cleaned in a ultrasound bath of acetone for about ten minutes and were packed in aluminium foil. During assembly electrodes were only handled with gloves and pliers.

### Preparations before the experiment

The chamber became evacuated and filled with He up to 1500 *hPa* for a couple of times. After that the backing pump evacuated the chamber for about ten minutes. Then cooling water was switched on. The chamber became evacuated for ten minutes again to allow the chamber to reach a stable temperature. The next step was to set the pressure to 100 *hPa* and to sputter each electrode for five minutes. Finally the chamber was evacuated again and was ready for further use.

### How to use the experiment

Distances are adjusted with a micrometer head. The scale has 15 ticks ( $1' \equiv 0.05 \text{ mm}$ ). Pressure is adjusted with two valves. One at the gas inlet and the second one at the backing pump inlet (Fig.2.4). The coolant water is directly regulated at the tap.

### Long-time measurements with the Ni6008 USB card

A *Ni6008* was used for the measurements in Sec.3.7.4. The maximum input voltage for the USB card is 12 V. Therefore a voltage divider is necessary (Fig.2.7). The input impedance of the *Ni6008* card is 144  $k\Omega$ . The used setup isn't suitable for high accuracy measurements but well enough to investigate the voltage drop in Fig.(3.39). The maximum of  $V_1$  was limited to

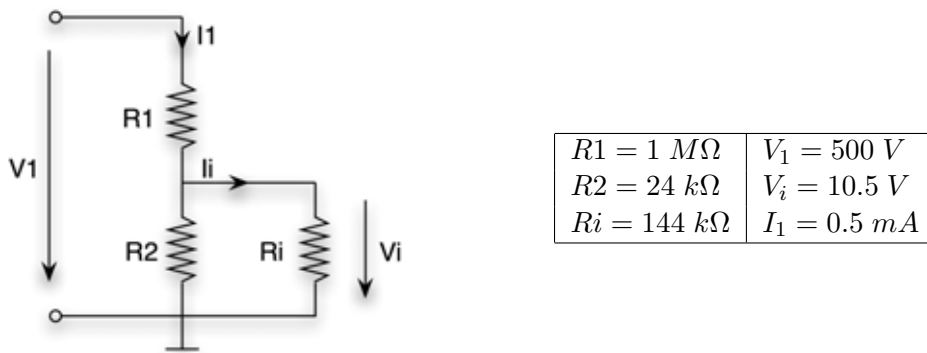


Figure 2.7: Equivalent circuit of the voltage divider

500 V to ensure a sufficient resolution of the usb card. A draw back is that it is not possible to connect the card permanently to the setup (Fig.2.3) because of ignition voltages up to 2 *kV*.

## 2.2 Difficulties and imperfectness of the experiment

### 2.2.1 Contamination of the plasma due to Teflon-shieldings

A couple of measurements show strong voltage drifts and a change in the optical behaviour of the discharge (Sec.3.7.4). Because of the fact that the optical spectra showed no fluorine lines (e.g. Fig.3.40) and that the shieldings (Sec.C.1, PL1) made a very good optical impression, Teflon wasn't thought as cause of this behaviour.

As measurements went on new shieldings made of ceramic ( $Al_2O_3$ ) were tested for experiments at higher powers. An old electrode which was priorly used with Teflon shieldings became grinded at the front-side and was used again. After the experiment the anode made an impression if it was covered with silver. It was likely that aluminium from the shield could have deposited at the anodes surface. Therefore XPS and Auger measurements were performed (Fig.2.8 and Fig.2.10).

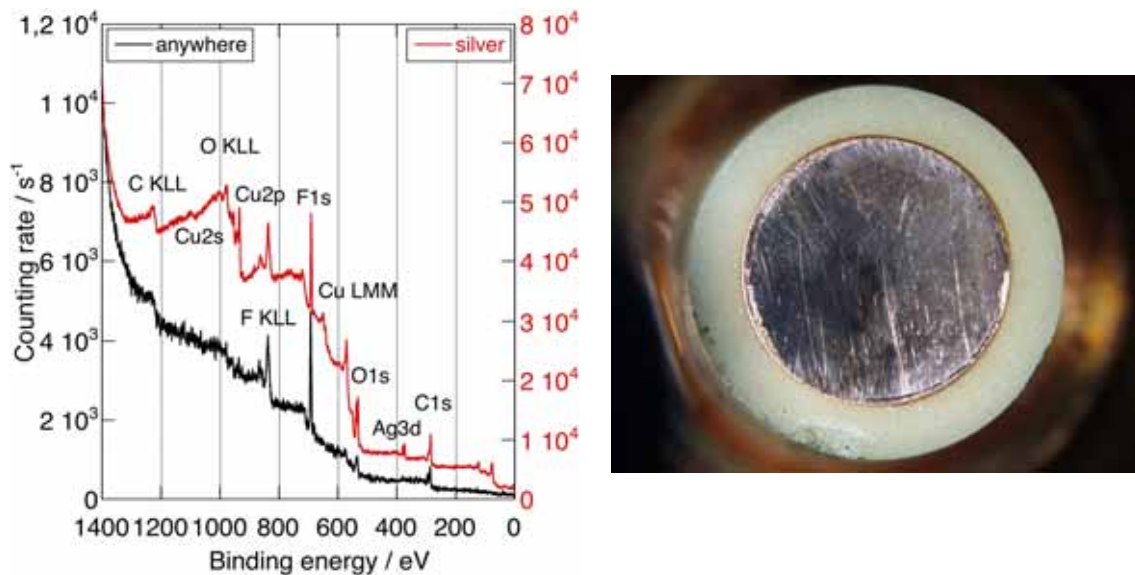


Figure 2.8: XPS of a possibly coated anode with an ESCALAB MkII, Al  $K_{\alpha}$  15 kV, 40 mA

XPS measurements showed among copper, oxygen, silver (conductive silver) and surprisingly also fluorine and carbon on the surface. The only material in the discharge chamber that persists of these elements was Teflon (Fig.2.9). A possible candidate for carbon were also the used silicon carbide abrasive papers.

The reason why it was possible to measure these elements although the front side was grinded is, that it was not possible to focus the X-ray beam completely on the grinded front-side. Therefore also surfaces from behind became measured which were not treated.

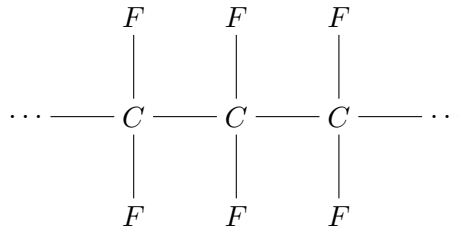


Figure 2.9: Chemical structure of Teflon (PTFE)

Auger-electron spectroscopy showed only a single silicon-peak, copper- and oxygen- but no fluorine- or carbon-peaks (Fig.2.10). The explanation is because of the well focused electron beam compared to the widespread X-ray beam from the XPS measurement. The silicon peak may originate from sandpaper crystals (SiC) which became integrated in the surface during the grinding process.

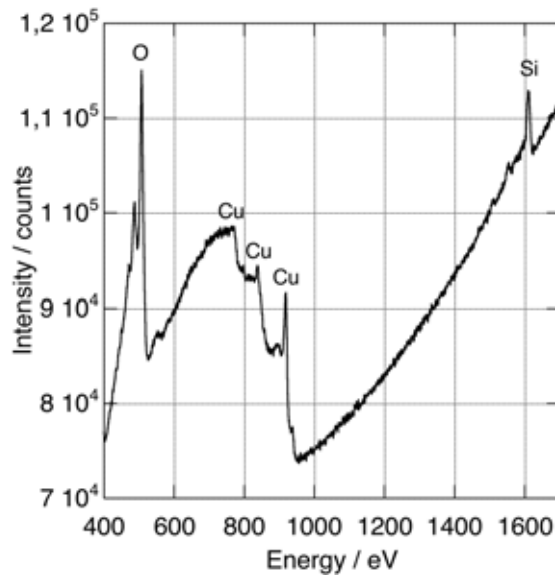


Figure 2.10: VG Microlab 310F Auger-electron spectrometer

Subsequent long-time measurements showed (Fig.2.11 and Fig.2.12) that the used Teflon-shieldings became decomposed. Teflon was used in the beginning because working on it is easy. It was also believed that the thermal stress would be minimal.

Fig.2.11 shows the anode after  $t > 5 h$  of use. The surface is coloured which may arise from oxides and other deposited elements. There is one single metallic looking spot which was the foot of one single very bright anode spot (Fig.3.39).

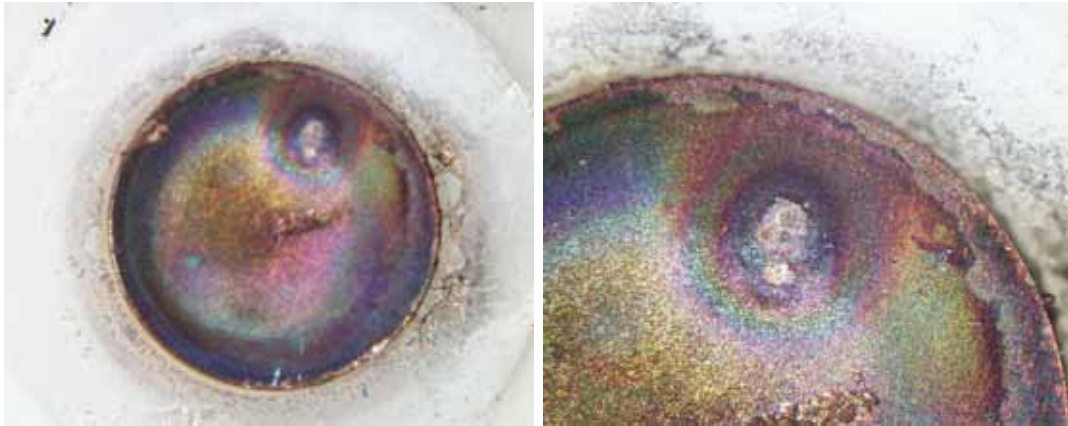


Figure 2.11: Anode after  $t > 5 h$  of use. The surface is coloured which may arise from oxides.

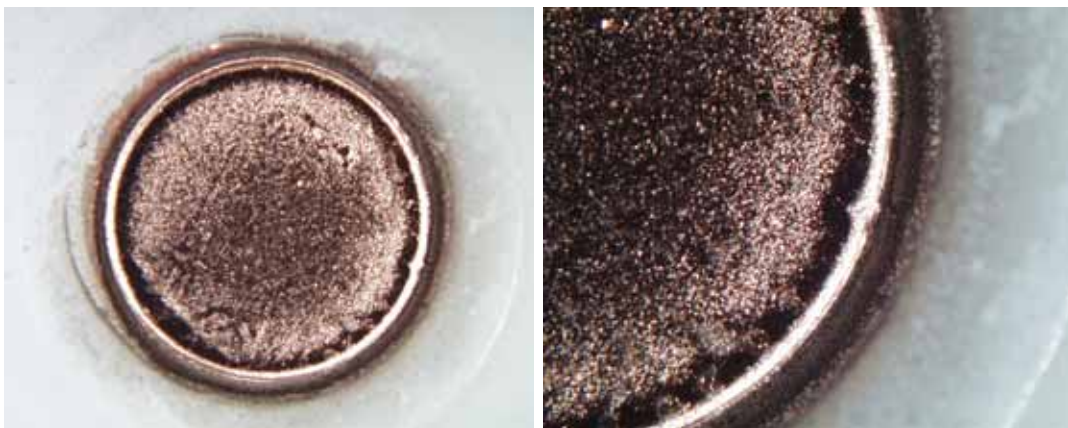


Figure 2.12: Cathode after  $t > 5 h$  of use. The surface is eroded by ion bombardment. Unfortunately, no profilometer measurements are available.

### 2.2.2 Increased ignition and discharge voltages due to contaminated helium

One big problem of all measurements was that it was impossible to monitor the gas composition and the gas flow. A contamination of helium with ambient air for example lead to a significant increase in ignition and discharge voltages.

Fig.A.4 ( $T = 445\text{ K}$ ) for example shows a typical spectrum. Additional to the helium lines, oxygen, hydrogen and the OH-band can be seen. These lines may arise from the unavoidable water film on the electrodes. An increase of the gas temperature also led to an increased line intensity of the OH band (e.g. Fig.A.11  $T = 975\text{ K}$ ). It's supposable that the line intensity corresponds to the fraction of water vapor in the gas.

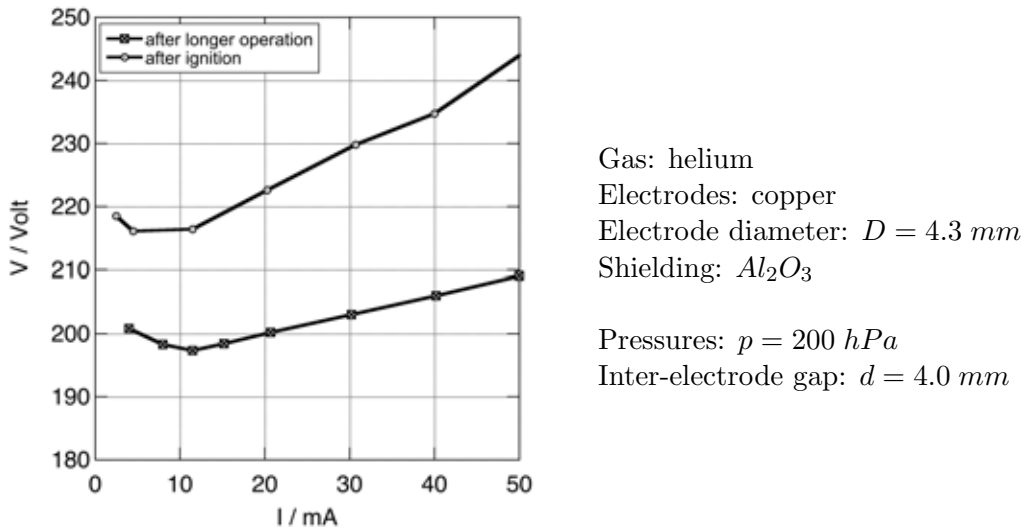


Figure 2.13: Influence of operation time on the discharge voltage

Investigations on the influence of gas composition and discharge voltage was not a subject of this study. Nevertheless Fig.2.13 shows two measurements with the same conditions. The measurement with the higher voltages were carried out directly after assembly of the chamber although the cleaning and preparation methods described in Sec.2.1.2 had been performed. The voltages are about 20 – 35 V higher than in the subsequent measurement. Other not documented measurements showed deviations up to 50 V.

## 2.3 Recommendations for improvements

### 2.3.1 Improvement of breakdown voltage determination

The breakdown probability depends on the preset  $pd$  value and on the amount of initial electrons (Sec.3.1.3). Higher  $pd$  values or a lack of initial electrons decrease the ignition probability. The fact that the voltage was raised by hand in the presented experiment is a big drawback.

- There is no feasible way to document the rise rate (volts/second).
- Slow and smooth ramp functions are not possible.
- It's possible to "overshoot" the lowest breakdown voltage depending on the ignition probability.
- The reproducibility is reduced.

All these facts reduce the reliability of the measurements. It's impossible to quantify the influence of breakdown delay times, memory effects [7] and the breakdown probability on the measurements. Fig.2.14 is a proposal for an enhanced measurement method using devices available at the institute.

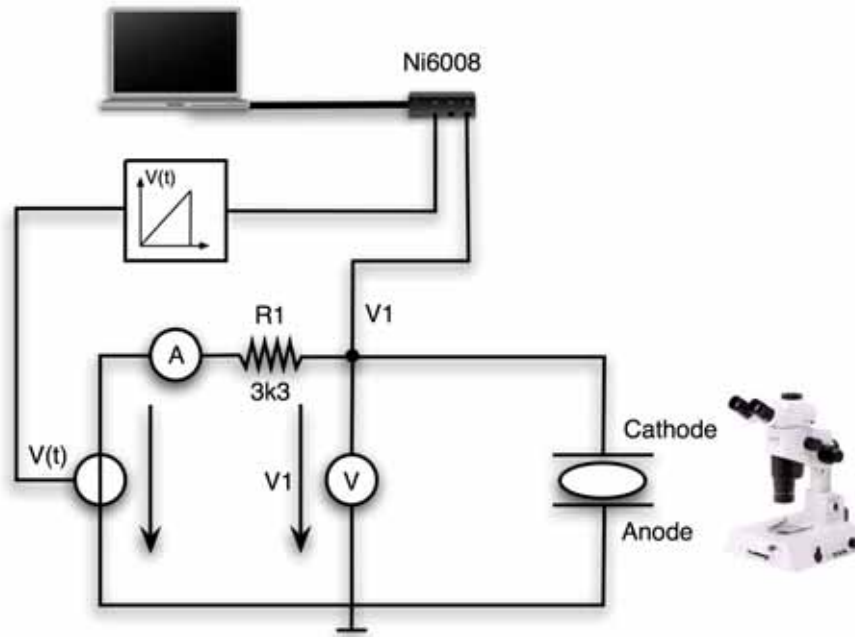


Figure 2.14: Proposal for an improved breakdown voltage determination

Requirements are a PC, an ADC-USB card and a power supply with control input. The flow chart (Fig.2.15) explains the principle in short. The PC triggers a ramp function generator (software) with adjustable rise rate. The voltage output of the ADC-USB card controls the power supply  $V(t)$ . One input of the ADC-USB card is used to measure the voltage  $V_1$ .

If the difference  $V(t) - V_1$  is larger than a preset value depending on the shunt resistor and the estimated current, the actual voltage level  $V(t)$  and the rise rate become saved (ignition voltage), the power supply is set to 0 V. If breakdown delay times or memory effects are the matter of interest [7] a photo-multiplier is necessary to detect the discharge.

### 2.3.2 Methods to monitor and improve the gas quality

As described in Sec.2.2.2 the gas composition and the gas flow are unknown parameters in all measurements.

A flow controller is recommend to control the gas flow. A quadrupole mass spectrometer should be used to control the composition of the gas flowing through the discharge tube. helium 5.0 (purity 99.999 %) was used for all experiments. A rather expensive way to improve the gas quality is to use helium 6.0. A purification cartridge in the gas main can be used to remove oxygen and water vapour from the gas cylinder.

A standard method to improve the gas quality is to bake the chamber out before use. A couple of minutes at 150 °C with continuous pumping should be enough to remove water vapour from the chamber. According to the data sheets of the Teflon parts and the Viton o-rings this temperature is permissible. Although a life time reduction of the o-ring seals is possible.

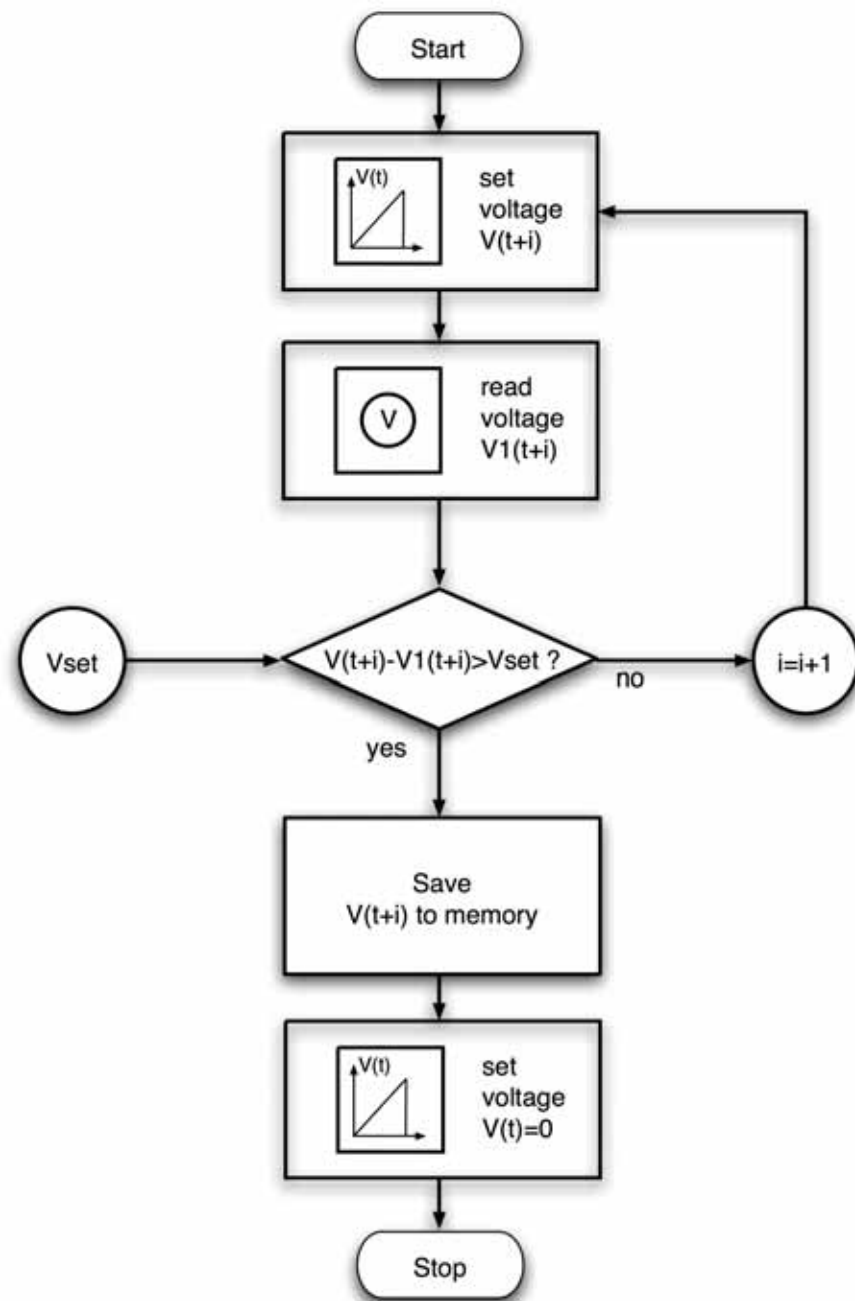


Figure 2.15: Flow chart for a possible breakdown voltage measurement software



## Chapter 3

# Results & Discussion

Measurements within one measurement series were performed on the same day without interruptions or breaks. The whole set of results and the appendant measurement tables are in appendix Sec.A. Photographs (the anode is always at the left-hand side) and optical spectra of the discharges complete the data-sheets. The optical spectra are used to determine the gas composition [25] and the temperature. For temperature determination the *OH*-band [16] was used. Simulations of the *OH* spectra were performed with *Lifbase 2.0* [12] (e.g. Fig.3.1 and Fig.3.2). The program settings are given in separate tables. The integration times of the optical spectrometer are given in the figure caption.

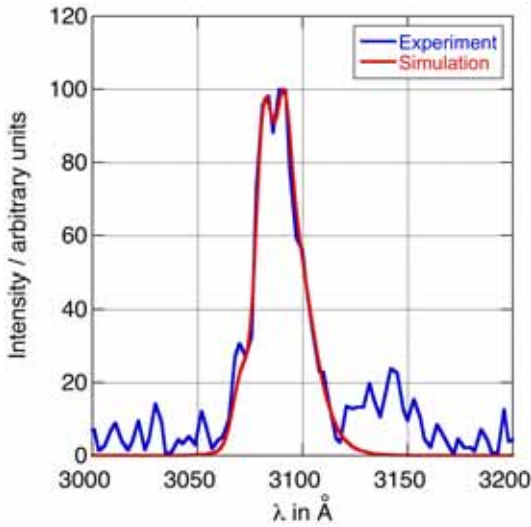


Figure 3.1: *OH*-band at  $p = 400 \text{ hPa}$   
 $T = 305 \text{ K}$  for  $P = 2.5 \text{ W}$

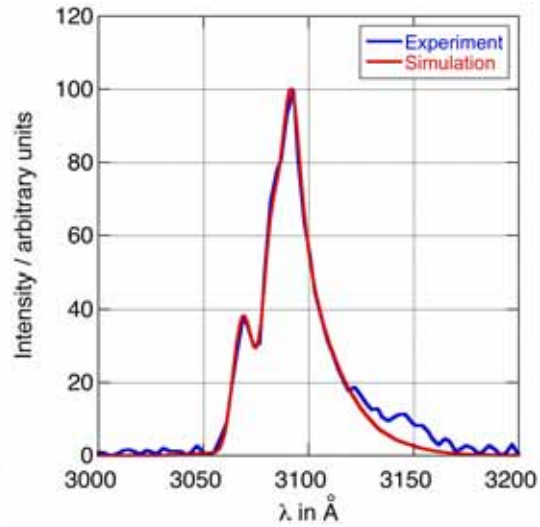


Figure 3.2: *OH*-band at  $p = 1200 \text{ hPa}$   
 $T = 950 \text{ K}$  for  $P = 10.4 \text{ W}$

The photos and spectra for Sec.A.1 were taken at the maximum possible inter-electrode gap distance  $l_{i_{max}}$  ( $i = 1, 2, 3$ ). All photos exhibited in Sec.A.2 were taken at full coverage of the cathode with negative glow.

### 3.1 Investigations on breakdown voltages

This section deals with the measurement of Paschen curves in the high pressure case. Helium was used for all experiments. Measurements were performed for nickel (coated copper electrodes) and copper electrodes.

Additional to the standard setup (Fig.2.3) the cathode became irradiated by ultraviolet light (Fig.3.3). The idea was to generate initial electrons by secondary electron emission from the cathode's surface. The amount of initial electrons corresponds to the breakdown probability. The breakdown probability also depends on the gas pressure and gap spacing (Sec.3.1.3).

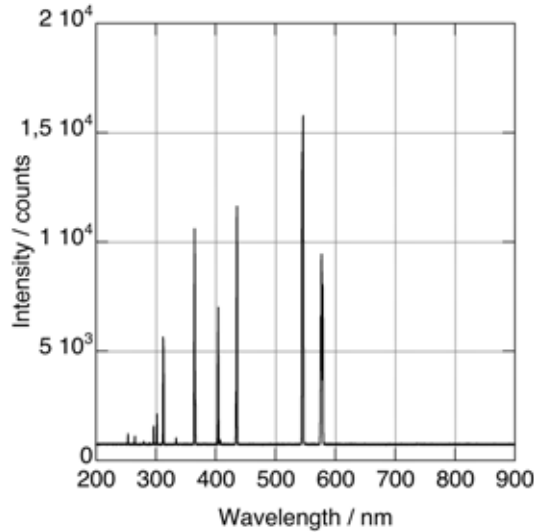


Figure 3.3: Optical spectrum of the ultraviolet mercury-vapour lamp (not calibrated)

In order to determine if ignition occurred the current limiter of the power supply was used. The current limiter was set to  $\sim 1 \text{ mA}$ . A current rise above this limit was indicated by a green control light. The current limiter also made sure that no stable glow discharge could establish. The ignition process was observable as flash in the discharge chamber.

The units of the Fig.3.4 - Fig.3.6 are not in the old cgs system as used by Raizer [19]. Electrode diameters are always named with an upper-case  $D$ , the length of the inter-electrode gap with  $d$  and the has number density with  $N$ . The temperature  $T = 293 \text{ K}$  for all measurements ( $p = NkT$ ).

Due to the complicated influence of gas composition, temperature, electrode condition on the discharge voltage an error analysis is very difficult. Therefore the maximum error in the voltage measurement is estimated to  $50 \text{ V}$  (Sec.2.2.2). The error of the voltmeter is neglected. The maximum error in the product  $pd$  is estimated to  $25 \text{ hPa mm}$  ( $dN = 0,62 \cdot 10^{21} \text{ m}^{-2}$ ) with an assumed maximum error of  $0,5 \text{ mm}$  in the distance measurement and an assumed error of  $50 \text{ hPa}$  in the pressure measurement.

### 3.1.1 Paschen curves with fixed inter-electrode gaps and variable pressures

For the following measurements (Fig.3.4) the inter-electrode gap was set to 8.8 mm. The pressure varied from 50 to 1600 hPa. The cathode became irradiated by ultra-violet light (Fig.3.3). The measurement method was as described in Sec.3.1.

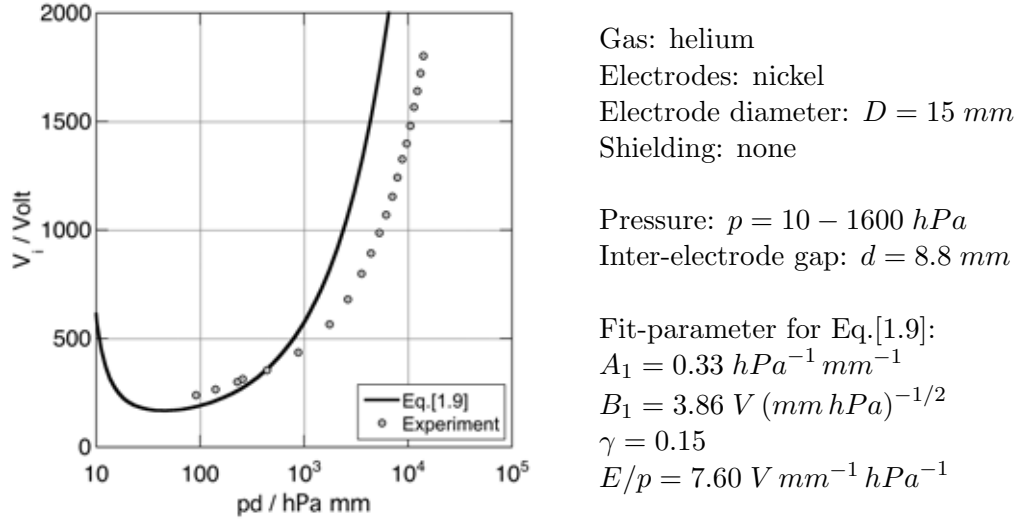
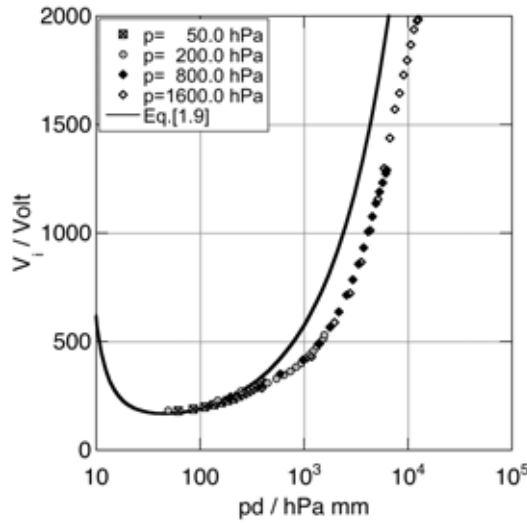


Figure 3.4: Paschen curve:  $d = 8.8 \text{ mm}$ ,  $D = 15 \text{ mm}$ ,  $p = 10 - 1600 \text{ hPa}$ , Gas: helium, Electrodes: nickel

### 3.1.2 Paschen curves with fixed pressures and variable inter-electrode gaps

For the measurement presented in Fig.3.5 the inter-electrode gap varied from 0.25 to 8.0 mm. In order to cover the same  $pd$  range  $pd = 90 - 14 \cdot 10^3 \text{ hPa mm}$  ( $dN = 2 - 350 \cdot 10^{21} \text{ m}^{-2}$ ) as in Fig. 3.4 the pressure  $p$  was set to 50, 200, 800, 1600 hPa. The cathode became irradiated by ultra-violet light (Fig.3.3). The measurement method was as described in Sec.3.1.

A similar measurement was performed for copper electrodes ( Fig.3.6). The inter-electrode gap varied from 0.1 to 7.8 mm. The pressure  $p$  was set to  $p = 200, 800, 1400, 2000, \text{ hPa}$ . The cathode became irradiated by ultra-violet light (Fig.3.3). The measurement method was as described in Sec.3.1.

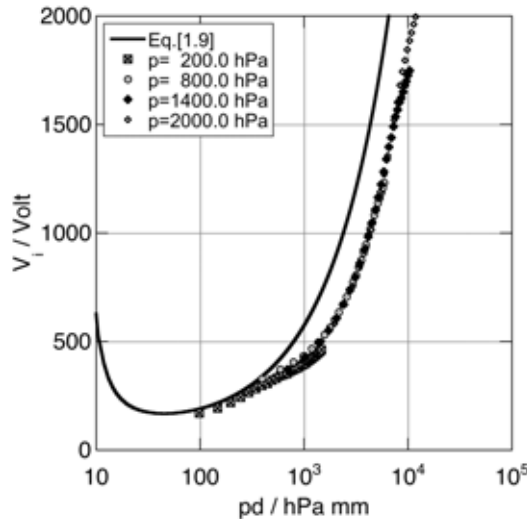


Gas: helium  
 Electrodes: nickel  
 Electrode diameter:  $D = 15 \text{ mm}$   
 Shielding: none

Pressures:  $p = 50, 200, 800, 1600 \text{ hPa}$   
 Inter-electrode gap:  $d = 0.25 - 8.0 \text{ mm}$

Fit-parameter for Eq.[1.9]:  
 $A_1 = 0.33 \text{ hPa}^{-1} \text{ mm}^{-1}$   
 $B_1 = 3.86 \text{ V} (\text{mm hPa})^{-1/2}$   
 $\gamma = 0.15$   
 $E/p = 7.60 \text{ V mm}^{-1} \text{ hPa}^{-1}$

Figure 3.5: Paschen curve:  $d = 0.25 - 8.0 \text{ mm}$ ,  $D = 15 \text{ mm}$ ,  $p = 50, 200, 800, 1600 \text{ hPa}$ , Gas: helium, Electrodes: nickel



Gas: helium  
 Electrodes: copper  
 Electrode diameter:  $D = 15 \text{ mm}$   
 Shielding: none

Pressures:  $p = 200, 800, 1400, 2000, \text{ hPa}$   
 Inter-electrode gap:  $d = 0.1 - 7.8 \text{ mm}$

Fit-parameter for Eq.[1.9]:  
 $A_1 = 0.33 \text{ hPa}^{-1} \text{ mm}^{-1}$   
 $B_1 = 3.86 \text{ V} (\text{mm hPa})^{-1/2}$   
 $\gamma = 0.15$   
 $E/p = 7.60 \text{ V mm}^{-1} \text{ hPa}^{-1}$

Figure 3.6: Paschen curve:  $d = 0.1 - 7.8 \text{ mm}$ ,  $D = 15 \text{ mm}$ ,  $p = 200, 800, 1400, 2000, \text{ hPa}$ , Gas: helium, Electrodes: copper

### 3.1.3 Discussion

Eq.1.9 implies that pressures  $p$  or distances between the electrodes  $d$  can be changed independently giving the same ignition voltage  $V_i$  for the same  $pd$  values. The measurements in Sec.3.1.1 and Sec.3.1.2 were performed to test this concept.

(1)  $d = \text{const}$ ,  $p = 10 - 1600 \text{ hPa}$  (Sec.3.1.1, Fig.3.4)

(2)  $p = \text{const}$ ,  $d = 0.25 - 8.0 \text{ mm}$  (Sec.3.1.2, Fig.3.5)

Fig.3.7 presents Fig.3.4 (1) and Fig.3.5 (2) in the same graph. The first obvious thing is that both measurements deviate from the theoretical Paschen curve for  $pd$  values higher than  $513 \text{ hPa mm}$ .

The next remarkable observation is that the curves start to diverge from each other for  $pd$  values higher than  $2700 \text{ hPa mm}$ . The deviation for smaller  $pd$  values is in the range of the estimated error of  $50 \text{ V}$  (Sec.2.2.2) and mainly caused by the gas composition (Sec.2.2.2). The deviation at  $pd = 13500 \text{ hPa mm}$  is about  $280 \text{ V}$  therefore significant above the estimated error.

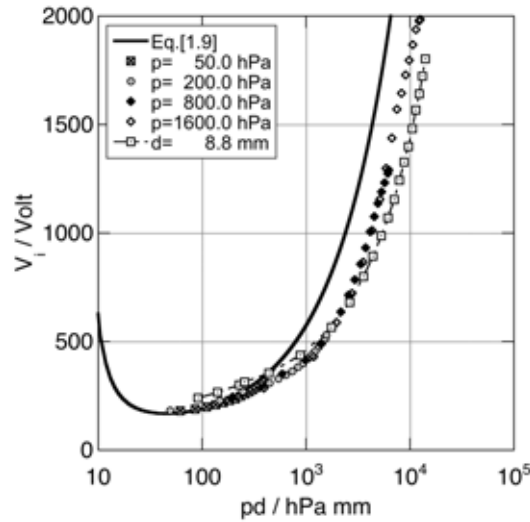


Figure 3.7: Comparison of two methods to determine Paschen curves.

An analysis of the graph shows that the ratio  $d/D$  between the inter-electrode gap  $d$  and the electrode diameter  $D$  seems to be important [10]. For narrow gaps with small  $d$  both curves fit very well together. The two examples below give the upper limit of the  $d/D$  ratio for the curves  $p = 800 \text{ hPa}$  and  $p = 1600 \text{ hPa}$ .

- $p = 800 \text{ hPa}$ ,  $pd = 3000 \text{ hPa mm}$ ,  $d/D = 0.25$
- $p = 1600 \text{ hPa}$ ,  $pd = 3600 \text{ hPa mm}$ ,  $d/D = 0.15$

Above these limits the curves start to deviate. The two examples give a hint that it's supposable that the value of the  $d/D$  limit decreases with increasing pressure. Further measurements

would be necessary to clear the situation.

Lisovskiy et al. [10] suggest that method (1) is not acceptable to determine the ignition behavior. In their opinion each point of method (1) represents a point on a different genuine Paschen curve. Lisovskiy et al. propose a modified fit formular Eq.[3.1] with the additional parameter  $d/D$  for cylindrical vessels.

$$V_i = f(pd, d/D) \quad (3.1)$$

They suggest that Paschen's law Eq.[1.8] is only valid for short discharge tubes with  $d/D \rightarrow 0$ . In their work there is no explanation of the pressure dependence on the ignition potential ( $p \approx 1.3 \cdot 10^{-2} - 13 \text{ hPa}$ ) in the high pressure case.

The equation obtained by [10] explains the differences between both curves (Fig.3.7) measured with method (1) and (2) quite well, but it is not capable to explain the deviations from the theoretical Paschen curve Eq.[1.9] for  $pd > 6750 \text{ hPa mm}$ . Furthermore, there is no physical explanation. It's unclear if this behaviour is induced by higher pressures, because of the geometrical shape of the electrodes respectively the discharge chamber or because of the uncertain value of the effective secondary emission coefficient for the cathode  $\gamma$ . It's important to keep in mind that Paschen's law is a semi-empirical fit formula. One assumption is a constant electric field  $E_i = V_i/d$ . In our case field amplification on the edges of the electrodes (Sec.C, PL1) is most likely which probably decreases the required breakdown potential. A theoretical treatment of this problem with numerical methods [6] may clarify this question.

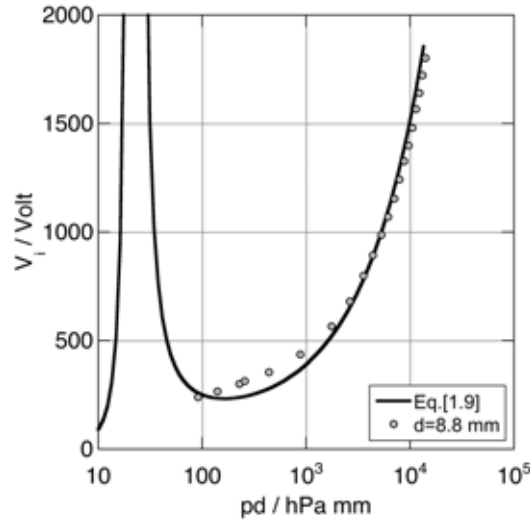


Figure 3.8: Fitted Paschen curve:

$$A_1 = 0.076 \text{ hPa}^{-1} \text{ mm}^{-1}, B_1 = 2.26 \text{ V} (\text{mm hPa})^{-1/2}, \gamma = 0.15$$

Another point to keep in mind is that the parameters  $A_1$  and  $B_1$  of Eq.[1.3] are only valid for a certain field strength range [19]. For Helium  $A_1 = 0.33 \text{ hPa}^{-1} \text{ mm}^{-1}$  and

$B_1 = 3.86 V (mm hPa)^{-1/2}$  valid for  $E/p = 7.60 V mm^{-1} hPa^{-1}$ . The range of  $E/p$  in Fig.3.4 varies from 0.13 to  $2.7 V mm^{-1} hPa^{-1}$  and is therefore far below  $E/p = 7.6 V mm^{-1} hPa^{-1}$ .

In Fig.3.8 the parameters  $A_1$  and  $B_1$  are altered to fit the experimental data ( $A_1 = 0.076 hPa^{-1} mm^{-1}$  and  $B_1 = 3.86 V (mm hPa)^{-1/2}$ ). This leads to a non-physical behaviour below  $pd = 0.76 V mm^{-1} hPa^{-1}$  and don't match the data [19] in the low pressure case.

Also the work of Marić et al. [14] gives no better results. The reason is buried in the ionisation coefficient  $\alpha$  (Fig.3.9). For high pressures the reduced field strength  $E/p$  ( $E/N$ ) is very low. In Fig.3.5 around  $E/N \sim 5 \cdot 10^{-21} Vm^2$  for the highest  $pd$  values. This is below all ranges in Tab.1.1. For this  $E/N$  regions  $\alpha$  shows very strong gradients (Fig.3.9).

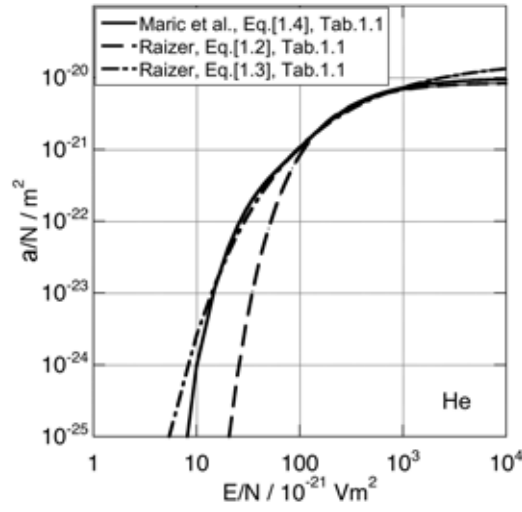


Figure 3.9: Comparison of three fit-formulas for the ionisation coefficient  $\alpha$

The third problem is the uncertain value of the effective secondary emission coefficient for the cathode  $\gamma$ . It was impossible to find tabulated data for helium and copper or a nickel cathode. An extensive search in the literature was not successful. Due to the good agreement of the Paschen curve for helium in [19] and the experimental data around  $pd \sim 132 hPa mm$ ,  $\gamma$  was set to 0.15. That's the reason why the theoretical Paschen curve fits that data in the described region. It's also interesting that the measurements for nickel (Fig.3.5) and copper (Fig.3.6) show almost the same results. For both fits  $\gamma$  was set to 0.15. Therefore, it's important to get assured information about  $\gamma$ ,  $C$  and  $D$  and the influence of field amplification on the electrodes edges before concrete statements about the influence of higher pressures on the ignition behaviour can be done.

Finally, the influence of breakdown delay times, memory effects [7] and the breakdown probability on the measurements is unclear and undocumented. For low  $pd$  values several ignitions per second occurred when the breakdown voltage was reached. For the highest  $pd$  values one or two ignitions happened per ten seconds. Therefore, the improved method presented in Sec.2.3.1 is recommended to clarify the situation.

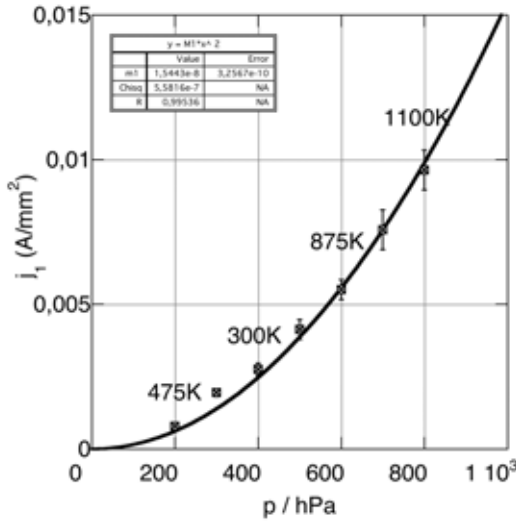
### 3.2 Determination of the reduced normal current density

During the I-V characterisation of different glow discharges also the reduced normal current densities  $(j/p^2)_n$  were determined. Tab.3.1 gives the parameters of the three measurement series. Sec.A.2 contains the raw data for the following chapter.

Table 3.1: I-V characterisation for three different electrode diameters

Nr.	Diameter	Distance	Pressure	Scaling factor	Figure
1	$D_1 = 4.3 \text{ mm}$	$l_1 = 4.0 \text{ mm}$	$p = 200 - 1000 \text{ hPa}$	$a = D_1/D_3 \approx 2.0$	Fig.3.10
2	$D_2 = 3.0 \text{ mm}$	$l_2 = 2.8 \text{ mm}$	$p = 290 - 1430 \text{ hPa}$	$a = D_2/D_3 \approx 1.4$	Fig.3.11
3	$D_3 = 2.1 \text{ mm}$	$l_3 = 2.0 \text{ mm}$	$p = 400 - 1600 \text{ hPa}$	$a = 1$	Fig.3.12

For each measurement the current was increased until the whole cathode's surface was covered by negative glow. At this transition point from a normal to an abnormal glow discharge (Sec.1.5) a photograph and an optical spectrum were taken. The spectrum was used to determine the temperature in the cathode fall region. Note that the cathode is at the right-hand side of the pictures. The photos were taken from above. Especially at higher pressures it was difficult to say whether the whole surface was fully covered due to the increased light intensity. This uncertainty is represented by error bars in Fig.3.10 to Fig.3.12.



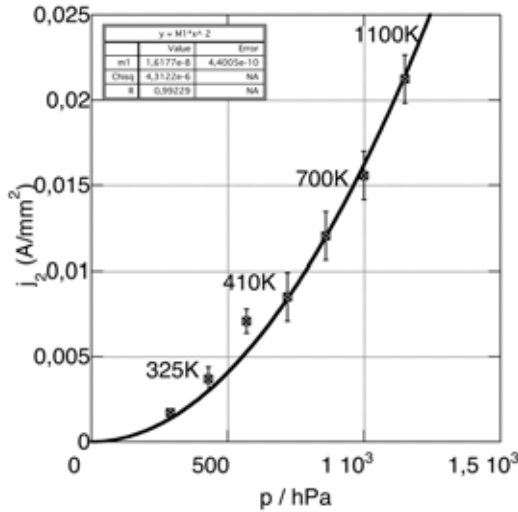
Gas: helium  
 Electrodes: copper  
 Electrode diameter:  $D_1 = 4.3 \text{ mm}$   
 Shielding:  $Al_2O_3$

Pressure:  $p = 200 - 1000 \text{ hPa}$   
 Inter-electrode gap:  $l_1 = 4.0 \text{ mm}$

Figure 3.10: Current density  $j_1$  versus pressure  $p$  from 200 to 1000 hPa

Fig.3.10, Fig.3.11 and Fig.3.12 depict the results for the three measurement series. The fit curves are in the form  $j = M1 \cdot p^2$  (Sec.1.6) and are least square fits. The temperatures were determined from the measured spectral data using Lifbase 2.0 [12].

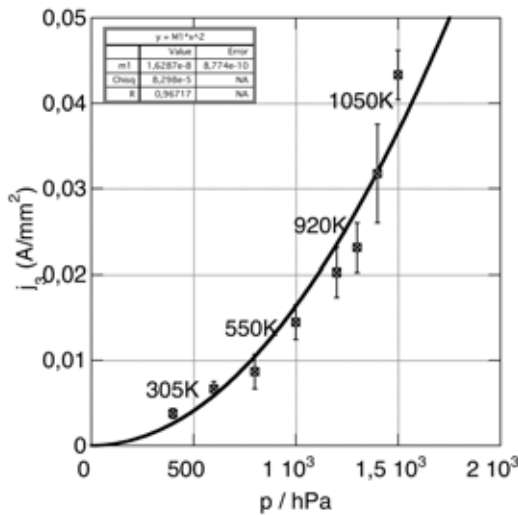
The results for the reduced normal current densities in Tab.3.2 are obtained from the least squares fit. The quadratic similarity law  $j = M1 \cdot p^2$  was used to fit the experimental data.



Gas: helium  
 Electrodes: copper  
 Electrode diameter:  $D_2 = 3.0 \text{ mm}$   
 Shielding:  $Al_2O_3$

Pressure:  $p = 290 - 1430 \text{ hPa}$   
 Inter-electrode gap:  $l_2 = 2.8 \text{ mm}$

Figure 3.11: Current density  $j_2$  versus pressure  $p$  from 290 to 1430 hPa



Gas: helium  
 Electrodes: copper  
 Electrode diameter:  $D_3 = 2.1 \text{ mm}$   
 Shielding:  $Al_2O_3$

Pressure:  $p = 400 - 1600 \text{ hPa}$   
 Inter-electrode gap:  $l_3 = 2.0 \text{ mm}$

Figure 3.12: Current density  $j_3$  versus pressure  $p$  from 400 to 1600 hPa

$M1$  is therefore the reduced normal current density  $(j_i/p^2)_n$ .

Table 3.2: Reduced normal current densities for three different electrode diameters

Figure	i	$(j_i/p^2)_n$ in $A/(mm^2hPa^2)$	Pearson's R	Uncertainty $s_i$ in $A/(mm^2hPa^2)$
Fig.3.10	1	$1.543 \cdot 10^{-8}$	0.99536	$7.166 \cdot 10^{-11}$
Fig.3.11	2	$1.618 \cdot 10^{-8}$	0.99229	$1.247 \cdot 10^{-10}$
Fig.3.12	3	$1.629 \cdot 10^{-8}$	0.96717	$5.347 \cdot 10^{-10}$

The arithmetic mean value for  $j_1$ ,  $j_2$  and  $j_3$  is

$$\left(\frac{\bar{j}}{p^2}\right)_n = \frac{1}{3} \cdot \sum_{i=1}^3 \left(\frac{j_i}{p^2}\right)_n = 1.597 \cdot 10^{-8} \frac{A}{mm^2 hPa^2} \quad (3.2)$$

and the standard deviation using the uncertainties  $s_i$  from Tab.3.2 is

$$s = \sqrt{\frac{1}{9} \cdot \sum_{i=1}^3 s_i^2} = 1.846 \cdot 10^{-10} \frac{A}{mm^2 hPa^2}. \quad (3.3)$$

The reduced normal current density for copper electrodes and helium is therefore (without temperature correction)

$$\left(\frac{j}{p^2}\right)_n = 1.597 \cdot 10^{-8} \pm 1.846 \cdot 10^{-10} \frac{A}{mm^2 hPa^2}. \quad (3.4)$$

Unfortunately, no tabulated values for copper electrodes and helium could be found. A comparison with data from [19] in Tab.3.3 at room temperature shows that the result are in the same order of magnitude.

Table 3.3: Reduced normal current densities  $(j/p^2)_n$  [ $A/(mm^2hPa^2)$ ] at room temperature from [19]

cathode	helium
Fe, Ni	$1.238 \cdot 10^{-8}$
Mg	$1.688 \cdot 10^{-8}$
Pt	$2.813 \cdot 10^{-8}$

It is important to keep in mind that the values in Tab.3.3 are at room temperature (285 K).

### 3.2.1 Discussion

First a few concerns about the reliability of the measurements. It was not possible to take pictures of the cathode and to identify the area covered by negative glow. Instead the current was increased until the surface appeared to be fully covered. This method has a few disadvantages:

- At low pressures the negative glow is diffuse. Sharp boundaries are not detectable.
- At high pressure the negative glow is very bright. The unprotected eye is dazzled.
- The negative glow seems to be not always homogenous.
- The negative glow seems to grow not always uniformly.

Usually the light intensity remains constant until the surface is fully covered and the glow discharge transforms into an abnormal glow discharge. Nevertheless, the current can be increased significantly above the current density of a normal glow discharge without a visible change in the optical impression. This is also an important source of error. Error bars in the graphs try to specify this current range. Finally, also the surface quality of the electrodes (Sec.2.2.1 and Sec.2.1.2) and the purity of the gas (Sec.2.2.2) have an important influence.

A. v. Engel et al. [27] reported that measured values of current densities showed deviations from the quadratic similarity law ( $p^2$ -law) at higher pressures. The exponent of  $p$  converged from 2 to  $4/3$ . A. v. Engel et al. suggested that this behaviour is based on increased gas temperatures and therefore introduced a method to incorporate the right density in the similarity law (Sec.1.7.1). Fig.3.13 presents the theoretical curves of v. Engel et al. for hydrogen, air and helium and the results from the experiments from Sec.3.2.

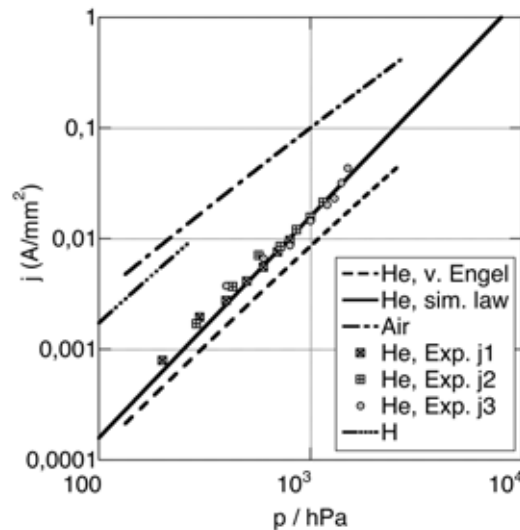


Figure 3.13: Comparison of results from [27] and the experiments in Sec.3.2

Mezei et al. [15] also reported a similar characteristic. The exponent of  $p$  converged from 2 to  $1/2$  in their experiments. Dissociative recombination of molecular ions was considered to

be the main factor causing loss of positive ions and therefore violating the similarity law. Although this is unlikely because no temperature correction was made. The work of A. v. Engel et al. showed that the temperature (density) has to be taken into account.

Fig.3.10, Fig.3.11, Fig.3.12 and Fig.3.13 show that no deviations from the similarity law are observable in the range of error. The current densities for all three measurement series (Tab.3.2) are in the same order of magnitude. Declarations about the behavior of the normal current density in the high pressure case are almost impossible because of the mentioned concerns and the lack of measured data. Anyhow, there is a slight tendency to higher normal current densities for increased pressures and smaller electrode diameters and inter-electrode gaps (Tab.3.2). This might be an indication for a violation of the similarity law. A possible explanation is gas heating.

A comparison of measured temperatures and temperatures calculated with Eq.[1.31] in Fig.3.18 show that the calculated values are too low. The measured temperatures were determined with Lifibase 2.0 [12]. The results and the parameters of the simulation are summarized in Sec.A.2. Sec.3.3 discuss this behaviour in more detail.

### 3.3 On the pressure dependence of the positive column cross section

The summarised data in Sec.A.2 show a pressure dependence of the cross section of the positive column (e.g. Fig.3.14). The positive column becomes contracted at higher pressures. The photo on p.114 for example shows also that the cross section next to anode (left-hand side) is bigger than the cross section next to the cathode (right-hand side). The view of the picture is from above. All pictures were taken when the cathode was fully covered by negative glow.

The discharge diameter was obtained from a gray value profile of these pictures. The profiles were measured with ImageJ [20]. Fig.3.14 shows the location of two profiles and Fig.3.15 the results. All profiles were taken at the middle of the discharge. The only exception were discharges with striations. In this case the profiles were taken at the right-hand side of the striations. In the next step the profiles were normalised with respect to the maximum value. Afterwards the discharge diameter was calculated from the full-width-at-half-maximum (FWHM).

Fig.3.16 shows the pressure dependence of the positive column for the measurement series 2 in Tab.3.1 (Fig.3.11). It is assumed that at  $p = 290 \text{ hPa}$  the positive column has its maximum diameter. The diameter  $D$  and the pressure  $p$  is therefore normalized with respect to the diameter  $D_{290 \text{ hPa}}$  and the pressure  $p_{290 \text{ hPa}}$  at  $p = 290 \text{ hPa}$ . The fit-formula is

$$\frac{D}{D_{290 \text{ hPa}}} = 1 + \frac{1}{C} \left( 1 - \frac{p}{p_{290 \text{ hPa}}} \right) \quad C = \frac{1}{6}. \quad (3.5)$$

Fig.3.17 shows the pressure dependence of the positive column for the measurement series 1 in Tab.3.1 (Fig.3.10). It is assumed that at  $p = 290 \text{ hPa}$  the positive column has its max-

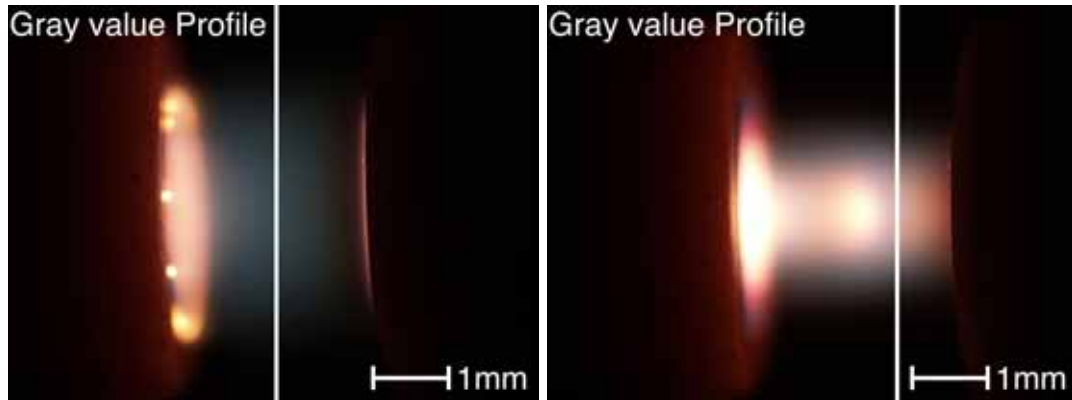
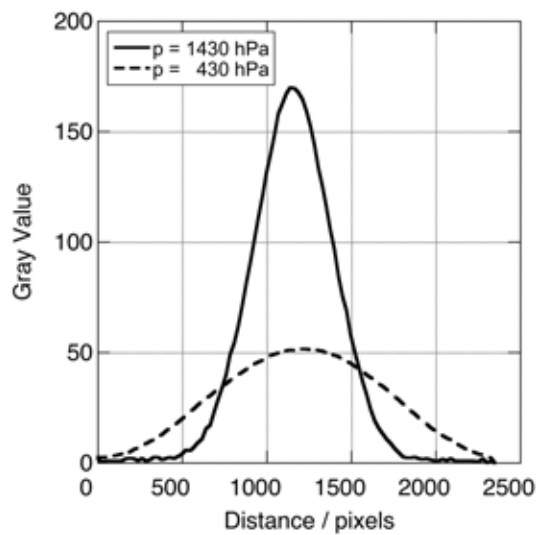


Figure 3.14: Locations of the gray value profile for Fig.3.15



Gas: helium  
 Electrodes: copper  
 Electrode diameter:  $D_2 = 3.0 \text{ mm}$   
 Shielding:  $Al_2O_3$

Pressure:  $p = 290, 1430 \text{ hPa}$   
 Inter-electrode gap:  $l_2 = 2.8 \text{ mm}$

Figure 3.15: Gray value profile of two selected discharges

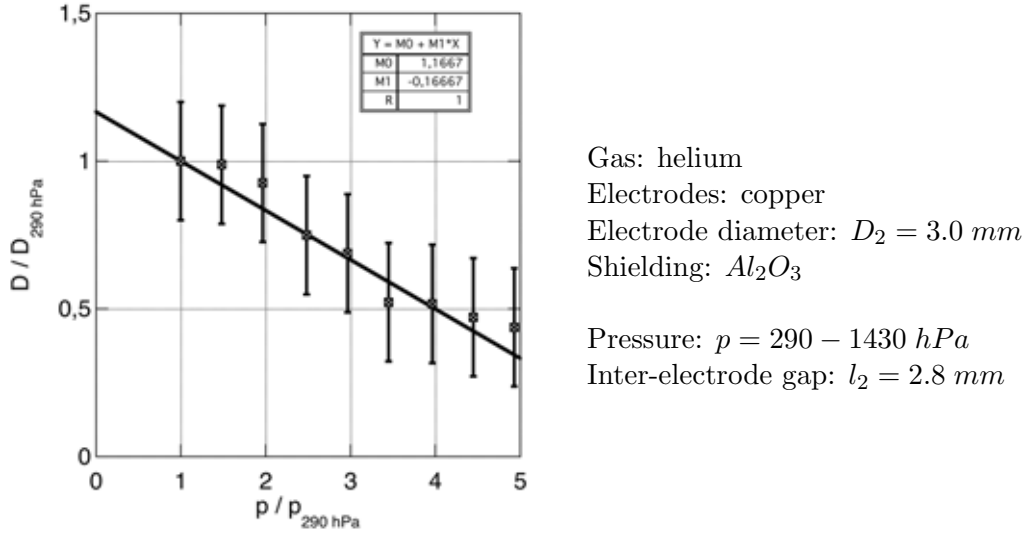


Figure 3.16: Pressure dependence of the positive column diameter 290 – 1430  $hPa$

imum diameter. The measurements below  $p = 500 \text{ hPa}$  are too inaccurate. The diameter  $D$  and the pressure  $p$  is therefore normalized with respect to the diameter  $D_{290 \text{ hPa}}$  and the pressure  $p_{290 \text{ hPa}}$  at  $p = 290 \text{ hPa}$  from Fig3.16. The fit-formula is

$$\frac{D}{D_{290 \text{ hPa}}} = 1 + \frac{1}{C} \left( 1 - \frac{p}{p_{290 \text{ hPa}}} \right) \quad C = \frac{1}{4}. \quad (3.6)$$

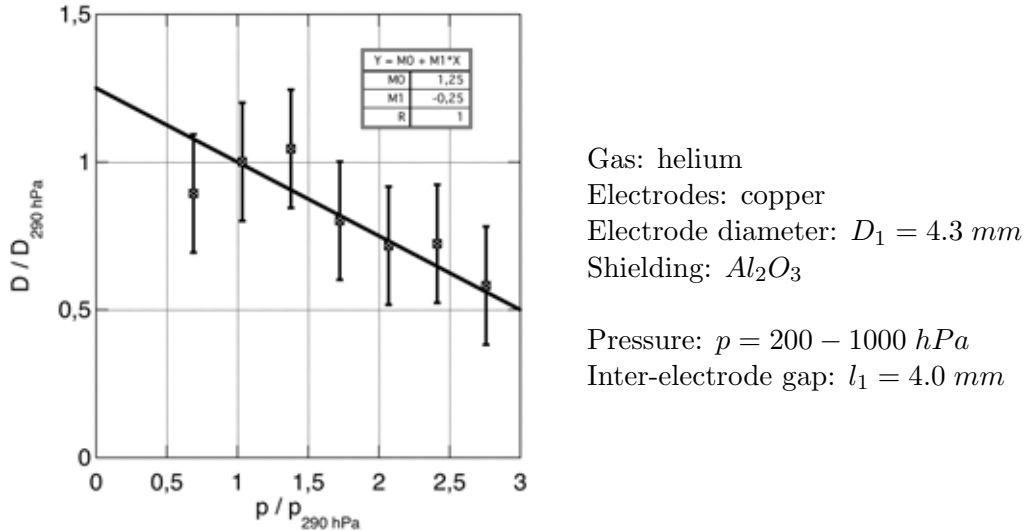
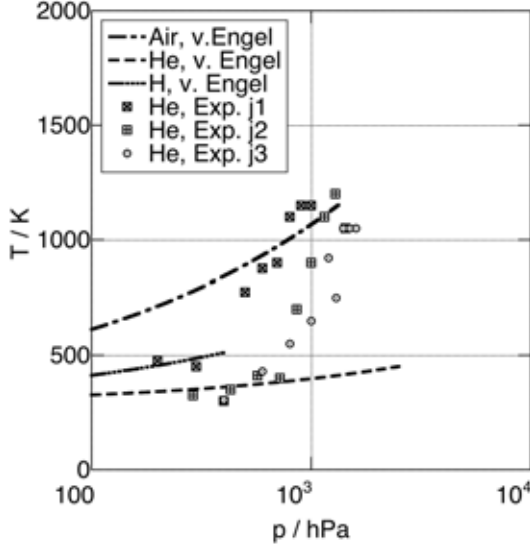


Figure 3.17: Pressure dependence of the positive column diameter 200 – 1000  $hPa$

The results of measurement series 3 (Tab.3.1, Fig.3.12) are not presented in this text. Accurate diameter measurements are almost impossible due to the strongly contracted and striated discharge.

### 3.3.1 On the temperature in the cathode fall region

As explained in Sec.3.2 the temperatures calculated with Eq.[1.31] for Helium are too low (Fig.3.18). The rotational temperatures rise stronger than a model based on the friction of ions and neutral gas atoms can explain [27]. The constants for the helium fit are summarised in Tab.3.4. As a first approximation for  $\alpha$  the thermal conductivity of helium  $\lambda = 0.152 \text{ W}/(\text{m K})$  is divided by  $T = 286 \text{ K}$ .



Gas: helium  
 Electrodes: copper  
 Electrode diameter:  $D_i = 4.3, 3.0, 2.1 \text{ mm}$   
 Shielding:  $Al_2O_3$   
 Pressure:  $p = 200 - 1600 \text{ hPa}$   
 Inter-electrode gap:  $l_i = 4.0, 2.8, 2.0 \text{ mm}$   
 $i = 1, 2, 3$

Figure 3.18: Pressure dependence of the temperature in the cathode fall region.

In A. v. Engel et al.'s approach the generated heat per area unit and sheath thickness  $dx$  is given by

$$dQ = j_0 E_0 \cdot \left(1 - \frac{x}{d}\right)^2 dx. \quad (3.7)$$

$j_0 E_0$  can be understood as a power density. e.g. This power density increases in case of a radial contraction of the cathode fall region. The additional generated heat leads to an increased temperature in the cathode fall region. Trials to incorporate a volume correction factor  $f(p)$  (Eq.[3.8]) in Eq.[3.9] ( $p \rightarrow p/f(p)$ ) according to the measurements in Sec.3.3 gave a good fit for the experimental data but lacked a plausible physical interpretation. It's not clear how to connect the shape of the positive column with the shape of the cathode fall. Additional measurements could testify if the diameter of cathode fall also becomes contracted. The presented measurements lack this information.

$$f(p) = \left(1 + \frac{1}{C} \left(1 - \frac{p}{p_{290 \text{ hPa}}}\right)\right)^2 \quad C = \frac{1}{6} \quad (3.8)$$

Several reasons are possible why the measured temperatures are higher than the calculated ones. It's possible that the "real" current densities in the cathode fall  $j_0$  are higher than the current densities in the model (Eq.[3.9]). This yields higher temperatures because more mechanical work becomes transformed into thermal energy (Eq.[3.7]). Note that  $j_0$  in Eq.[3.9] is substituted by the similarity law Eq.[1.30].

$$\bar{T} - T_k = \frac{2}{3} \sqrt{\frac{V_k j_1 d_1}{3\alpha}} \sqrt{\frac{p T_1}{\bar{T}}} \quad (3.9)$$

Another source of error is that the measured temperatures are not gas kinetic temperatures. The temperatures are determined via rotational bands of  $OH$  and therefore are upper boundaries.

Table 3.4: Constants for Eq.[3.9] from [19]

$V_k$ in Volt	$\alpha$ in $\frac{W}{mm K^2}$	$d_1$ in $mm hPa$	$j_1$ in $\frac{A}{mm^2 hPa^2}$	$T_1$ in K	$T_k$ in K
177	$5.3 \cdot 10^{-7}$	14.3	$1.597 \cdot 10^{-8}$	285	288.15

Another problem is the unsure spatial resolution of the spectrometer. It's almost impossible to point the fibre only to cathode fall. Light from the positive column or anode spots (Sec.3.7) is always part of the measurements.

### 3.3.2 Discussion

The measurement of diameters of the positive column is difficult. Fig.3.14 shows two different discharges at 290 and 1430  $hPa$ . The diameter of the discharge at the cathode (right-hand side) is smaller than at the anode (left-hand side). The light intensity at 290  $hPa$  is very low. The discharge at 1430  $hPa$  is very bright and striated. Striations are also a problem in the determination of the diameter. It is not possible to measure all profiles at the same location. A gray value profile through the striations results in steps in the almost Gaussian gray value profile (Fig.3.15). Therefore, measurements were performed between the striations. Fig.3.15 shows only a small step for the line  $p = 1430 hPa$  at 780 and 1520 pixels.

The results in Fig.3.16 and Fig.3.17 show a linear characteristic. The fit parameter  $C$  (Eq.[3.5] and Eq.[3.6]) is in the range from 1/6 to 1/4. In the range of the error bars fit parameters from 1/10 to 1/3 are possible.

The temperature values were obtained from optical spectra (Sec.A.2). Lifbase 2.0 [12] was used to simulate the spectra of the  $OH$ -band and to compare them with the measured spectra. This method only works fine at high temperatures, strong light intensities and therefore in our case at higher pressures. Fig.3.18 shows the pressure dependence of the temperature in the cathode fall region.

The cathode fall can reach up to 1100  $K$ . The positive column is colder depending on the heat conduction. The surrounding gas is at room temperature. Note that the measured temperatures are controversial (Sec.3.3.1).

Due to the pressure dependence of the positive column cross-section and the strong temperature gradients a comparison between low-pressure and high pressure glow-discharges is difficult. In the low pressure case the positive column fills the whole discharge chamber and is in thermodynamical equilibrium with the chamber wall. A proper consideration of momentum transfer to the chamber wall leads to realistic temperatures for the discharge. The main mechanism of losses is ambipolar diffusion [3].

In the high pressure case the discharge is contracted. There is no contact with the chamber walls. The discharge is surrounded by cold neutral gas. The discharge itself can be very hot. The main mechanism of losses is recombination [3]. Potentially  $j$  is of more importance than in the low pressure case. Gas heating plays an important role in the appearance and the behaviour of the high pressure glow-discharge. Further investigations and work should be based on this fact. Improved methods should be found for more accurate current density measurements.

### 3.4 I-V characterisation of similar glow discharges

Two glow-discharges with the same voltage drop  $V_1$  and drawing the same current  $I$  (Fig.1.4) are said to be similar if they fulfill the relations explained in Sec.1.6. Similar discharges should therefore have the same current voltage (I-V) characteristic. The raw data (I-V diagrams) for this section is summarized in Sec.A.2.

#### 3.4.1 Measurement series with scaling factors $a=2$ and $1.4$

The pressures  $p_i$  ( $i = 1, 2, 3$ ) and inter-electrode gaps distances  $l_i$  were set according to the three different diameters  $D_i$  and the similarity relations. The three used diameters are  $D_1 = 4.3 \text{ mm}$ ,  $D_2 = 3.0 \text{ mm}$  and  $D_3 = 2.1 \text{ mm}$ . The scaling factor  $a$  is  $D_1/D_2 \approx 1.4$  or  $D_1/D_3 \approx 2.0$  (Tab.3.5).

Table 3.5: I-V characterisation for three different electrode diameters

Nr.	Diameter	Distance	Pressure	Scaling factor
1	$D_1 = 4.3 \text{ mm}$	$l_1 = 4.0 \text{ mm}$	$p_1 = 200 - 1000 \text{ hPa}$	$a = 1$
2	$D_2 = 3.0 \text{ mm}$	$l_2 = 2.8 \text{ mm}$	$p_2 = 290 - 1430 \text{ hPa}$	$a = p_2/p_1 \approx 1.4$
3	$D_3 = 2.1 \text{ mm}$	$l_3 = 2.0 \text{ mm}$	$p_3 = 400 - 1600 \text{ hPa}$	$a = p_3/p_1 \approx 2.0$

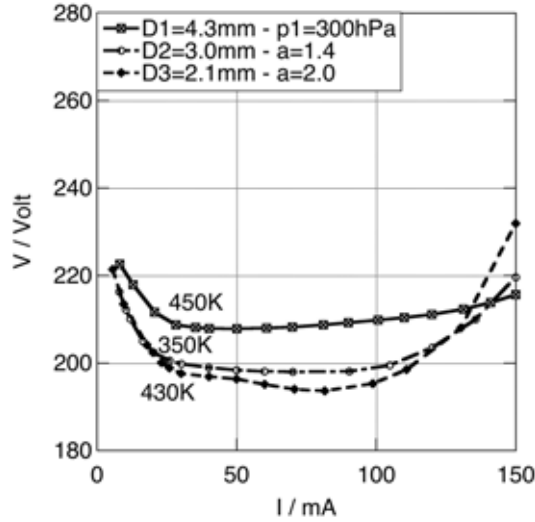


Figure 3.19: Comparison of three similar discharges with  $p_1 = 300 \text{ hPa}$  and  $a = 1.4$  or  $2.0$

The pressure range of the setup with the index  $i = 1$  is from 200 to 1000  $\text{hPa}$ . The inter-electrode gap distance  $l_1 = 4.0 \text{ mm}$ . The pressures and the inter-electrode gap distances for setup 2 and 3 were calculated according to the scaling factors.

The measurements were performed using the current limiter of the power supply. The current

was raised and discharge voltages  $V_i$  and the currents  $I_i$  were recorded. Fig.3.19 for example shows such a comparison of three similar discharges. The temperature was measured via optical spectroscopy when the cathode was fully covered by negative glow. Note the remarks about the temperature measurements in Sec.3.3.1 and Sec.3.5.2. Tab.3.6 is a list of all triples of similar discharges. The complete set of diagrams is in Sec.A.2.2 (p. 130).

Table 3.6: Overview of all triples of similar discharges

Series	Pressures	Raw data	Comparison I-V
1	$p_1 = 200 \text{ hPa}$ $p_2 = 290 \text{ hPa}$ $p_3 = 400 \text{ hPa}$	p. 103 p. 112 p. 121	p. 130
2	$p_1 = 300 \text{ hPa}$ $p_2 = 290 \text{ hPa}$ $p_3 = 600 \text{ hPa}$	p. 104 p. 113 p. 122	p. 131
3	$p_1 = 400 \text{ hPa}$ $p_2 = 570 \text{ hPa}$ $p_3 = 800 \text{ hPa}$	p. 105 p. 114 p. 123	p. 131
4	$p_1 = 500 \text{ hPa}$ $p_2 = 720 \text{ hPa}$ $p_3 = 1000 \text{ hPa}$	p. 106 p. 115 p. 124	p. 132
5	$p_1 = 600 \text{ hPa}$ $p_2 = 860 \text{ hPa}$ $p_3 = 1200 \text{ hPa}$	p. 107 p. 116 p. 125	p. 132
6	$p_1 = 700 \text{ hPa}$ $p_2 = 1000 \text{ hPa}$ $p_3 = 1400 \text{ hPa}$	p. 108 p. 117 p. 127	p. 133
7	$p_1 = 800 \text{ hPa}$ $p_2 = 1150 \text{ hPa}$ $p_3 = 1600 \text{ hPa}$	p. 109 p. 118 p. 129	p. 133
8	$p_1 = 900 \text{ hPa}$ $p_2 = 1290 \text{ hPa}$ -	p. 110 p. 119 -	p. 134
9	$p_1 = 1000 \text{ hPa}$ $p_2 = 1430 \text{ hPa}$ -	p. 111 p. 120 -	p. 134

### 3.4.2 Discussion

The curves in Fig.3.20 show the typical characteristic for a DC glow discharge. The left hand side shows a negative  $dV/dI < 0$  but is not the transition region from Townsend dark discharge to normal glow discharge. The minimum current is around 4 mA and therefore too high for the transition region from Townsend dark to a normal glow discharge (Sec.1.5).

The explanation is that after ignition the cathode become bombarded by ions. The voltage

decreases until an equilibrium is reached. This can take a couple of minutes. This explanation is likely because the region of normal glow ( $V = \text{const.}$ ) is too small. One would expect such a behaviour for very small cathode diameters. The right hand side  $dV/dI > 0$  is explained as the region of abnormal glow. The voltage minimum is the point where the cathode is fully covered with negative glow.

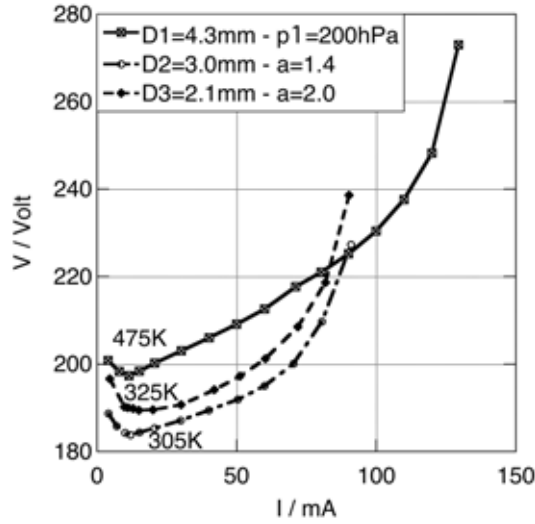


Figure 3.20: Comparison of three similar discharges with  $p_1 = 200 \text{ hPa}$  and  $a = 1.4$  or  $2.0$

The voltage minimum is shifted to higher currents with increasing pressure. The region of normal glow discharge where the voltage remains constant is very small. Fig.3.20 shows the characteristic which one would expect. In Fig.3.19 the situation changes. The curve  $D_1$  still shows the characteristic as described above. But  $D_2$  and  $D_3$  show a different behaviour. Although the cathode's surface is fully covered with negative glow ( $I_2 = 26.0 \text{ mA}$ ,  $I_3 = 23.0 \text{ mA}$ ) the curves still show a negative  $dV/dI < 0$ . All other measurements in Sec.A.2 show also this behaviour. It seems that for pressures above  $p = 300 \text{ hPa}$  the V-I characteristic has a negative  $dV/dI < 0$  and a negative resistance. Additionally the curve  $D_3$  in Fig.3.19 has an unusual voltage drop for  $I > 50 \text{ mA}$ . A possible explanation is a sudden contraction of the positive column [5]. Normally, considering this facts yields two explanations.

- There is an error in the measurement of the normal current density. The normal current density is in fact higher than measured (Sec.3.2).
- There are unshielded areas in the discharge chamber where the negative glow can grow furthermore (Sec.2.1.1).

It is unlikely that the errors in the determination of the normal current density are that high. The measured normal current density for curve  $D_3$  in Fig.3.19 is  $(j_3/p^2)_n = 1.8 \cdot 10^{-8} \text{ A}/(\text{mm}^2 \text{ hPa}^2)$  with  $I_3 = 23.0 \text{ mA}$ . The voltage minimum of the curve is at  $I_3 = 81.0 \text{ mA}$ . This yields a normal current density of  $(j_3/p^2)_n = 6.5 \cdot 10^{-8} \text{ A}/(\text{mm}^2 \text{ hPa}^2)$ . An error of  $53 \text{ mA}$  is almost impossible for the experimenter.

The second point is also not very supposable. At very low pressures  $p < 1 \text{ hPa}$  the  $Al_2O_3$  shieldings malfunction. The negative glow covers the whole cathode electrode head and carrier (Sec.2.1.1). The situation improves with higher pressures. 200  $\text{hPa}$  or higher are far beyond from this point. Additionally the current range in the normal mode is the greater the higher the pressure and the longer the tube [19]. This behaviour is explained by the ratio of the normal cathode fall current  $j_n$  and the limiting current for the existence of dark discharge  $j_L$

$$\frac{j_n}{j_L} \approx \tilde{L}(1 + \ln \tilde{L})^2 \quad \tilde{L} = \frac{(pL)}{(pd)_n}. \quad (3.10)$$

Staack et al. [24] reported a similar behaviour for increasing gap distances. At larger electrode spacings the  $V - I$  characteristics have a negative slope ( $dV/dI < 0$ ) hence a negative resistance. Staack et al. suggest that this may be due to lateral neutral gas temperature gradients in the positive column. Another in their opinion more unlikely explanation is atmospheric pressure GAT (glow to arc transition).

According to Staack et al. GAT is

*(a) contraction and thermalization of the discharge resulting from heating of the neutrals and (b) heating of the cathode resulting in transition from secondary electron emission to thermionic emissions of electrons at the cathode. Generally the thermal instability is suppressed in low pressure discharges by cooling the walls.*

Some of Staack et al. results are possibly applicable to the presented measurements. For discharges with negative  $dV/dI < 0$  the GAT (glow to arc transition) region is of interest. The atmospheric pressure GAT region is different from that of the traditional vacuum V-I characteristics. Staack et al.'s explain the absence of abnormal glow in their measurements due to the unlimited cathode area. The fascinating thing is that although the cathode area is limited in the presented measurements in this text (Sec.A.2), no region of abnormal glow is observable for pressures above  $p = 400 \text{ hPa}$ .

There are two key properties that are different in Arc and DC glow. The ionisation process in the positive column and the mechanism of cathode electron emission are different respectively. The mechanisms for DC glow are electron impact ionisation and secondary electron emission from the cathode. The electric field is independent of the current for direct electron impact ionisation. Arc discharges show thermal ionisation in the positive column and thermal electron emission from the cathode's surface. Thermal ionisation lead to a voltage drop with growing current. Therefore the discharge has a negative  $dV/dI < 0$ .

The transition from electron impact ionisation to thermal ionisation is smooth [24]. For higher pressures the positive column becomes contracted due to thermal instabilities [19]. Glow to arc transition (GAT) occurs and yields a negative  $dV/dI < 0$ . The electrode gap becomes more conductive and thus reduces the gap voltage [19].

Obvious in all diagrams (Sec.A.2.2) is that the curves are not congruent. All diagrams have in common that setup 1 with the biggest electrode diameter and therefore the biggest inter-electrode gap has the highest and setup 3 the lowest operating voltages. Fig.A.57 is the only exception. For pressures above  $p = 300 \text{ hPa}$  the V-I characteristic has a negative  $dV/dI < 0$ . It is not likely that atmospheric pressure GAT is the right explanation for the presented results. Helium has a far better heat conductivity than air (used by Staack et al.).

Therefore the gas remains cooler. Step (b) (Staack et al.) is not applicable in our case. The electrodes are cooled to prevent thermionic emissions of electrons at the cathode. Thermalization as mentioned in step (a) occurs only in current filaments and arcs and is also excluded. The only remaining explanation is the contraction due to heating of neutrals. Higher temperatures means lower densities and therefore a reduced field strength in the positive column to replace losses. A reduced voltage drop at the positive column yields a reduced discharge voltage. If one compares the photos of each set of similar discharges in Sec.A.2 (e.g. Photos on page 106, 115 and 124) one will find that the contraction of the positive column is stronger at higher pressures.

A theoretical approach of Shi and Kong [23] hardens this explanation. Shi and Kong used a hybrid model for simulation of a capacitively coupled DC plasma system. The model for the positive column (equilibrium region) is based on a hydrodynamic model. The cathode fall region is modelled kinetically. Their results show that large current densities cause severe gas heating. The gap becomes more conductive and thus reduces the gap voltage. This is in good agreement with Staack et al.. Shi and Kong states that the inverse proportionality between the voltage and the current density is more prominent in the high pressure case. This is also confirmed experimentally by Eijkel et al. [5].

The diagrams Fig.A.57 and Fig.A.58 show the only measurements in the region of abnormal glow ( $dV/dI > 0$ ). The other diagrams are in the region of a normal glow discharge because of the limited current of the power supply ( $< 150 \text{ mA}$ ). Note the remarks about the temperature measurements in Sec.3.3.1 and Sec.3.5.2.

The curves of each set show a similiar behaviour and appear almost parallel. However, it is also possible that contaminated gas is the reason why the curves are not congruent (Sec.2.2.2). Errors in the pressure measurement and therefore wrong pressures in the chamber also influence the I-V characteristic.

At the moment it seems that the similarity laws for pressures above  $p = 200 \text{ hPa}$  are violated. Recommendations for future research are to solely investigate the influence of the pressure on the cathode fall, i.e. to reduce the inter-electrode gap insofar as no positive column can establish. This may help to clarify the situation. A comparison with the presented results may help to distinguish between effects which may originate from the positive column or the cathode fall.

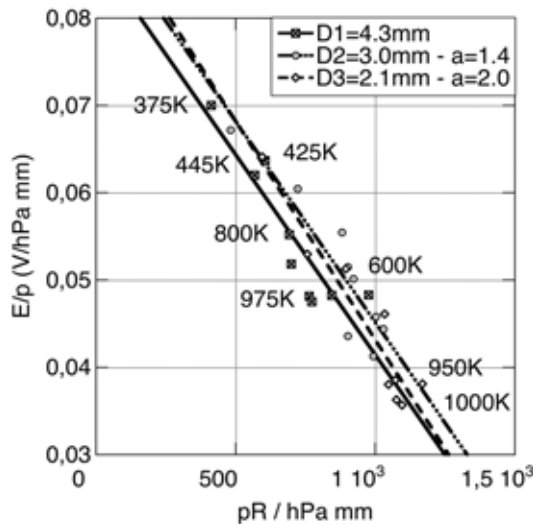
### 3.5 Reduced field strength in the positive column

This section deals with the measurement of the field-strength in the positive column and gives a comparison of similar discharges. As described in Sec.1.5 the field-strength  $E$  is constant in the positive column. Therefore it's possible to measure the field strength by keeping the current constant and varying the inter-electrode gap distance. An increased distance also increases the voltage drop at the discharge. In order to have comparable results the field strength was always calculated in a certain range. The slope of the voltage decreases a little bit for very large inter-electrode gaps (e.g. Fig.A.5 at  $d = 3 \text{ mm}$ ). The raw data can be found in appendix Sec.A.1.

Furthermore photographs and optical spectra of the discharges were taken. The optical spectra are used to determine the gas composition and the temperature. All photos and spectra were taken at the maximum possible inter-electrode gap  $l_{i \max}$  ( $i = 1, 2, 3$ ). All temperatures are therefore upper boundaries and maximum temperatures. The maximum distance is equivalent to the maximum power consumption of the discharge. For temperature determination the OH band was used. Simulations of the OH spectra were performed with *Lifbase 2.0* [12]. The program settings are given in separate tables. The integration times of the optical spectrometer are given in the figure caption.

#### 3.5.1 Measurement series with scaling factors $a=2$ and $1.4$

For all measurements the current was kept at  $I = 25 \text{ mA}$  to allow a comparison with the results in [19]. The electrodes distance became varied and the readings from the voltmeter were noted. At the maximum inter-electrode gap a photo and a spectra were taken.



Gas: helium  
 Electrodes: copper  
 Electrode diameters:  $D_1 = 4.3 \text{ mm}$ ,  
 $D_2 = 3.0 \text{ mm}$ ,  $D_3 = 2.1 \text{ mm}$   
 Shielding:  $Al_2O_3$   
 Pressure:  $p = 200 - 1600 \text{ hPa}$   
 Current:  $I = 25 \text{ mA}$   
 Inter-electrode gap: variable

Figure 3.21: Reduced field strengths for three similar discharges

### 3.5.2 Discussion

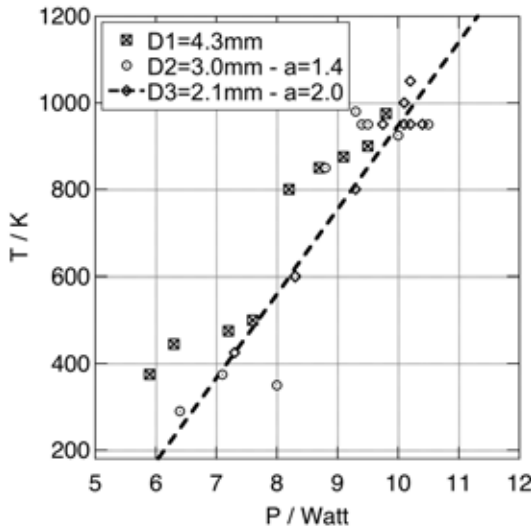
The first problem is how to present the results in a proper diagram (Fig.3.21). In standard literature e.g Raizer [19], von Engel [28] ... the reduced field strength  $E/p$  is plotted over the product of the pressure  $p$  and the radius of the discharge tube  $R$ . This is practical because the positive column fills the whole discharge tube and is in equilibrium with the chamber walls. But this is only a convenient approximation. The main source of losses in the low pressures case is diffusion towards the chamber walls. Therefore  $R$  in fact should be the diffusion length  $\Lambda$  ( $\Lambda = R/2.4$  for cylindrical geometries [8]).

In the presented case the circumstances are different. Due to the construction the discharge is not bounded by chamber walls. Instead it's surrounded by neutral gas (Fig.2.2). Additionally the discharge is contracted due to instabilities in the high pressure case (Sec.3.3). Last but not least the main source of losses in the high pressure case is volume recombination and not ambipolar diffusion [3].

Therefore, the radius of the positive column was chosen for  $R$  in Fig.3.21.  $R$  was determined according to the method described in Sec.3.3.

An interesting detail is that  $E/p$  is not constant for high  $pR$  values. Results in [19] show an almost constant value of  $E/p = 0.08 \text{ V}/(\text{mm} \cdot \text{hPa})$  for  $pR$  values bigger than  $105 \text{ hPa} \cdot \text{mm}$ . The measured values around  $1000 \text{ hPa} \cdot \text{mm}$  are in the same order of magnitude as the data in [19]. Higher  $pR$  values lead to a decrease of  $E/p$ .

This is not surprising if one looks at the temperatures in Fig.3.21. High  $pR$  values lead to increased temperatures. Higher gas temperatures imply a reduced gas density and therefore an increased mean free path. Therefore electrons can gain more energy from the electric field and perform more ionisations to compensate losses due to diffusion and recombination. This yields a contracted positive column and a decreased value of  $E/p$ .



Gas: helium  
 Electrodes: copper  
 Electrode diameters:  $D_1 = 4.3 \text{ mm}$ ,  
 $D_2 = 3.0 \text{ mm}$ ,  $D_3 = 2.1 \text{ mm}$   
 Shielding:  $\text{Al}_2\text{O}_3$

Pressure:  $p = 200 - 1600 \text{ hPa}$   
 Current:  $I = 25 \text{ mA}$   
 Inter-electrode gap: variable

Figure 3.22: Temperature-power characteristics of similar discharges

The next remarkable thing is that although the three discharges are said to be "similar" the linear fits are not congruent (Fig.3.21). Again the temperature is believed to be the main source of this behaviour. It is likely that the thermal stress overlies possible atomic processes for a violation of similarity laws (Sec.1.7). For example note the decreased gradient in Fig.A.18 at  $d > 4 \text{ mm}$ . This behaviour also influenced by the temperature.

The temperatures show an approximately linear characteristic with increasing power Fig.3.22. It is remarkable that the data-points for  $D1$  and  $D2$  show a jump discontinuity at  $P \approx 8 \text{ W}$ . The reason for this behaviour is unknown. Possibly it's a transition point from normal to abnormal glow. But that is only speculation.

Unfortunately the temperature measurements don't fit in the overall picture. It is believed that the determined temperatures using the  $OH$  band are too high (Sec.3.3.1). The problem is that the temperatures in Fig.3.21 are not exactly the gas kinetic temperatures. These temperatures are determined from the rotational spectra of the  $OH$  bands and therefore upper boundaries. Nevertheless, these temperatures should fit nicely in the high pressure case.

One big source of error is the measurement itself. It was impossible to point the fibre of the spectrometer only to the positive column. The fraction of light from the very intense negative glow is unclear but estimated as rather high.

A standard methode to compensate the influence of the temperature in Fig.3.21 is to use the gas number density  $N$  instead of the pressure  $p$  for the presentation. Attempts to use these temperatures to calculate the densities  $N$  failed. As described in Sec.3.3.1 the rotational temperatures rise stronger than a model based on the friction of ions and neutral gas atoms can explain. Therefore the pressure  $p$  is still used because it's a directly measurable quantity. Therefore it's impossible to investigate how atomic processes influence the similarity laws. Maybe it's possible to get better results with a better measuring method. Most distances were varied up to  $6 \text{ mm}$  in steps of  $\approx 0.5 \text{ mm}$ . A maximum distance of  $6 \text{ mm}$  is wide compared to the electrodes diameter. A better way would be to use a step-width of  $\approx 0.05 \text{ mm}$  (minimum step width of the used micro-meter head screw) and maximum distances of  $\approx 2 \text{ mm}$ . This would keep the power consumption and also the thermal stress low and might give far better and more interesting results.

### 3.6 Sheath measurements of the cathode dark-space

Sheath thickness ( $d_C$ ) measurements of the cathode dark-space of normal glow discharges were one of the first measurements. These measurements were performed with tungsten electrodes and with problematic Teflon shieldings (Sec.2.2.1). Measurements for copper or nickel electrodes with  $Al_2O_3$  were not performed.

The thickness  $d_C$  of the cathode dark-space was measured with a microscope. Therefore the discharge chamber became inclined until the thickness of the dark-space became maximum in the ocular. e.g. Fig.3.23 shows a microscope picture. The discharge chamber is in horizontal position. Due to the projection the anode's surface is fully visible (left-hand side). The cathode's surface is covered by the upper edge (right-hand side).

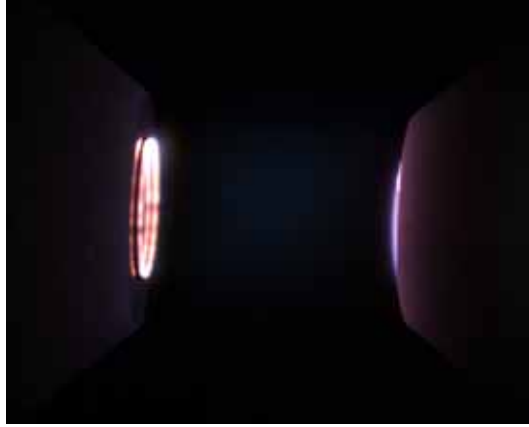


Figure 3.23: The anode glow at the left-hand side has a ring-like appearance.

Fig.3.24 to Fig.3.27 show pictures of the cathode's dark space for helium at variable pressures. The measured data is summarized in Tab.3.7 and plotted in Fig.3.28. The current for all measurements was set to  $I = 12 \text{ mA}$ .

The normal cathode layer thickness at room temperature is given by

$$(p \cdot d_C)_n = \text{const} \quad (3.11)$$

where  $p$  is the pressure and  $d_C$  the cathode dark-space thickness. Fig.3.28 shows graphs for tungsten and helium (experiment) and iron and helium [19]. The curve fit for the reduced normal cathode layer thickness for tungsten and helium gives

$$(p \cdot d_C)_n = 26.8 \text{ mm hPa} \quad (3.12)$$

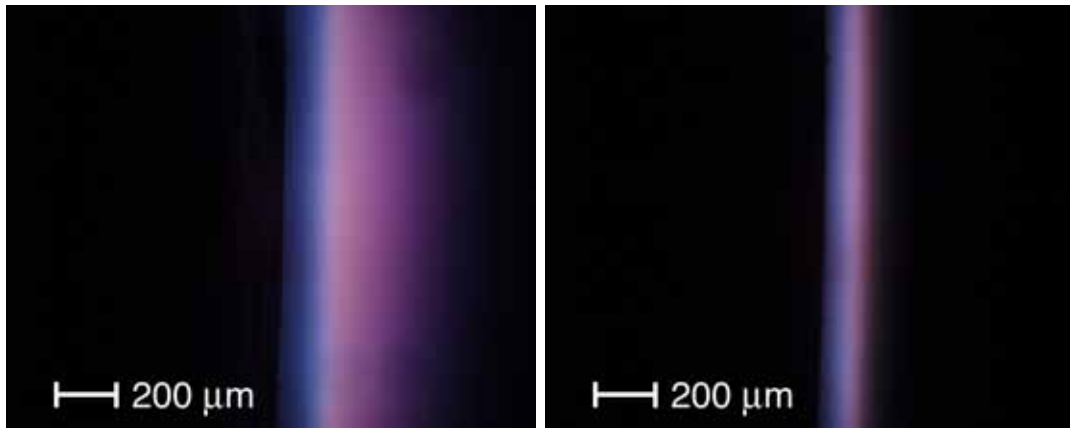


Figure 3.24:  $d_C = 144 \mu m$ ,  $p = 200 hPa$       Figure 3.25:  $d_C = 89 \mu m$ ,  $p = 300 hPa$

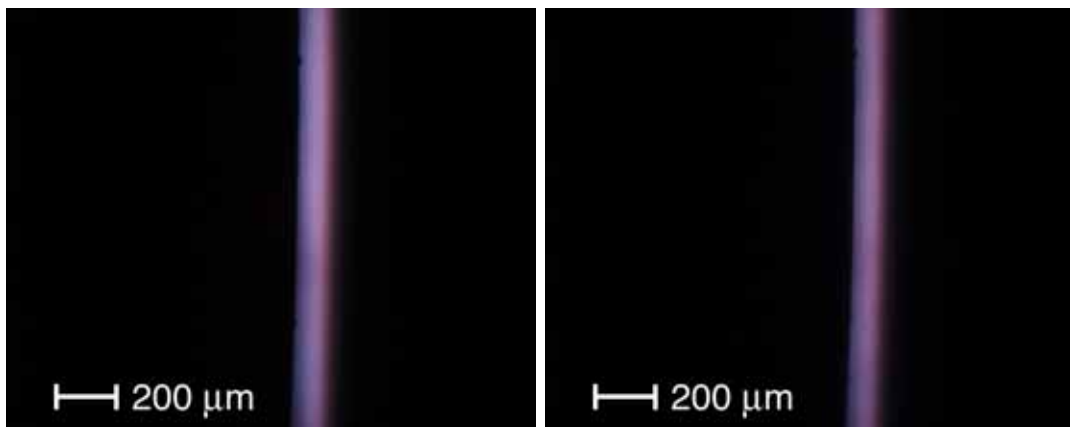
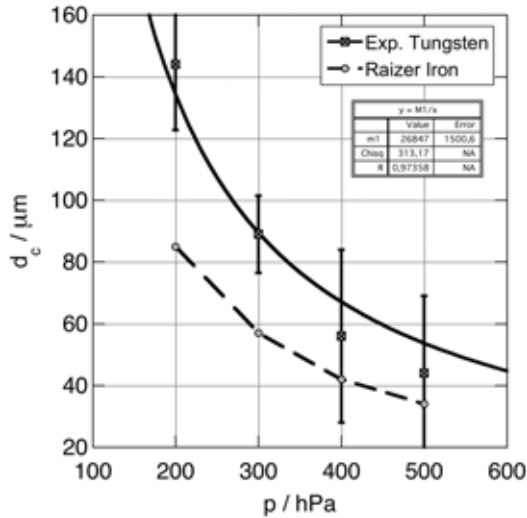


Figure 3.26:  $d_C = 56 \mu m$ ,  $p = 400 hPa$       Figure 3.27:  $d_C = 44 \mu m$ ,  $p = 500 hPa$

Table 3.7: Raw-data for Fig.3.28 in Sec.3.6

$p$ in $hPa$	$d_C$ in $\mu m$	$V_1$ in Volt
200	144	319
300	89	241
400	56	233
500	44	239



Gas: helium

Electrodes: tungsten

Electrode diameters:  $D = 2.4 \text{ mm}$

Shielding: Teflon

Pressure:  $p = 200, 300, 400$  and  $500 \text{ hPa}$

Inter-electrode gap:  $d = 2.6 \text{ mm}$

Current:  $I = 12 \text{ mA}$

Figure 3.28: Pressure dependence of the cathode dark-space for iron and tungsten electrodes

### 3.6.1 Discussion

Good measurements are difficult because of the diffuse glow and a lack of sharp boundaries. Photographs (Fig.3.24 to Fig.3.27) were taken with the old microscope camera Olympus DP10. Unfortunately this camera has bad contrast and resolution. Therefore distances were measured with the scale in the ocular of the microscope. This explains the huge error bars in Fig.3.28. More accurate results could be achieved in future with the new camera Olympus E-330 (Tab.2.1) and a similar method as described in Sec.3.3 using ImageJ [20].

In literature no value for the normal current density of tungsten and helium could be found. Therefore is not possible to compare the presented result of  $26.8 \text{ mm hPa}$  with other works. Iron and helium for example gives a value of  $17 \text{ mm hPa}$  which is in the same order of magnitude [19].

A look at the discharge voltages (Tab.3.7) show that the voltage is decreasing with increasing pressure. A serious discussion is impossible because of the lack of data. Subsequent measurements should contain more data points and use a similar method as presented in the first part of the discussion.

### 3.7 Anode light spots & anode glow

During all measurements bright and dim light spots and anode glow were observed. The palette reaches from very dim spots with an appearance like "foam" bubbles to very bright spots.

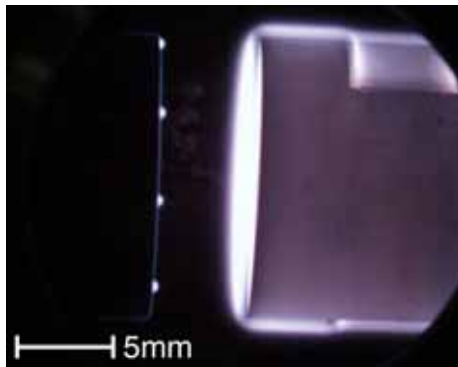
A. von Engel (1983):

*Anode glow covers the anode in the form of a layer or it consists of "individual" luminous spheres "struck" to the anode surface; their origin is still not clearly understood.*

Although investigations on anode spots initially were no objective of this thesis a phenomenological description is provided due to some interesting and curious results.

#### 3.7.1 Anode spots at large electrode surfaces

For the following measurements the inter-electrode gap was set to  $d = 5 \text{ mm}$  and the largest copper electrode with  $D = 15 \text{ mm}$  was taken. Measurements started with an initial pressure of  $p = 100 \text{ hPa}$  and an initial current of  $I = 6 \text{ mA}$ . At this current the front-side of the cathode was fully covered with negative glow. The positive column was not visible at these conditions. Increasing the current to  $I = 96 \text{ mA}$  led to the first appearance of anodic spots at the edge of the anode and a spreading negative glow at the cathode. A further increase of the current to the maximum current of the power-supply ( $I = 150 \text{ mA}$ ) led to an equidistant organization of anode spots at the anodes edge (Fig. 3.29). Sometimes these spots are rotating while their distance to each other remains constant. Unfortunately these phenomenon is not trigger-able and seems to be stochastic.



Gas: helium  
Electrodes: copper  
Shielding: none

$p$ in hPa	$I$ in mA	$V_0$ in Volt	$V_1$ in Volt
100	150	713	232

Figure 3.29: Equidistant anode spots at the anode edge

Figure 3.30 shows a single magnified anode spot at the lower edge and its reflection at the anode surface. The shape of the spot is like a foam bubble on a flat surface. The height of the spot is around  $0.4 \text{ mm}$  and the diameter is about  $0.7 \text{ mm}$ . Note that all measurements of the size of the anode spot are not very accurate. No sharp boundaries can be found. The average error is around 10% for height and diameter measurements. Sheath thicknesses can only be given by minimum and maximum values.

The intensity of the light decreases towards the anodes surface. There are indications that there is a dark region between the spot and the surface (Fig. 3.31) with a sheath thickness around  $d_{as} = 11 - 24 \mu m$ . Although it is possible that this is only an optical illusion. Further measurements are necessary. In comparison the measured sheath thickness of the cathodes dark space is in the range of  $d_{cs} = 0.35 - 0.55 mm$ . For this measurement the current was set to  $I = 6 mA$  to reduce the intensity of the negative glow.

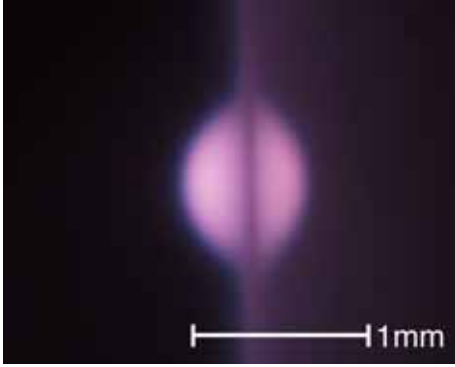


Figure 3.30: Magnified anode spot at the lower edge

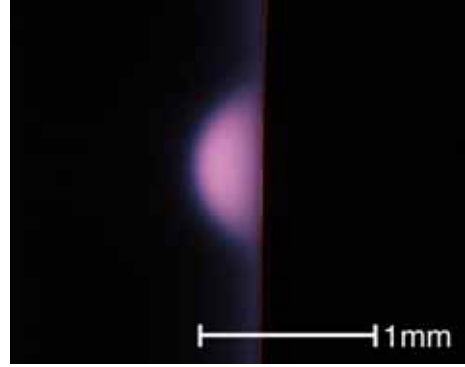
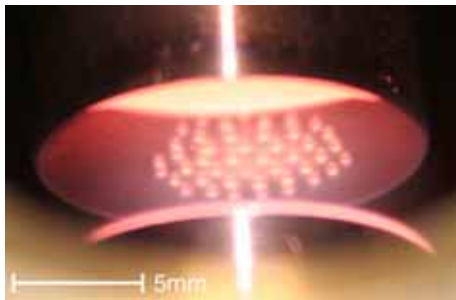


Figure 3.31: Magnified anode spot at the upper edge

An increase in pressure to  $p = 250 hPa$  forces the anode spots to contract to the anodes center. On large anodes the spots form hexagonal self-organized structures (Fig 3.32). Again the current was set to  $I = 150 mA$  and the negative glow covered the whole front-side of the cathode. Measurements at higher pressures were not performed. The power-supply was not able to provide higher currents.



Gas: helium  
Electrodes: copper  
Shielding: none

$p$ in hPa	$I$ in mA	$V_0$ in Volt	$V_1$ in Volt
250	150	686	206

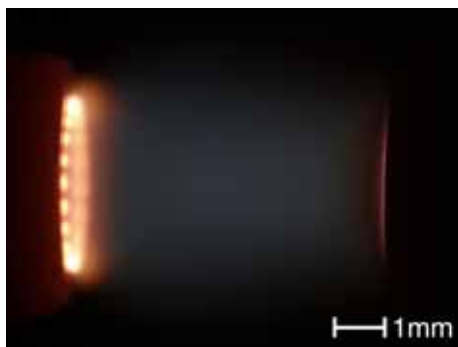
Figure 3.32: Hexagonal self-organized structures at the anode's surface

The distance of the spots to each other measured from center to center in the middle of the structure is about  $1.3 mm$ . The outer boundary of the whole structure is shaped hexagonal. The self-organized pattern was stable for several minutes. The electrodes showed no marks from the spots after disassembling which indicates low temperatures.

### 3.7.2 Anode spots at small electrode surfaces

Small electrodes ( $D < 5 \text{ mm}$ ) show a slightly different behaviour in the investigated pressure range from  $0.1 - 2.0 \text{ bar}$ . It's not possible to trigger the appearance of anode spots as easily as described in Sec.3.7.1. For electrode diameters of  $D = 2.1 \text{ mm}$  and pressures above  $p = 0.4 \text{ bar}$  the spots are always visible and independent of the current. Two types of anode spots can be described.

One type is similar to the earlier described "bubble" type at the edges (Fig. 3.33). The second kind is one single bright area or spot near the anode's center (Fig. 3.34). The intensity of the emitted light is comparable to the intensity of the negative glow. Refer to Sec.A.1 and Sec.A.2 for more examples.

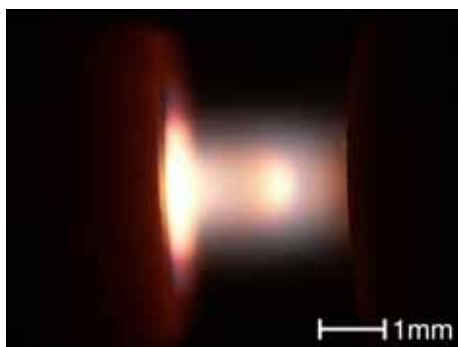


Gas: helium  
Electrodes: copper  
Shielding:  $Al_2O_3$

$p$ in hPa	$I$ in mA	$V_0$ in Volt	$V_1$ in Volt
430	25	366	284

Figure 3.33: Equidistant spots at the anode's edge (elec.:  $D = 3.0 \text{ mm}$ , gap:  $d = 6.1 \text{ mm}$ )

Fig. 3.33 shows an example for spots at the anode's edge. Both electrodes are shielded with ceramic tubes to restrict the glow to the front-side of the electrodes. This shielding ensures well defined conditions (two parallel circular surfaces). The density of spots is increased compared to Fig. 3.29.



Gas: helium  
Electrodes: copper  
Shielding:  $Al_2O_3$

$p$ in hPa	$I$ in mA	$V_0$ in Volt	$V_1$ in Volt
1290	150	702	214

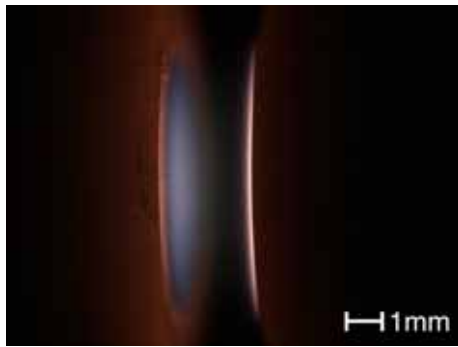
Figure 3.34: Bright centered anodic glow (elec.:  $D = 3.0 \text{ mm}$ , gap:  $d = 2.8 \text{ mm}$ )

Fig. 3.34 presents an example for one very bright area. The striated positive column and the spot is contracted to the middle axis. No self-organised structures are visible anymore.

### 3.7.3 Relation between anode spots and voltage drop in the high pressure case

One remarkable discovery is, that it's possible to operate glow discharges below the normal cathode fall voltage  $V_n$ . As tabulated in [19]  $V_n$  is 177 V for copper electrodes and helium. This voltage drop is usually necessary to sustain a glow discharge. If for example the inter-electrode gap is too small to allow the forming of the cathode fall, no stable glow discharge will develop.

The occurrence of very low operating voltages was discovered during measurements of column gradients to determine the reduced field strength in the positive column (Sec. A.1). Prerequisites are small electrode diameters, small inter-electrode gaps and increased pressures.

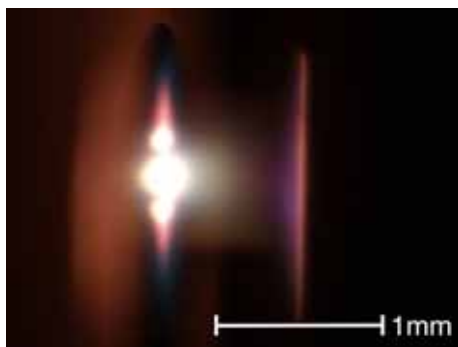


Gas: helium  
Electrodes: copper  
Shielding:  $Al_2O_3$

$p$ in hPa	$I$ in mA	$V_0$ in Volt	$V_1$ in Volt
300	16	219	167

Figure 3.35: Glow discharge below  $V_n = 177$  V (elec.:  $D = 4.3$  mm, gap:  $d = 1.7$  mm)

Fig. 3.35 show such a discharge. Although there are no light spots a weak diffuse glow at the anode's surface is visible. The discharge was stable and was operated at slightly higher gas flow rates to avoid contamination of the plasma. The measured discharge voltage was 10 V below  $V_n$ . The cathode was full covered by negative glow.



Gas: helium  
Electrodes: copper  
Shielding:  $Al_2O_3$

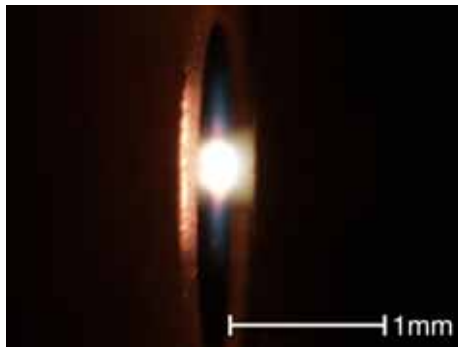
$p$ in hPa	$I$ in mA	$V_0$ in Volt	$V_1$ in Volt
1470	30	254	156

Figure 3.36: Glow discharge below  $V_n = 177$  V (elec.:  $D = 2.1$  mm, gap:  $d = 0.75$  mm)

In Fig. 3.36 there are three very bright anode spots at the surface. The positive column is visible and contracted. The negative glow covers the whole cathode's surface. The discharge voltage was 21 V below  $V_n$ .

The lowest measured voltage was 149.8 V (Fig.3.37). This voltage drop is 27.2 V below the normal cathode fall voltage  $V_n$  (177 V).

Voltages around  $\sim 119$  V were also measured (Fig.A.25 in Sec.A.1) with very narrow gaps (0.1 mm). Unfortunately this discharge wasn't observable with our setup and is therefore not reliable. Discrepancies in parallelism of the electrodes or not well rounded edges at this narrow inter-electrode gaps affect the measurements significantly.

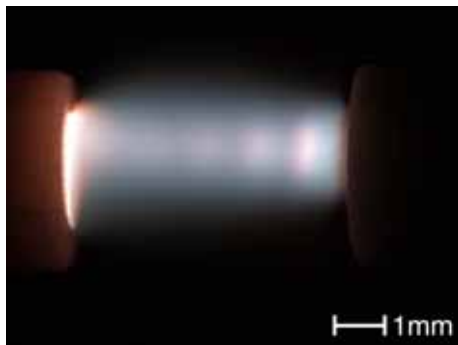


Gas: helium  
Electrodes: copper  
Shielding:  $Al_2O_3$

$p$ in $hPa$	$I$ in $mA$	$V_0$ in $Volt$	$V_1$ in $Volt$
1300	25	230	149.8

Figure 3.37: Glow discharge below  $V_n = 177$  V (elec.:  $D = 2.1$  mm, gap:  $d = 0.5$  mm)

It's obvious (Fig.3.37) that the discharge is very contracted. There is a single bright spot surrounded by a diffuse glow. This discharge seems to have a positive column but the optical impression may be misleading.



Gas: helium  
Electrodes: copper  
Shielding:  $Al_2O_3$

$p$ in $hPa$	$I$ in $mA$	$V_0$ in $Volt$	$V_1$ in $Volt$
1300	25	489	407

Figure 3.38: Glow discharge above  $V_n = 177$  V (elec.:  $D = 2.1$  mm, gap:  $d = 5.5$  mm)

In comparison Fig. 3.38 shows the same discharge with an increased inter-electrode gap and a current fixed to 25 mA. The positive column is striated and not as contracted as in Fig.(3.37). The whole discharge is shifted towards the upper edges of the electrode due to thermal heating. The positive column looks like a bow presumably due to the rather high gas flow. The gas inlet points straight to the discharge area.

### 3.7.4 Time evolution from anodic glow to anodic light spots

The following measurements were performed when Teflon-shieldings for the electrodes were used. Refer to Sec.(2.2.1) for more details! In short, decomposition of the Teflon-shieldings led to contamination of the plasma and the electrodes. The following measurements are mentioned for completeness of the presentation (Tab.3.8).

Gas: helium	$D$	$d$	$p$	$I$
Electrodes: copper	in mm	in mm	in hPa	in mA
Shielding: Teflon	2.5	5.0	220	10

Table 3.8: Experimental parameters

During the measurements very slow voltage drifts were observed (Fig.3.39). These voltage drifts were accompanied with a change in the optical impression at the anode (Fig.3.39). Usually it took several minutes for the discharge to reach a condition with unrecognisable slow voltage variations. The optical impression changed from a ring-like structure at  $t_0 = 0$  s to a single very bright spot at  $t_8 = 352$  s and reached a possibly stable state at this point .

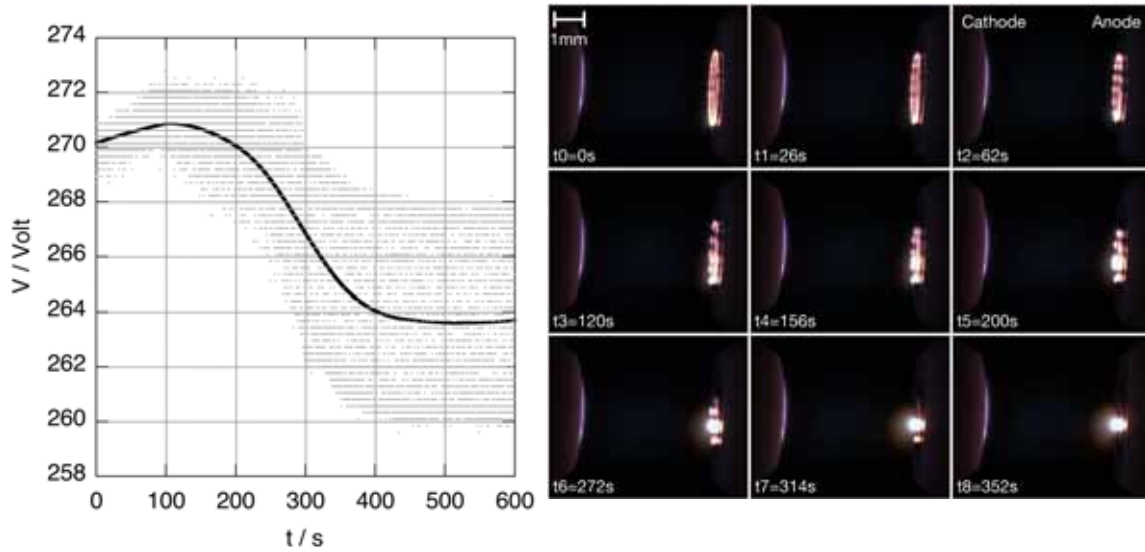


Figure 3.39: Time evolution from anodic glow to anodic light spots

The voltage increased for 150 s after ignition. The diameter of the anodic glow decreased during that time. After 62 s the anodic glow was divided into several almost equidistant anodic spots. After 200 s a significant voltage drop could be observed. The amplitude of the superposed noise in the voltage measurement was increased. The anodic spots reduced into one very bright spot. The voltage dropped to a value 8 V lower than the initial level. A frequency analyses of the superposed noise found the 50 Hz line-frequency in the signal. This suggests an inaccurate setup.

Additional to the photos optical spectra were measured. Due to the setup it was not possible to move the fibre of the spectrometer close to the negative glow or the anodic light

spots. Therefore, the glass-fibre pointed directly towards the surface of one of the electrodes. This position was fixed during the whole experiment. Therefore, it's possible to compare the line intensities of the spectra with the same integration time directly (Fig.3.41 and Fig.3.42). In order to get spectra of the anodic glow and the negative glow the polarity of the electrodes was changed during the experiment.

The measurements started with the spectrum of the negative glow (Fig.3.40). A useful side-effect was the preparation and cleaning of the surface for the time-evolution experiments by sputtering. The current was raised from 10 mA to 20 mA to get a higher light intensity.

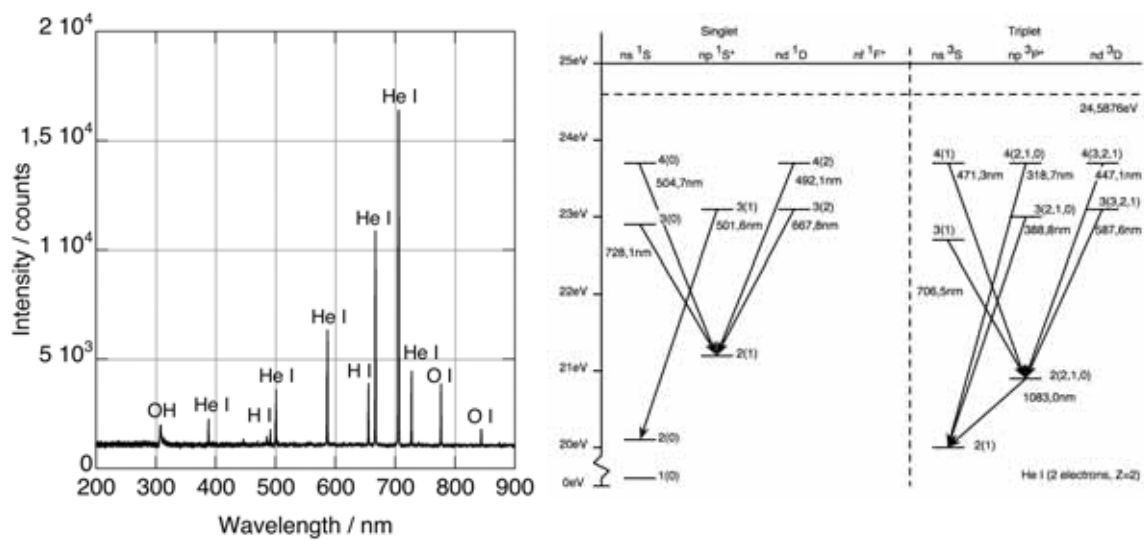


Figure 3.40: Optical spectrum of the cathode (integration time: 120 ms)

Fig.3.40 shows the measured spectrum and the Grotrian diagram of He at the right-hand side. OH, He, H and O can be found in the spectrum. The He I line with 706 nm wavelength is the most intense line. There are several transitions to the meta-stable  $2s^1S$  (singlet) and  $2s^3S$  (triplet) states.

After the measurement of the negative glow the polarity was changed. Fig. 3.41 shows the spectrum of the anodic glow at  $t = 0$  s. Fig.3.43 depicts the time-evolution of the spectra from negative glow to anodic light spots. At the beginning the light intensity is very low. A comparison with Fig. 3.40 shows that the relative heights of the lines are similar. It's likely that the intensity of the anodic glow was too low and that the spectrometer therefore measured scattered light from the negative glow.

Fig.3.42 shows the spectrum after 966 s. The appearance of the spectrum changed compared with the spectrum of the negative glow. The lines with 504.7 nm, 471.3 nm and 318.7 nm are missing. The He I line with 587.6 nm is now the line with the most intensity.

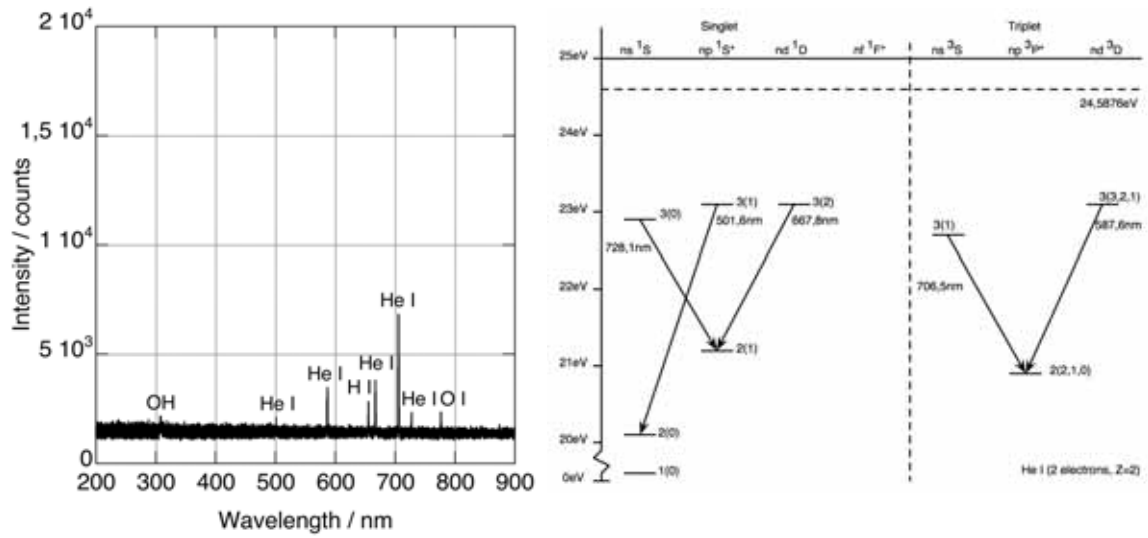
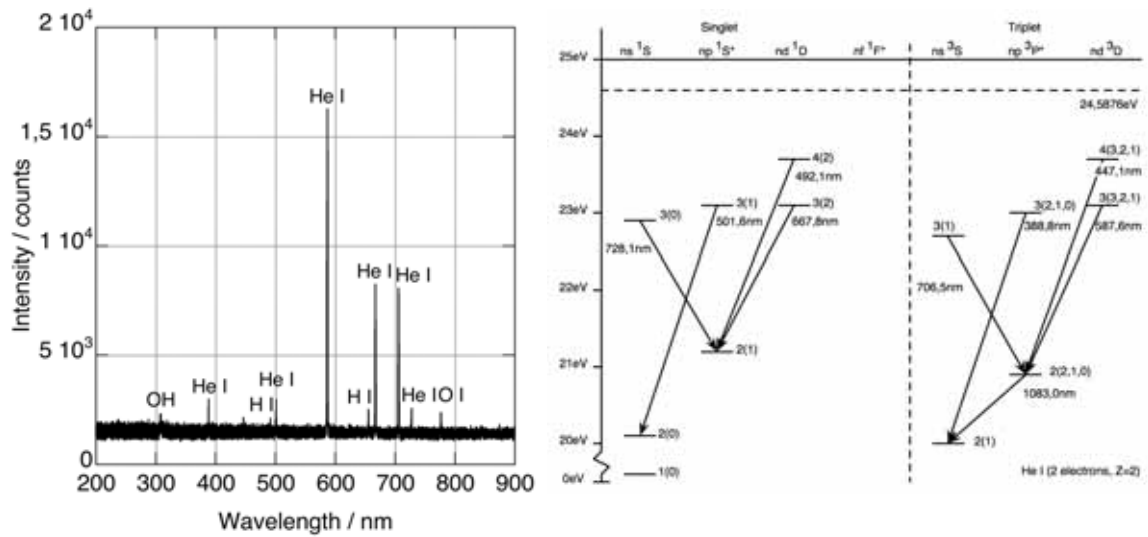


Figure 3.41: Optical spectrum of the anode after ignition (integration time: 300 ms)

Figure 3.42: Optical spectrum of the anode after  $t = 966$  s (integration time: 300 ms)

### 3.7.5 Discussion

Reports about ALPs are found in a lot of papers. Ammelt et al. [1] reported the observation of hexagonal structures like in Fig.3.32 but also possible transitions to a stripe pattern. Some authors found similarities between self-organized plasma structures and Turing structures obtained in biology and chemistry [18]. Popescu explains the transition from a planar to a spherical double layer by the minimisation of the free energy of the system [18]. Continuitive considerations about Turing structures lead to molecules and quasi-particle behaviours of the anodic light spots [2]. Finally anode double layer oscillations [17] and negative differential resistance related to self-organization phenomena [11] were reported.

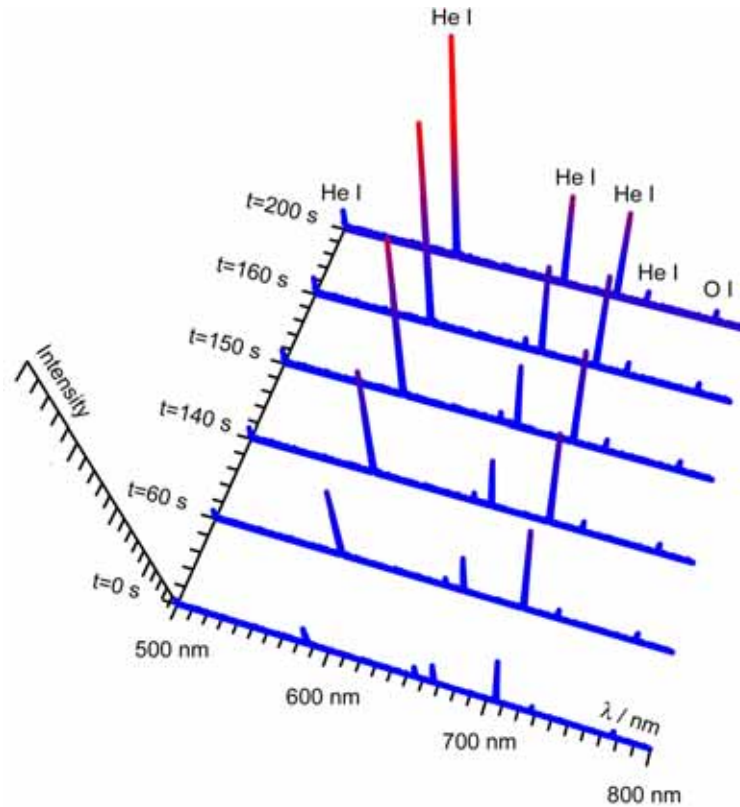


Figure 3.43: Time evolution of the spectral data from anodic glow to anodic light spots

As described in Sec.3.7.1 at low pressures and low currents (e.g.  $I = 6 \text{ mA}$ ,  $p = 0.1 \text{ bar}$ ) anode spots or anodic glows are not visible. With increased current ( $I = 96 \text{ mA}$ ) equidistant anode spots appear (Fig.3.29) at the anode's edge. This current limit for transition to anode spots is reduced with increasing pressure or decreasing electrode diameters. Although at  $p = 0.25 \text{ bar}$  and  $I = 150 \text{ mA}$  (Fig.3.32) the discharge is in the region of normal glow self-organized anode spots appear at the anode's surface.

Due to increased current densities with decreasing surface areas (Sec. 3.7.2) the density of anode spots is increased (Fig.3.33). High currents and therefore high powers led to very bright spots at the anode's center.

A possible explanation is a filamentation of the current due to instabilities in the anode sheath induced by high currents or pressures [26]. This is indicated by the self-organized structure of the anode spots. The current filaments form a hexagonal equidistant pattern or equidistant spots at the anode edge to gain the possible maximum distance from each other. Furthermore there is an amplification of the electric field strength at the electrode edges yielding an in-homogenous field which possibly support this process. According to Strümpel and Purwins [26]

*Individual current filaments are formed by repetitive electrical breakdown of the gas layer. The experimental data suggest that filamentary patterns arise as a result of losing the stability of the spatially homogeneous stationary discharge. The instability appears at the increase of current density in the device above some threshold value.*

The anode spots itself have a double layer structure. This double layer play the role initially played by the anode [22]. This is verified by probe measurements at low pressure by Conde and León [4]. Unfortunately no declarations about connecting conditions from the double layer to the anode could be found. Another not completely satisfactory solved question is why single spots are energetic favourable? Thinking about an ALP as a "cellular" structure with a membrane-like envelope corresponds to a local energy minimum and therefore its formation takes place spontaneously [22]. The idea of a membrane-like structure is not far-fetched because an electric double layer provides a selective enclosure of an environment that differs qualitatively from the surrounding medium.

There are indications that the anode sheath develops like in the case of a small anode. The cathode fall is therefore still 177 V and unaltered. The highest reliable measured voltage drop is around 26.8 V which is in the order of the first ionization potential of helium (24.587 eV).

- High currents or pressures are the source of instabilities in the anode sheath and induce anode spots and self-organized structures.
- Higher pressures force the spots to the anode's center.
- It's supposable that the anode sheath develops like in the small anode case.
- Anode spots and bright anode spots are always visible for small electrode diameters  $D < 2.1 \text{ mm}$  and pressures above  $p > 0.4 \text{ bar}$ .
- High current densities and therefore high powers destroy self-organized structures.

Furthermore voltage drifts occurred when Teflon-shieldings were used (Fig.3.39). It is not clear if the noisy signal is caused by anode spots oscillations [17] or an inaccurate setup. The optical appearance and spectra of the discharge changed too (Fig.3.43). XPS and Auger measurements showed (Sec.2.2.1) that oxides, silicon and fluor can be found on the surfaces. Therefore it's likely that the Teflon-shield became decomposed and that fluorides and oxides started to build areas with reduced conductivity on the anode's surface. The result was an increased discharge voltage (Fig.3.39). This thesis is supported by the fact that the diameter of the anodic glow decreases although the power consumption and therefore gas heating is

low. The loss of conductivity beginning at the anode's edge was followed by an increased current density with locally high temperatures in the center of the anode which prevented the deposition of fluorides and oxides in this region. This is followed by a drop in the discharge voltage. Optical spectra showed that the level of excited states of one single very bright anodic spot is comparable to the states of the negative glow. Excitations energies in the anodic spots are therefore higher than in the normal anode sheath. This phenomenon may help to sustain the discharge in the high pressure case.

It is likely that a possibly transitional effect from anodic glow to a single ALP is superposed by the deposition of Teflon. Further investigations without any shieldings are necessary and recommend to clarify the situation.



## Chapter 4

# Conclusion and Outlook

The investigation on breakdown voltages in Sec.3.1 shows clearly that the pressure  $p$  or the distance between the electrodes  $d$  cannot be changed independently giving the same ignition voltage  $V_i$  for the same  $pd$  values. Furthermore, it turned out that neither of the established formulas for the ignition potential is capable to fit the experimental data. The reason is the very low value of the reduced field strength for large inter-electrode gaps or high pressures.

The reduced normal current density for copper electrodes and helium is  $(j/p^2)_n = 1.597 \cdot 10^{-8} A/(mm^2 hPa^2)$ . The fits for the measured current densities show no significant deviation from the quadratic similarity law (Sec.3.2). Anyhow, there is a slight tendency to higher reduced normal current densities for increased pressures and smaller electrodes. This might be an indication for a violation of the similarity law. A possible explanation is gas heating.

The diameter of the positive column shows a strong, linear pressure dependence (Sec.3.3). This is most likely due to thermal instabilities. High pressure discharges feature strong temperature gradients, are contracted and in the presented case are not in contact with the chamber walls. The discharge is surrounded by cold and neutral gas. The gas density in the positive column is surely not homogeneous. Potentially, the current density  $j$  is of more importance than in the low pressure case.

The  $I - V$  characteristics at high pressures deviate from the characteristic in the low pressure case (Sec.3.4). The  $I - V$  diagrams show a negative  $dV/dI < 0$ . No region of abnormal glow is directly observable. Gas heating reduces the resistance and therefore decreases the operating voltage. The discharges with the highest pressures or smallest electrode show the lowest operating voltages. The curves of each set of similar discharges show an analogue behaviour and appear almost parallel. If its possible to eliminate contaminations from the gas, the similarity relations are probably still violated due to thermal stress.

It was not possible to present the reduced field strength  $E/p$  in the positive column as in the standard literature (Sec.3.5). Due to the contracted positive column and the recombination dominated regime the radius of the positive column was used to plot the data.  $E/p$  shows a linear, negative trend. The values of  $E/p$  decrease linearly from  $0.07 V/(hPa mm)$  at  $pR = 410 hPa mm$  to  $0.035 V/(hPa mm)$  at  $pR = 1100 hPa mm$ . Again the temperature is believed to be the cause of this behaviour. Deviations from the similarity relation are

not observable. However, measurements of the radius of the positive column are not very accurate. Statements about the similarity laws are difficult because of the inaccurate radius measurements.

Sheath measurements of the cathode dark-space were performed (Sec.3.6). The reduced thickness of a normal cathode sheath  $(p \cdot d_C)_n$  was measured for the first time for helium and tungsten. A value of  $26.8 \text{ mm hPa}$  for  $(p \cdot d_C)_n$  was determined.

Investigations on anode light spots and anode glows delivered a lot of interesting results (Sec.3.7). Two different types of anode spots, ring-like structures and self-organised hexagonal structures were observed. Another exciting feature was the operation of glow discharges below the normal cathode fall voltage  $V_n$  ( $177 \text{ V}$  for helium). The lowest measured discharge voltage is  $149.8 \text{ V}$ . The voltage drop is in the order of the first ionisation potential of helium ( $24.587 \text{ eV}$ ). Voltage drifts and changes in the optical behaviour were also observed.

Most of the measurements showed stationary striations which are unusual in noble gases. Normally they are moving too fast to be observed with the naked eyes.

Finally, a couple of concluding remarks about the validity of similarity relations in the high pressure case are given. There are indications that the similarity relations are violated in the high pressure case. Mathematically similar discharges show different  $I - V$  characteristics (Sec.3.4). The current densities show no deviation from the quadratic similarity law for higher pressures. However, there is a slight tendency to higher reduced normal current densities for increased pressures and smaller electrodes (Sec.3.2). This is also a hint for a possible violation of the similarity relations.

One absolute necessary prerequisite for further measurements is a method for accurate temperature determination. Measurements without reliable temperature measurements are hard to interpret. Only an accurate compensation of temperature effects would allow a more advanced study of the influence of high pressures on similarity laws. Furthermore, detailed information about the gas and the electrode composition is required. Methods must be found to purify the operating gas in the discharge chamber. Field amplification due to the electrode edges should also be compensated by optimising the shape of the electrodes. This will most probably give more reliable ignition voltages.

## Chapter 5

## References



# Bibliography

- [1] E. Ammelt, Yuri A. Astrov, and Hans-Georg Purwins. Hexagon structures in a two-dimensional dc-driven gas discharge system. *Physical Review E*, 58(6):7109–7117, 1998.
- [2] Yuri A. Astrov and Hans-Georg Purwins. Plasma spots in a gas discharge system: birth, scattering and formation of molecules. *Physics Letters A*, 283:349–354, 2001.
- [3] Francis F. Chen. *Introduction to Plasma Physics and Controlled Fusion*, volume 1. Plenum Press, 2 edition, 1984. ISBN 0306413329.
- [4] L. Conde and L. León. Multiple double layers in a glow discharge. *Physics of Plasmas*, 1(8):2441–2447, August 1994.
- [5] Jan Eijkel, Herbert Störi, and Andreas Manz. An atmospheric pressure dc glow discharge on a microchip and its application as a molecular emission detector. *Journal of Analytical Atomic Spectroscopy*, 15:297–300, 2000.
- [6] PDE Solutions Inc. *FlexPDE: A Flexible Solution System for Partial Differential Equations*. PDE Solutions Inc., 2006. URL [www.pdesolutions.com](http://www.pdesolutions.com).
- [7] V. Kudrle, E. LeDuc, and M. Fitaire. Breakdown delay times and memory effects in helium at low pressure. *Journal of Applied Physics D*, 32:2049–2055, 1999.
- [8] J. Laimer. *Plasmatechnologie*, volume 1. Vorlesungsskriptum IAP, 1. edition, 2005.
- [9] Irving Langmuir. Oscillations in ionized gases. *Proceedings of the National Academy of Sciences USA*, 14(8):627–637, August 1928.
- [10] V. A. Lisovskiy, S. D. Yakovin, and V. D. Yegorenkov. Low-pressure gas breakdown in uniform dc electric field. *Journal of Applied Physics D*, 33:2722–2730, July 2000.
- [11] E. Lozneau, V. Popescu, and M. Sanduloviciu. Negative differential resistance related to self-organization phenomena in a dc gas discharge. *Journal of Applied Physics*, 92(3): 1195–1199, August 2002.
- [12] J. Luque and D. R. Crosley. *Lifbase: Database and spectral simulation (version 2.0)*. SRI International Report MP 99-009, 1999.
- [13] M. Mantler and P. Varga. *Physikalische Analytik*, volume 1. Vorlesungsskriptum IAP und IFP, 5. edition, 2002.

- [14] D. Marić, M. Radmilović-Radenović, and Z. Lj. Petrović. On parametrization and mixture laws for electron ionization coefficients. *The European Physical Journal D*, 35:313–321, 2005.
- [15] P. Mezei, T. Cserfalvi, M. Jánossy, K. Szöcs, and H. J. Kim. Similarity law for glow discharges with cathodes of metal and an electrolyte. *Journal of Applied Physics D*, 31: 2818–2825, 1998.
- [16] R. W. B. Pearse and A. G. Gaydon. *The identification of molecular spectra*, volume 1. Chapman and Hall, 4. edition, 1976. ISBN 041214350X.
- [17] Valentin Pohoata, Gheorghe Popa, Roman Schrittwieser, Codrina Ionita, and Milan Cercek. Properties and control of anode double layer oscillations and related phenomena. *Physical Review E*, 68:016405–1 – 8, 2003.
- [18] S. Popescu. Turing structures in dc gas discharges. *Europhysics letters*, 73(2):190–196, 2006.
- [19] Yuri P. Raizer. *Gas discharge physics*, volume 1. Springer-Verlag, 1. edition, 1991. ISBN 3540194622.
- [20] Wayne. S. Rasband. *ImageJ: Image Processing with ImageJ*. 1.36b. National Institutes of Health, USA, Bethesda, Maryland, USA, 1997-2007. URL <http://rsb.info.nih.gov/ij/>.
- [21] J. Reece Roth. *Industrial Plasma Engineering*, volume 1. Institute of Physics Publishing, Bristol and Philadelphia, 1. edition, 1995. ISBN 0750303182.
- [22] M. Sanduloviciu, C. Borcia, and Gabriela Leu. Self-organization phenomena in current carrying plasmas related to the non-linearity of the current versus voltage characteristic. *Physics Letters A*, 208:136–142, 1995.
- [23] J. J. Shi and M. G. Kong. Cathode fall characteristics in a dc atmospheric pressure glow discharge. *Journal of Applied Physics*, 94(9):5504–5513, November 2003.
- [24] David Staack, Bakhtier Farouk, Alexander Gutsol, and Alexander Fridman. Characterization of a dc atmospheric pressure normal glow discharge. *Plasma Sources Science and Technology*, 14:700–711, 2005.
- [25] A. R. Strignov and N. S. Sventitskii. *Tables of spectral lines of neutral and ionized atoms*, volume 1. IFI/Lenum New York, 1. edition, 1968.
- [26] C. Strümpel and Hans-Georg Purwins. Spatiotemporal filamentary patterns in a dc-driven planar gas discharge system. *Physical Review E*, 63:026409–1 – 7, 2001.
- [27] A. v. Engel, R. Seeliger, and M. Steenbeck. Über die glimmentladung bei hohen drucken. *Zeitschrift für Physik (Berlin)*, 85(144-160), 1933.
- [28] A. von Engel. *Ionized Gases*. American Vacuum Society Classics. American Institute of Physics, 1994. ISBN 1563962721.

# Appendix A

## Measured raw-data

Measurements within one measurement series were performed on the same day without interruptions or breaks. The whole set of results and the appendant measurement tables are in appendix Sec.A. Photographs (the anode is always at the left-hand side) and optical spectra of the discharges complete the data-sheets. The optical spectra are used to determine the gas composition [25] and the temperature. For temperature determination the *OH*-band [16] was used. Simulations of the *OH* spectra were performed with *Lifbase 2.0* [12] (e.g. Fig.A.1 and Fig.A.2). The program settings are given in separate tables. The integration times of the optical spectrometer are given in the figure caption.

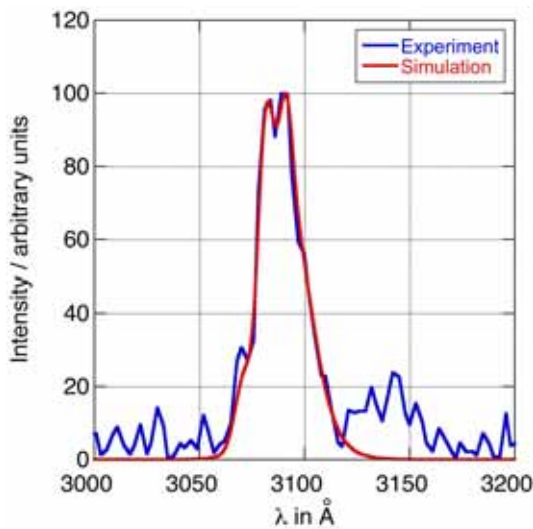


Figure A.1: *OH*-band at  $p = 400 \text{ hPa}$   
 $T = 305 \text{ K}$  for  $P = 2.5 \text{ W}$

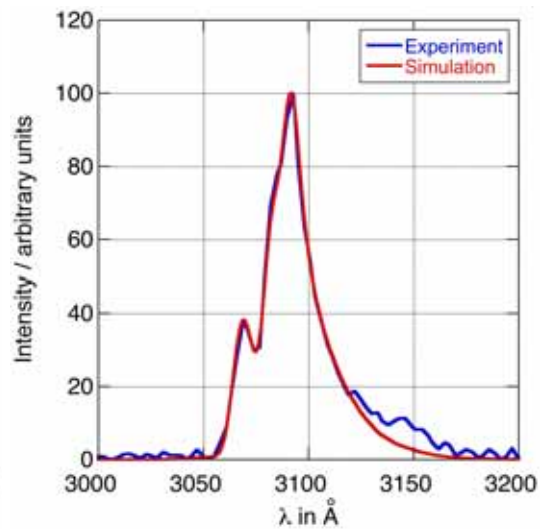


Figure A.2: *OH*-band at  $p = 1200 \text{ hPa}$   
 $T = 950 \text{ K}$  for  $P = 10.4 \text{ W}$

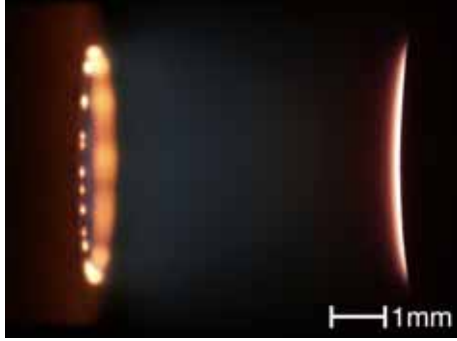
The photos and spectra for Sec.A.1 were taken at the maximum possible inter-electrode gap distance  $l_{i_{max}}$  ( $i = 1, 2, 3$ ). All photos exhibited in Sec.A.2 were taken at full coverage of the cathode with negative glow.

## A.1 Reduced field strength in the positive column

Table A.1: Overview of all triples of similar discharges for Sec.A.1 (Appendix)

Series	Pressures	Raw data	Table
1	$p_1 = 200 \text{ hPa}$	p. 75	TabA.66 on p. 143
	$p_2 = 290 \text{ hPa}$	p. 84	TabA.75 on p. 147
	$p_3 = 400 \text{ hPa}$	p. 93	TabA.84 on p. 152
2	$p_1 = 300 \text{ hPa}$	p. 76	TabA.67 on p. 143
	$p_2 = 290 \text{ hPa}$	p. 85	TabA.76 on p. 148
	$p_3 = 600 \text{ hPa}$	p. 94	TabA.85 on p. 152
3	$p_1 = 400 \text{ hPa}$	p. 77	TabA.68 on p. 144
	$p_2 = 570 \text{ hPa}$	p. 86	TabA.77 on p. 148
	$p_3 = 800 \text{ hPa}$	p. 95	TabA.86 on p. 153
4	$p_1 = 500 \text{ hPa}$	p. 78	TabA.69 on p. 144
	$p_2 = 720 \text{ hPa}$	p. 87	TabA.78 on p. 149
	$p_3 = 1000 \text{ hPa}$	p. 96	TabA.87 on p. 153
5	$p_1 = 600 \text{ hPa}$	p. 79	TabA.70 on p. 145
	$p_2 = 860 \text{ hPa}$	p. 88	TabA.79 on p. 149
	$p_3 = 1200 \text{ hPa}$	p. 97	TabA.88 on p. 154
6	$p_1 = 700 \text{ hPa}$	p. 80	TabA.71 on p. 145
	$p_2 = 1000 \text{ hPa}$	p. 89	TabA.80 on p. 150
	$p_3 = 1400 \text{ hPa}$	p. 99	TabA.90 on p. 155
7	$p_1 = 800 \text{ hPa}$	p. 81	TabA.72 on p. 146
	$p_2 = 1150 \text{ hPa}$	p. 90	TabA.81 on p. 150
	$p_3 = 1600 \text{ hPa}$	p. 101	TabA.92 on p. 156
8	$p_1 = 900 \text{ hPa}$	p. 82	TabA.73 on p. 146
	$p_2 = 1290 \text{ hPa}$	p. 91	TabA.82 on p. 151
	-	-	
9	$p_1 = 1000 \text{ hPa}$	p. 83	TabA.74 on p. 147
	$p_2 = 1430 \text{ hPa}$	p. 92	Tab.A.83 on p. 151
	-	-	

A.1.1 Measurement series with scaling factors  $a=2$  and  $1.4$ 

Column gradients for  $D_1 = 4.3 \text{ mm}$ ,  $p_1 = 200 \text{ hPa}$  and  $I = 25 \text{ mA}$ 


Gas: helium  
Electrodes: copper  
Shielding:  $Al_2O_3$

$p_1$ in hPa	$I$ in mA	$D_1$ in mm	$l_{1max}$ in mm
200	25	4.3	5.95

The field strength  $E_1$  in the positive column was determined from diagram Fig.A.3 between 2 and 4 mm.

$$E_1 = 14.1 \frac{V}{mm} \quad \frac{E_1}{p_1} = 0.071 \frac{V}{hPa \cdot mm} \quad T_1 = 375 \text{ K} \quad (\text{A.1})$$

The spectrum was taken at  $l_{1max} = 5.95 \text{ mm}$  and a power consumption of  $P_1 = 5.9 \text{ W}$ .

Resolution:	8nm	Baseline correction:	8	Multiplication:	13.9
Temperature:	375K	Wavelength correction:	-6nm	Doppler broad.:	yes

Table A.2: Lifbase 2.0 settings for  $p_1 = 200 \text{ hPa}$  and  $T = 375 \text{ K}$  ( $P_1 = 5.9 \text{ W}$ )

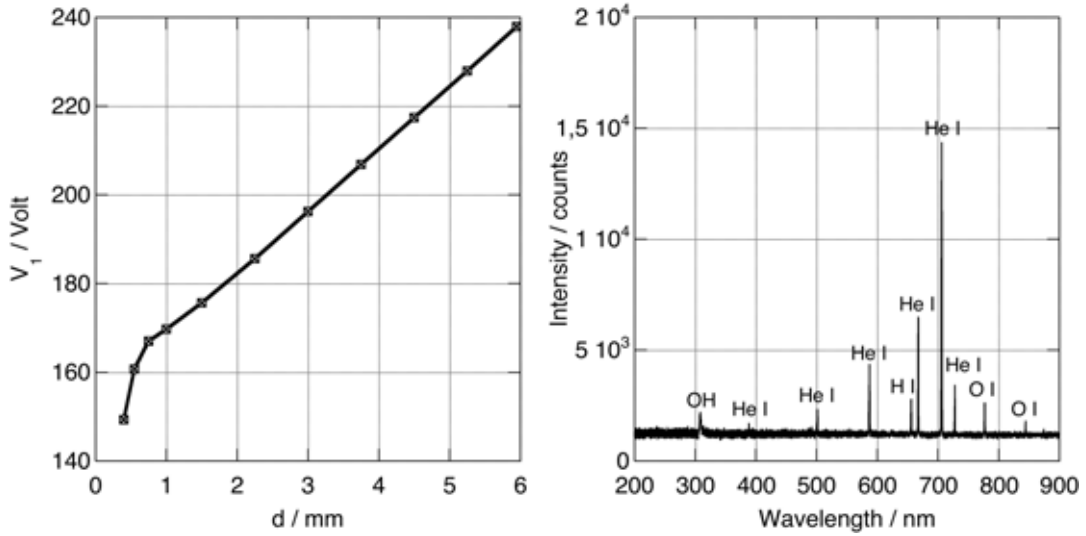
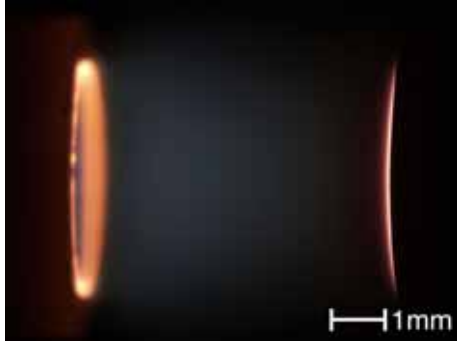


Figure A.3: Column gradient (Tab.A.66) and spectrum (integration time: 200 ms)

Column gradients for  $D_1 = 4.3 \text{ mm}$ ,  $p_1 = 300 \text{ hPa}$  and  $I = 25 \text{ mA}$



Gas: helium  
Electrodes: copper  
Shielding:  $Al_2O_3$

$p_1$ in hPa	$I$ in mA	$D_1$ in mm	$l_{1max}$ in mm
300	25	4.3	5.95

The field strength  $E_1$  in the positive column was determined from diagram Fig.A.4 between 2 and 4mm.

$$E_1 = 19.1 \frac{V}{mm} \quad \frac{E_1}{p_1} = 0.064 \frac{V}{hPa \cdot mm} \quad T_1 = 445 K \quad (\text{A.2})$$

The spectrum was taken at  $l_{1max} = 5.95 \text{ mm}$  and a power consumption of  $P_1 = 6.3 \text{ W}$ .

Resolution:	8nm	Baseline correction:	8	Multiplication:	10.3
Temperature:	445K	Wavelength correction:	-4nm	Doppler broad.:	yes

Table A.3: Lifbase 2.0 settings for  $p_1 = 300 \text{ hPa}$  and  $T = 445 \text{ K}$  ( $P_1 = 6.3 \text{ W}$ )

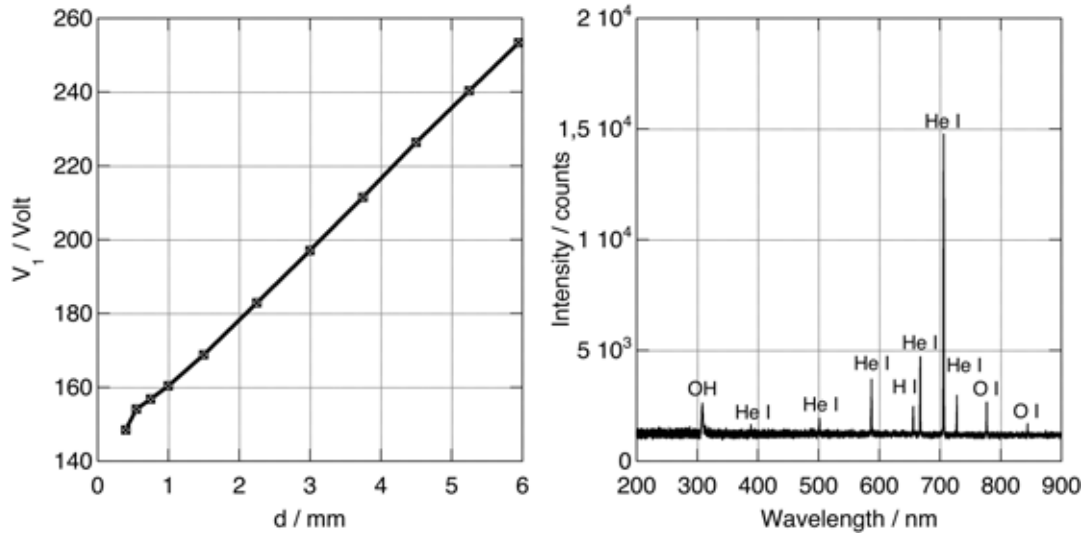
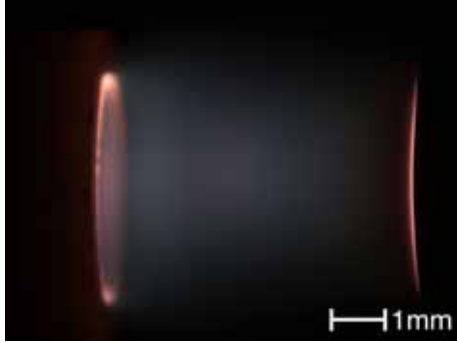


Figure A.4: Column gradient (Tab.A.67) and spectrum (integration time: 200 ms)

Column gradients for  $D_1 = 4.3 \text{ mm}$ ,  $p_1 = 400 \text{ hPa}$  and  $I = 25 \text{ mA}$



Gas: helium  
Electrodes: copper  
Shielding:  $Al_2O_3$

$p_1$ in hPa	$I$ in mA	$D_1$ in mm	$l_{1max}$ in mm
400	25	4.3	5.95

The field strength  $E_1$  in the positive column was determined from diagram Fig.A.5 between 2 and 4mm.

$$E_1 = 24.6 \frac{V}{mm} \quad \frac{E_1}{p_1} = 0.062 \frac{V}{hPa \cdot mm} \quad T_1 = 475 K \quad (A.3)$$

The spectrum was taken at  $l_{1max} = 5.95 \text{ mm}$  and a power consumption of  $P_1 = 7.2 \text{ W}$ .

Resolution:	8nm	Baseline correction:	10	Multiplication:	4.1
Temperature:	475K	Wavelength correction:	-4nm	Doppler broad.:	yes

Table A.4: Lifbase 2.0 settings for  $p_1 = 400 \text{ hPa}$  and  $T = 475 \text{ K}$  ( $P_1 = 7.2 \text{ W}$ )

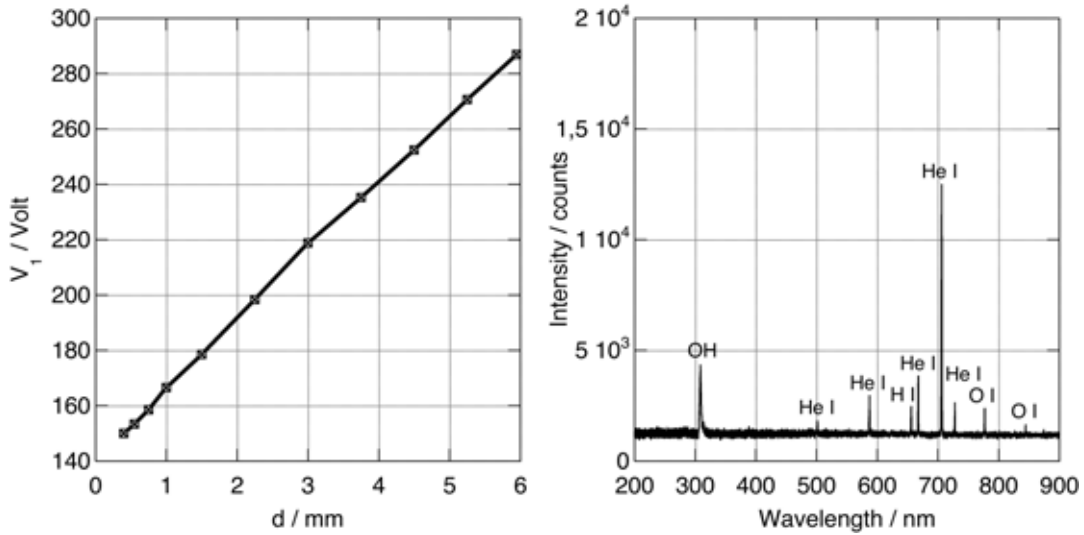
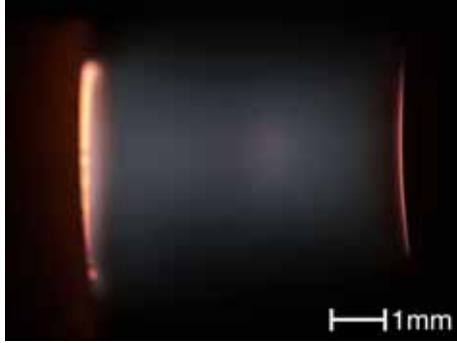


Figure A.5: Column gradient (Tab.A.68) and spectrum (integration time: 200 ms)

Column gradients for  $D_1 = 4.3 \text{ mm}$ ,  $p_1 = 500 \text{ hPa}$  and  $I = 25 \text{ mA}$



Gas: helium  
Electrodes: copper  
Shielding:  $Al_2O_3$

$p_1$ in hPa	$I$ in mA	$D_1$ in mm	$l_{1max}$ in mm
500	25	4.3	5.95

The field strength  $E_1$  in the positive column was determined from diagram Fig.A.6 between 2 and 4mm.

$$E_1 = 26.7 \frac{V}{mm} \quad \frac{E_1}{p_1} = 0.053 \frac{V}{hPa \cdot mm} \quad T_1 = 500 \text{ K} \quad (\text{A.4})$$

The spectrum was taken at  $l_{1max} = 5.95 \text{ mm}$  and a power consumption of  $P_1 = 7.6 \text{ W}$ .

Resolution:	8nm	Baseline correction:	8.5	Multiplication:	3.5
Temperature:	500K	Wavelength correction:	-3.5nm	Doppler broad.:	yes

Table A.5: Lifbase 2.0 settings for  $p_1 = 500 \text{ hPa}$  and  $T = 500 \text{ K}$  ( $P_1 = 7.2 \text{ W}$ )

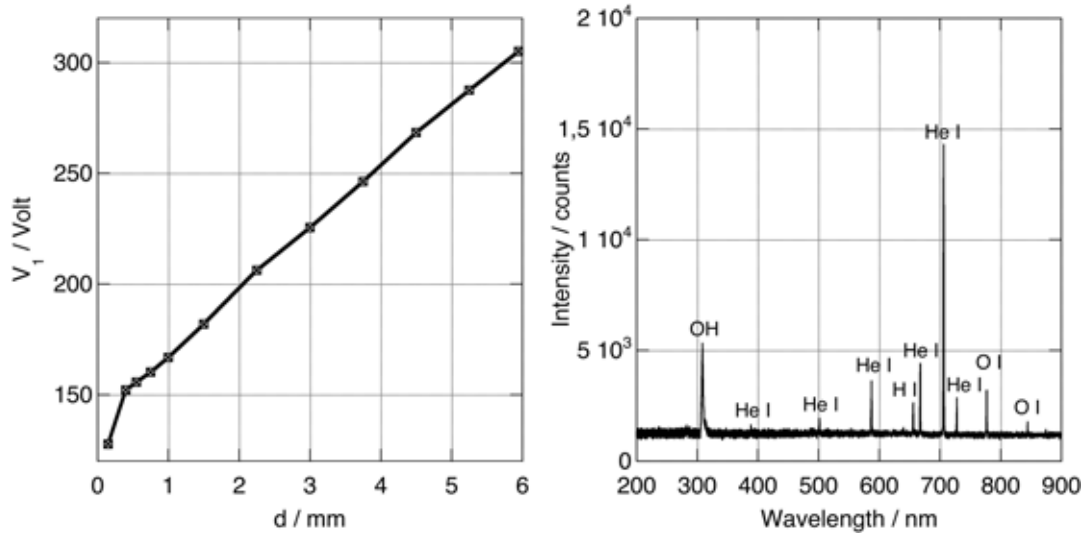
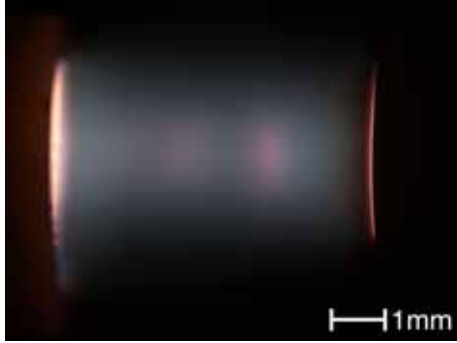


Figure A.6: Column gradient (Tab.A.69) and spectrum (integration time: 200 ms)

Column gradients for  $D_1 = 4.3 \text{ mm}$ ,  $p_1 = 600 \text{ hPa}$  and  $I = 25 \text{ mA}$



Gas: helium  
Electrodes: copper  
Shielding:  $Al_2O_3$

$p_1$ in hPa	$I$ in mA	$D_1$ in mm	$l_{1max}$ in mm
600	25	4.3	5.95

The field strength  $E_1$  in the positive column was determined from diagram Fig.A.7 between 2 and 4mm.

$$E_1 = 31.6 \frac{V}{mm} \quad \frac{E_1}{p_1} = 0.053 \frac{V}{hPa \cdot mm} \quad T_1 = 800 K \quad (A.5)$$

The spectrum was taken at  $l_{1max} = 5.95 \text{ mm}$  and a power consumption of  $P_1 = 8.2 \text{ W}$ .

Resolution:	8nm	Baseline correction:	13.5	Multiplication:	1.54
Temperature:	800K	Wavelength correction:	-4nm	Doppler broad.:	yes

Table A.6: Lifbase 2.0 settings for  $p_1 = 600 \text{ hPa}$  and  $T = 800 \text{ K}$  ( $P_1 = 8.2 \text{ W}$ )

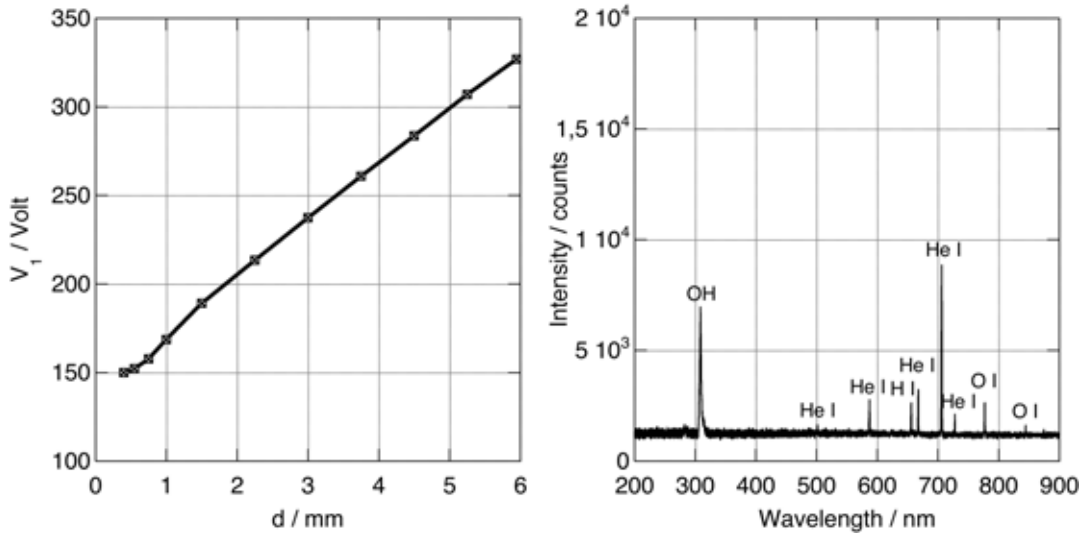
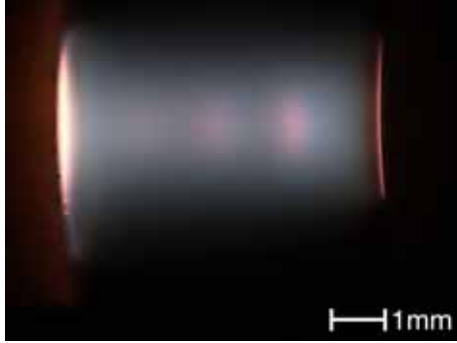


Figure A.7: Column gradient (Tab.A.70) and spectrum (integration time: 200 ms)

Column gradients for  $D_1 = 4.3 \text{ mm}$ ,  $p_1 = 700 \text{ hPa}$  and  $I = 25 \text{ mA}$



Gas: helium  
Electrodes: copper  
Shielding:  $Al_2O_3$

$p_1$ in hPa	$I$ in mA	$D_1$ in mm	$l_{1max}$ in mm
700	25	4.3	5.95

The field strength  $E_1$  in the positive column was determined from diagram Fig.A.8 between 2 and 4mm.

$$E_1 = 34.3 \frac{V}{mm} \quad \frac{E_1}{p_1} = 0.049 \frac{V}{hPa \cdot mm} \quad T_1 = 850 \text{ K} \quad (\text{A.6})$$

The spectrum was taken at  $l_{1max} = 5.95 \text{ mm}$  and a power consumption of  $P_1 = 8.7 \text{ W}$ .

Resolution:	8nm	Baseline correction:	12.5	Multiplication:	1.14
Temperature:	850K	Wavelength correction:	-4.5nm	Doppler broad.:	yes

Table A.7: Lifbase 2.0 settings for  $p_1 = 700 \text{ hPa}$  and  $T = 850 \text{ K}$  ( $P_1 = 8.7 \text{ W}$ )

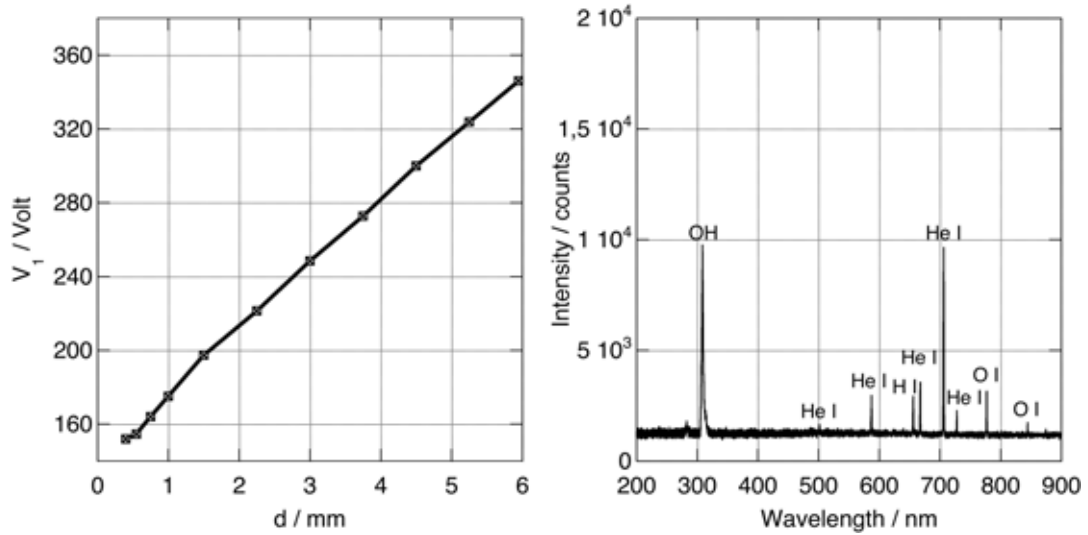
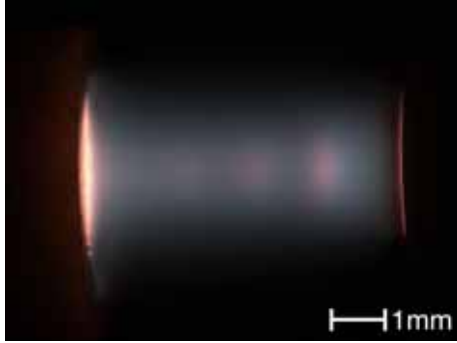


Figure A.8: Column gradient (Tab.A.71) and spectrum (integration time: 200 ms)

Column gradients for  $D_1 = 4.3 \text{ mm}$ ,  $p_1 = 800 \text{ hPa}$  and  $I = 25 \text{ mA}$



Gas: helium  
Electrodes: copper  
Shielding:  $Al_2O_3$

$p_1$ in hPa	$I$ in mA	$D_1$ in mm	$l_{1max}$ in mm
800	25	4.3	5.95

The field strength  $E_1$  in the positive column was determined from diagram Fig.A.9 between 2 and 4mm.

$$E_1 = 37.5 \frac{V}{mm} \quad \frac{E_1}{p_1} = 0.047 \frac{V}{hPa \cdot mm} \quad T_1 = 875 K \quad (A.7)$$

The spectrum was taken at  $l_{1max} = 5.95 \text{ mm}$  and a power consumption of  $P_1 = 9.1 \text{ W}$ .

Resolution:	8nm	Baseline correction:	11.5	Multiplication:	1.13
Temperature:	875K	Wavelength correction:	-4nm	Doppler broad.:	yes

Table A.8: Lifbase 2.0 settings for  $p_1 = 800 \text{ hPa}$  and  $T = 875 \text{ K}$  ( $P_1 = 9.1 \text{ W}$ )

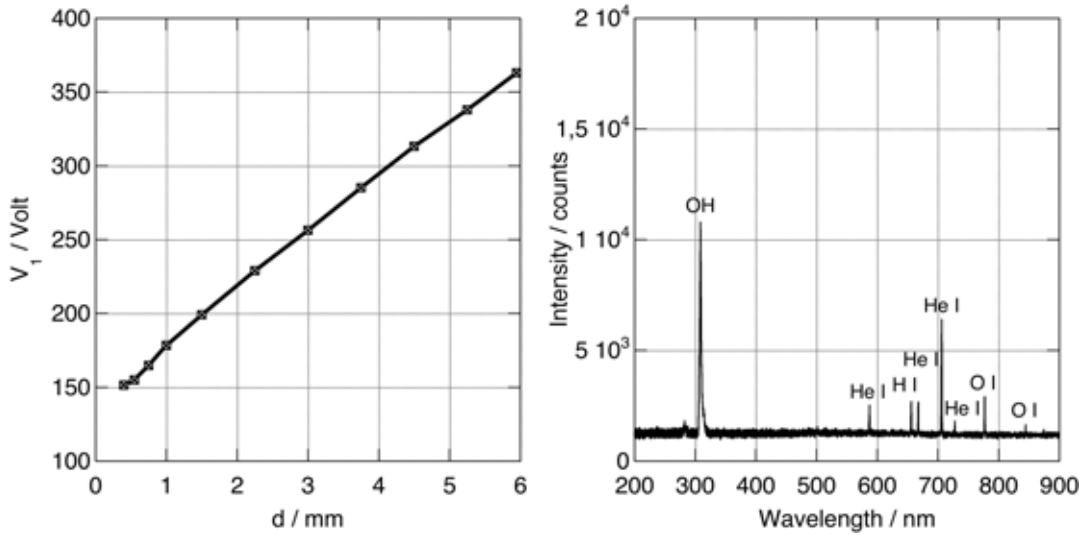
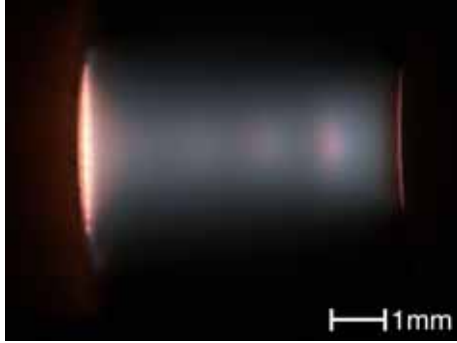


Figure A.9: Column gradient (Tab.A.72) and spectrum (integration time: 200 ms)

Column gradients for  $D_1 = 4.3 \text{ mm}$ ,  $p_1 = 900 \text{ hPa}$  and  $I = 25 \text{ mA}$



Gas: helium  
Electrodes: copper  
Shielding:  $Al_2O_3$

$p_1$ in hPa	$I$ in mA	$D_1$ in mm	$l_{1max}$ in mm
900	25	4.3	5.95

The field strength  $E_1$  in the positive column was determined from diagram Fig.A.10 between 2 and 4mm.

$$E_1 = 42.7 \frac{V}{mm} \quad \frac{E_1}{p_1} = 0.047 \frac{V}{hPa \cdot mm} \quad T_1 = 900 \text{ K} \quad (\text{A.8})$$

The spectrum was taken at  $l_{1max} = 5.95 \text{ mm}$  and a power consumption of  $P_1 = 9.5 \text{ W}$ .

Resolution:	8nm	Baseline correction:	12	Multiplication:	1.14
Temperature:	900K	Wavelength correction:	-4nm	Doppler broad.:	yes

Table A.9: Lifbase 2.0 settings for  $p_1 = 900 \text{ hPa}$  and  $T = 900 \text{ K}$  ( $P_1 = 9.5 \text{ W}$ )

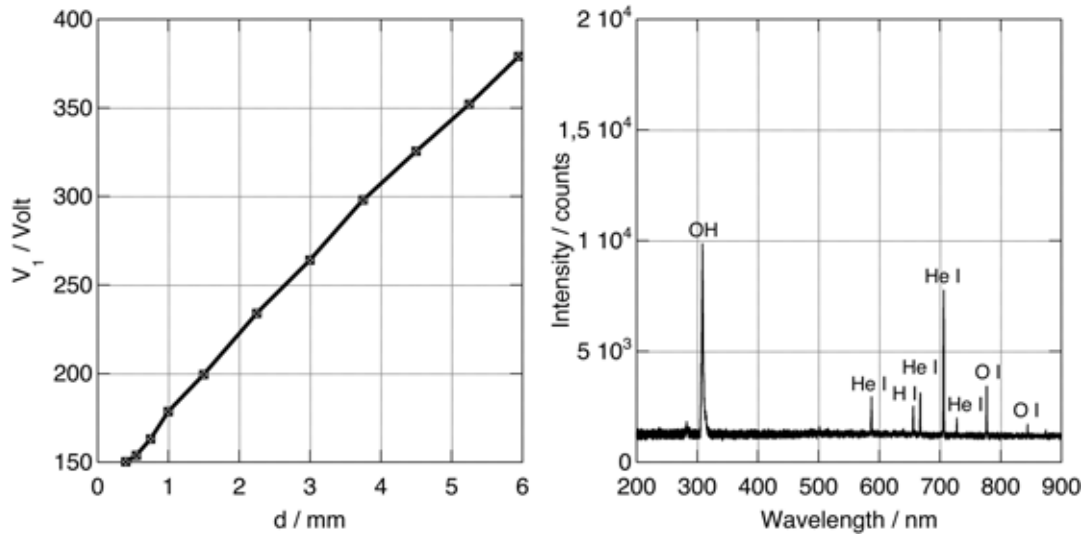
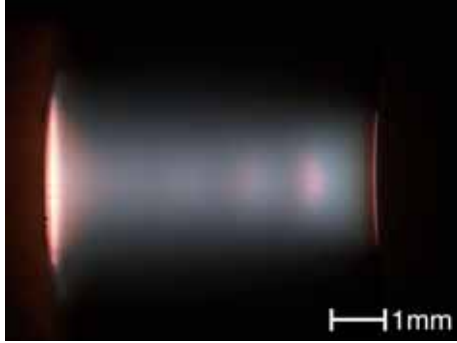


Figure A.10: Column gradient (Tab.A.73) and spectrum (integration time: 200 ms)

Column gradients for  $D_1 = 4.3 \text{ mm}$ ,  $p_1 = 1000 \text{ hPa}$  and  $I = 25 \text{ mA}$



Gas: helium  
Electrodes: copper  
Shielding:  $Al_2O_3$

$p_1$ in hPa	$I$ in mA	$D_1$ in mm	$l_{1max}$ in mm
1000	25	4.3	5.95

The field strength  $E_1$  in the positive column was determined from diagram Fig.A.11 between 2 and 4mm.

$$E_1 = 46.9 \frac{V}{mm} \quad \frac{E_1}{p_1} = 0.047 \frac{V}{hPa \cdot mm} \quad T_1 = 975 K \quad (A.9)$$

The spectrum was taken at  $l_{1max} = 5.95 \text{ mm}$  and a power consumption of  $P_1 = 9.9 \text{ W}$ .

Resolution:	8nm	Baseline correction:	11.5	Multiplication:	1.13
Temperature:	975K	Wavelength correction:	-4nm	Doppler broad.:	yes

Table A.10: Lifbase 2.0 settings for  $p_1 = 1000 \text{ hPa}$  and  $T = 975 \text{ K}$  ( $P_1 = 9.9 \text{ W}$ )

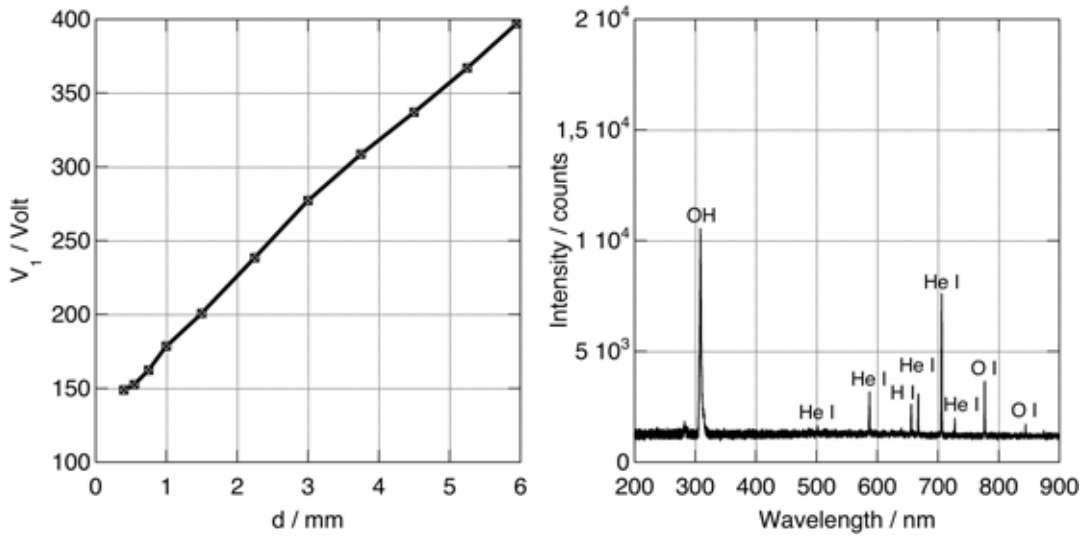
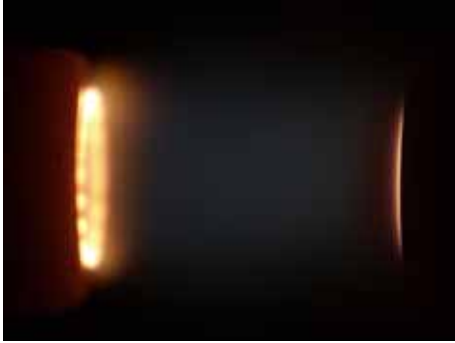


Figure A.11: Column gradient (Tab.A.74) and spectrum (integration time: 200 ms)

Column gradients for  $D_2 = 3.0 \text{ mm}$ ,  $p_2 = 290 \text{ hPa}$  and  $I = 25 \text{ mA}$



Gas: helium  
Electrodes: copper  
Shielding:  $Al_2O_3$

$p_2$ in hPa	$I$ in mA	$D_2$ in mm	$l_{2max}$ in mm
290	25	3.0	6.1

The field strength  $E_2$  in the positive column was determined from diagram Fig.A.12 between 2 and 5 mm.

$$E_2 = 19.5 \frac{V}{mm} \quad \frac{E_2}{p_2} = 0.067 \frac{V}{hPa \cdot mm} \quad T_2 = 290K \quad (\text{A.10})$$

The spectrum was taken at  $l_{2max} = 6.1 \text{ mm}$  and a power consumption of  $P_2 = 6.4 \text{ W}$ .

Resolution:	7nm	Baseline correction:	7	Multiplication:	19.9
Temperature:	290K	Wavelength correction:	-3nm	Doppler broad.:	yes

Table A.11: Lifbase 2.0 settings for  $p_2 = 290 \text{ hPa}$  and  $T_2 = 290 \text{ K}$  ( $P_2 = 6.4 \text{ W}$ )

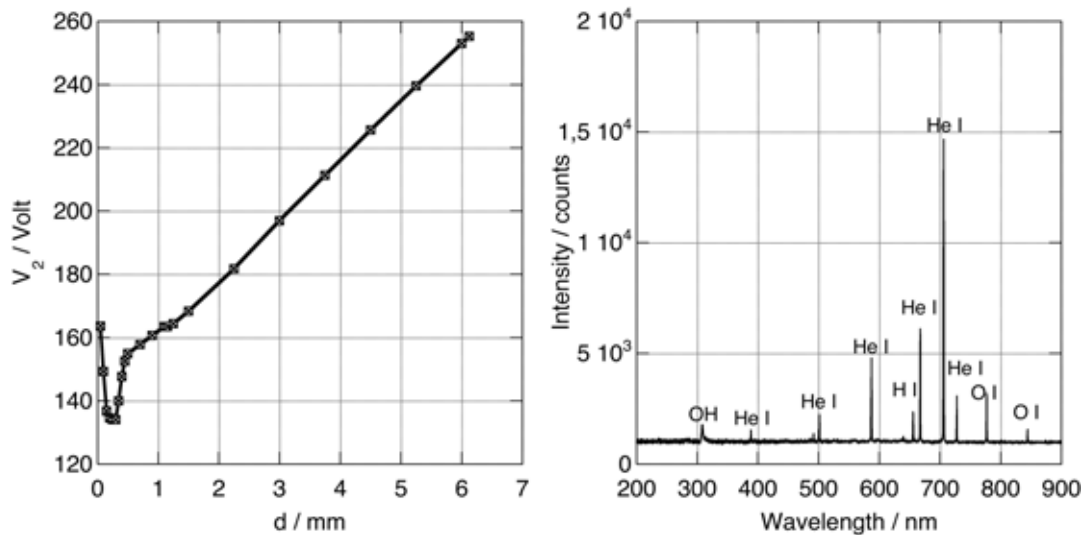


Figure A.12: Column gradient (Tab.A.75) and spectrum (integration time: 100 ms)

Column gradients for  $D_2 = 3.0 \text{ mm}$ ,  $p_2 = 430 \text{ hPa}$  and  $I = 25 \text{ mA}$



Gas: helium  
 Electrodes: copper  
 Shielding:  $Al_2O_3$

$p_2$ in hPa	$I$ in mA	$D_2$ in mm	$l_{2max}$ in mm
430	25	3.0	6.1

The field strength  $E_2$  in the positive column was determined from diagram Fig.A.13 between 2 and 5 mm.

$$E_2 = 26.0 \frac{V}{mm} \quad \frac{E_2}{p_2} = 0.060 \frac{V}{hPa \cdot mm} \quad T_2 = 375 K \quad (A.11)$$

The spectrum was taken at  $l_{2max} = 6.1 \text{ mm}$  and a power consumption of  $P_2 = 7.1 \text{ W}$ .

Resolution:	8nm	Baseline correction:	6.5	Multiplication:	15.2
Temperature:	375K	Wavelength correction:	-3nm	Doppler broad.:	yes

Table A.12: Lifbase 2.0 settings for  $p_2 = 430 \text{ hPa}$  and  $T = 375 \text{ K}$  ( $P_2 = 7.1 \text{ W}$ )

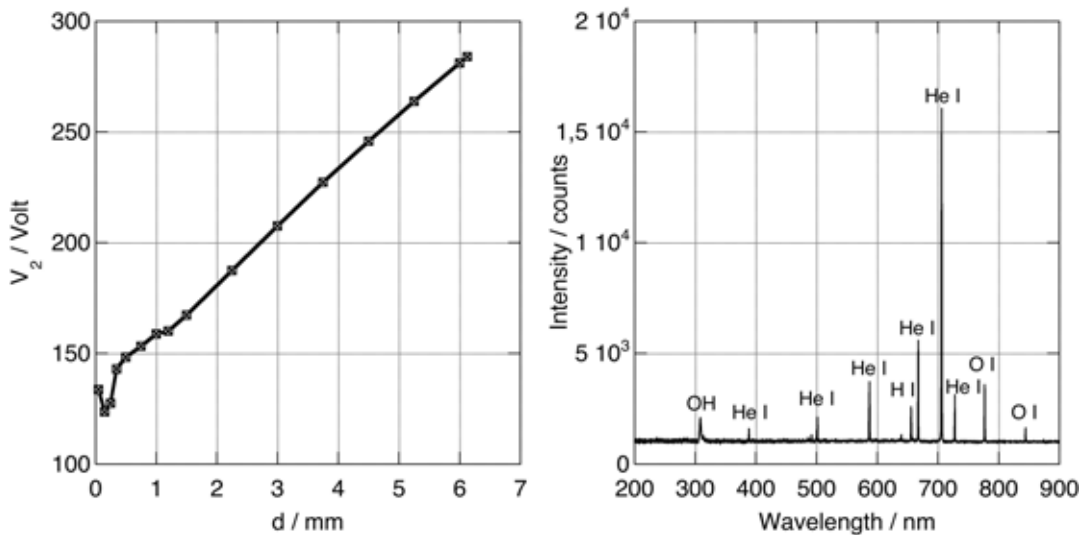
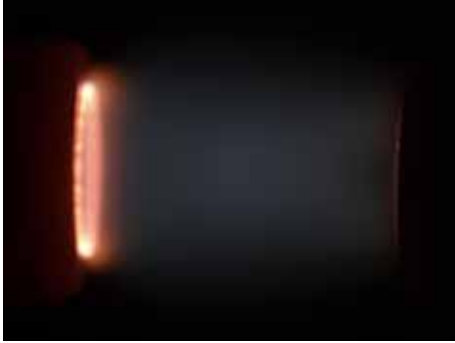


Figure A.13: Column gradient (Tab.A.76) and spectrum (integration time: 100 ms)

Column gradients for  $D_2 = 3.0 \text{ mm}$ ,  $p_2 = 570 \text{ hPa}$  and  $I = 25 \text{ mA}$



Gas: helium  
Electrodes: copper  
Shielding:  $Al_2O_3$

$p_2$ in hPa	$I$ in mA	$D_2$ in mm	$l_{2max}$ in mm
570	25	3.0	6.1

The field strength  $E_2$  in the positive column was determined from diagram Fig.A.14 between 2 and 5 mm.

$$E_2 = 31.6 \frac{V}{mm} \quad \frac{E_2}{p_2} = 0.055 \frac{V}{hPa \cdot mm} \quad T_2 = 350 K \quad (\text{A.12})$$

The spectrum was taken at  $l_{2max} = 6.1 \text{ mm}$  and a power consumption of  $P_2 = 8.0 \text{ W}$ .

Resolution:	8nm	Baseline correction:	6.2	Multiplication:	17.8
Temperature:	350K	Wavelength correction:	-4nm	Doppler broad.:	yes

Table A.13: Lifbase 2.0 settings for  $p_2 = 570 \text{ hPa}$  and  $T_2 = 350 \text{ K}$  ( $P_2 = 8.0 \text{ W}$ )

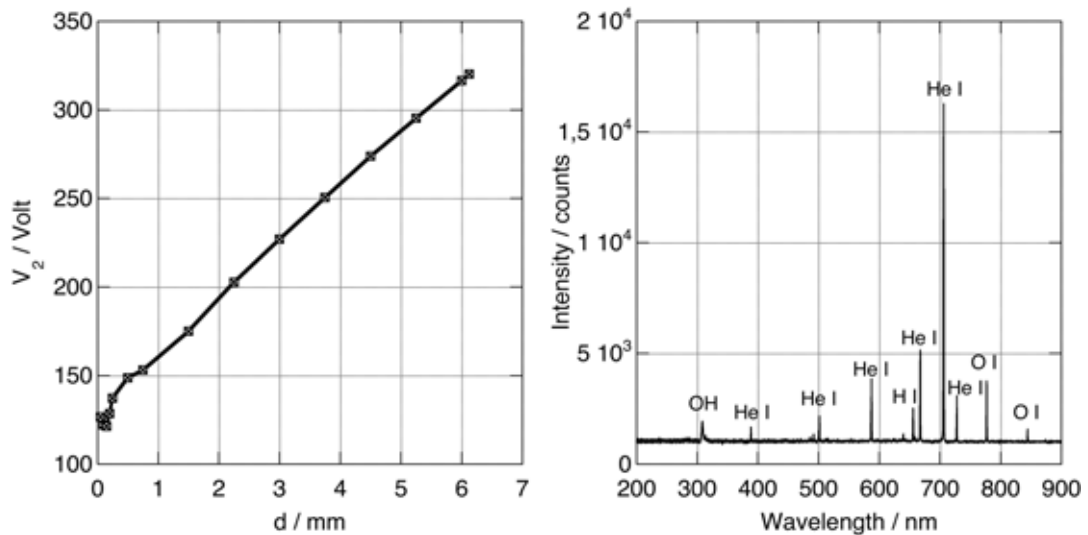
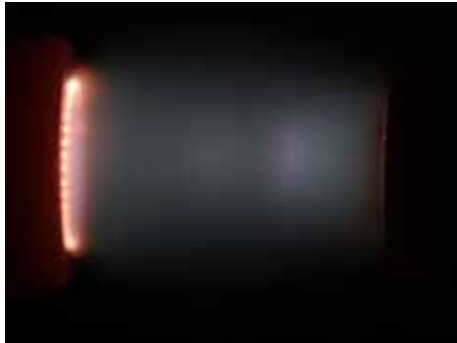


Figure A.14: Column gradient (Tab.A.75) and spectrum (integration time: 100 ms)

Column gradients for  $D_2 = 3.0 \text{ mm}$ ,  $p_2 = 720 \text{ hPa}$  and  $I = 25 \text{ mA}$



Gas: helium  
 Electrodes: copper  
 Shielding:  $Al_2O_3$

$p_2$ in hPa	$I$ in mA	$D_2$ in mm	$l_{2max}$ in mm
720	25	3.0	6.1

The field strength  $E_2$  in the positive column was determined from diagram Fig.A.15 between 2 and 5 mm.

$$E_2 = 37.1 \frac{V}{mm} \quad \frac{E_2}{p_2} = 0.052 \frac{V}{hPa \cdot mm} \quad T_2 = 850 K \quad (A.13)$$

The spectrum was taken at  $l_{2max} = 6.1 \text{ mm}$  and a power consumption of  $P_2 = 8.8 \text{ W}$ .

Resolution:	8nm	Baseline correction:	8.3	Multiplication:	5.45
Temperature:	850K	Wavelength correction:	-4nm	Doppler broad.:	yes

Table A.14: Lifbase 2.0 settings for  $p_2 = 720 \text{ hPa}$  and  $T_2 = 850 \text{ K}$  ( $P_2 = 8.8 \text{ W}$ )

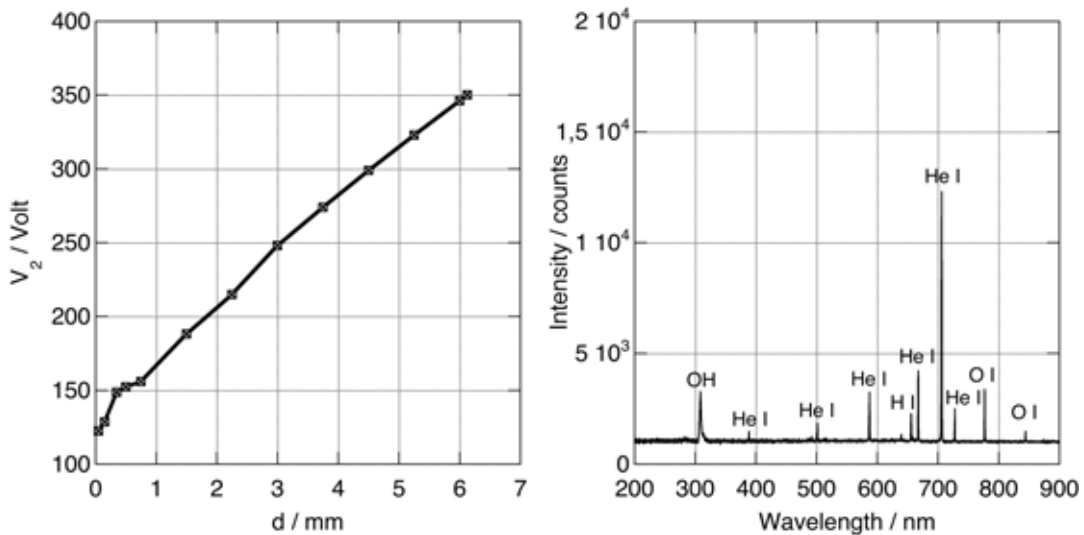
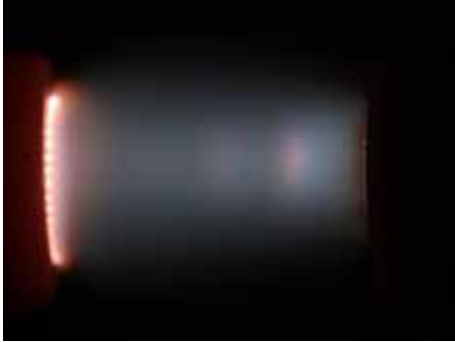


Figure A.15: Column gradient (Tab.A.78) and spectrum (integration time: 100 ms)

Column gradients for  $D_2 = 3.0 \text{ mm}$ ,  $p_2 = 860 \text{ hPa}$  and  $I = 25 \text{ mA}$



Gas: helium  
Electrodes: copper  
Shielding:  $Al_2O_3$

$p_2$ in hPa	$I$ in mA	$D_2$ in mm	$l_{2max}$ in mm
860	25	3.0	6.1

The field strength  $E_2$  in the positive column was determined from diagram Fig.A.16 between 2 and 5 mm.

$$E_2 = 43.1 \frac{V}{mm} \quad \frac{E_2}{p_2} = 0.050 \frac{V}{hPa \cdot mm} \quad T_2 = 950 K \quad (\text{A.14})$$

The spectrum was taken at  $l_{2max} = 6.1 \text{ mm}$  and a power consumption of  $P_2 = 9.4 \text{ W}$ .

Resolution:	8nm	Baseline correction:	9	Multiplication:	5.4
Temperature:	950K	Wavelength correction:	-4.5nm	Doppler broad.:	yes

Table A.15: Lifbase 2.0 settings for  $p_2 = 860 \text{ hPa}$  and  $T_2 = 950 \text{ K}$  ( $P_2 = 9.4 \text{ W}$ )

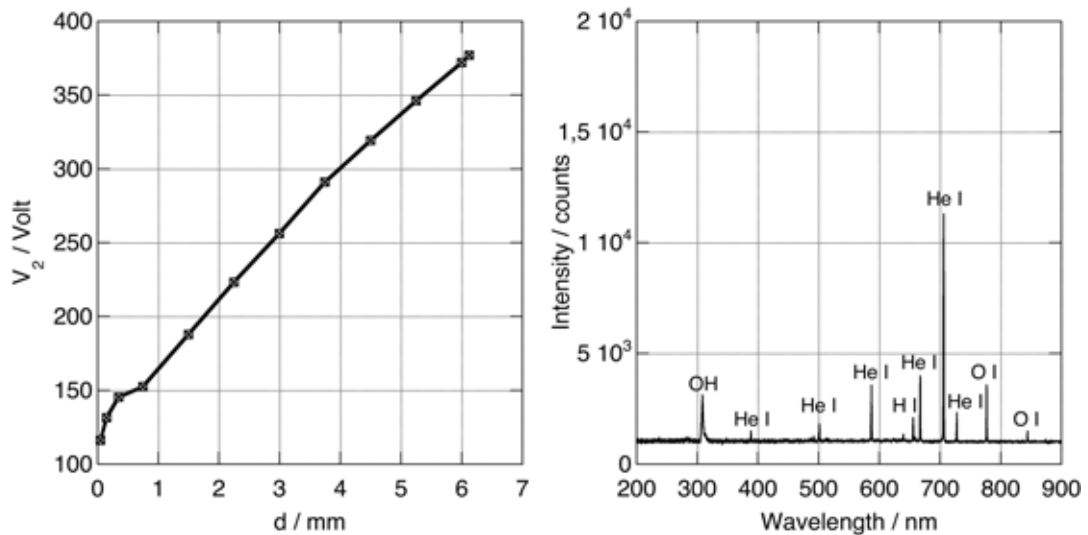
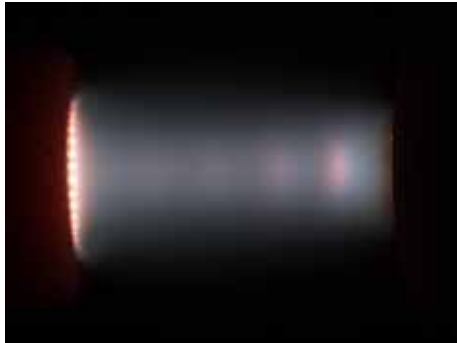


Figure A.16: Column gradient (Tab.A.79) and spectrum (integration time: 100 ms)

Column gradients for  $D_2 = 3.0 \text{ mm}$ ,  $p_2 = 1000 \text{ hPa}$  and  $I = 25 \text{ mA}$



Gas: helium  
 Electrodes: copper  
 Shielding:  $Al_2O_3$

$p_2$ in hPa	$I$ in mA	$D_2$ in mm	$l_{2max}$ in mm
1000	25	3.0	6.1

The field strength  $E_2$  in the positive column was determined from diagram Fig.A.17 between 2 and 5 mm.

$$E_2 = 43.6 \frac{V}{mm} \quad \frac{E_2}{p_2} = 0.044 \frac{V}{hPa \cdot mm} \quad T_2 = 925 \text{ K} \quad (\text{A.15})$$

The spectrum was taken at  $l_{2max} = 6.1 \text{ mm}$  and a power consumption of  $P_2 = 10.0 \text{ W}$ .

Resolution:	8nm	Baseline correction:	10	Multiplication:	2.11
Temperature:	925K	Wavelength correction:	-4nm	Doppler broad.:	yes

Table A.16: Lifbase 2.0 settings for  $p_2 = 1000 \text{ hPa}$  and  $T_2 = 925 \text{ K}$  ( $P_2 = 10.0 \text{ W}$ )

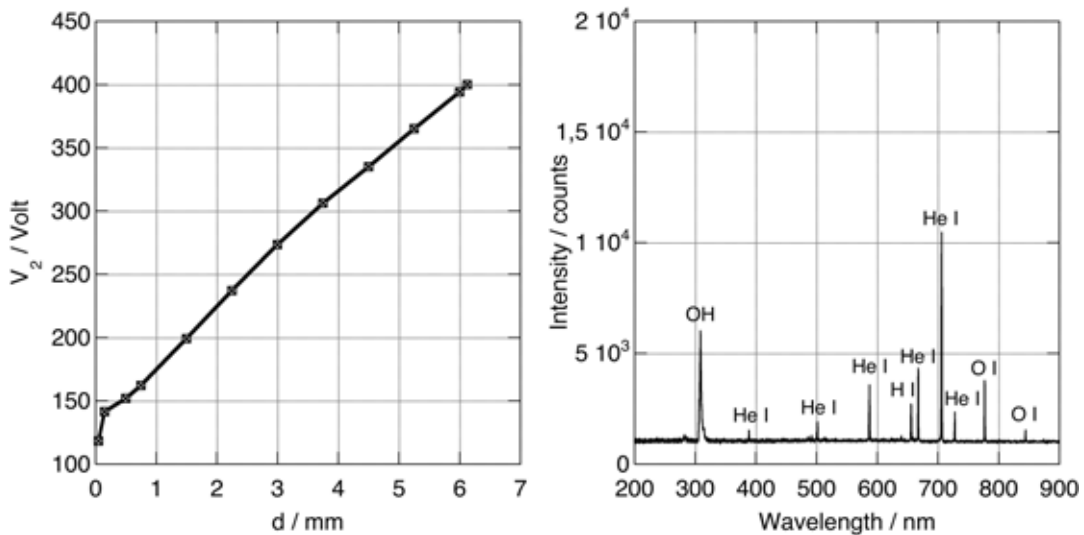
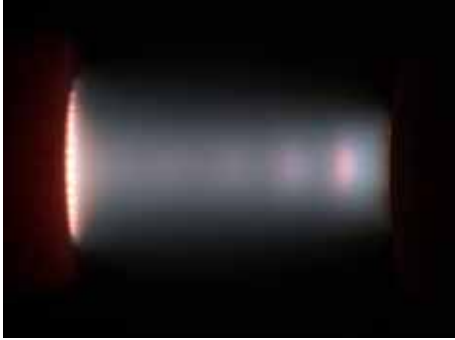


Figure A.17: Column gradient (Tab.A.80) and spectrum (integration time: 100 ms)

Column gradients for  $D_2 = 3.0 \text{ mm}$ ,  $p_2 = 1150 \text{ hPa}$  and  $I = 25 \text{ mA}$



Gas: helium  
Electrodes: copper  
Shielding:  $Al_2O_3$

$p_2$ in hPa	$I$ in mA	$D_2$ in mm	$l_{2max}$ in mm
1150	25	3.0	6.1

The field strength  $E_2$  in the positive column was determined from diagram Fig.A.18 between 2 and 5 mm.

$$E_2 = 47.5 \frac{V}{mm} \quad \frac{E_2}{p_2} = 0.041 \frac{V}{hPa \cdot mm} \quad T_2 = 950 \text{ K} \quad (\text{A.16})$$

The spectrum was taken at  $l_{2max} = 6.1 \text{ mm}$  and a power consumption of  $P_2 = 10.5 \text{ W}$ .

Resolution:	8nm	Baseline correction:	11.3	Multiplication:	1.88
Temperature:	950K	Wavelength correction:	-4nm	Doppler broad.:	yes

Table A.17: Lifbase 2.0 settings for  $p_2 = 1150 \text{ hPa}$  and  $T_2 = 950 \text{ K}$  ( $P_2 = 10.5 \text{ W}$ )

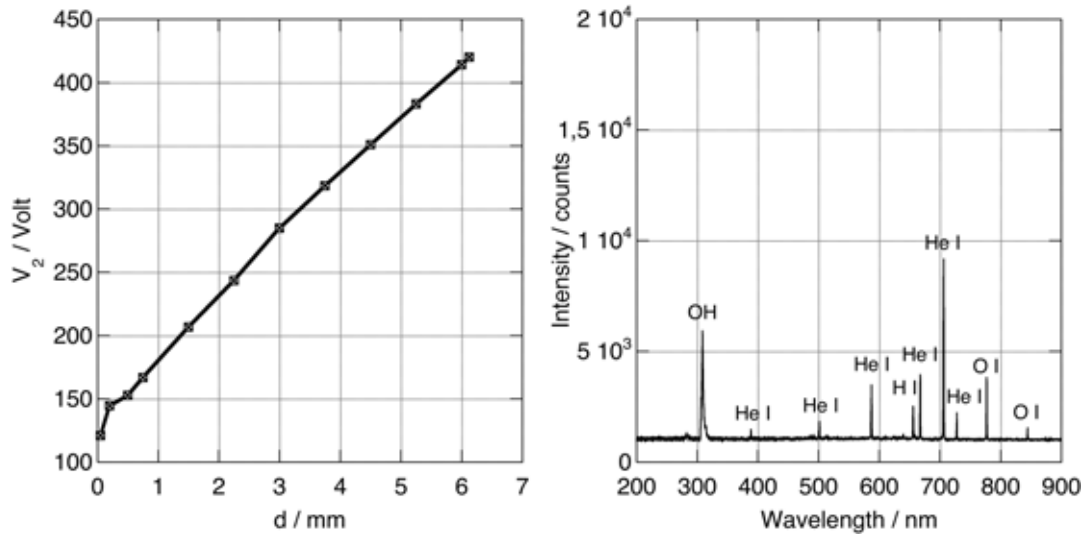
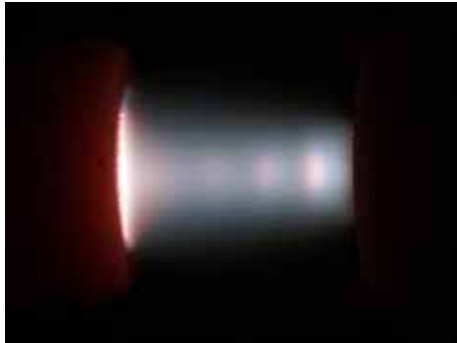


Figure A.18: Column gradient (Tab.A.81) and spectrum (integration time: 100 ms)

Column gradients for  $D_2 = 3.0 \text{ mm}$ ,  $p_2 = 1290 \text{ hPa}$  and  $I = 25 \text{ mA}$



Gas: helium  
 Electrodes: copper  
 Shielding:  $Al_2O_3$

$p_2$ in hPa	$I$ in mA	$D_2$ in mm	$l_{2max}$ in mm
1290	25	3.0	6.1

The field strength  $E_2$  in the positive column was determined from diagram Fig.A.19 between 1.5 and 3 mm.

$$E_2 = 59.1 \frac{V}{mm} \quad \frac{E_2}{p_2} = 0.046 \frac{V}{hPa \cdot mm} \quad T_2 = 950 K \quad (A.17)$$

The spectrum was taken at  $l_{2max} = 4.5 \text{ mm}$  and a power consumption of  $P_2 = 9.3 \text{ W}$ .

Resolution:	8nm	Baseline correction:	12.8	Multiplication:	1.71
Temperature:	950K	Wavelength correction:	-4nm	Doppler broad.:	yes

Table A.18: Lifbase 2.0 settings for  $p_2 = 1290 \text{ hPa}$  and  $T_2 = 950 \text{ K}$  ( $P_2 = 9.3 \text{ W}$ )

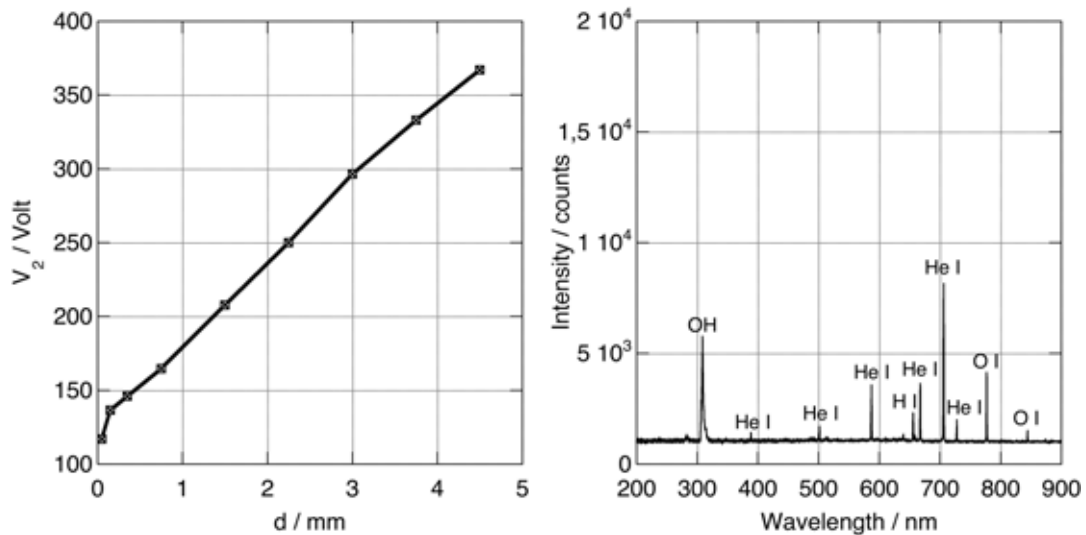
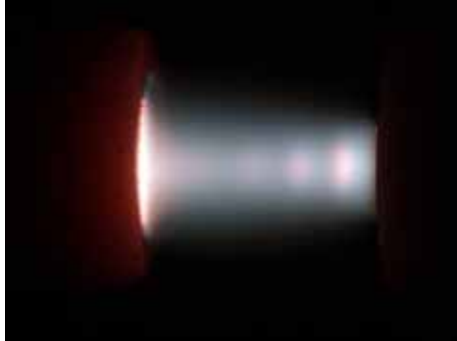


Figure A.19: Column gradient (Tab.A.82) and spectrum (integration time: 100 ms)

Column gradients for  $D_2 = 3.0 \text{ mm}$ ,  $p_2 = 1430 \text{ hPa}$  and  $I = 25 \text{ mA}$



Gas: helium  
Electrodes: copper  
Shielding:  $Al_2O_3$

$p_2$ in hPa	$I$ in mA	$D_2$ in mm	$l_{2max}$ in mm
1430	25	3.0	6.1

The field strength  $E_2$  in the positive column was determined from diagram Fig.A.20 between 1.5 and 3 mm.

$$E_2 = 63.5 \frac{V}{mm} \quad \frac{E_2}{p_2} = 0.044 \frac{V}{hPa \cdot mm} \quad T_2 = 950 K \quad (\text{A.18})$$

The spectrum was taken at  $l_{2max} = 4.5 \text{ mm}$  and a power consumption of  $P_2 = 9.5 \text{ W}$ .

Resolution:	8nm	Baseline correction:	14.3	Multiplication:	1.65
Temperature:	950K	Wavelength correction:	-4nm	Doppler broad.:	yes

Table A.19: Lifbase 2.0 settings for  $p_2 = 1430 \text{ hPa}$  and  $T_2 = 950 \text{ K}$  ( $P_2 = 9.5 \text{ W}$ )

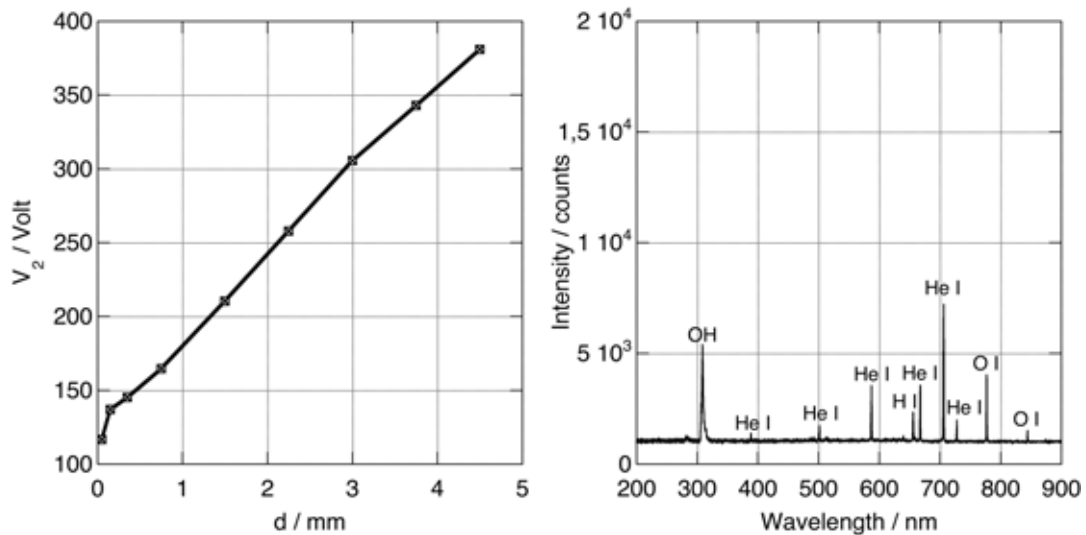
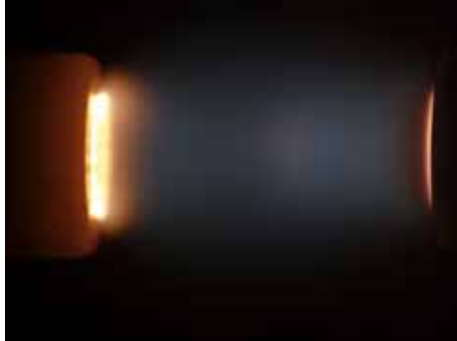


Figure A.20: Column gradient (Tab.A.83) and spectrum (integration time: 100 ms)

Column gradients for  $D_3 = 2.1 \text{ mm}$ ,  $p_3 = 400 \text{ hPa}$  and  $I = 25 \text{ mA}$



Gas: helium  
 Electrodes: copper  
 Shielding:  $Al_2O_3$

$p_3$ in hPa	$I$ in mA	$D_3$ in mm	$l_{3max}$ in mm
400	25	2.1	6.6

The field strength  $E_3$  in the positive column was determined from diagram Fig.A.21 between 2 and 4 mm.

$$E_3 = 25.6 \frac{V}{mm} \quad \frac{E_3}{p_3} = 0.064 \frac{V}{hPa \cdot mm} \quad T_3 = 425 \text{ K} \quad (\text{A.19})$$

The spectrum was taken at  $l_{3max} = 6.6 \text{ mm}$  and a power consumption of  $P_3 = 7.3 \text{ W}$ .

Resolution:	8nm	Baseline correction:	8.1	Multiplication:	10.8
Temperature:	425K	Wavelength correction:	-4nm	Doppler broad.:	yes

Table A.20: Lifbase 2.0 settings for  $p_3 = 400 \text{ hPa}$  and  $T_3 = 425 \text{ K}$  ( $P_3 = 7.3 \text{ W}$ )

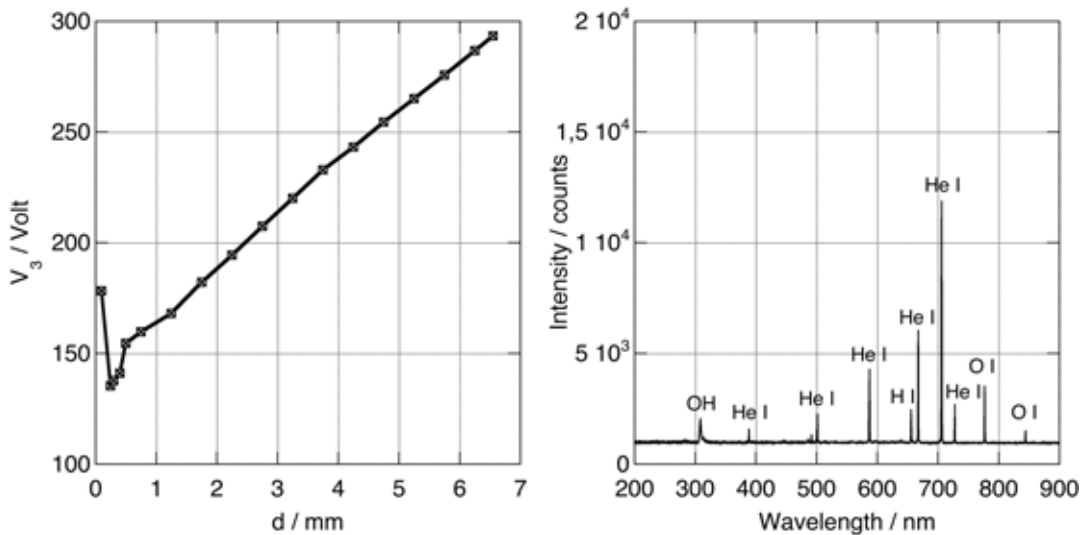
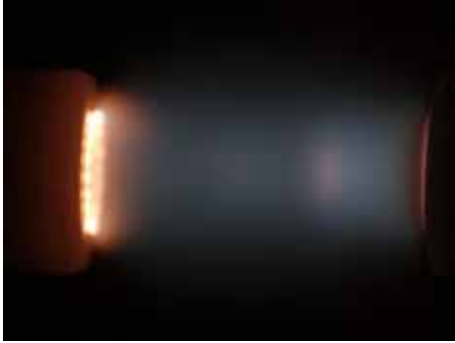


Figure A.21: Column gradient (Tab.A.84) and spectrum (integration time: 70 ms)

Column gradients for  $D_3 = 2.1 \text{ mm}$ ,  $p_3 = 600 \text{ hPa}$  and  $I = 25 \text{ mA}$



Gas: helium  
Electrodes: copper  
Shielding:  $Al_2O_3$

$p_3$ in hPa	$I$ in mA	$D_3$ in mm	$l_{3max}$ in mm
600	25	2.1	6.6

The field strength  $E_3$  in the positive column was determined from diagram Fig.A.22 between 2 and 4 mm.

$$E_3 = 31.8 \frac{V}{mm} \quad \frac{E_3}{p_3} = 0.053 \frac{V}{hPa \cdot mm} \quad T_3 = 600 K \quad (\text{A.20})$$

The spectrum was taken at  $l_{3max} = 6.6 \text{ mm}$  and a power consumption of  $P_3 = 8.3 \text{ W}$ .

Resolution:	9nm	Baseline correction:	6.5	Multiplication:	10.5
Temperature:	600K	Wavelength correction:	-2.5nm	Doppler broad.:	yes

Table A.21: Lifbase 2.0 settings for  $p_3 = 600 \text{ hPa}$  and  $T_3 = 600 \text{ K}$  ( $P_3 = 8.3 \text{ W}$ )

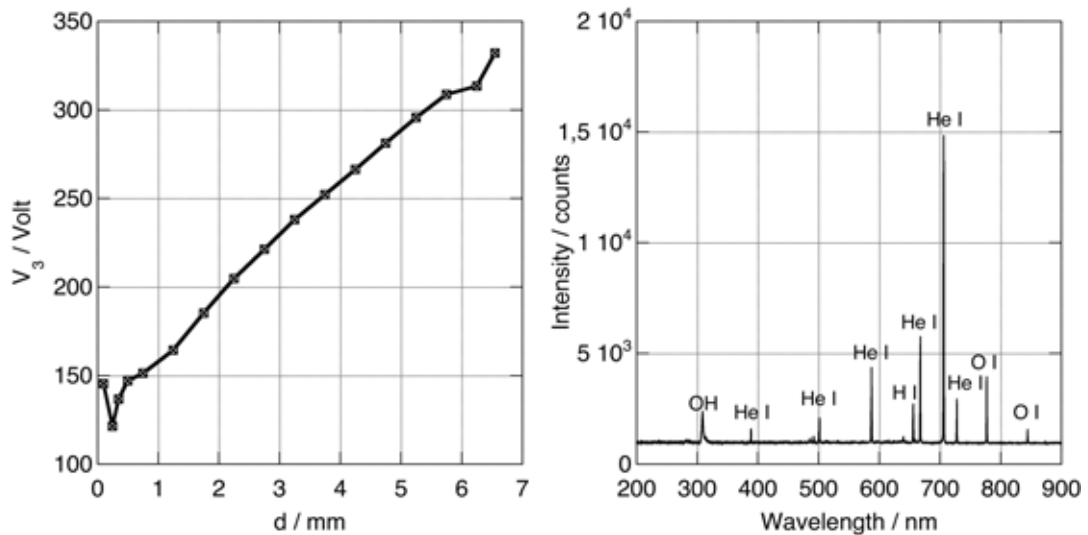


Figure A.22: Column gradient (Tab.A.85) and spectrum (integration time: 70 ms)

Column gradients for  $D_3 = 2.1 \text{ mm}$ ,  $p_3 = 800 \text{ hPa}$  and  $I = 25 \text{ mA}$



Gas: helium  
 Electrodes: copper  
 Shielding:  $Al_2O_3$

$p_3$ in hPa	$I$ in mA	$D_3$ in mm	$l_{3max}$ in mm
800	25	2.1	6.6

The field strength  $E_3$  in the positive column was determined from diagram Fig.A.23 between 2 and 4 mm.

$$E_3 = 41.0 \frac{V}{mm} \quad \frac{E_3}{p_3} = 0.051 \frac{V}{hPa \cdot mm} \quad T_3 = 800 \text{ K} \quad (\text{A.21})$$

The spectrum was taken at  $l_{3max} = 6.6 \text{ mm}$  and a power consumption of  $P_3 = 9.3 \text{ W}$ .

Resolution:	7nm	Baseline correction:	9	Multiplication:	6.3
Temperature:	800K	Wavelength correction:	-4.5nm	Doppler broad.:	yes

Table A.22: Lifbase 2.0 settings for  $p_3 = 800 \text{ hPa}$  and  $T_3 = 800 \text{ K}$  ( $P_3 = 9.3 \text{ W}$ )

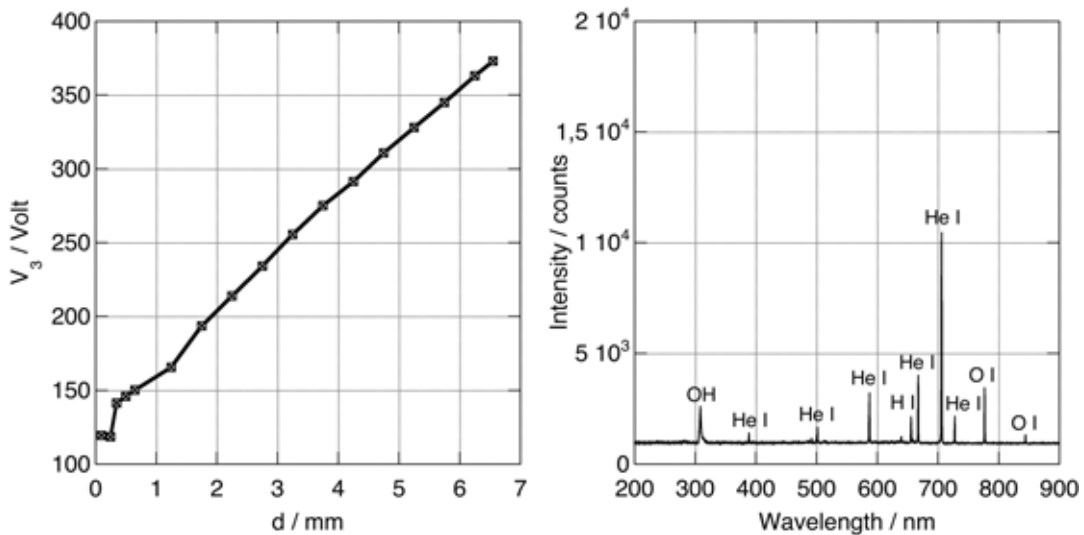
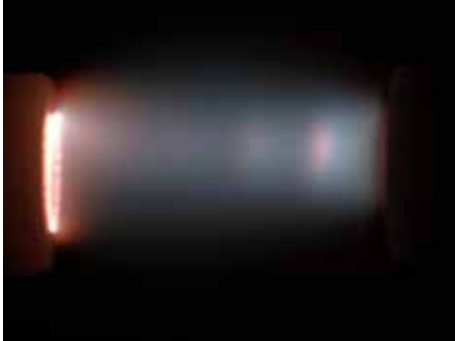


Figure A.23: Column gradient (Tab.A.86) and spectrum (integration time: 70 ms)

Column gradients for  $D_3 = 2.1 \text{ mm}$ ,  $p_3 = 1000 \text{ hPa}$  and  $I = 25 \text{ mA}$



Gas: helium  
Electrodes: copper  
Shielding:  $Al_2O_3$

$p_3$ in hPa	$I$ in mA	$D_3$ in mm	$l_{3max}$ in mm
1000	25	2.1	6.6

The field strength  $E_3$  in the positive column was determined from diagram Fig.A.24 between 2 and 4 mm.

$$E_3 = 46.1 \frac{V}{mm} \quad \frac{E_3}{p_3} = 0.046 \frac{V}{hPa \cdot mm} \quad T_3 = 1050 \text{ K} \quad (\text{A.22})$$

The spectrum was taken at  $l_{3max} = 6.6 \text{ mm}$  and a power consumption of  $P_3 = 10.2 \text{ W}$ .

Resolution:	9nm	Baseline correction:	12.5	Multiplication:	4.45
Temperature:	1050K	Wavelength correction:	-5nm	Doppler broad.:	yes

Table A.23: Lifbase 2.0 settings for  $p_3 = 1000 \text{ hPa}$  and  $T_3 = 1050 \text{ K}$  ( $P_3 = 10.2 \text{ W}$ )

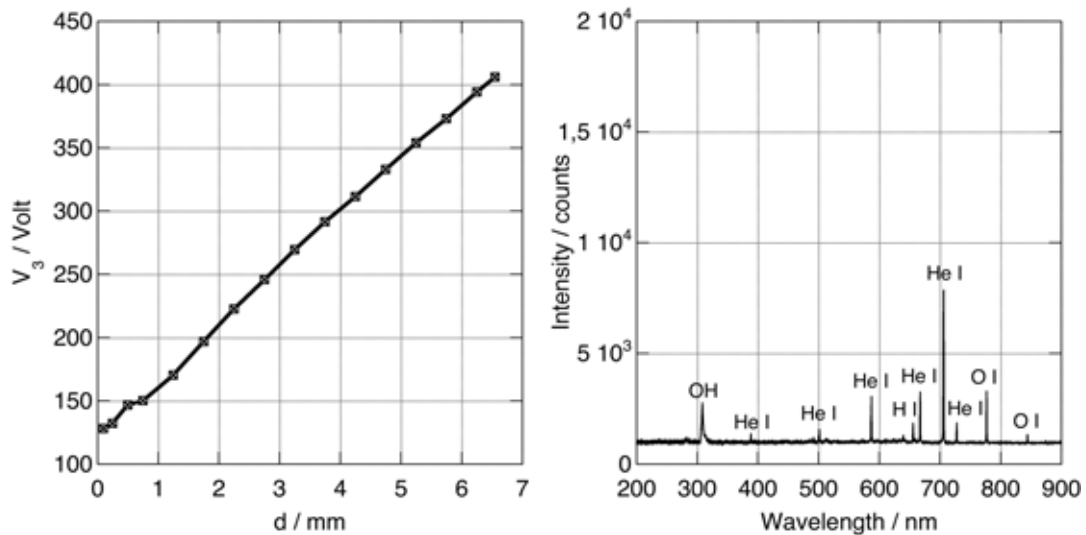
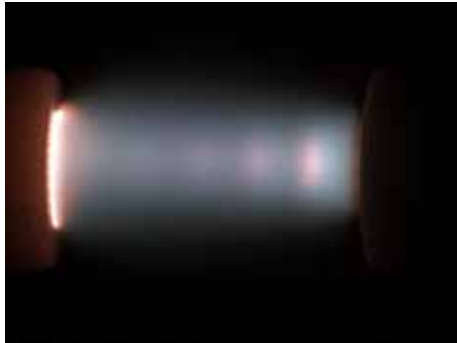


Figure A.24: Column gradient (Tab.A.87) and spectrum (integration time: 100 ms)

Column gradients for  $D_3 = 2.1 \text{ mm}$ ,  $p_3 = 1200 \text{ hPa}$  and  $I = 25 \text{ mA}$



Gas: helium  
 Electrodes: copper  
 Shielding:  $Al_2O_3$

$p_3$ in hPa	$I$ in mA	$D_3$ in mm	$l_{3max}$ in mm
1200	25	2.1	6.6

The field strength  $E_3$  in the positive column was determined from diagram Fig.A.25 between 2 and 4 mm.

$$E_3 = 45.6 \frac{V}{mm} \quad \frac{E_3}{p_3} = 0.038 \frac{V}{hPa \cdot mm} \quad T_3 = 950 K \quad (A.23)$$

The spectrum was taken at  $l_3 = 6.0 \text{ mm}$  and a power consumption of  $P_3 = 10.4 \text{ W}$ .

Resolution:	8nm	Baseline correction:	17.8	Multiplication:	1.35
Temperature:	950K	Wavelength correction:	-5nm	Doppler broad.:	yes

Table A.24: Lifbase 2.0 settings for  $p_3 = 1200 \text{ hPa}$  and  $T_3 = 950 \text{ K}$  ( $P_3 = 10.4 \text{ W}$ )

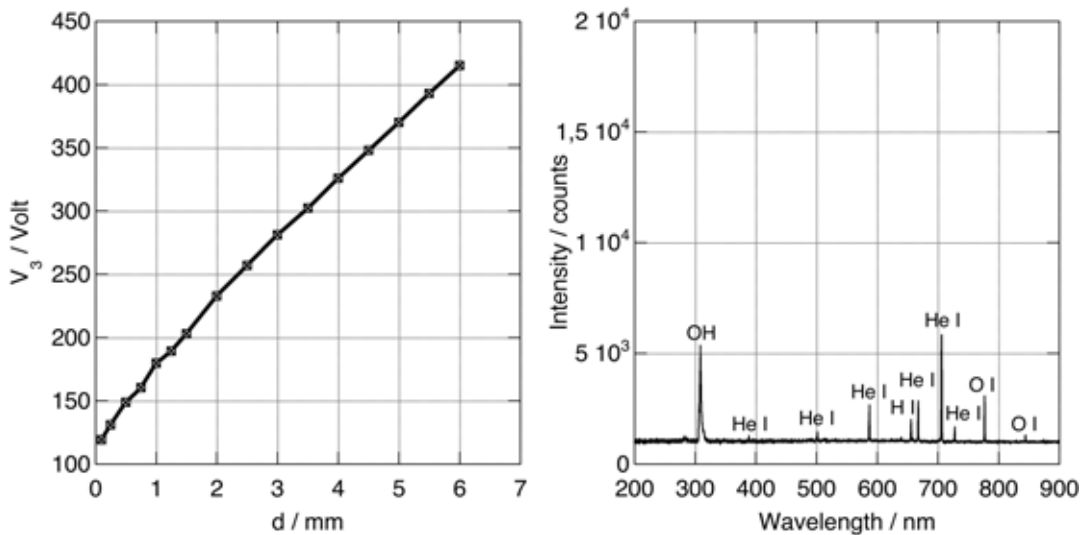
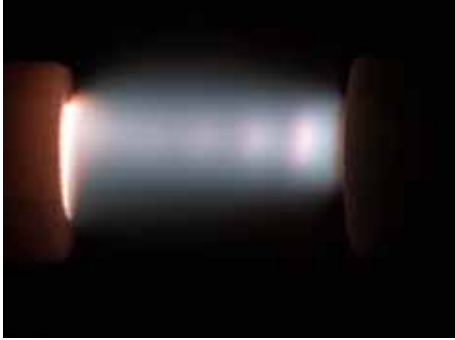


Figure A.25: Column gradient (Tab.A.88) and spectrum (integration time: 100 ms)

Column gradients for  $D_3 = 2.1 \text{ mm}$ ,  $p_3 = 1300 \text{ hPa}$  and  $I = 25 \text{ mA}$



Gas: helium  
Electrodes: copper  
Shielding:  $Al_2O_3$

$p_3$ in hPa	$I$ in mA	$D_3$ in mm	$l_{3max}$ in mm
1300	25	2.1	6.6

The field strength  $E_3$  in the positive column was determined from diagram Fig.A.21 between 2 and 4 mm.

$$E_3 = 50.1 \frac{V}{mm} \quad \frac{E_3}{p_3} = 0.039 \frac{V}{hPa \cdot mm} \quad T_3 = 950 K \quad (\text{A.24})$$

The spectrum was taken at  $l_3 = 5.5 \text{ mm}$  and a power consumption of  $P_3 = 10.2 \text{ W}$ .

Resolution:	8nm	Baseline correction:	15.8	Multiplication:	1.6
Temperature:	950K	Wavelength correction:	-5nm	Doppler broad.:	yes

Table A.25: Lifbase 2.0 settings for  $p_3 = 1300 \text{ hPa}$  and  $T_3 = 950 \text{ K}$  ( $P_3 = 10.2 \text{ W}$ )

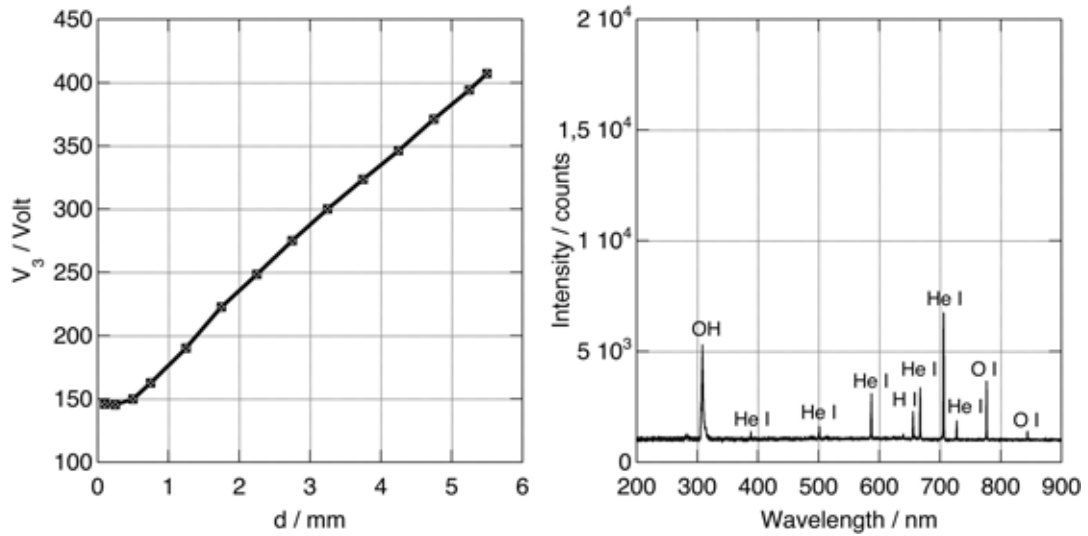
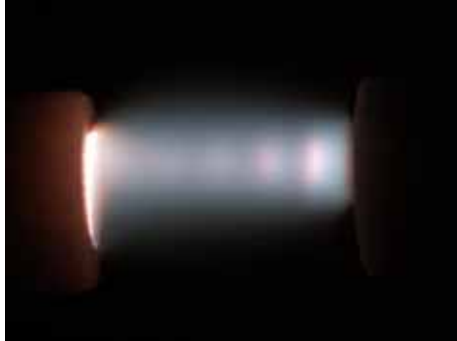


Figure A.26: Column gradient (Tab.A.89) and spectrum (integration time: 100 ms)

Column gradients for  $D_3 = 2.1 \text{ mm}$ ,  $p_3 = 1400 \text{ hPa}$  and  $I = 25 \text{ mA}$



Gas: helium  
 Electrodes: copper  
 Shielding:  $Al_2O_3$

$p_3$ in hPa	$I$ in mA	$D_3$ in mm	$l_{3max}$ in mm
1400	25	2.1	6.6

The field strength  $E_3$  in the positive column was determined from diagram Fig.A.27 between 2 and 4 mm.

$$E_3 = 50.8 \frac{V}{mm} \quad \frac{E_3}{p_3} = 0.036 \frac{V}{hPa \cdot mm} \quad T_3 = 950 K \quad (A.25)$$

The spectrum was taken at  $l_3 = 4.75 \text{ mm}$  and a power consumption of  $P_3 = 10.1 \text{ W}$ .

Resolution:	8nm	Baseline correction:	15	Multiplication:	1.49
Temperature:	950K	Wavelength correction:	-4nm	Doppler broad.:	yes

Table A.26: Lifbase 2.0 settings for  $p_3 = 1400 \text{ hPa}$  and  $T_3 = 950 \text{ K}$  ( $P_3 = 10.1 \text{ W}$ )

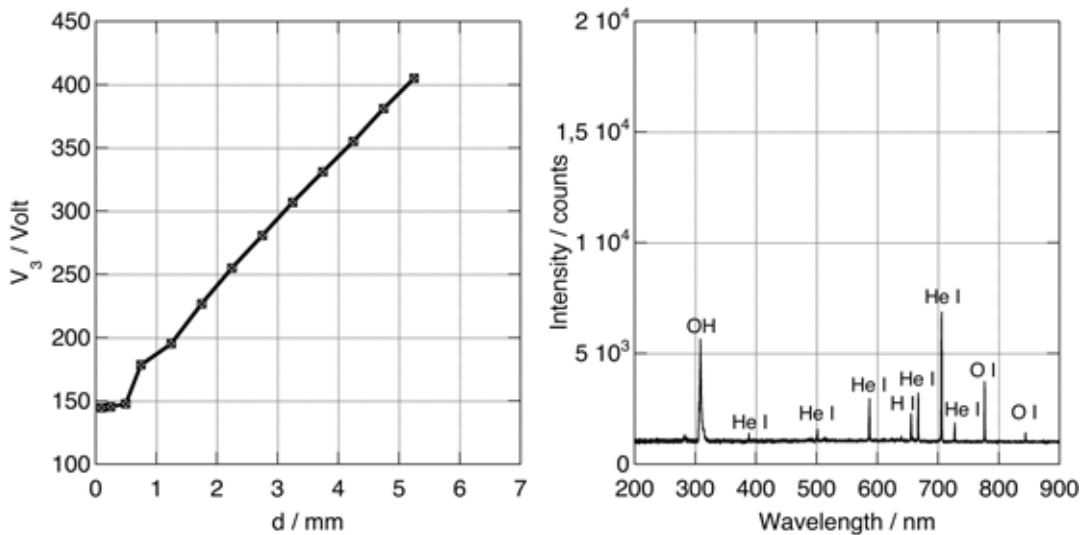
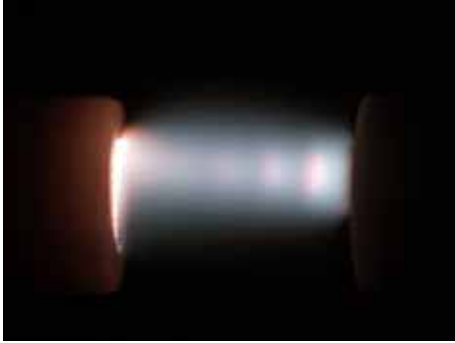


Figure A.27: Column gradient (Tab.A.90) and spectrum (integration time: 100 ms)

Column gradients for  $D_3 = 2.1 \text{ mm}$ ,  $p_3 = 1500 \text{ hPa}$  and  $I = 25 \text{ mA}$



Gas: helium  
Electrodes: copper  
Shielding:  $Al_2O_3$

$p_3$ in hPa	$I$ in mA	$D_3$ in mm	$l_{3max}$ in mm
1500	25	2.1	6.6

The field strength  $E_3$  in the positive column was determined from diagram Fig.A.28 between 2 and 4 mm.

$$E_3 = 53.5 \frac{V}{mm} \quad \frac{E_3}{p_3} = 0.036 \frac{V}{hPa \cdot mm} \quad T_3 = 950 \text{ K} \quad (\text{A.26})$$

The spectrum was taken at  $l_3 = 5.5 \text{ mm}$  and a power consumption of  $P_3 = 9.8 \text{ W}$ .

Resolution:	8nm	Baseline correction:	17	Multiplication:	1.46
Temperature:	950K	Wavelength correction:	-4nm	Doppler broad.:	yes

Table A.27: Lifbase 2.0 settings for  $p_3 = 1500 \text{ hPa}$  and  $T_3 = 950 \text{ K}$  ( $P_3 = 9.8 \text{ W}$ )

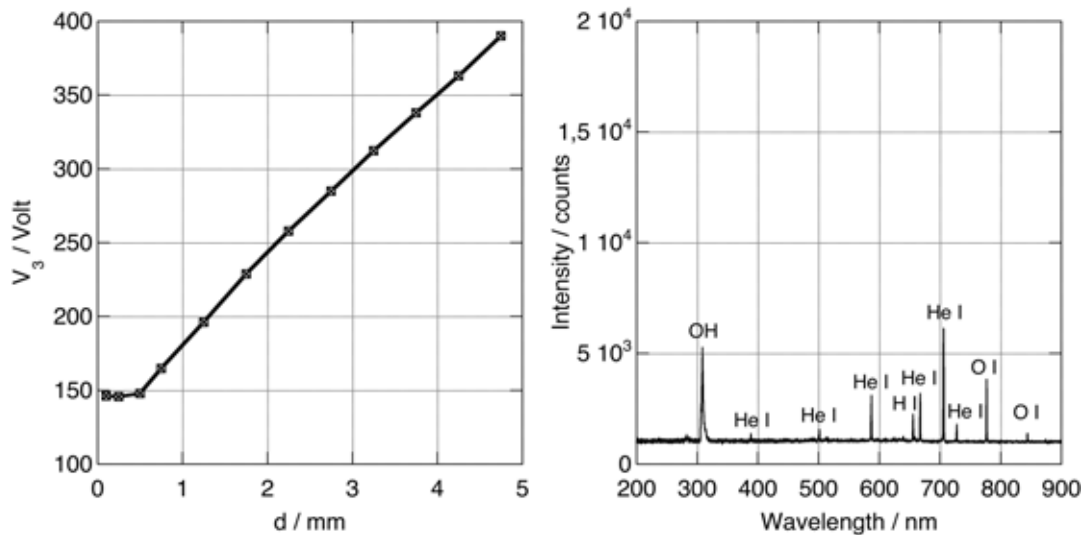
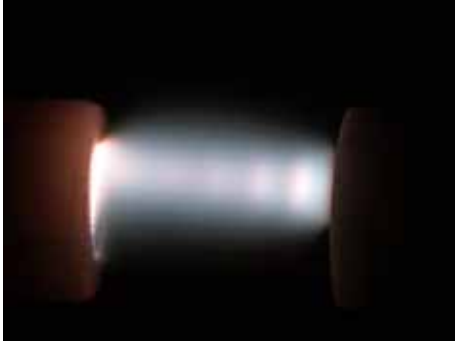


Figure A.28: Column gradient (Tab.A.91) and spectrum (integration time: 100 ms)

Column gradients for  $D_3 = 2.1 \text{ mm}$ ,  $p_3 = 1600 \text{ hPa}$  and  $I = 25 \text{ mA}$



Gas: helium  
Electrodes: copper  
Shielding:  $Al_2O_3$

$p_3$ in hPa	$I$ in mA	$D_3$ in mm	$l_{3max}$ in mm
1600	25	2.1	6.6

The field strength  $E_3$  in the positive column was determined from diagram Fig.A.29 between 1 and 3 mm.

$$E_3 = 61.0 \frac{V}{mm} \quad \frac{E_3}{p_3} = 0.038 \frac{V}{hPa \cdot mm} \quad T_3 = 1000 \text{ K} \quad (\text{A.27})$$

The spectrum was taken at  $l_3 = 5.5 \text{ mm}$  and a power consumption of  $P_3 = 10.1 \text{ W}$ .

Resolution:	8nm	Baseline correction:	17.5	Multiplication:	1.2
Temperature:	1000K	Wavelength correction:	-4.5nm	Doppler broad.:	yes

Table A.28: Lifbase 2.0 settings for  $p_3 = 1600 \text{ hPa}$  and  $T_3 = 1000 \text{ K}$  ( $P_3 = 10.1 \text{ W}$ )

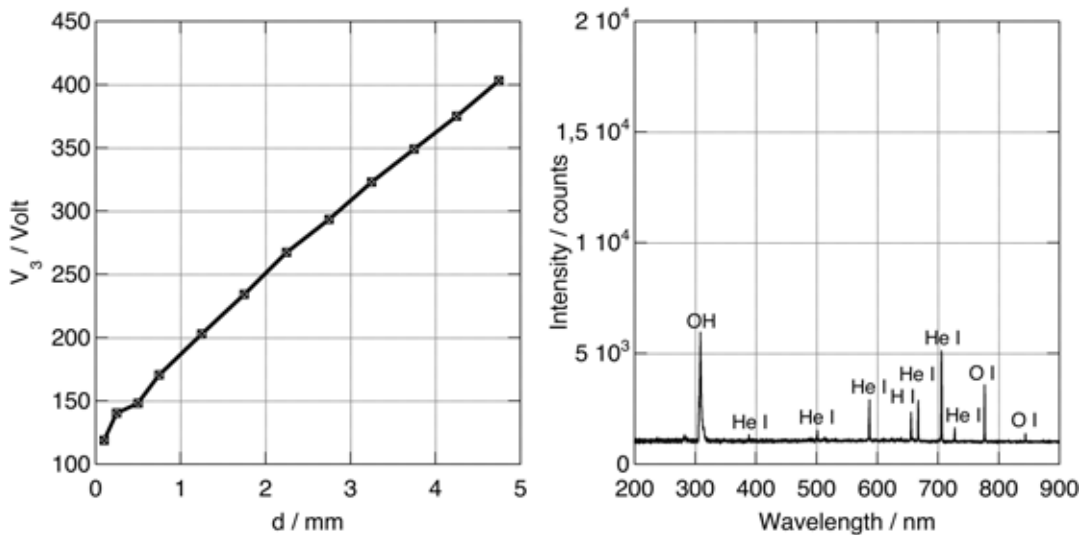


Figure A.29: Column gradient (Tab.A.92) and spectrum (integration time: 100 ms)

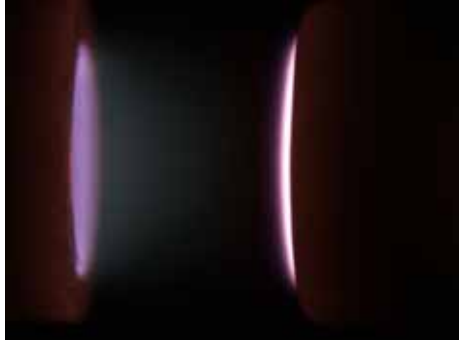
## A.2 I-V characterisation of similar glow discharges

Table A.29: Overview of all triples of similar discharges for Sec.A.2 (Appendix)

Series	Pressures	Raw data	Comparison I-V
1	$p_1 = 200 \text{ hPa}$ $p_2 = 290 \text{ hPa}$ $p_3 = 400 \text{ hPa}$	p. 103 p. 112 p. 121	p. 130
2	$p_1 = 300 \text{ hPa}$ $p_2 = 290 \text{ hPa}$ $p_3 = 600 \text{ hPa}$	p. 104 p. 113 p. 122	p. 131
3	$p_1 = 400 \text{ hPa}$ $p_2 = 570 \text{ hPa}$ $p_3 = 800 \text{ hPa}$	p. 105 p. 114 p. 123	p. 131
4	$p_1 = 500 \text{ hPa}$ $p_2 = 720 \text{ hPa}$ $p_3 = 1000 \text{ hPa}$	p. 106 p. 115 p. 124	p. 132
5	$p_1 = 600 \text{ hPa}$ $p_2 = 860 \text{ hPa}$ $p_3 = 1200 \text{ hPa}$	p. 107 p. 116 p. 125	p. 132
6	$p_1 = 700 \text{ hPa}$ $p_2 = 1000 \text{ hPa}$ $p_3 = 1400 \text{ hPa}$	p. 108 p. 117 p. 127	p. 133
7	$p_1 = 800 \text{ hPa}$ $p_2 = 1150 \text{ hPa}$ $p_3 = 1600 \text{ hPa}$	p. 109 p. 118 p. 129	p. 133
8	$p_1 = 900 \text{ hPa}$ $p_2 = 1290 \text{ hPa}$ -	p. 110 p. 119 -	p. 134
9	$p_1 = 1000 \text{ hPa}$ $p_2 = 1430 \text{ hPa}$ -	p. 111 p. 120 -	p. 134

A.2.1 Measurement series with scaling factors a=2 and 1.4

I-V diagram for  $D_1 = 4.3 \text{ mm}$ ,  $l_1 = 4.0 \text{ mm}$  and  $p_1 = 200 \text{ hPa}$



Gas: helium  
 Electrodes: copper  
 Shielding:  $Al_2O_3$

$p_1$ in hPa	$I_1$ in mA	$D_1$ in mm	$l_1$ in mm
200	11.5	4.3	4.0

The current  $I_1$  was determined when the cathode was full covered with negative glow. The estimated error is  $\pm 1 \text{ mA}$ .

$$I_1 = 11.5 \text{ mA} \quad \frac{j_1}{p_1^2} = 19.8 \frac{\text{nA}}{\text{hPa}^2 \cdot \text{mm}^2} \quad T_1 = 475 \text{ K} \quad (\text{A.28})$$

The spectrum was taken at  $I_1 = 11.5 \text{ mA}$  and a power consumption of  $P_1 = 2.3 \text{ W}$ .

Resolution:	7nm	Baseline correction:	13.47	Multiplication:	13
Temperature:	475K	Wavelength correction:	-6nm	Doppler broad.:	yes

Table A.30: Lifbase 2.0 settings for  $p_1 = 200 \text{ hPa}$  and  $T = 475 \text{ K}$  ( $P_1 = 2.3 \text{ W}$ )

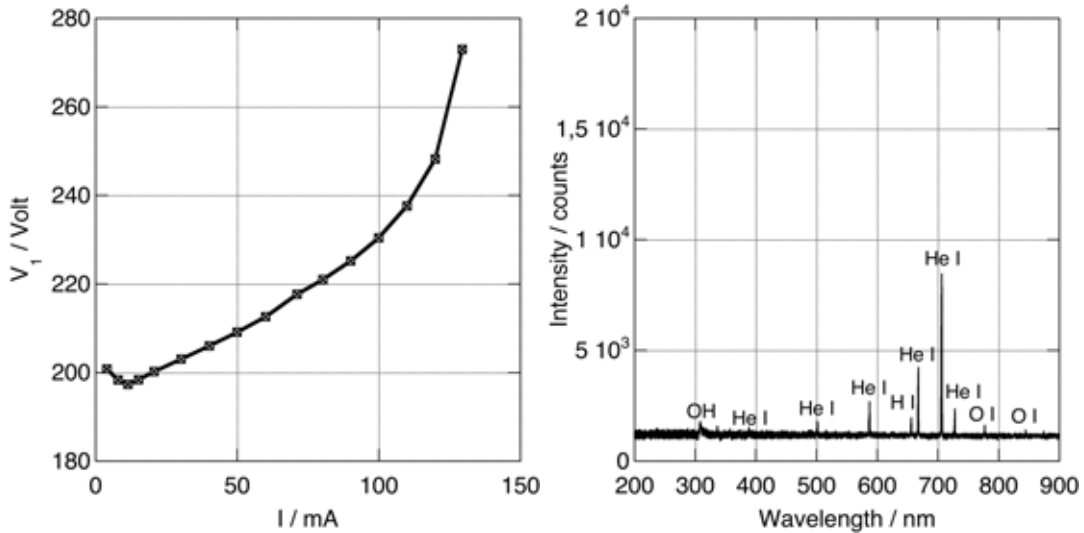


Figure A.30: I-V diagram (Tab.A.93) and spectrum (integration time: 200 ms)

**I-V diagram for  $D_1 = 4.3 \text{ mm}$ ,  $l_1 = 4.0 \text{ mm}$  and  $p_1 = 300 \text{ hPa}$**



Gas: helium  
Electrodes: copper  
Shielding:  $Al_2O_3$

$p_1$ in hPa	$I_1$ in mA	$D_1$ in mm	$l_1$ in mm
300	28.3	4.3	4.0

The current  $I_1$  was determined when the cathode was full covered with negative glow. The estimated error is  $\pm 2 \text{ mA}$ .

$$I_1 = 28.3 \text{ mA} \quad \frac{j_1}{p_1^2} = 21.6 \frac{\text{nA}}{\text{hPa}^2 \cdot \text{mm}^2} \quad T_1 = 450 \text{ K} \quad (\text{A.29})$$

The spectrum was taken at  $I_1 = 28.3 \text{ mA}$  and a power consumption of  $P_1 = 5.9 \text{ W}$ .

Resolution:	6nm	Baseline correction:	9.0	Multiplication:	18
Temperature:	450K	Wavelength correction:	-6nm	Doppler broad.:	yes

Table A.31: Lifbase 2.0 settings for  $p_1 = 300 \text{ hPa}$  and  $T = 450 \text{ K}$  ( $P_1 = 5.9 \text{ W}$ )

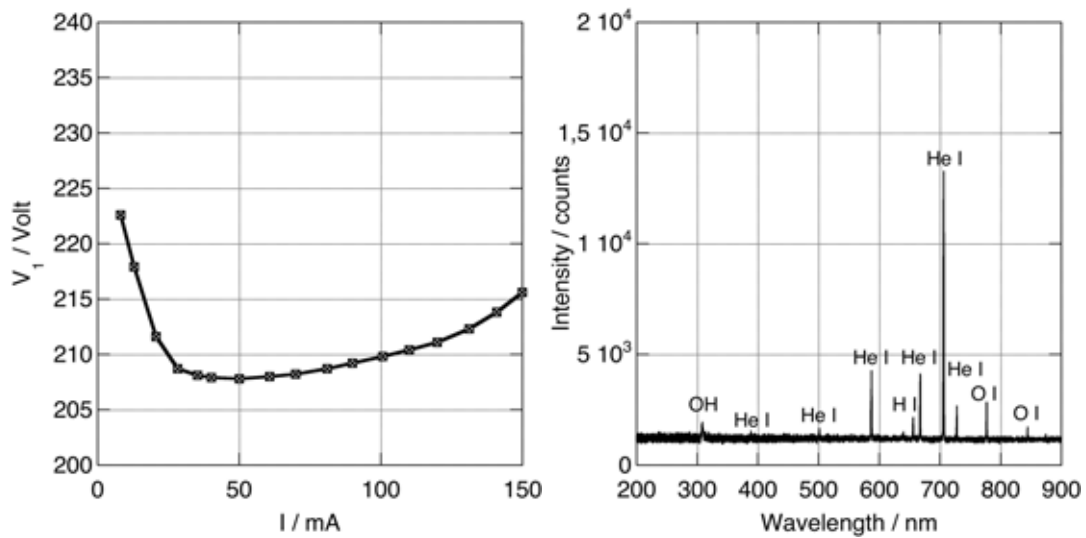
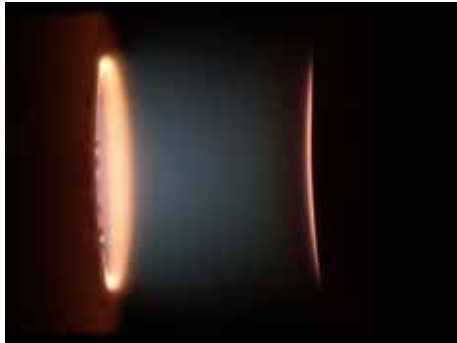


Figure A.31: I-V diagram (Tab.A.94) and spectrum (integration time: 200 ms)

**I-V diagram for  $D_1 = 4.3 \text{ mm}$ ,  $l_1 = 4.0 \text{ mm}$  and  $p_1 = 400 \text{ hPa}$**



Gas: helium  
 Electrodes: copper  
 Shielding:  $Al_2O_3$

$p_1$ in hPa	$I_1$ in mA	$D_1$ in mm	$l_1$ in mm
400	40	4.3	4.0

The current  $I_1$  was determined when the cathode was full covered with negative glow. The estimated error is  $\pm 3 \text{ mA}$ .

$$I_1 = 40.0 \text{ mA} \quad \frac{j_1}{p_1^2} = 17.2 \frac{\text{nA}}{\text{hPa}^2 \cdot \text{mm}^2} \quad T_1 = 300 \text{ K} \quad (\text{A.30})$$

The spectrum was taken at  $I_1 = 40.0 \text{ mA}$  and a power consumption of  $P_1 = 9.1 \text{ W}$ .

Resolution:	7nm	Baseline correction:	8	Multiplication:	7.2
Temperature:	300K	Wavelength correction:	-4nm	Doppler broad.:	yes

Table A.32: Lifbase 2.0 settings for  $p_1 = 400 \text{ hPa}$  and  $T = 300 \text{ K}$  ( $P_1 = 9.1 \text{ W}$ )

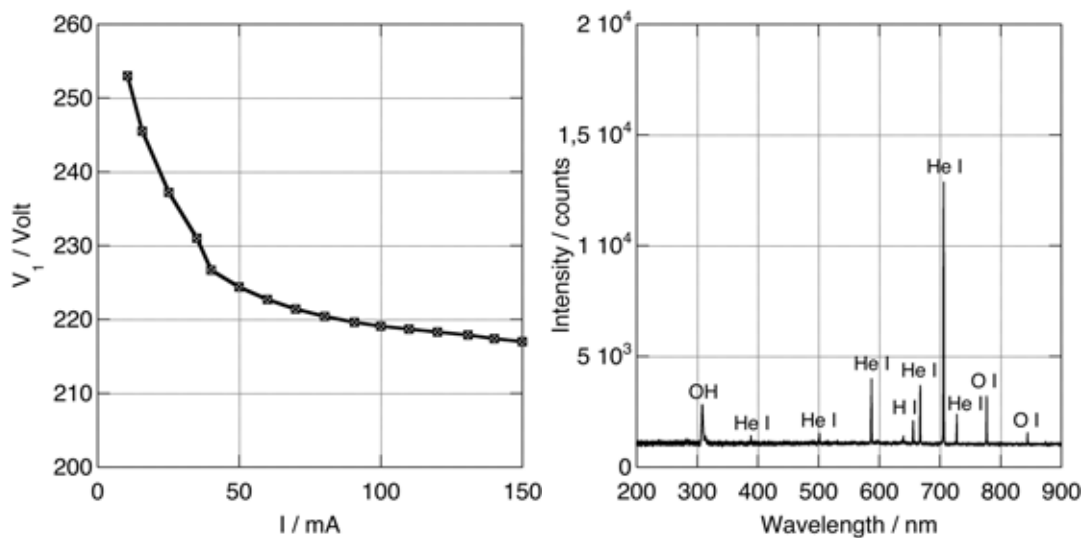


Figure A.32: I-V diagram (Tab.A.95) and spectrum (integration time: 120 ms)

**I-V diagram for  $D_1 = 4.3 \text{ mm}$ ,  $l_1 = 4.0 \text{ mm}$  and  $p_1 = 500 \text{ hPa}$**



Gas: helium  
Electrodes: copper  
Shielding:  $Al_2O_3$

$p_1$ in hPa	$I_1$ in mA	$D_1$ in mm	$l_1$ in mm
500	60	4.3	4.0

The current  $I_1$  was determined when the cathode was full covered with negative glow. The estimated error is  $\pm 5 \text{ mA}$ .

$$I_1 = 60.0 \text{ mA} \quad \frac{j_1}{p_1^2} = 16.5 \frac{\text{nA}}{\text{hPa}^2 \cdot \text{mm}^2} \quad T_1 = 775 \text{ K} \quad (\text{A.31})$$

The spectrum was taken at  $I_1 = 60.0 \text{ mA}$  and a power consumption of  $P_1 = 14.0 \text{ W}$ .

Resolution:	8nm	Baseline correction:	6.5	Multiplication:	4.6
Temperature:	775K	Wavelength correction:	-4.5nm	Doppler broad.:	yes

Table A.33: Lifbase 2.0 settings for  $p_1 = 500 \text{ hPa}$  and  $T = 775 \text{ K}$  ( $P_1 = 14.0 \text{ W}$ )

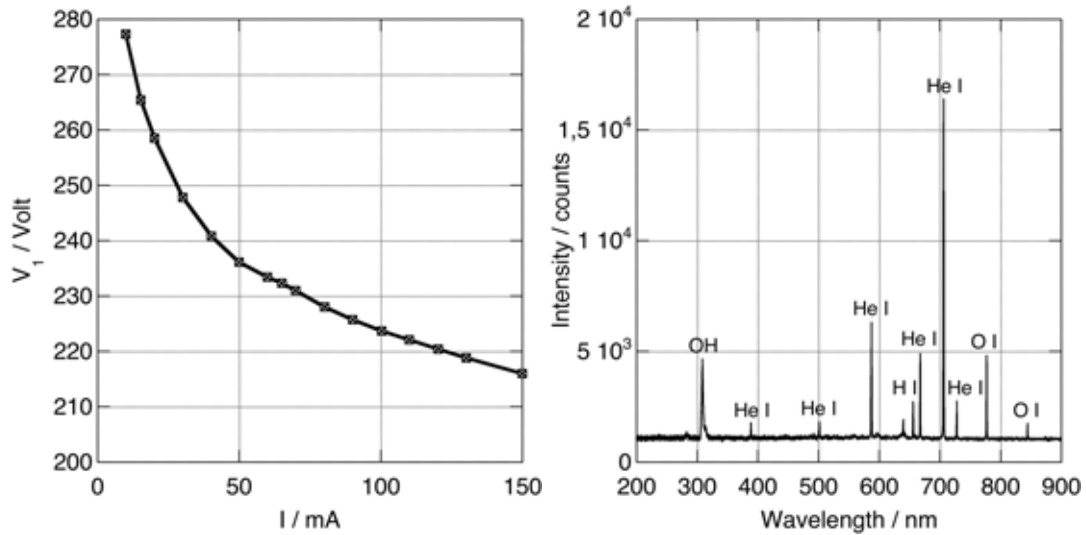
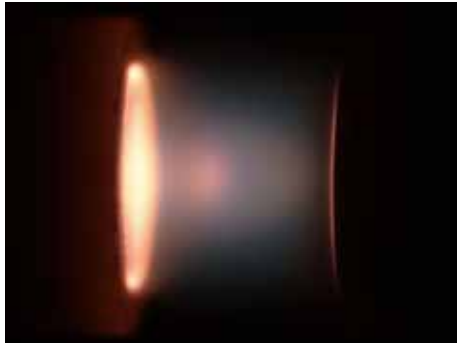


Figure A.33: I-V diagram (Tab.A.96) and spectrum (integration time: 120 ms)

**I-V diagram for  $D_1 = 4.3 \text{ mm}$ ,  $l_1 = 4.0 \text{ mm}$  and  $p_1 = 600 \text{ hPa}$**



Gas: helium  
 Electrodes: copper  
 Shielding:  $Al_2O_3$

$p_1$ in hPa	$I_1$ in mA	$D_1$ in mm	$l_1$ in mm
600	80	4.3	4.0

The current  $I_1$  was determined when the cathode was full covered with negative glow. The estimated error is  $\pm 5 \text{ mA}$ .

$$I_1 = 80.0 \text{ mA} \quad \frac{j_1}{p_1^2} = 15.3 \frac{\text{nA}}{\text{hPa}^2 \cdot \text{mm}^2} \quad T_1 = 875 \text{ K} \quad (\text{A.32})$$

The spectrum was taken at  $I_1 = 80.0 \text{ mA}$  and a power consumption of  $P_1 = 18.7 \text{ W}$ .

Resolution:	7nm	Baseline correction:	6.8	Multiplication:	15.7
Temperature:	875K	Wavelength correction:	-4.5nm	Doppler broad.:	yes

Table A.34: Lifbase 2.0 settings for  $p_1 = 600 \text{ hPa}$  and  $T = 875 \text{ K}$  ( $P_1 = 18.7 \text{ W}$ )

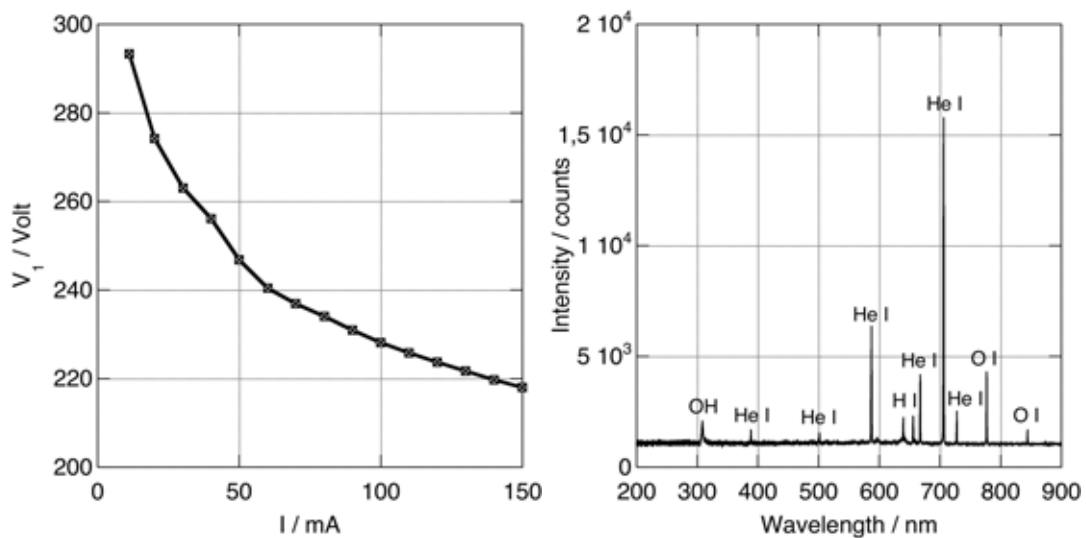


Figure A.34: I-V diagram (Tab.A.97) and spectrum (integration time: 120 ms)

**I-V diagram for  $D_1 = 4.3 \text{ mm}$ ,  $l_1 = 4.0 \text{ mm}$  and  $p_1 = 700 \text{ hPa}$**



Gas: helium  
Electrodes: copper  
Shielding:  $Al_2O_3$

$p_1$ in hPa	$I_1$ in mA	$D_1$ in mm	$l_1$ in mm
700	110	4.3	4.0

The current  $I_1$  was determined when the cathode was full covered with negative glow. The estimated error is  $\pm 10 \text{ mA}$ .

$$I_1 = 110 \text{ mA} \quad \frac{j_1}{p_1^2} = 15.5 \frac{\text{nA}}{\text{hPa}^2 \cdot \text{mm}^2} \quad T_1 = 900 \text{ K} \quad (\text{A.33})$$

The spectrum was taken at  $I_1 = 110.0 \text{ mA}$  and a power consumption of  $P_1 = 25.9 \text{ W}$ .

Resolution:	8nm	Baseline correction:	6.6	Multiplication:	6.6
Temperature:	900K	Wavelength correction:	-4nm	Doppler broad.:	yes

Table A.35: Lifbase 2.0 settings for  $p_1 = 700 \text{ hPa}$  and  $T = 900 \text{ K}$  ( $P_1 = 25.9 \text{ W}$ )

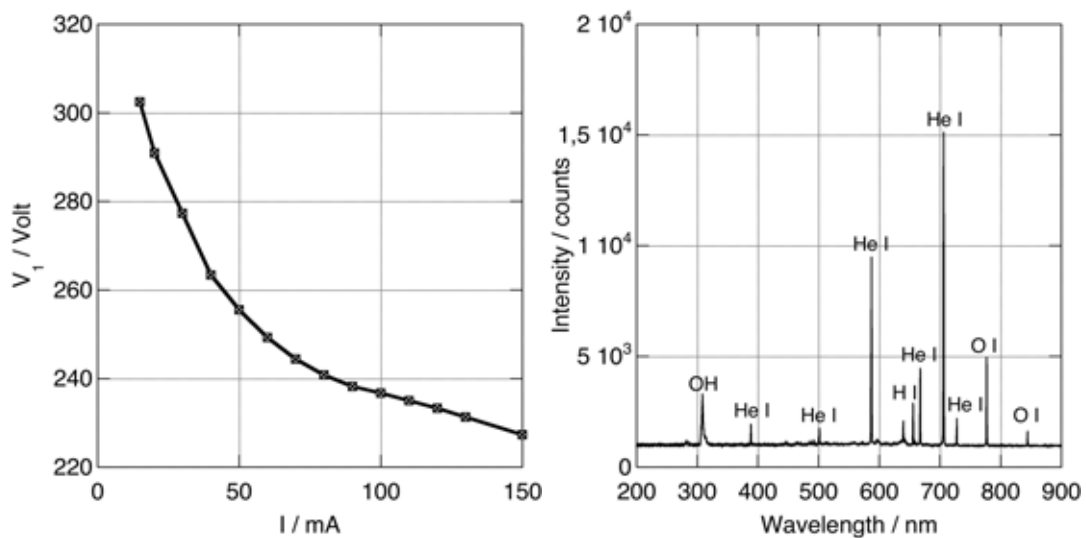
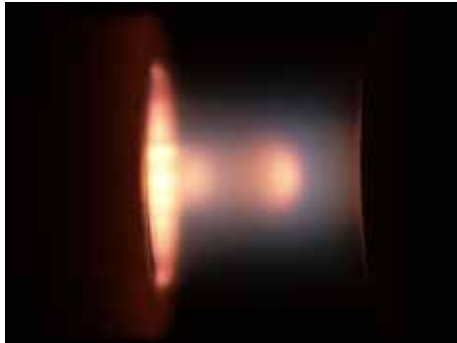


Figure A.35: I-V diagram (Tab.A.98) and spectrum (integration time: 80 ms)

**I-V diagram for  $D_1 = 4.3 \text{ mm}$ ,  $l_1 = 4.0 \text{ mm}$  and  $p_1 = 800 \text{ hPa}$**



Gas: helium  
 Electrodes: copper  
 Shielding:  $Al_2O_3$

$p_1$ in hPa	$I_1$ in mA	$D_1$ in mm	$l_1$ in mm
800	140	4.3	4.0

The current  $I_1$  was determined when the cathode was full covered with negative glow. The estimated error is  $\pm 10 \text{ mA}$ .

$$I_1 = 140 \text{ mA} \quad \frac{j_1}{p_1^2} = 15.1 \frac{\text{nA}}{\text{hPa}^2 \cdot \text{mm}^2} \quad T_1 = 1100 \text{ K} \quad (\text{A.34})$$

The spectrum was taken at  $I_1 = 140.0 \text{ mA}$  and a power consumption of  $P_1 = 32.7 \text{ W}$ .

Resolution:	8nm	Baseline correction:	6.9	Multiplication:	6.8
Temperature:	1100K	Wavelength correction:	-4.5nm	Doppler broad.:	yes

Table A.36: Lifbase 2.0 settings for  $p_1 = 800 \text{ hPa}$  and  $T = 1100 \text{ K}$  ( $P_1 = 32.7 \text{ W}$ )

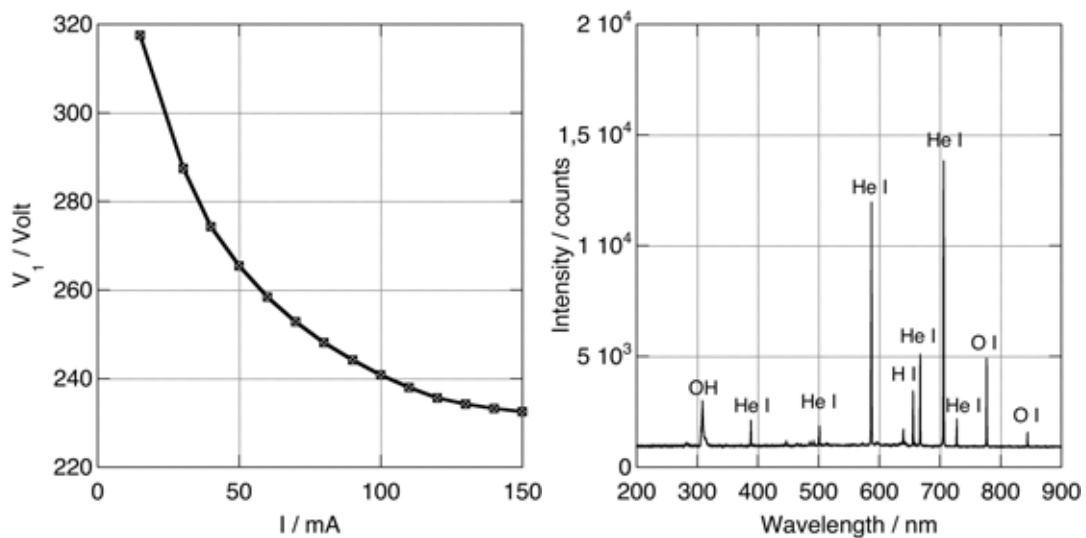
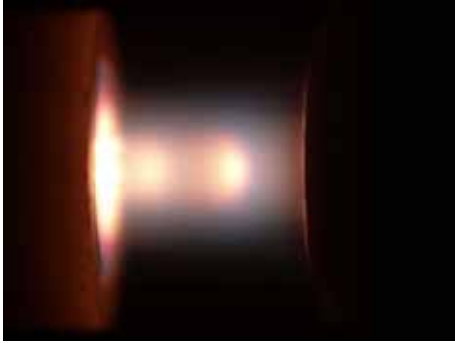


Figure A.36: I-V diagram (Tab.A.99) and spectrum (integration time: 60 ms)

**I-V diagram for  $D_1 = 4.3 \text{ mm}$ ,  $l_1 = 4.0 \text{ mm}$  and  $p_1 = 900 \text{ hPa}$**



Gas: helium  
Electrodes: copper  
Shielding:  $Al_2O_3$

$p_1$ in hPa	$I_1$ in mA	$D_1$ in mm	$l_1$ in mm
900	150	4.3	4.0

The current  $I_1$  was determined when the cathode was full covered with negative glow. The estimated error is  $\pm - \text{mA}$ .

$$I_1 = - \text{mA} \quad \frac{j_1}{p_1^2} = - \frac{nA}{\text{hPa}^2 \cdot \text{mm}^2} \quad T_1 = 1150 \text{ K} \quad (\text{A.35})$$

The spectrum was taken at  $I_1 = 150.0 \text{ mA}$  and a power consumption of  $P_1 = 34.2 \text{ W}$ .

Resolution:	8nm	Baseline correction:	7.5	Multiplication:	11.4
Temperature:	1150K	Wavelength correction:	-4.5nm	Doppler broad.:	yes

Table A.37: Lifbase 2.0 settings for  $p_1 = 900 \text{ hPa}$  and  $T = 1150 \text{ K}$  ( $P_1 = 34.2 \text{ W}$ )

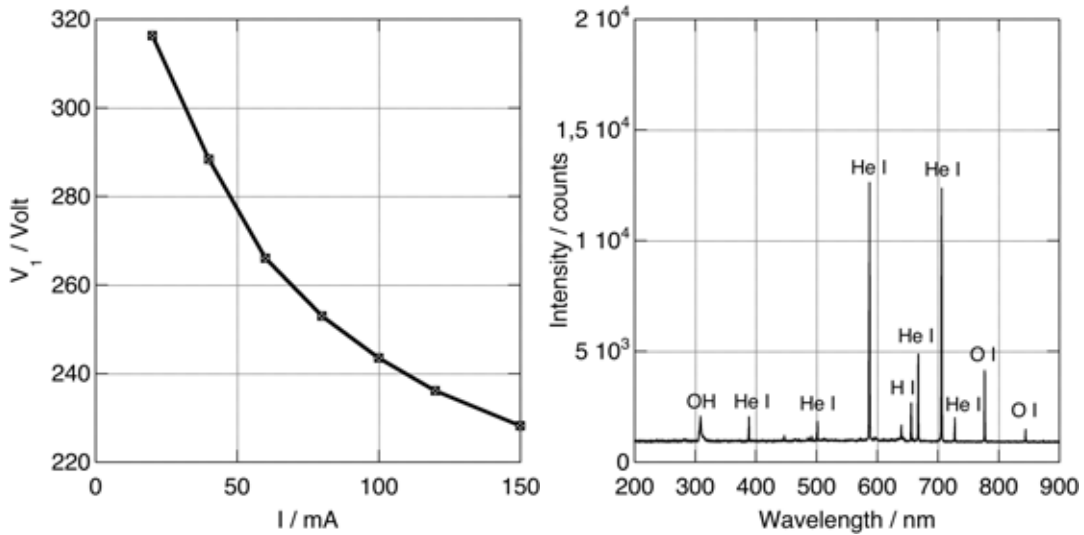
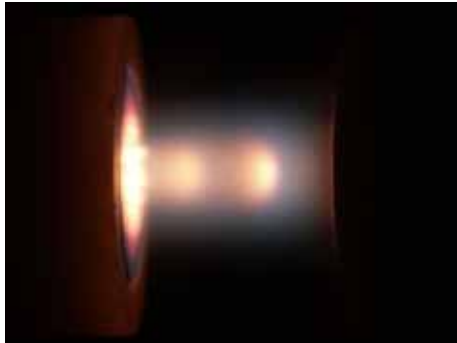


Figure A.37: I-V diagram (Tab.A.100) and spectrum (integration time: 60 ms)

I-V diagram for  $D_1 = 4.3 \text{ mm}$ ,  $l_1 = 4.0 \text{ mm}$  and  $p_1 = 1000 \text{ hPa}$



Gas: helium  
 Electrodes: copper  
 Shielding:  $Al_2O_3$

$p_1$ in hPa	$I_1$ in mA	$D_1$ in mm	$l_1$ in mm
1000	150.0	4.3	4.0

The current  $I_1$  was determined when the cathode was full covered with negative glow. The estimated error is  $\pm - \text{mA}$ .

$$I_1 = - \text{mA} \quad \frac{j_1}{p_1^2} = - \frac{nA}{\text{hPa}^2 \cdot \text{mm}^2} \quad T_1 = 1150 \text{ K} \quad (\text{A.36})$$

The spectrum was taken at  $I_1 = 150.0 \text{ mA}$  and a power consumption of  $P_1 = 34.8 \text{ W}$ .

Resolution:	8nm	Baseline correction:	7.5	Multiplication:	11.5
Temperature:	1150K	Wavelength correction:	-4nm	Doppler broad.:	yes

Table A.38: Lifbase 2.0 settings for  $p_1 = 1000 \text{ hPa}$  and  $T = 1150 \text{ K}$  ( $P_1 = 34.8 \text{ W}$ )

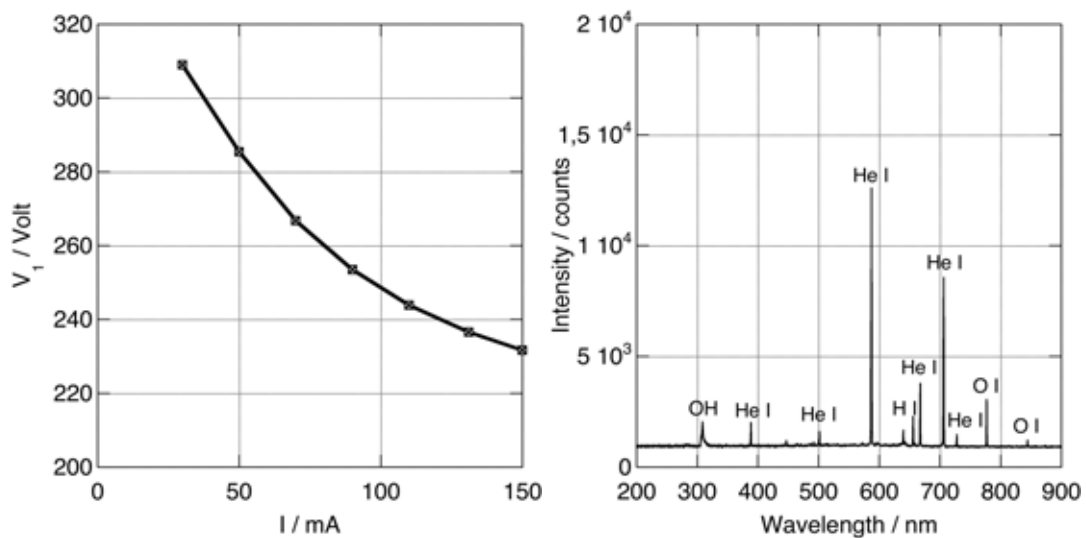
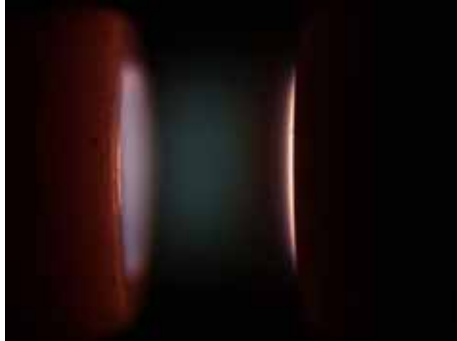


Figure A.38: I-V diagram (Tab.A.101) and spectrum (integration time: 60 ms)

**I-V diagram for  $D_2 = 3.0\text{mm}$ ,  $l_2 = 2.8\text{mm}$  and  $p_2 = 290\text{ hPa}$**



Gas: helium  
Electrodes: copper  
Shielding:  $Al_2O_3$

$p_2$ in hPa	$I_2$ in mA	$D_2$ in mm	$l_2$ in mm
290	12	3.0	2.8

The current  $I_2$  was determined when the cathode was full covered with negative glow. The estimated error is  $\pm 1\text{ mA}$ .

$$I_2 = 12.0\text{ mA} \quad \frac{j_2}{p_2^2} = 20.2 \frac{\text{nA}}{\text{hPa}^2 \cdot \text{mm}^2} \quad T_2 = 325\text{ K} \quad (\text{A.37})$$

The spectrum was taken at  $I_2 = 12.0\text{ mA}$  and a power consumption of  $P_2 = 2.2\text{ W}$ .

Resolution:	7nm	Baseline correction:	7	Multiplication:	19
Temperature:	325K	Wavelength correction:	-5nm	Doppler broad.:	yes

Table A.39: Lifbase 2.0 settings for  $p_2 = 290\text{ hPa}$  and  $T = 325\text{ K}$  ( $P_2 = 2.2\text{ W}$ )

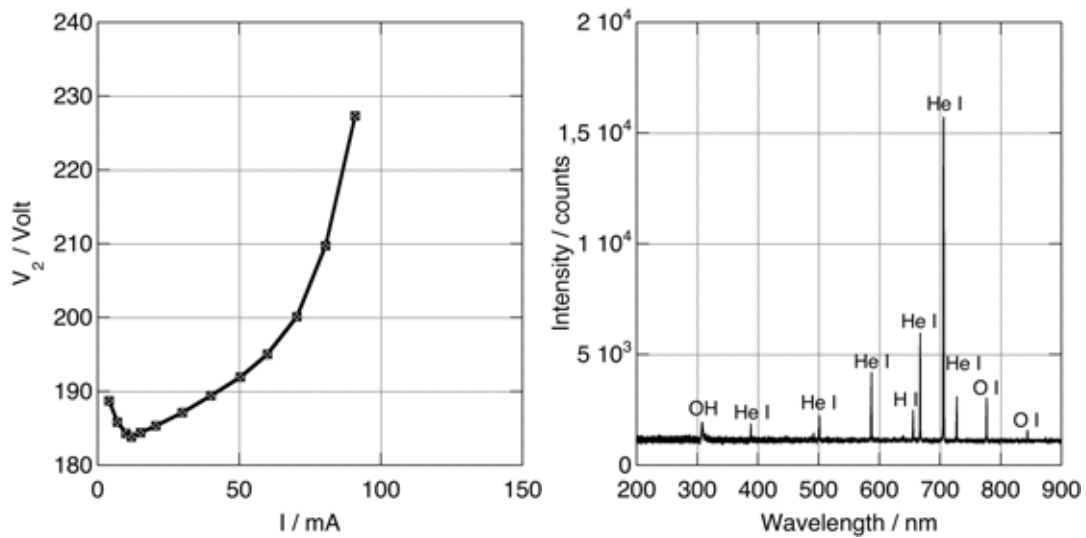


Figure A.39: I-V diagram (Tab.A.102) and spectrum (integration time: 150ms)

I-V diagram for  $D_2 = 3.0\text{mm}$ ,  $l_2 = 2.8\text{mm}$  and  $p_2 = 430\text{ hPa}$



Gas: helium  
 Electrodes: copper  
 Shielding:  $Al_2O_3$

$p_2$ in hPa	$I_2$ in mA	$D_2$ in mm	$l_2$ in mm
430	26	3.0	2.8

The current  $I_2$  was determined when the cathode was full covered with negative glow. The estimated error is  $\pm 5\text{ mA}$ .

$$I_2 = 26.0\text{ mA} \quad \frac{j_2}{p_2^2} = 19.9 \frac{\text{nA}}{\text{hPa}^2 \cdot \text{mm}^2} \quad T_2 = 350\text{ K} \quad (\text{A.38})$$

The spectrum was taken at  $I_2 = 26.0\text{ mA}$  and a power consumption of  $P_2 = 5.2\text{ W}$ .

Resolution:	7nm	Baseline correction:	6.8	Multiplication:	16
Temperature:	350K	Wavelength correction:	-5nm	Doppler broad.:	yes

Table A.40: Lifbase 2.0 settings for  $p_2 = 430\text{ hPa}$  and  $T = 350\text{ K}$  ( $P_2 = 5.2\text{ W}$ )

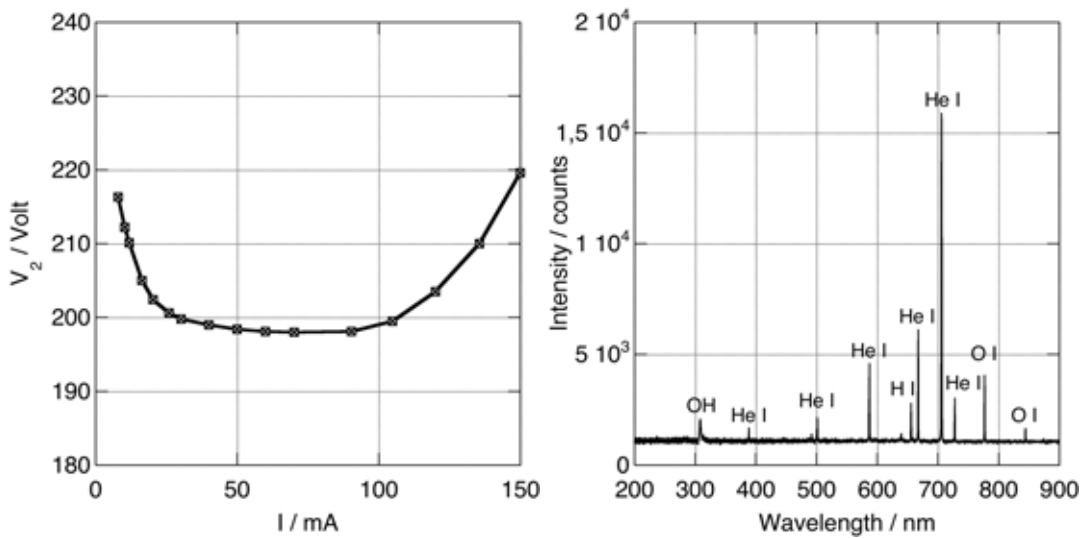


Figure A.40: I-V diagram (Tab.A.103) and spectrum (integration time: 125ms)

**I-V diagram for  $D_2 = 3.0\text{mm}$ ,  $l_2 = 2.8\text{mm}$  and  $p_2 = 570\text{ hPa}$**



Gas: helium  
Electrodes: copper  
Shielding:  $Al_2O_3$

$p_2$ in hPa	$I_2$ in mA	$D_2$ in mm	$l_2$ in mm
570	50	3.0	2.8

The current  $I_2$  was determined when the cathode was full covered with negative glow. The estimated error is  $\pm 1\text{ mA}$ .

$$I_2 = 50.0\text{ mA} \quad \frac{j_2}{p_2^2} = 21.8 \frac{\text{nA}}{\text{hPa}^2 \cdot \text{mm}^2} \quad T_2 = 410\text{ K} \quad (\text{A.39})$$

The spectrum was taken at  $I_2 = 50.0\text{ mA}$  and a power consumption of  $P_2 = 10.5\text{ W}$ .

Resolution:	7nm	Baseline correction:	6.5	Multiplication:	12.6
Temperature:	410K	Wavelength correction:	-5nm	Doppler broad.:	yes

Table A.41: Lifbase 2.0 settings for  $p_2 = 570\text{ hPa}$  and  $T = 410\text{ K}$  ( $P_2 = 10.5\text{ W}$ )

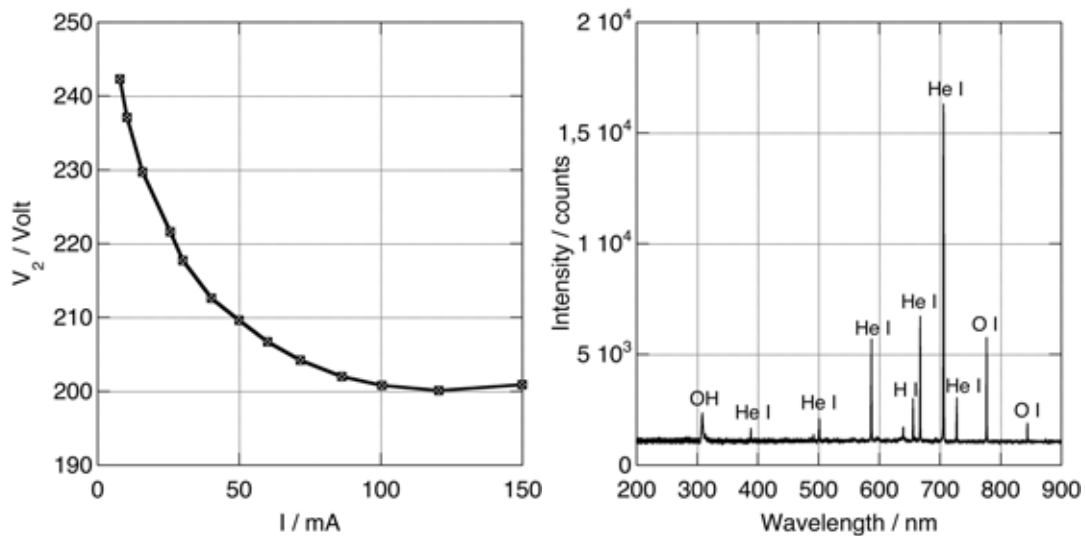
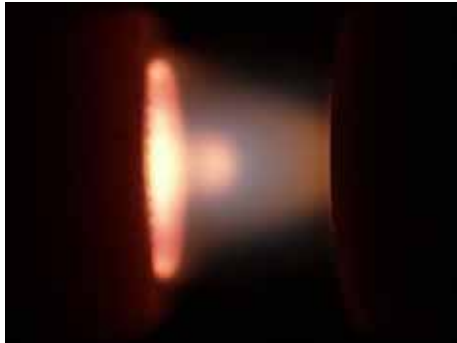


Figure A.41: I-V diagram (Tab.A.104) and spectrum (integration time: 120ms)

I-V diagram for  $D_2 = 3.0\text{mm}$ ,  $l_2 = 2.8\text{mm}$  and  $p_2 = 720\text{ hPa}$



Gas: helium  
 Electrodes: copper  
 Shielding:  $Al_2O_3$

$p_2$ in hPa	$I_2$ in mA	$D_2$ in mm	$l_2$ in mm
720	60	3.0	2.8

The current  $I_2$  was determined when the cathode was full covered with negative glow. The estimated error is  $\pm 10\text{ mA}$ .

$$I_2 = 60.0\text{ mA} \quad \frac{j_2}{p_2^2} = 16.4 \frac{\text{nA}}{\text{hPa}^2 \cdot \text{mm}^2} \quad T_1 = 400\text{ K} \quad (\text{A.40})$$

The spectrum was taken at  $I_2 = 60.0\text{ mA}$  and a power consumption of  $P_2 = 12.7\text{ W}$ .

Resolution:	7nm	Baseline correction:	6.5	Multiplication:	13.6
Temperature:	400K	Wavelength correction:	-5nm	Doppler broad.:	yes

Table A.42: Lifbase 2.0 settings for  $p_2 = 720\text{ hPa}$  and  $T = 400\text{ K}$  ( $P_2 = 12.7\text{ W}$ )

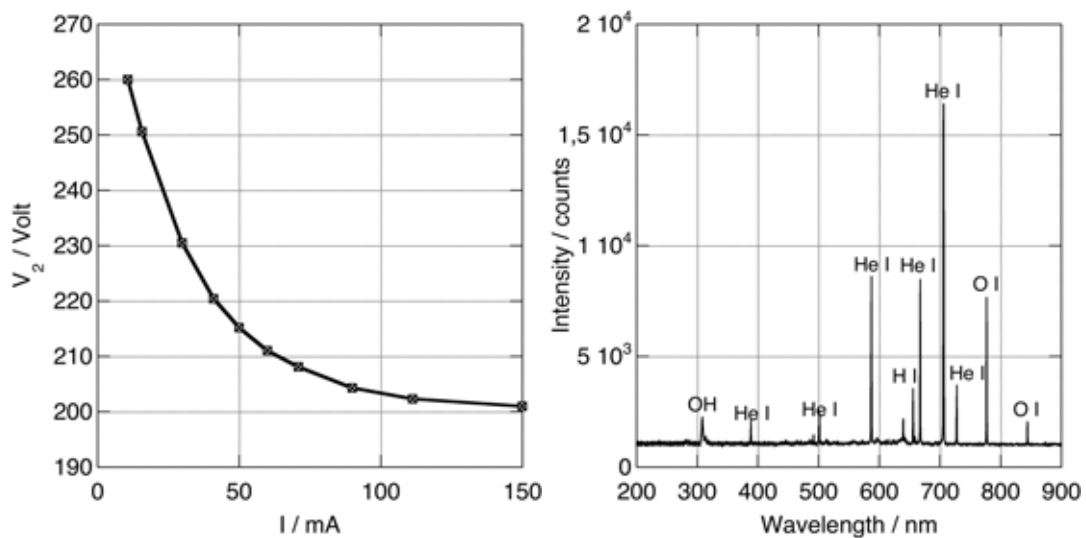


Figure A.42: I-V diagram (Tab.A.105) and spectrum (integration time: 100ms)

**I-V diagram for  $D_2 = 3.0\text{mm}$ ,  $l_2 = 2.8\text{mm}$  and  $p_2 = 860\text{ hPa}$**



Gas: helium  
Electrodes: copper  
Shielding:  $Al_2O_3$

$p_2$ in hPa	$I_2$ in mA	$D_2$ in mm	$l_2$ in mm
860	85	3.0	2.8

The current  $I_2$  was determined when the cathode was full covered with negative glow. The estimated error is  $\pm 10\text{ mA}$ .

$$I_2 = 85.0\text{ mA} \quad \frac{j_2}{p_2^2} = 16.3 \frac{\text{nA}}{\text{hPa}^2 \cdot \text{mm}^2} \quad T_2 = 700\text{ K} \quad (\text{A.41})$$

The spectrum was taken at  $I_2 = 85.0\text{ mA}$  and a power consumption of  $P_2 = 17.4\text{ W}$ .

Resolution:	7nm	Baseline correction:	6.5	Multiplication:	20.7
Temperature:	700K	Wavelength correction:	-5nm	Doppler broad.:	yes

Table A.43: Lifbase 2.0 settings for  $p_2 = 860\text{ hPa}$  and  $T = 700\text{ K}$  ( $P_2 = 17.4\text{ W}$ )

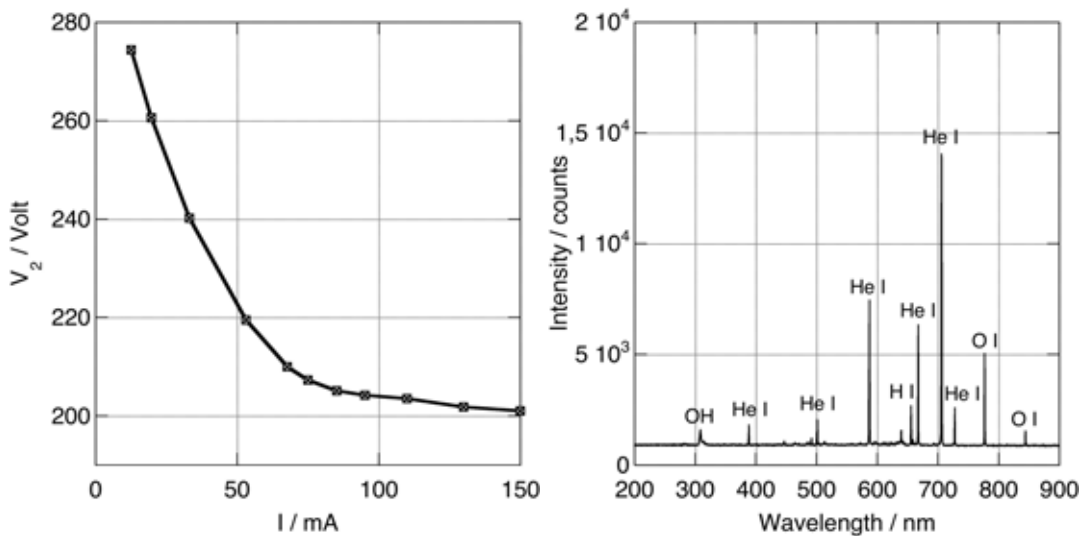
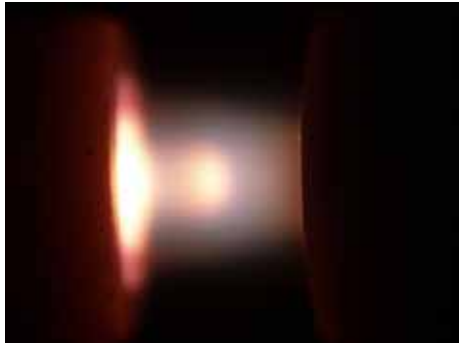


Figure A.43: I-V diagram (Tab.A.106) and spectrum (integration time: 40ms)

I-V diagram for  $D_2 = 3.0\text{mm}$ ,  $l_2 = 2.8\text{mm}$  and  $p_2 = 1000\text{ hPa}$



Gas: helium  
 Electrodes: copper  
 Shielding:  $Al_2O_3$

$p_2$ in hPa	$I_2$ in mA	$D_2$ in mm	$l_2$ in mm
1000	110	3.0	2.8

The current  $I_2$  was determined when the cathode was full covered with negative glow. The estimated error is  $\pm 10\text{ mA}$ .

$$I_2 = 110.0\text{ mA} \quad \frac{j_2}{p_2^2} = 15.6 \frac{\text{nA}}{\text{hPa}^2 \cdot \text{mm}^2} \quad T_2 = 900\text{ K} \quad (\text{A.42})$$

The spectrum was taken at  $I_2 = 110.0\text{ mA}$  and a power consumption of  $P_2 = 20.8\text{ W}$ .

Resolution:	7nm	Baseline correction:	6.5	Multiplication:	22
Temperature:	900K	Wavelength correction:	-5nm	Doppler broad.:	yes

Table A.44: Lifbase 2.0 settings for  $p_2 = 1000\text{ hPa}$  and  $T = 900\text{ K}$  ( $P_2 = 20.8\text{ W}$ )

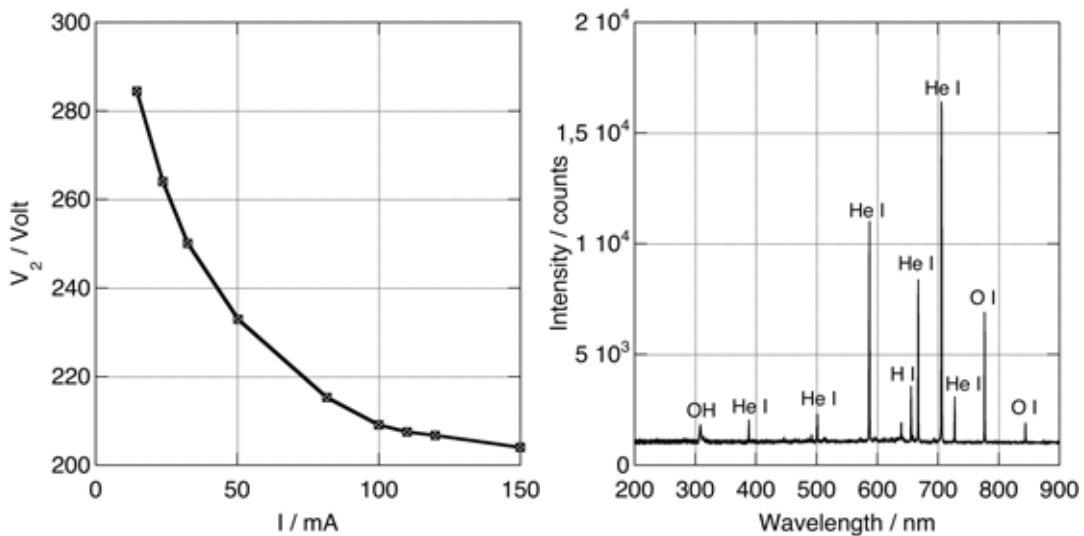
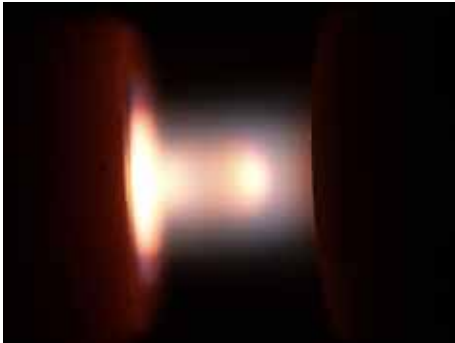


Figure A.44: I-V diagram (Tab.A.107) and spectrum (integration time: 100ms)

**I-V diagram for  $D_2 = 3.0\text{mm}$ ,  $l_2 = 2.8\text{mm}$  and  $p_2 = 1150\text{ hPa}$**



Gas: helium  
Electrodes: copper  
Shielding:  $Al_2O_3$

$p_2$ in hPa	$I_2$ in mA	$D_2$ in mm	$l_2$ in mm
1150	150	3.0	2.8

The current  $I_2$  was determined when the cathode was full covered with negative glow. The estimated error is  $\pm 10\text{ mA}$ .

$$I_2 = 150.0\text{ mA} \quad \frac{j_2}{p_2^2} = 16.0 \frac{\text{nA}}{\text{hPa}^2 \cdot \text{mm}^2} \quad T_2 = 1100\text{ K} \quad (\text{A.43})$$

The spectrum was taken at  $I_2 = 150.0\text{ mA}$  and a power consumption of  $P_2 = 32.7\text{ W}$ .

Resolution:	7nm	Baseline correction:	6.2	Multiplication:	4.8
Temperature:	1100K	Wavelength correction:	-5nm	Doppler broad.:	yes

Table A.45: Lifbase 2.0 settings for  $p_2 = 1150\text{ hPa}$  and  $T = 1100\text{ K}$  ( $P_2 = 32.7\text{ W}$ )

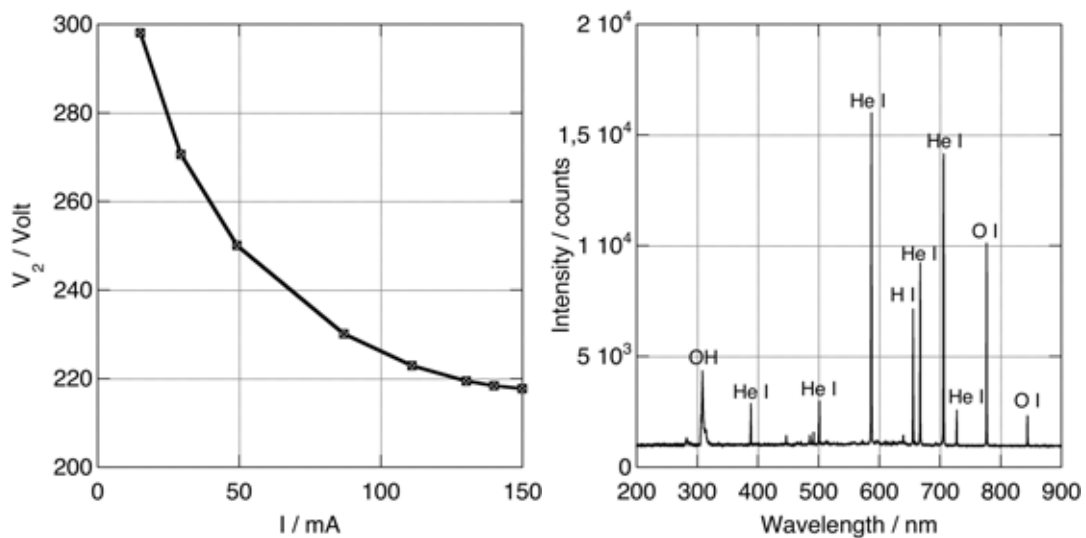
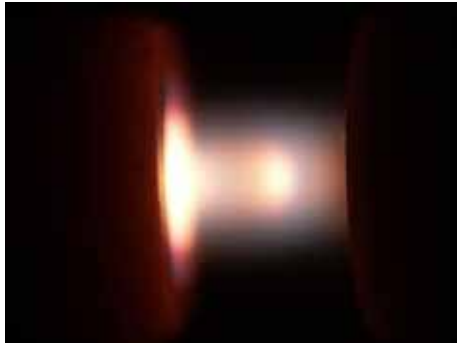


Figure A.45: I-V diagram (Tab.A.108) and spectrum (integration time: 70ms)

I-V diagram for  $D_2 = 3.0\text{mm}$ ,  $l_2 = 2.8\text{mm}$  and  $p_2 = 1290\text{ hPa}$



Gas: helium  
 Electrodes: copper  
 Shielding:  $Al_2O_3$

$p_2$ in hPa	$I_2$ in mA	$D_2$ in mm	$l_2$ in mm
1290	150	3.0	2.8

The current  $I_2$  was determined when the cathode was full covered with negative glow. The estimated error is  $\pm -\text{mA}$ .

$$I_2 = -\text{mA} \quad \frac{j_2}{p_2^2} = -\frac{nA}{\text{hPa}^2 \cdot \text{mm}^2} \quad T_2 = 1200\text{ K} \quad (\text{A.44})$$

The spectrum was taken at  $I_2 = 150.0\text{ mA}$  and a power consumption of  $P_2 = 32.0\text{ W}$ .

Resolution:	7nm	Baseline correction:	6.2	Multiplication:	13.9
Temperature:	1200K	Wavelength correction:	-5nm	Doppler broad.:	yes

Table A.46: Lifbase 2.0 settings for  $p_2 = 1290\text{ hPa}$  and  $T = 1200\text{ K}$  ( $P_2 = 32.0\text{ W}$ )

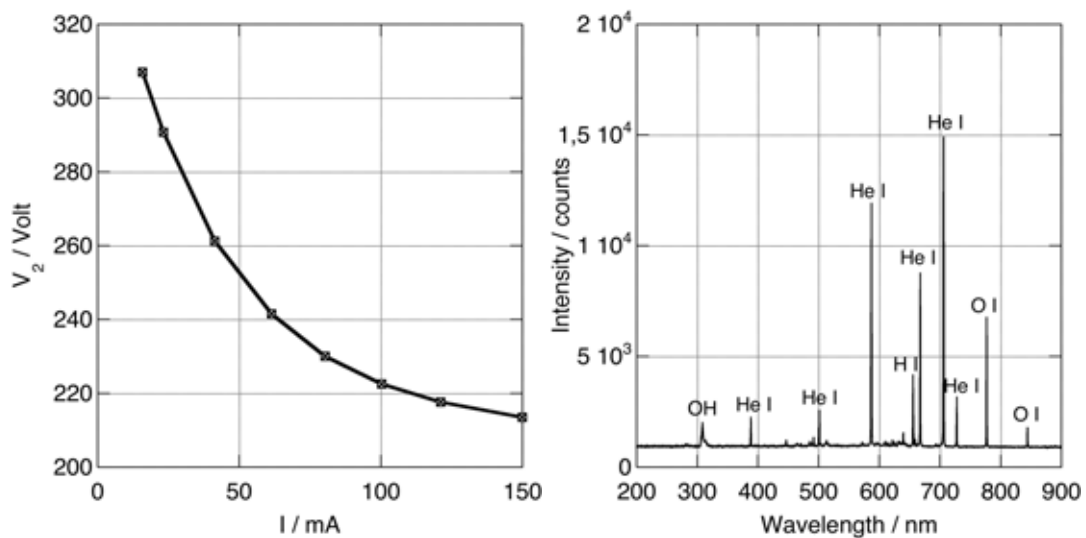
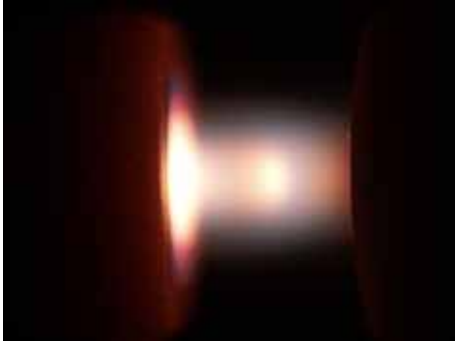


Figure A.46: I-V diagram (Tab.A.109) and spectrum (integration time: 50ms)

**I-V diagram for  $D_2 = 3.0\text{mm}$ ,  $l_2 = 2.8\text{mm}$  and  $p_2 = 1430\text{ hPa}$**



Gas: helium  
Electrodes: copper  
Shielding:  $Al_2O_3$

$p_2$ in hPa	$I_2$ in mA	$D_2$ in mm	$l_2$ in mm
1430	150	3.0	2.8

The current  $I_2$  was determined when the cathode was full covered with negative glow. The estimated error is  $\pm -\text{mA}$ .

$$I_2 = -\text{mA} \quad \frac{j_3}{p_2^2} = -\frac{nA}{\text{hPa}^2 \cdot \text{mm}^2} \quad T_2 = 1050\text{ K} \quad (\text{A.45})$$

The spectrum was taken at  $I_2 = 150.0\text{ mA}$  and a power consumption of  $P_2 = 32.7\text{ W}$ .

Resolution:	7nm	Baseline correction:	5.5	Multiplication:	15.8
Temperature:	1050K	Wavelength correction:	-5nm	Doppler broad.:	yes

Table A.47: Lifbase 2.0 settings for  $p_2 = 1430\text{ hPa}$  and  $T = 1050\text{ K}$  ( $P_2 = 32.7\text{ W}$ )

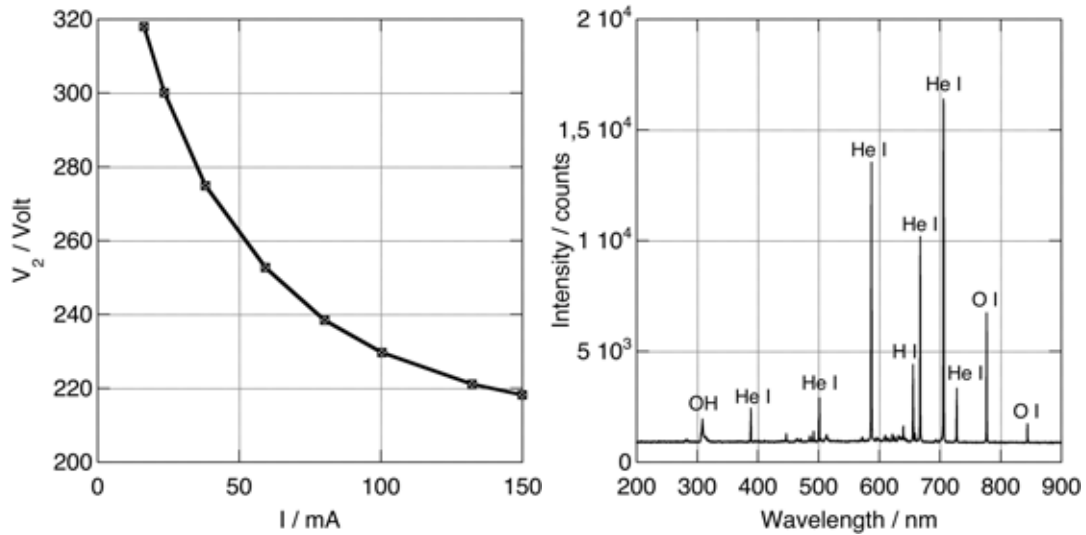


Figure A.47: I-V diagram (Tab.A.110) and spectrum (integration time: 40ms)

I-V diagram for  $D_3 = 2.1\text{mm}$ ,  $l_3 = 1.95\text{mm}$  and  $p_3 = 400\text{ hPa}$



Gas: helium  
 Electrodes: copper  
 Shielding:  $Al_2O_3$

$p_3$ in hPa	$I_3$ in mA	$D_3$ in mm	$l_3$ in mm
400	13	2.1	1.95

The current  $I_3$  was determined when the cathode was full covered with negative glow. The estimated error is  $\pm 2\text{ mA}$ .

$$I_3 = 13.0\text{ mA} \quad \frac{j_2}{p_2^2} = 23.5 \frac{\text{nA}}{\text{hPa}^2 \cdot \text{mm}^2} \quad T_3 = 305\text{ K} \quad (\text{A.46})$$

The spectrum was taken at  $I_3 = 13.0\text{ mA}$  and a power consumption of  $P_3 = 2.5\text{ W}$ .

Resolution:	8nm	Baseline correction:	7.5	Multiplication:	17.6
Temperature:	305K	Wavelength correction:	-4nm	Doppler broad.:	yes

Table A.48: Lifbase 2.0 settings for  $p_3 = 400\text{ hPa}$  and  $T = 305\text{ K}$  ( $P_3 = 2.5\text{ W}$ )

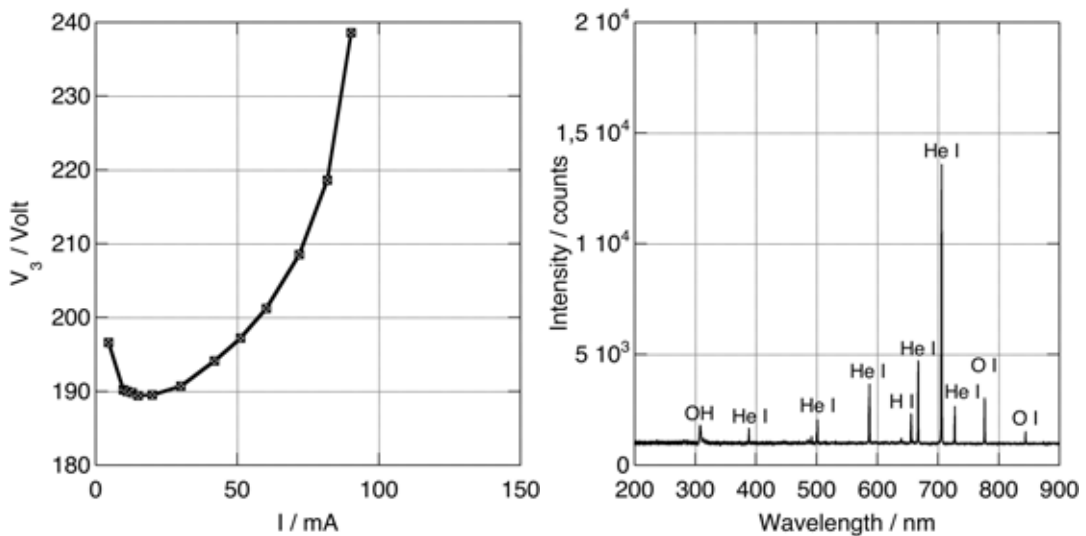


Figure A.48: I-V diagram (Tab.A.111) and spectrum (integration time: 100ms)

**I-V diagram for  $D_3 = 2.1\text{mm}$ ,  $l_3 = 1.95\text{mm}$  and  $p_3 = 600\text{ hPa}$**



Gas: helium  
Electrodes: copper  
Shielding:  $Al_2O_3$

$p_3$ in hPa	$I_3$ in mA	$D_3$ in mm	$l_3$ in mm
600	23	2.1	1.95

The current  $I_3$  was determined when the cathode was full covered with negative glow. The estimated error is  $\pm 3\text{ mA}$ .

$$I_3 = 23.0\text{ mA} \quad \frac{j_3}{p_3^2} = 18.4 \frac{\text{nA}}{\text{hPa}^2 \cdot \text{mm}^2} \quad T_3 = 430\text{ K} \quad (\text{A.47})$$

The spectrum was taken at  $I_3 = 23.0\text{ mA}$  and a power consumption of  $P_3 = 4.6\text{ W}$ .

Resolution:	8nm	Baseline correction:	8.5	Multiplication:	6.5
Temperature:	430K	Wavelength correction:	-4.3nm	Doppler broad.:	yes

Table A.49: Lifbase 2.0 settings for  $p_3 = 600\text{ hPa}$  and  $T = 430\text{ K}$  ( $P_3 = 4.6\text{ W}$ )

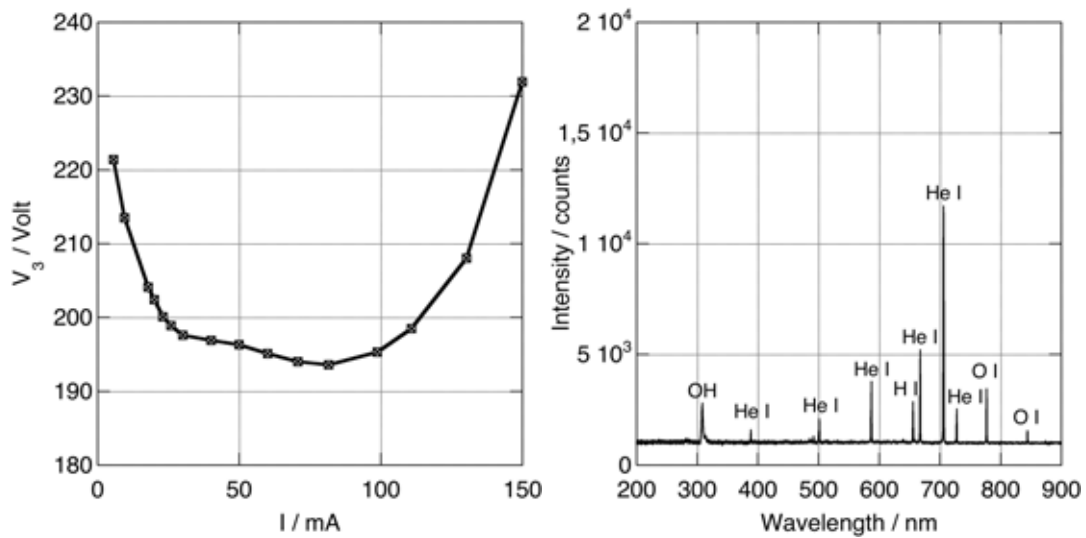
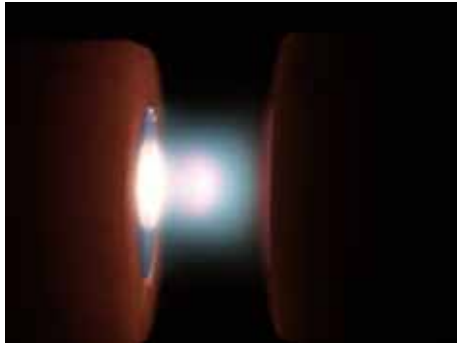


Figure A.49: I-V diagram (Tab.A.112) and spectrum (integration time: 100ms)

I-V diagram for  $D_3 = 2.1\text{mm}$ ,  $l_3 = 1.95\text{mm}$  and  $p_3 = 800\text{ hPa}$



Gas: helium  
 Electrodes: copper  
 Shielding:  $Al_2O_3$

$p_3$ in hPa	$I_3$ in mA	$D_3$ in mm	$l_3$ in mm
800	30	2.1	1.95

The current  $I_3$  was determined when the cathode was full covered with negative glow. The estimated error is  $\pm 7\text{ mA}$ .

$$I_3 = 30.0\text{ mA} \quad \frac{j_3}{p_3^2} = 13.5 \frac{\text{nA}}{\text{hPa}^2 \cdot \text{mm}^2} \quad T_3 = 550\text{ K} \quad (\text{A.48})$$

The spectrum was taken at  $I_3 = 30.0\text{ mA}$  and a power consumption of  $P_3 = 6.3\text{ W}$ .

Resolution:	8nm	Baseline correction:	7.5	Multiplication:	2.85
Temperature:	550K	Wavelength correction:	-4nm	Doppler broad.:	yes

Table A.50: Lifbase 2.0 settings for  $p_3 = 800\text{ hPa}$  and  $T = 550\text{ K}$  ( $P_3 = 6.3\text{ W}$ )

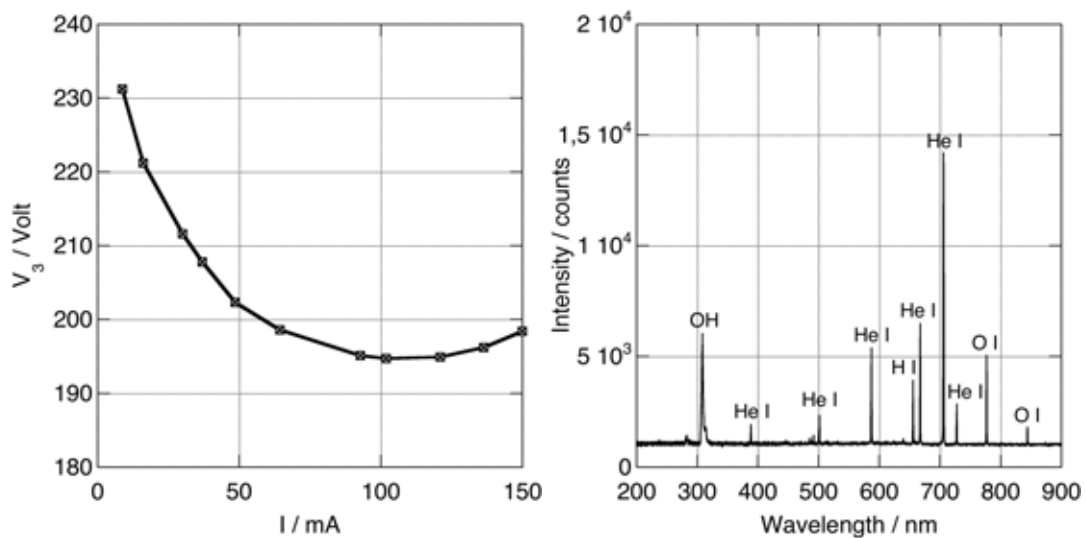
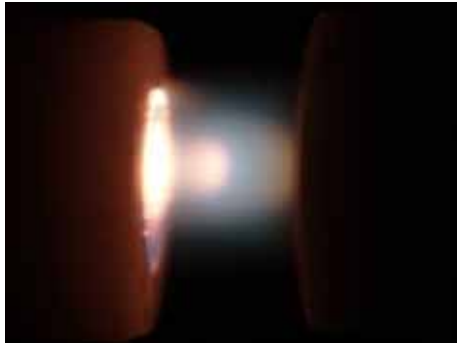


Figure A.50: I-V diagram (Tab.A.113) and spectrum (integration time: 100ms)

**I-V diagram for  $D_3 = 2.1\text{mm}$ ,  $l_3 = 1.95\text{mm}$  and  $p_3 = 1000\text{ hPa}$**



Gas: helium  
Electrodes: copper  
Shielding:  $Al_2O_3$

$p_3$ in hPa	$I_3$ in mA	$D_3$ in mm	$l_3$ in mm
1000	50	2.1	1.95

The current  $I_3$  was determined when the cathode was full covered with negative glow. The estimated error is  $\pm 7\text{ mA}$ .

$$I_3 = 50.0\text{ mA} \quad \frac{j_3}{p_3^2} = 14.4 \frac{\text{nA}}{\text{hPa}^2 \cdot \text{mm}^2} \quad T_3 = 650\text{ K} \quad (\text{A.49})$$

The spectrum was taken at  $I_3 = 50.0\text{ mA}$  and a power consumption of  $P_3 = 10.5\text{ W}$ .

Resolution:	8nm	Baseline correction:	6.7	Multiplication:	10.7
Temperature:	650K	Wavelength correction:	-5nm	Doppler broad.:	yes

Table A.51: Lifbase 2.0 settings for  $p_3 = 1000\text{ hPa}$  and  $T = 650\text{ K}$  ( $P_3 = 10.5\text{ W}$ )

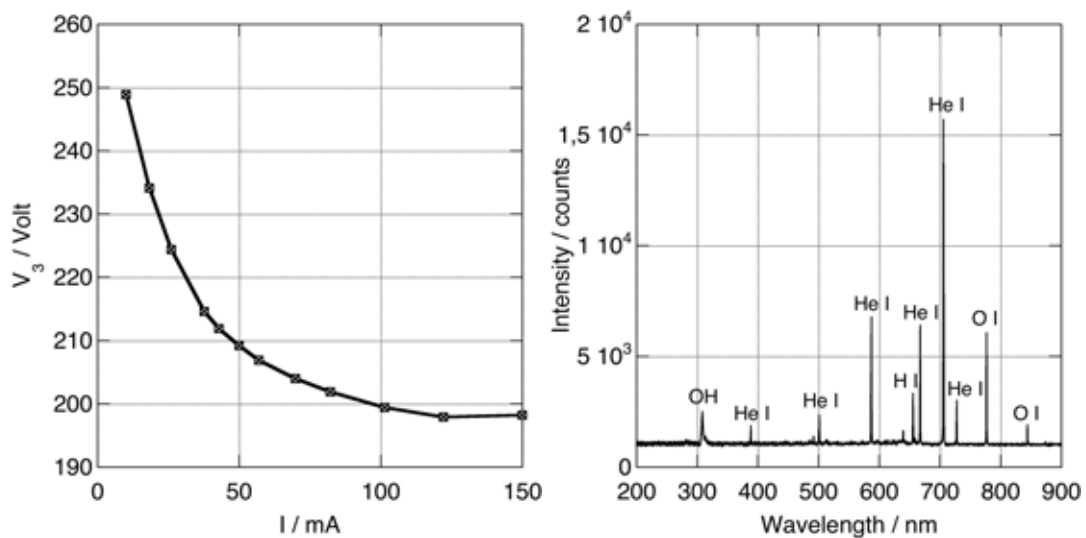
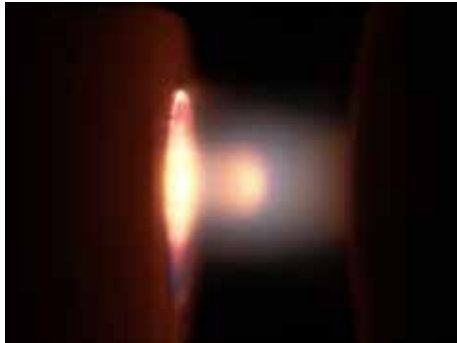


Figure A.51: I-V diagram (Tab.A.114) and spectrum (integration time: 100ms)

I-V diagram for  $D_3 = 2.1\text{mm}$ ,  $l_3 = 1.95\text{mm}$  and  $p_3 = 1200\text{ hPa}$



Gas: helium  
 Electrodes: copper  
 Shielding:  $Al_2O_3$

$p_3$ in hPa	$I_3$ in mA	$D_3$ in mm	$l_3$ in mm
1200	70	2.1	1.95

The current  $I_3$  was determined when the cathode was full covered with negative glow. The estimated error is  $\pm 10\text{ mA}$ .

$$I_3 = 70.0\text{ mA} \quad \frac{j_3}{p_3^2} = 14.0 \frac{\text{nA}}{\text{hPa}^2 \cdot \text{mm}^2} \quad T_3 = 920\text{ K} \quad (\text{A.50})$$

The spectrum was taken at  $I_3 = 70.0\text{ mA}$  and a power consumption of  $P_3 = 13.9\text{ W}$ .

Resolution:	6nm	Baseline correction:	6.9	Multiplication:	18
Temperature:	920K	Wavelength correction:	-5.5nm	Doppler broad.:	yes

Table A.52: Lifbase 2.0 settings for  $p_3 = 1200\text{ hPa}$  and  $T = 920\text{ K}$  ( $P_3 = 13.9\text{ W}$ )

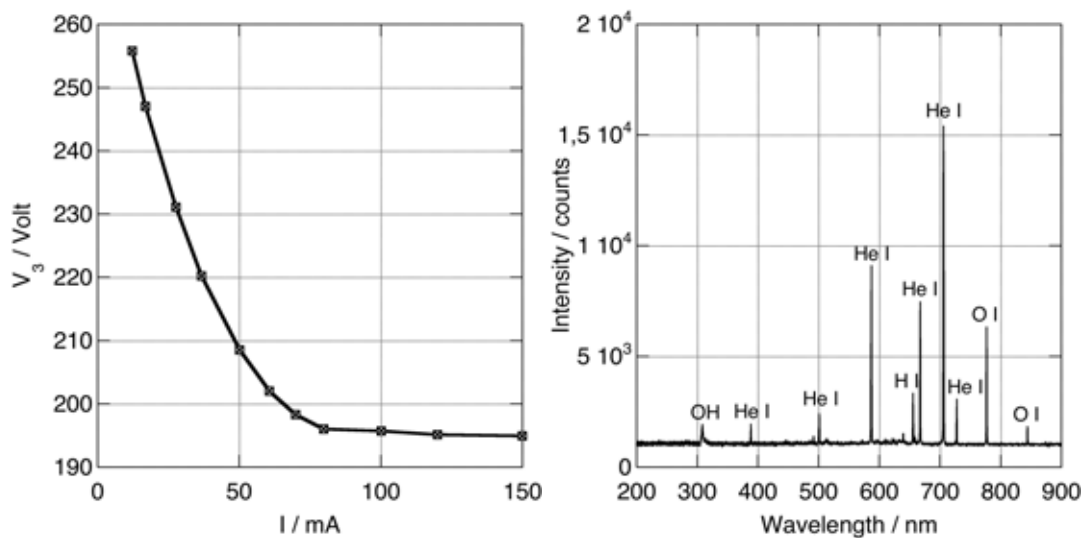
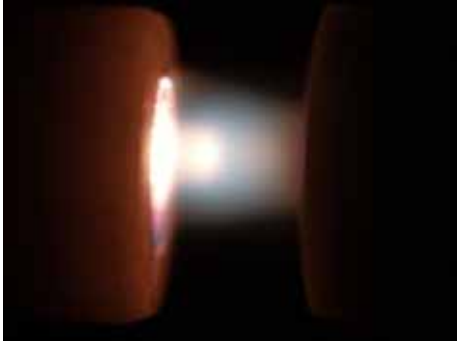


Figure A.52: I-V diagram (Tab.A.115) and spectrum (integration time: 100ms)

**I-V diagram for  $D_3 = 2.1\text{mm}$ ,  $l_3 = 1.95\text{mm}$  and  $p_3 = 1300\text{ hPa}$**



Gas: helium  
Electrodes: copper  
Shielding:  $Al_2O_3$

$p_3$ in hPa	$I_3$ in mA	$D_3$ in mm	$l_3$ in mm
1300	80	2.1	1.95

The current  $I_3$  was determined when the cathode was full covered with negative glow. The estimated error is  $\pm 10\text{ mA}$ .

$$I_3 = 80.0\text{ mA} \quad \frac{j_3}{p_3^2} = 13.7 \frac{\text{nA}}{\text{hPa}^2 \cdot \text{mm}^2} \quad T_3 = 750\text{ K} \quad (\text{A.51})$$

The spectrum was taken at  $I_3 = 80.0\text{ mA}$  and a power consumption of  $P_3 = 15.8\text{ W}$ .

Resolution:	8nm	Baseline correction:	5.8	Multiplication:	16.2
Temperature:	750K	Wavelength correction:	-4nm	Doppler broad.:	yes

Table A.53: Lifbase 2.0 settings for  $p_3 = 1300\text{ hPa}$  and  $T = 750\text{ K}$  ( $P_3 = 15.8\text{ W}$ )

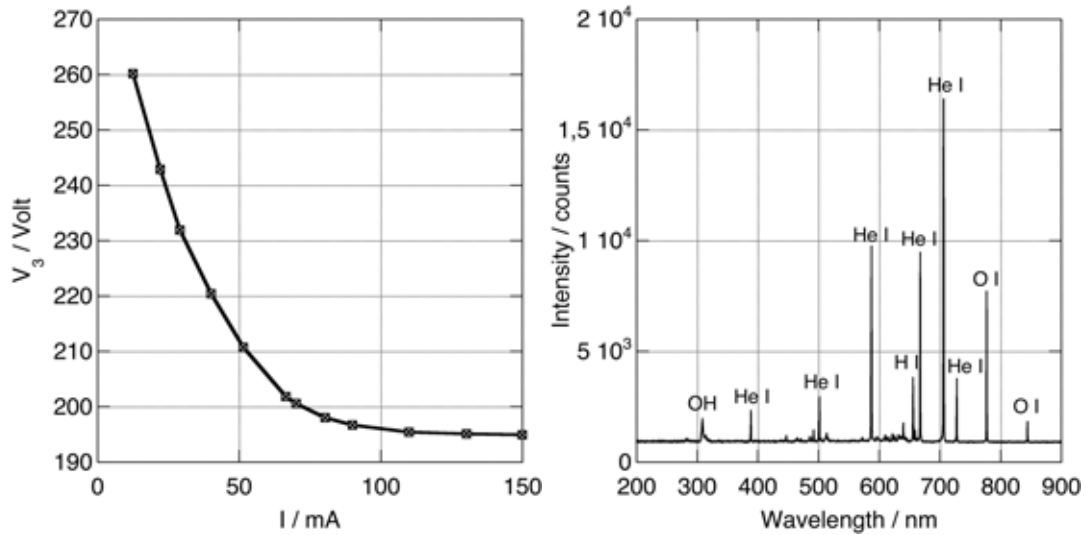
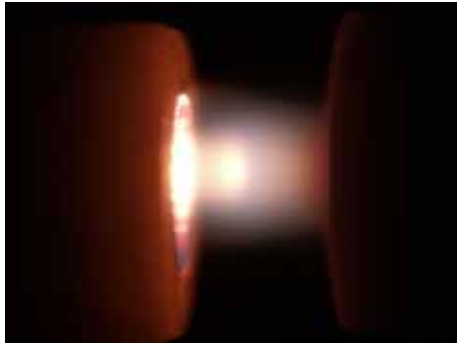


Figure A.53: I-V diagram (Tab.A.116) and spectrum (integration time: 50ms)

**I-V diagram for  $D_3 = 2.1\text{mm}$ ,  $l_3 = 1.95\text{mm}$  and  $p_3 = 1400\text{ hPa}$**



Gas: helium  
 Electrodes: copper  
 Shielding:  $Al_2O_3$

$p_3$ in hPa	$I_3$ in mA	$D_3$ in mm	$l_3$ in mm
1400	110	2.1	1.95

The current  $I_3$  was determined when the cathode was full covered with negative glow. The estimated error is  $\pm 20\text{ mA}$ .

$$I_3 = 110.0\text{ mA} \quad \frac{j_3}{p_3^2} = 16.2 \frac{\text{nA}}{\text{hPa}^2 \cdot \text{mm}^2} \quad T_3 = 1050\text{ K} \quad (\text{A.52})$$

The spectrum was taken at  $I_3 = 110.0\text{ mA}$  and a power consumption of  $P_3 = 22.0\text{ W}$ .

Resolution:	8nm	Baseline correction:	6.2	Multiplication:	19
Temperature:	1050K	Wavelength correction:	-4.5nm	Doppler broad.:	yes

Table A.54: Lifbase 2.0 settings for  $p_3 = 1400\text{ hPa}$  and  $T = 1050\text{ K}$  ( $P_3 = 22.0\text{ W}$ )

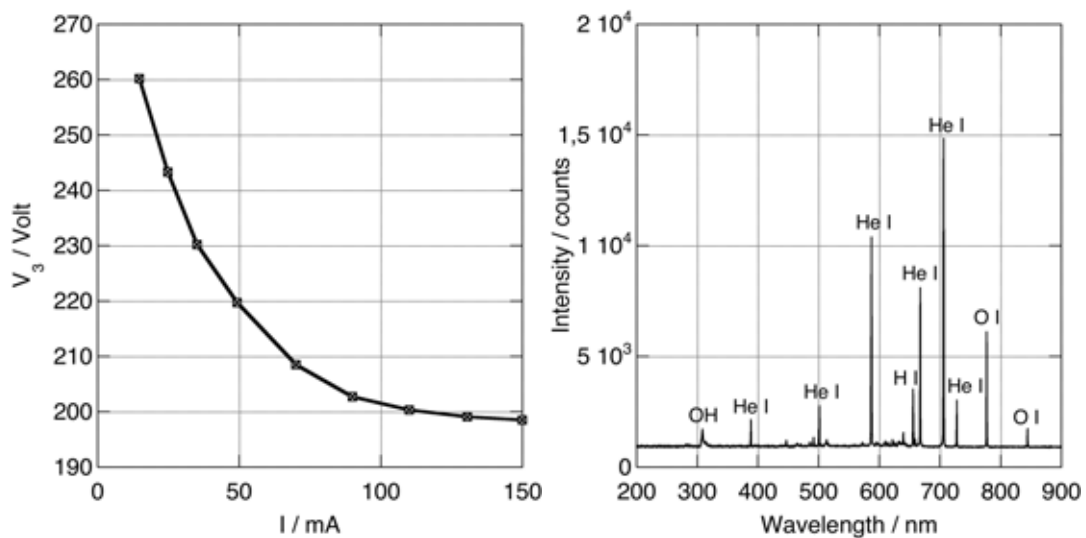
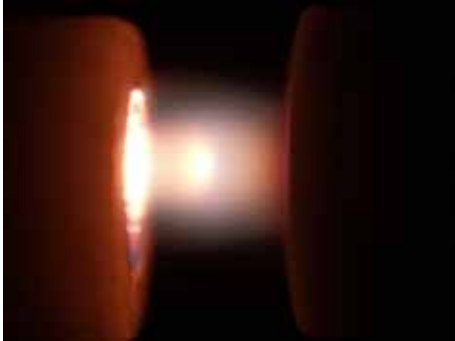


Figure A.54: I-V diagram (Tab.A.117) and spectrum (integration time: 50ms)

**I-V diagram for  $D_3 = 2.1\text{mm}$ ,  $l_3 = 1.95\text{mm}$  and  $p_3 = 1500\text{ hPa}$**



Gas: helium  
Electrodes: copper  
Shielding:  $Al_2O_3$

$p_3$ in hPa	$I_3$ in mA	$D_3$ in mm	$l_3$ in mm
1500	150	2.1	1.95

The current  $I_3$  was determined when the cathode was full covered with negative glow. The estimated error is  $\pm 10\text{ mA}$ .

$$I_3 = 150.0\text{ mA} \quad \frac{j_3}{p_3^2} = 19.2 \frac{\text{nA}}{\text{hPa}^2 \cdot \text{mm}^2} \quad T_3 = 1050\text{ K} \quad (\text{A.53})$$

The spectrum was taken at  $I_3 = 150.0\text{ mA}$  and a power consumption of  $P_3 = 29.9\text{ W}$ .

Resolution:	8nm	Baseline correction:	6.5	Multiplication:	19.2
Temperature:	1050K	Wavelength correction:	-5nm	Doppler broad.:	yes

Table A.55: Lifbase 2.0 settings for  $p_3 = 1500\text{ hPa}$  and  $T = 1050\text{ K}$  ( $P_3 = 29.9\text{ W}$ )

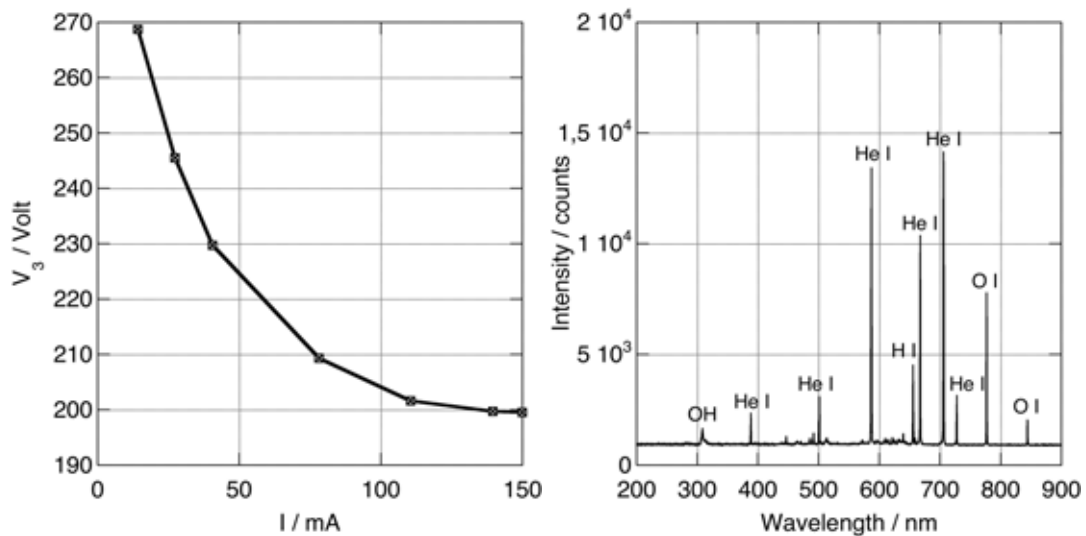
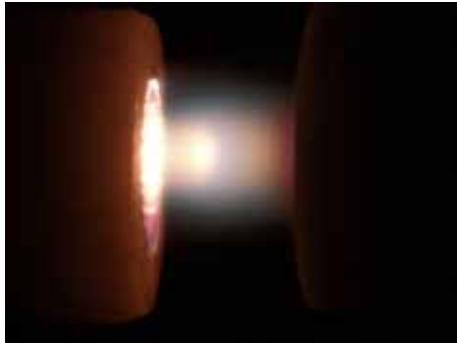


Figure A.55: I-V diagram (Tab.A.118) and spectrum (integration time: 50ms)

I-V diagram for  $D_3 = 2.1\text{mm}$ ,  $l_3 = 1.95\text{mm}$  and  $p_3 = 1600\text{ hPa}$



Gas: helium  
 Electrodes: copper  
 Shielding:  $Al_2O_3$

$p_3$ in hPa	$I_3$ in mA	$D_3$ in mm	$l_3$ in mm
1600	150	2.1	1.95

The current  $I_3$  was determined when the cathode was full covered with negative glow. The estimated error is  $\pm -\text{mA}$ .

$$I_3 = -\text{mA} \quad \frac{j_3}{p_3^2} = -\frac{nA}{\text{hPa}^2 \cdot \text{mm}^2} \quad T_3 = 1050\text{ K} \quad (\text{A.54})$$

The spectrum was taken at  $I_3 = 150.0\text{ mA}$  and a power consumption of  $P_3 = 29.9\text{ W}$ .

Resolution:	8nm	Baseline correction:	6.9	Multiplication:	22
Temperature:	1050K	Wavelength correction:	-4.5nm	Doppler broad.:	yes

Table A.56: Lifbase 2.0 settings for  $p_3 = 1600\text{ hPa}$  and  $T = 1050\text{ K}$  ( $P_3 = 29.9\text{ W}$ )

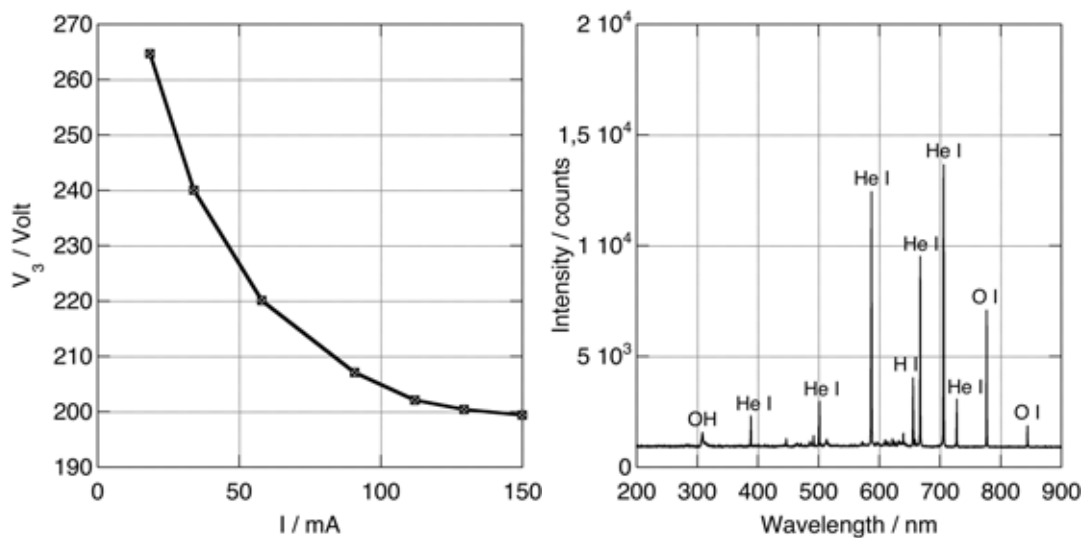


Figure A.56: I-V diagram (Tab.A.119) and spectrum (integration time: 50ms)

## A.2.2 Comparison of similar DC glow discharges (I-V)

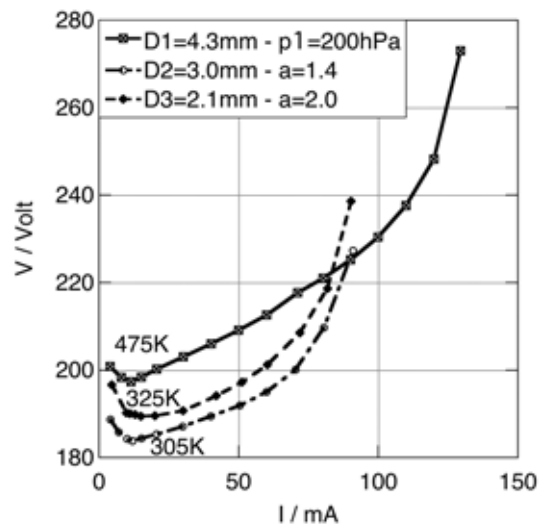


Figure A.57: Comparison of three similar discharges:  $p_1 = 200 \text{ hPa}$  (Fig.A.30, Fig.A.39 and Fig.A.48)

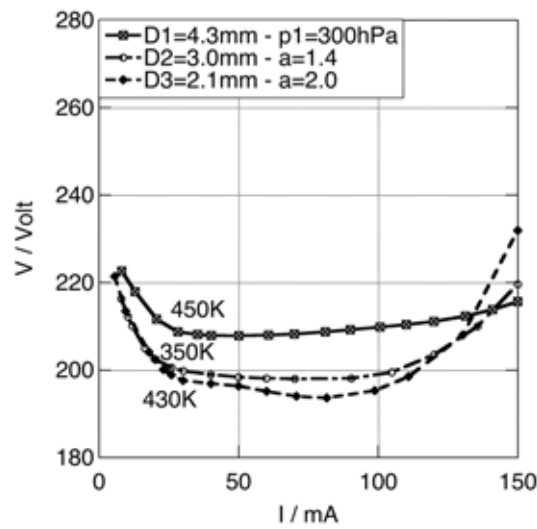


Figure A.58: Comparison of three similar discharges:  $p_1 = 300 \text{ hPa}$  (Fig.A.31, Fig.A.40 and Fig.A.49)

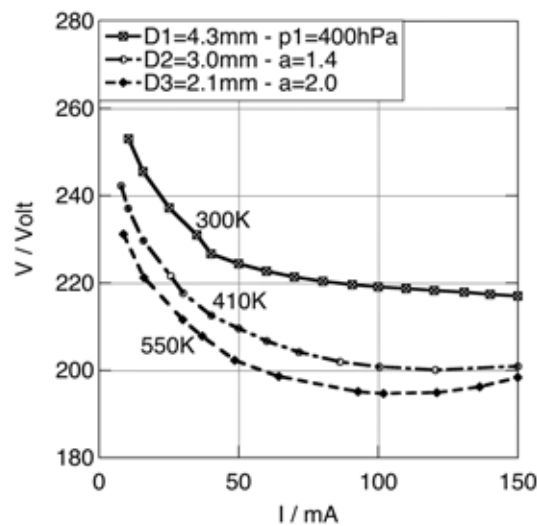


Figure A.59: Comparison of three similar discharges:  $p_1 = 400 \text{ hPa}$  (Fig.A.32, Fig.A.41 and Fig.A.50)

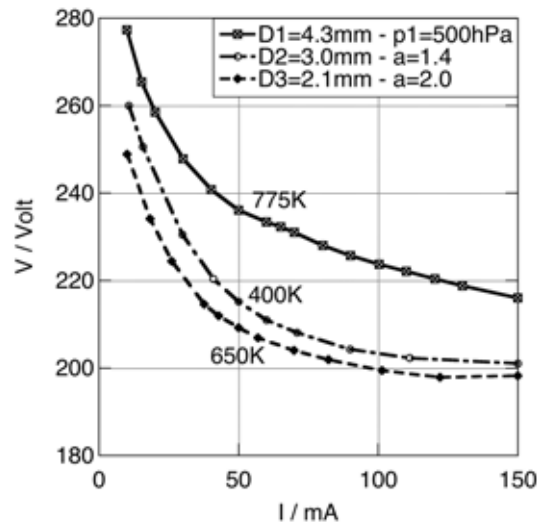


Figure A.60: Comparison of three similar discharges:  $p_1 = 500 \text{ hPa}$  (Fig.A.33, Fig.A.42 and Fig.A.51)

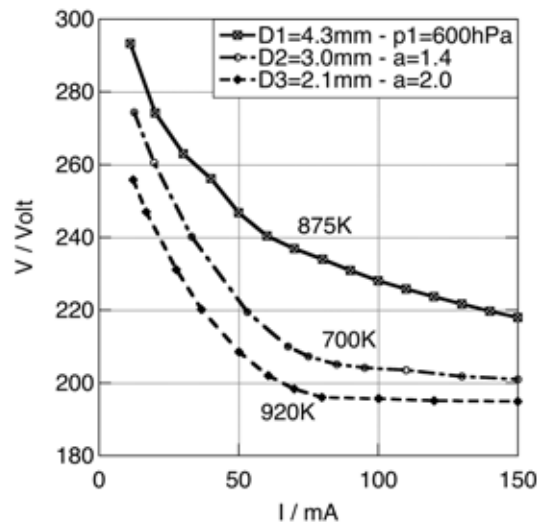


Figure A.61: Comparison of three similar discharges:  $p_1 = 600 \text{ hPa}$  (Fig.A.34, Fig.A.43 and Fig.A.52)

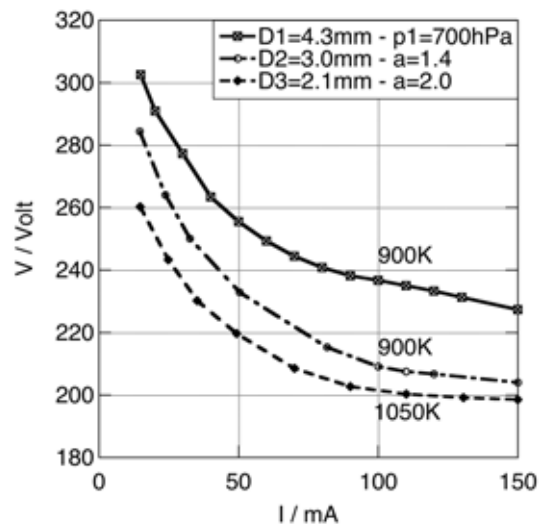


Figure A.62: Comparison of three similar discharges:  $p_1 = 700 \text{ hPa}$  (Fig.A.35, Fig.A.44 and Fig.A.54)

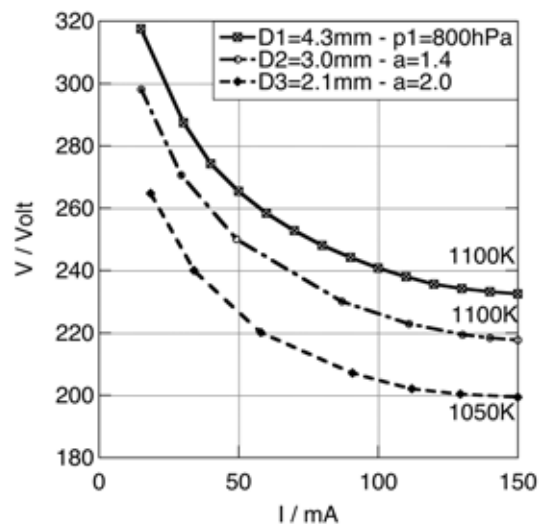


Figure A.63: Comparison of three similar discharges:  $p_1 = 800 \text{ hPa}$  (Fig.A.36, Fig.A.45 and Fig.A.56)

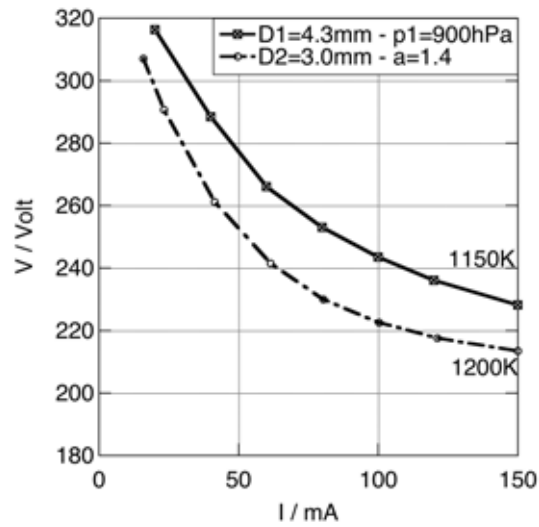


Figure A.64: Comparison of two similar discharges:  $p_1 = 900 \text{ hPa}$  (Fig.A.37 and Fig.A.46)

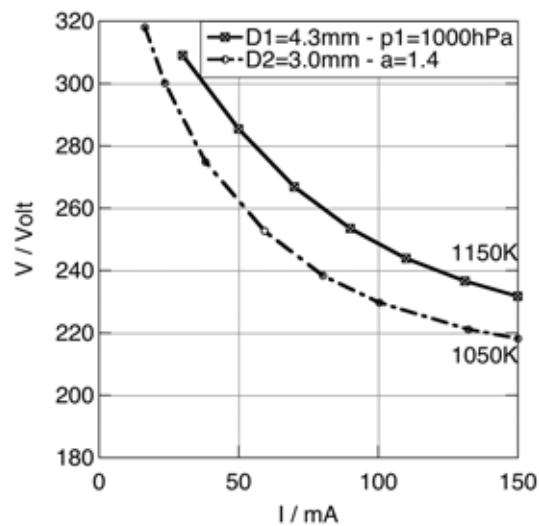


Figure A.65: Comparison of two similar discharges:  $p_1 = 1000 \text{ hPa}$  (Fig.A.37 and Fig.A.47)

**A.3 Measurement-tables for Sec.3.1, Sec.A.1 and Sec.A.2****A.3.1 Tables for Sec.3.1 - Investigations on breakdown voltages**

Table A.57: Raw-data for Fig.3.4 in Sec.3.1.1

$pd$ in $hPa\ mm$	$V_i$ in Volt
91.52	239.00
140.80	266.00
227.92	300.00
256.96	313.00
440.00	354.00
882.64	436.00
1764.40	565.00
2640.00	681.00
3581.60	799.00
4400.00	893.00
5306.40	987.00
6177.60	1070.00
7066.40	1154.00
7928.80	1242.00
8800.00	1326.00
9680.00	1399.00
10560.00	1480.00
11440.00	1567.00
12320.00	1641.00
13200.00	1723.00
14080.00	1802.00

Table A.58: Raw-data for Fig.3.5 in Sec.3.1.2 ( $p = 50 \text{ hPa}$ )

$pd$ in $hPa \text{ mm}$	$V_i$ in Volt
61.68	180.00
86.35	188.00
111.02	198.00
135.69	208.00
160.36	218.00
185.03	228.00
209.70	236.00
234.37	248.00
259.05	258.00
283.72	268.00
308.39	278.00
333.06	288.00
357.73	298.00
382.40	306.00
392.27	310.00

Table A.59: Raw-data for Fig.3.5 in Sec.3.1.2 ( $p = 200 \text{ hPa}$ )

$pd$ in $hPa \text{ mm}$	$V_i$ in Volt
182.00	49.34
228.00	148.03
270.00	246.71
444.08	345.39
542.76	309.00
641.45	329.00
740.13	347.00
838.82	363.00
937.50	383.00
1036.20	400.00
1134.90	420.00
1233.60	439.00
1332.20	457.00
1430.90	477.00
1529.60	495.00
1569.10	514.00

Table A.60: Raw-data for Fig.3.5 in Sec.3.1.2 ( $p = 800 \text{ hPa}$ )

$pd$ in $hPa \text{ mm}$	$V_i$ in Volt
197.37	245.00
592.11	350.00
986.84	416.00
1381.60	489.00
1776.30	565.00
2171.10	636.00
2565.80	714.00
2960.50	785.00
3355.30	856.00
3750.00	932.00
4144.70	1006.00
4539.50	1075.00
4934.20	1136.00
5328.90	1189.00
5723.70	1232.00
6118.40	1275.00
6276.30	1290.00

Table A.61: Raw-data for Fig.3.5 in Sec.3.1.2 ( $p = 1600 \text{ hPa}$ )

$pd$ in $hPa \text{ mm}$	$V_i$ in Volt
394.74	285.00
1184.20	430.00
1973.70	588.00
2763.20	722.00
3552.60	865.00
4342.10	1011.00
5131.60	1155.00
5921.10	1298.00
6710.50	1437.00
7500.00	1570.00
8289.50	1644.00
9078.90	1728.00
9868.40	1796.00
10658.00	1868.00
11447.00	1937.00
12237.00	1977.00
12553.00	1985.00

Table A.62: Raw-data for Fig.3.6 in Sec.3.1.2 ( $p = 200 \text{ hPa}$ )

$pd$ in $hPa \text{ mm}$	$V_i$ in Volt
98.68	170.00
148.03	193.00
197.37	218.00
246.71	242.00
296.05	264.00
345.39	282.00
394.74	297.00
444.08	306.00
493.42	321.00
542.76	330.00
592.11	341.00
641.45	346.00
690.79	352.00
740.13	362.00
789.47	369.00
838.82	375.00
888.16	380.00
937.50	388.00
986.84	393.00
1036.20	399.00
1085.50	407.00
1134.90	414.00
1184.20	420.00
1233.60	427.00
1282.90	434.00
1332.20	441.00
1381.60	448.00
1430.90	454.00
1480.30	461.00

Table A.63: Raw-data for Fig.3.6 in Sec.3.1.2 ( $p = 800 \text{ hPa}$ )

$pd$ in $hPa \text{ mm}$	$V_i$ in Volt
394.74	329.00
592.11	372.00
789.47	405.00
986.84	433.00
1184.20	467.00
1381.60	497.00
1578.90	531.00
1776.30	564.00
1973.70	600.00
2171.10	635.00
2368.40	670.00
2565.80	706.00
2763.20	739.00
2960.50	772.00
3157.90	805.00
3355.30	842.00
3552.60	875.00
3750.00	908.00
3947.40	946.00
4144.70	988.00
4342.10	1018.00
4539.50	1049.00
4736.80	1083.00
4934.20	1109.00
5131.60	1138.00
5328.90	1162.00
5526.30	1187.00
5723.70	1208.00
5921.10	1231.00

Table A.64: Raw-data for Fig.3.6 in Sec.3.1.2 ( $p = 1400 \text{ hPa}$ )

$pd$ in $hPa mm$	$V_i$ in Volt
690.79	371.00
1036.20	430.00
1381.60	495.00
1727.00	550.00
2072.40	608.00
2417.80	672.00
2763.20	736.00
3108.60	796.00
3453.90	860.00
3799.30	922.00
4144.70	983.00
4490.10	1044.00
4835.50	1106.00
5180.90	1164.00
5526.30	1224.00
5871.70	1282.00
6217.10	1340.00
6562.50	1396.00
6907.90	1440.00
7253.30	1490.00
7598.70	1535.00
7944.10	1568.00
8289.50	1602.00
8634.90	1622.00
8980.30	1649.00
9325.70	1680.00
9671.10	1699.00
10016.00	1726.00
10362.00	1748.00

Table A.65: Raw-data for Fig.3.6 in Sec.3.1.2 ( $p = 2000 \text{ hPa}$ )

$pd$ in $hPa \text{ mm}$	$V_i$ in Volt
986.84	415.00
1480.30	499.00
1973.70	583.00
2467.10	670.00
2960.50	755.00
3453.90	847.00
3947.40	932.00
4440.80	1015.00
4934.20	1105.00
5427.60	1189.00
5921.10	1270.00
6414.50	1355.00
6907.90	1443.00
7401.30	1520.00
7894.70	1602.00
8388.20	1680.00
8881.60	1744.00
9375.00	1796.00
9868.40	1844.00
10362.00	1886.00
10855.00	1923.00
11349.00	1962.00
11842.00	1996.00



## A.3.2 Tables for Sec.A.1 - Reduced field strength in the positive column

Table A.66: Raw-data for Fig.A.3 in Sec.A.1.1 ( $1' \equiv 0.05 \text{ mm}$ )

$d$ in $1'$	$d$ in mm	$V_1$ in Volt
8	0.40	149.30
11	0.55	160.70
15	0.75	167.00
20	1.00	169.70
30	1.50	175.60
45	2.25	185.60
60	3.00	196.20
75	3.75	206.80
90	4.50	217.40
105	5.25	227.90
119	5.95	237.90

Table A.67: Raw-data for Fig.A.4 in Sec.A.1.1 ( $1' \equiv 0.05 \text{ mm}$ )

$d$ in $1'$	$d$ in mm	$V_1$ in Volt
8	0.40	148.40
11	0.55	154.10
15	0.75	156.80
20	1.00	160.40
30	1.50	168.80
45	2.25	182.90
60	3.00	197.00
75	3.75	211.50
90	4.50	226.40
105	5.25	240.40
119	5.95	253.40

Table A.68: Raw-data for Fig.A.5 in Sec.A.1.1 ( $1' \equiv 0.05 \text{ mm}$ )

$d$ in $1'$	$d$ in mm	$V_1$ in Volt
8	0.40	150.00
11	0.55	153.40
15	0.75	158.50
20	1.00	166.60
30	1.50	178.50
45	2.25	198.30
60	3.00	218.80
75	3.75	235.20
90	4.50	252.40
105	5.25	270.60
119	5.95	286.90

Table A.69: Raw-data for Fig.A.6 in Sec.A.1.1 ( $1' \equiv 0.05 \text{ mm}$ )

$d$ in $1'$	$d$ in mm	$V_1$ in Volt
3	0.15	127.70
8	0.40	152.10
11	0.55	155.60
15	0.75	160.20
20	1.00	166.80
30	1.50	181.80
45	2.25	206.20
60	3.00	225.40
75	3.75	246.30
90	4.50	268.40
105	5.25	287.50
119	5.95	305.10

Table A.70: Raw-data for Fig.A.7 in Sec.A.1.1 ( $1' \equiv 0.05 \text{ mm}$ )

$d$ in $1'$	$d$ in mm	$V_1$ in Volt
8	0.40	150.00
11	0.55	152.20
15	0.75	157.70
20	1.00	168.60
30	1.50	189.00
45	2.25	213.40
60	3.00	237.40
75	3.75	260.80
90	4.50	283.60
105	5.25	307.10
119	5.95	327.00

Table A.71: Raw-data for Fig.A.8 in Sec.A.1.1 ( $1' \equiv 0.05 \text{ mm}$ )

$d$ in $1'$	$d$ in mm	$V_1$ in Volt
8	0.40	152.00
11	0.55	154.60
15	0.75	164.00
20	1.00	175.10
30	1.50	197.40
45	2.25	221.40
60	3.00	248.50
75	3.75	272.80
90	4.50	300.00
105	5.25	323.70
119	5.95	346.00

Table A.72: Raw-data for Fig.A.9 in Sec.A.1.1 ( $1' \equiv 0.05 \text{ mm}$ )

$d$ in $1'$	$d$ in mm	$V_1$ in Volt
8	0.40	151.50
11	0.55	155.00
15	0.75	164.80
20	1.00	178.40
30	1.50	199.10
45	2.25	228.90
60	3.00	256.30
75	3.75	285.20
90	4.50	313.30
105	5.25	338.00
119	5.95	363.00

Table A.73: Raw-data for Fig.A.10 in Sec.A.1.1 ( $1' \equiv 0.05 \text{ mm}$ )

$d$ in $1'$	$d$ in mm	$V_1$ in Volt
8	0.40	150.20
11	0.55	153.70
15	0.75	163.00
20	1.00	178.50
30	1.50	199.40
45	2.25	234.00
60	3.00	263.90
75	3.75	298.00
90	4.50	325.50
105	5.25	352.00
119	5.95	379.00

Table A.74: Raw-data for Fig.A.11 in Sec.A.1.1 ( $1' \equiv 0.05 \text{ mm}$ )

$d$ in $1'$	$d$ in mm	$V_1$ in Volt
8	0.40	148.80
11	0.55	152.40
15	0.75	162.30
20	1.00	178.50
30	1.50	200.70
45	2.25	238.40
60	3.00	277.00
75	3.75	308.70
90	4.50	337.00
105	5.25	367.00
119	5.95	397.00

Table A.75: Raw-data for Fig.A.12 in Sec.A.1.1 ( $1' \equiv 0.05 \text{ mm}$ )

$d$ in $1'$	$d$ in mm	$V_2$ in Volt
1	0.05	163.60
2	0.10	149.30
3	0.15	136.70
4	0.20	134.60
5	0.25	134.00
6	0.30	134.00
7	0.35	140.00
8	0.40	147.70
9	0.45	152.50
10	0.50	154.90
14	0.70	157.80
18	0.90	160.70
22	1.10	163.50
23	1.15	163.50
25	1.25	164.40
30	1.50	168.30
45	2.25	181.70
60	3.00	196.90
75	3.75	211.30
90	4.50	225.60
105	5.25	239.60
120	6.00	253.00
122	6.12	255.20

Table A.76: Raw-data for Fig.A.13 in Sec.A.1.1 ( $1' \equiv 0.05 \text{ mm}$ )

$d$ in $1'$	$d$ in mm	$V_2$ in Volt
1	0.05	133.60
3	0.15	123.60
5	0.25	127.50
7	0.35	143.00
10	0.50	148.20
15	0.75	153.20
20	1.00	158.70
24	1.20	160.10
30	1.50	167.30
45	2.25	187.40
60	3.00	207.50
75	3.75	227.20
90	4.50	245.80
105	5.25	263.80
120	6.00	281.10
122	6.12	284.00

Table A.77: Raw-data for Fig.A.14 in Sec.A.1.1 ( $1' \equiv 0.05 \text{ mm}$ )

$d$ in $1'$	$d$ in mm	$V_2$ in Volt
1	0.05	126.50
2	0.10	122.10
3	0.15	121.30
4	0.20	128.50
5	0.25	137.20
10	0.50	148.70
15	0.75	153.10
30	1.50	175.00
45	2.25	202.60
60	3.00	227.00
75	3.75	250.40
90	4.50	273.80
105	5.25	295.20
120	6.00	316.50
122	6.12	320.10

Table A.78: Raw-data for Fig.A.15 in Sec.A.1.1 ( $1' \equiv 0.05 \text{ mm}$ )

$d$ in $1'$	$d$ in mm	$V_2$ in Volt
1	0.05	122.50
3	0.15	128.50
7	0.35	148.70
10	0.50	152.30
15	0.75	156.00
30	1.50	188.10
45	2.25	214.80
60	3.00	248.10
75	3.75	273.90
90	4.50	298.90
105	5.25	322.90
120	6.00	346.00
122	6.12	350.00

Table A.79: Raw-data for Fig.A.16 in Sec.A.1.1 ( $1' \equiv 0.05 \text{ mm}$ )

$d$ in $1'$	$d$ in mm	$V_2$ in Volt
1	0.05	116.20
3	0.15	131.40
7	0.35	145.40
15	0.75	152.50
30	1.50	187.90
45	2.25	223.10
60	3.00	256.20
75	3.75	291.00
90	4.50	319.30
105	5.25	346.00
120	6.00	372.00
122	6.12	377.00

Table A.80: Raw-data for Fig.A.17 in Sec.A.1.1 ( $1' \equiv 0.05 \text{ mm}$ )

$d$ in $1'$	$d$ in mm	$V_2$ in Volt
1	0.05	118.20
3	0.15	141.40
10	0.50	151.90
15	0.75	162.10
30	1.50	199.20
45	2.25	237.00
60	3.00	273.50
75	3.75	306.30
90	4.50	335.00
105	5.25	365.00
120	6.00	394.00
122	6.12	400.00

Table A.81: Raw-data for Fig.A.18 in Sec.A.1.1 ( $1' \equiv 0.05 \text{ mm}$ )

$d$ in $1'$	$d$ in mm	$V_2$ in Volt
1	0.05	121.00
4	0.20	144.60
10	0.50	152.60
15	0.75	166.90
30	1.50	206.70
45	2.25	243.50
60	3.00	284.90
75	3.75	318.50
90	4.50	351.00
105	5.25	383.00
120	6.00	414.00
122	6.12	420.00

Table A.82: Raw-data for Fig.A.19 in Sec.A.1.1 ( $1' \equiv 0.05 \text{ mm}$ )

$d$ in $1'$	$d$ in mm	$V_2$ in Volt
1	0.05	117.00
3	0.15	136.60
7	0.35	146.00
15	0.75	164.60
30	1.50	207.80
45	2.25	250.10
60	3.00	296.40
75	3.75	333.00
90	4.50	367.00

Table A.83: Raw-data for Fig.A.20 in Sec.A.1.1 ( $1' \equiv 0.05 \text{ mm}$ )

$d$ in $1'$	$d$ in mm	$V_2$ in Volt
1	0.05	116.60
3	0.15	137.10
7	0.35	145.10
15	0.75	164.60
30	1.50	210.40
45	2.25	257.80
60	3.00	305.60
75	3.75	343.00
90	4.50	381.00

Table A.84: Raw-data for Fig.A.21 in Sec.A.1.1 ( $1' \equiv 0.05 \text{ mm}$ )

$d$ in $1'$	$d$ in mm	$V_3$ in Volt
2	0.10	178.20
5	0.25	135.30
6	0.30	137.70
8	0.40	141.00
10	0.50	154.60
15	0.75	159.80
25	1.25	168.10
35	1.75	182.10
45	2.25	194.40
55	2.75	207.40
65	3.25	220.10
75	3.75	232.90
85	4.25	243.20
95	4.75	254.40
105	5.25	265.10
115	5.75	275.70
125	6.25	286.80
131	6.55	293.40

Table A.85: Raw-data for Fig.A.22 in Sec.A.1.1 ( $1' \equiv 0.05 \text{ mm}$ )

$d$ in $1'$	$d$ in mm	$V_3$ in Volt
2	0.10	145.40
5	0.25	121.30
7	0.35	136.70
10	0.50	147.10
15	0.75	151.30
25	1.25	164.40
35	1.75	185.20
45	2.25	204.70
55	2.75	221.30
65	3.25	238.00
75	3.75	252.10
85	4.25	266.30
95	4.75	281.20
105	5.25	295.70
115	5.75	308.70
125	6.25	313.30
131	6.55	332.00

Table A.86: Raw-data for Fig.A.23 in Sec.A.1.1 ( $1' \equiv 0.05 \text{ mm}$ )

$d$ in $1'$	$d$ in mm	$V_3$ in Volt
2	0.10	119.50
5	0.25	118.50
7	0.35	141.30
10	0.50	145.90
13	0.65	150.20
25	1.25	165.60
35	1.75	193.60
45	2.25	213.80
55	2.75	234.10
65	3.25	255.60
75	3.75	275.00
85	4.25	291.30
95	4.75	310.80
105	5.25	328.00
115	5.75	345.00
125	6.25	363.00
131	6.55	373.00

Table A.87: Raw-data for Fig.A.24 in Sec.A.1.1 ( $1' \equiv 0.05 \text{ mm}$ )

$d$ in $1'$	$d$ in mm	$V_3$ in Volt
2	0.10	128.20
5	0.25	132.10
10	0.50	146.70
15	0.75	150.20
25	1.25	170.30
35	1.75	196.90
45	2.25	222.60
55	2.75	245.90
65	3.25	269.40
75	3.75	291.60
85	4.25	311.40
95	4.75	333.00
105	5.25	354.00
115	5.75	373.00
125	6.25	394.00
131	6.55	406.00

Table A.88: Raw-data for Fig.A.25 in Sec.A.1.1 ( $1' \equiv 0.05 \text{ mm}$ )

$d$ in $1'$	$d$ in mm	$V_3$ in Volt
2	0.10	119.20
5	0.25	131.10
10	0.50	148.90
15	0.75	160.50
20	1.00	179.70
25	1.25	189.30
30	1.50	203.10
40	2.00	232.80
50	2.50	257.00
60	3.00	281.30
70	3.50	302.40
80	4.00	326.00
90	4.50	348.00
100	5.00	370.00
110	5.50	393.00
120	6.00	415.00

Table A.89: Raw-data for Fig.A.26 in Sec.A.1.1 ( $1' \equiv 0.05 \text{ mm}$ )

$d$ in $1'$	$d$ in mm	$V_3$ in Volt
2	0.10	145.70
5	0.25	145.30
10	0.50	149.80
15	0.75	162.50
25	1.25	190.10
35	1.75	222.50
45	2.25	248.30
55	2.75	275.00
65	3.25	300.00
75	3.75	323.40
85	4.25	346.00
95	4.75	371.00
105	5.25	394.00
110	5.50	407.00

Table A.90: Raw-data for Fig.A.27 in Sec.A.1.1 ( $1' \equiv 0.05 \text{ mm}$ )

$d$ in $1'$	$d$ in mm	$V_3$ in Volt
2	0.10	144.60
5	0.25	145.10
10	0.50	147.70
15	0.75	178.50
25	1.25	195.10
35	1.75	226.60
45	2.25	255.00
55	2.75	280.70
65	3.25	306.70
75	3.75	331.00
85	4.25	355.00
95	4.75	381.00
105	5.25	405.00

Table A.91: Raw-data for Fig.A.28 in Sec.A.1.1 ( $1' \equiv 0.05 \text{ mm}$ )

$d$ in $1'$	$d$ in mm	$V_3$ in Volt
2	0.10	146.10
5	0.25	145.70
10	0.50	147.90
15	0.75	164.80
25	1.25	196.10
35	1.75	228.80
45	2.25	257.90
55	2.75	284.90
65	3.25	312.20
75	3.75	338.00
85	4.25	363.00
95	4.75	390.00

Table A.92: Raw-data for Fig.A.29 in Sec.A.1.1 ( $1' \equiv 0.05 \text{ mm}$ )

$d$ in $1'$	$d$ in mm	$V_3$ in Volt
2	0.10	118.80
5	0.25	140.20
10	0.50	148.00
15	0.75	170.50
25	1.25	202.90
35	1.75	234.20
45	2.25	267.20
55	2.75	293.50
65	3.25	322.80
75	3.75	349.00
85	4.25	375.00
95	4.75	403.00

**A.3.3 Tables for Sec.A.2 - I-V characterisation of similar glow discharges**

Table A.93: Raw-data for Fig.A.30 in Sec.A.2.1

$I$ in $mA$	$V$ in Volt
4.00	200.80
8.00	198.30
11.50	197.30
15.20	198.40
20.70	200.20
30.20	203.00
40.20	206.00
50.00	209.10
60.10	212.60
71.20	217.70
80.30	221.00
90.10	225.20
100.00	230.40
110.00	237.60
120.00	248.20
129.50	273.00

Table A.94: Raw-data for Fig.A.31 in Sec.A.2.1

$I$ in $mA$	$V_1$ in Volt
8.20	222.60
13.00	217.90
20.70	211.60
28.30	208.70
35.34	208.10
40.20	207.90
50.10	207.80
60.80	208.00
70.00	208.20
81.10	208.70
90.00	209.20
100.70	209.80
110.10	210.40
120.00	211.10
131.30	212.30
141.00	213.80
150.00	215.60

Table A.95: Raw-data for Fig.A.32 in Sec.A.2.1

$I$ in $mA$	$V_1$ in Volt
10.60	253.00
15.80	245.50
25.20	237.20
35.10	231.00
40.10	226.70
50.00	224.40
60.00	222.70
70.00	221.40
80.20	220.40
90.70	219.60
100.00	219.10
110.00	218.70
120.10	218.30
130.80	217.90
140.10	217.40
150.00	217.00

Table A.96: Raw-data for Fig.A.33 in Sec.A.2.1

$I$ in $mA$	$V_1$ in Volt
10.00	277.30
15.30	265.40
20.20	258.50
30.10	247.80
40.20	240.80
50.00	236.10
60.00	233.40
65.10	232.30
70.00	231.00
80.20	228.00
90.10	225.70
100.40	223.70
110.10	222.10
120.30	220.40
130.20	218.80
150.00	216.00

Table A.97: Raw-data for Fig.A.34 in Sec.A.2.1

$I$ in $mA$	$V_1$ in Volt
11.23	293.30
20.20	274.20
30.20	263.00
40.10	256.10
50.00	246.80
60.20	240.40
70.00	236.90
80.10	234.00
90.00	230.90
100.00	228.10
110.00	225.80
120.00	223.70
130.00	221.70
140.00	219.70
150.00	218.00

Table A.98: Raw-data for Fig.A.35 in Sec.A.2.1

$I$ in $mA$	$V_1$ in Volt
14.96	302.50
20.16	290.90
30.00	277.30
40.00	263.40
50.00	255.50
60.00	249.30
70.00	244.40
80.00	240.80
90.00	238.20
100.00	236.70
110.00	235.00
120.00	233.30
130.00	231.30
150.00	227.30

Table A.99: Raw-data for Fig.A.36 in Sec.A.2.1

$I$ in $mA$	$V_1$ in Volt
15.00	317.50
30.30	287.40
40.00	274.30
50.00	265.40
60.00	258.40
70.00	252.80
80.00	248.10
90.10	244.20
100.00	240.80
110.00	238.00
120.00	235.60
130.00	234.20
140.00	233.20
150.00	232.50

Table A.100: Raw-data for Fig.A.37 in Sec.A.2.1

$I$ in $mA$	$V_1$ in Volt
20.10	316.30
40.00	288.40
60.00	266.00
80.00	253.00
100.00	243.50
120.00	236.10
150.00	228.20

Table A.101: Raw-data for Fig.A.38 in Sec.A.2.1

$I$ in $mA$	$V_1$ in Volt
30.00	309.00
50.00	285.40
70.00	266.80
90.00	253.50
110.00	243.90
131.10	236.60
150.00	231.70

Table A.102: Raw-data for Fig.A.39 in Sec.A.2.1

$I$ in $mA$	$V_2$ in Volt
4.05	188.70
7.10	185.80
10.10	184.30
12.00	183.80
15.20	184.40
20.63	185.30
30.00	187.10
40.00	189.40
50.50	191.90
60.00	195.00
70.40	200.10
80.60	209.70
91.00	227.30

Table A.103: Raw-data for Fig.A.40 in Sec.A.2.1

$I$ in $mA$	$V_2$ in Volt
8.00	216.30
10.30	212.20
11.90	210.10
16.47	205.00
20.32	202.40
26.00	200.60
30.20	199.80
40.00	199.00
50.00	198.40
60.00	198.10
70.20	198.00
90.40	198.10
104.90	199.50
120.10	203.50
135.60	210.00
150.00	219.60

Table A.104: Raw-data for Fig.A.41 in Sec.A.2.1

$I$ in $mA$	$V_2$ in Volt
7.90	242.30
10.40	237.10
15.90	229.70
25.70	221.60
30.10	217.70
40.20	212.60
50.00	209.60
60.10	206.70
71.60	204.20
86.30	202.00
100.50	200.80
120.50	200.10
150.00	200.90

Table A.105: Raw-data for Fig.A.42 in Sec.A.2.1

$I$ in $mA$	$V_2$ in Volt
10.70	260.00
15.70	250.60
29.90	230.50
41.00	220.40
50.00	215.20
60.00	211.00
70.90	208.10
89.90	204.30
111.30	202.30
150.00	201.00

Table A.106: Raw-data for Fig.A.43 in Sec.A.2.1

$I$ in $mA$	$V_2$ in Volt
12.60	274.40
19.70	260.60
33.20	240.20
53.10	219.50
67.70	210.00
75.00	207.30
85.20	205.10
95.20	204.20
110.00	203.50
130.00	201.80
150.00	201.00

Table A.107: Raw-data for Fig.A.44 in Sec.A.2.1

$I$ in $mA$	$V_2$ in Volt
14.60	284.40
23.80	264.00
32.60	250.10
50.40	232.90
81.70	215.30
100.00	209.10
110.00	207.50
120.00	206.70
150.00	204.00

Table A.108: Raw-data for Fig.A.45 in Sec.A.2.1

$I$ in $mA$	$V_2$ in Volt
15.10	298.10
29.40	270.60
49.20	250.10
87.00	230.10
111.00	222.90
130.20	219.40
140.00	218.40
150.00	217.70

Table A.109: Raw-data for Fig.A.46 in Sec.A.2.1

$I$ in $mA$	$V_2$ in Volt
15.90	307.00
23.30	290.70
41.40	261.20
61.50	241.50
80.40	230.00
100.40	222.50
121.20	217.60
150.00	213.50

Table A.110: Raw-data for Fig.A.47 in Sec.A.2.1

$I$ in $mA$	$V_2$ in Volt
16.40	318.00
23.60	300.10
38.10	274.90
59.30	252.70
80.20	238.40
100.50	229.70
132.30	221.10
150.00	218.20

Table A.111: Raw-data for Fig.A.48 in Sec.A.2.1

$I$ in $mA$	$V_3$ in Volt
4.60	196.60
9.80	190.20
11.10	190.00
13.00	189.80
15.03	189.40
20.10	189.50
30.10	190.70
42.00	194.10
51.20	197.20
60.30	201.20
72.00	208.50
81.90	218.60
90.30	238.60

Table A.112: Raw-data for Fig.A.49 in Sec.A.2.1

$I$ in $mA$	$V_3$ in Volt
5.65	221.40
9.59	213.50
17.91	204.10
20.05	202.40
23.10	200.10
26.00	198.90
30.14	197.60
40.10	196.90
50.00	196.30
60.10	195.10
70.80	194.00
81.60	193.60
98.80	195.30
110.90	198.50
130.30	208.00
150.00	231.90

Table A.113: Raw-data for Fig.A.50 in Sec.A.2.1

$I$ in $mA$	$V_3$ in Volt
8.80	231.20
16.18	221.20
30.02	211.60
36.98	207.80
48.60	202.30
64.40	198.60
92.80	195.10
101.90	194.70
121.00	194.90
136.40	196.20
150.00	198.40

Table A.114: Raw-data for Fig.A.51 in Sec.A.2.1

$I$ in $mA$	$V_3$ in Volt
10.08	248.90
18.35	234.10
26.08	224.40
37.68	214.60
42.90	211.90
50.00	209.20
57.00	206.90
69.90	204.00
82.20	201.90
101.40	199.40
122.10	197.90
150.00	198.20

Table A.115: Raw-data for Fig.A.52 in Sec.A.2.1

$I$ in $mA$	$V_3$ in Volt
12.26	255.80
16.90	247.00
27.67	231.10
36.73	220.20
50.20	208.50
60.70	202.00
70.00	198.30
79.90	196.00
100.20	195.70
120.10	195.10
150.00	194.90

Table A.116: Raw-data for Fig.A.53 in Sec.A.2.1

$I$ in $mA$	$V_3$ in Volt
12.48	260.20
22.17	242.90
29.10	231.90
40.10	220.40
51.50	210.70
66.50	201.80
70.20	200.60
80.40	198.00
90.00	196.70
110.00	195.40
130.30	195.10
150.00	194.90

Table A.117: Raw-data for Fig.A.54 in Sec.A.2.1

$I$ in $mA$	$V_3$ in Volt
14.80	260.20
24.86	243.30
35.16	230.20
49.30	219.70
70.10	208.50
90.00	202.70
110.10	200.30
130.60	199.10
150.00	198.50

Table A.118: Raw-data for Fig.A.55 in Sec.A.2.1

$I$ in $mA$	$V_3$ in Volt
14.27	268.70
27.37	245.50
40.60	229.70
78.20	209.30
110.60	201.60
139.60	199.70
150.00	199.50

Table A.119: Raw-data for Fig.A.56 in Sec.A.2.1

$I$ in $mA$	$V_3$ in Volt
18.54	264.70
34.01	240.00
58.00	220.10
90.80	207.10
112.10	202.10
129.40	200.40
150.00	199.40

# Appendix B

## Construction

The experiment was designed during a project-work as predecessor for this diploma thesis. Discussions with Prof. Hans Laimer, Prof. Herbert Störi and Ing. Wolfgang Beck resulted in guidelines for the construction. The high pressure chamber was manufactured in the workshop of the "Institut für Allgemeine Physik, TU Wien". All experiments took place in the "Plasma chemistry" laboratory. The guidelines for the construction are summarized in Sec.(B.1). The construction plans can be found in the Sec.(C).

### B.1 Guidelines

#### Basic conditions

Pressure Range: 100 – 2000 *hPa*  
Operating Voltage:  $\sim 450$  V (max. 2 *kV* peak voltage)  
Maximum current: 150 *mA*  
Maximum height: 80 *mm*  
Maximum length: 1000 *mm*

#### Base body

The base body (Fig.B.1) is made of brass. At the top is a quartz window. At the front are the connections for a backing pump, gas inlet and a manometer ( $\varnothing 6$  *mm Swagelok*).

The insulated cathode is mounted at the right hand side. The moveable anode is mounted at the left hand side. The inner surface of the base body is colored with graphite (Fig.B.3) to minimize reflections.

The core of the system are two electrode carriers (Fig.B.5, brown). These electrodes are replaceable in order to change the electrode diameters. The discharge is located between the two white pins (e.g. tungsten) and can be observed through a quartz window. For pure copper electrodes the whole part is manufactured in one piece (brown+white) or coated with nickel for nickel electrodes.

**Anode** (moveable)

Electrode carrier: copper

Electrode: copper, nickel (coated) or tungsten (pin)

Electrode diameters: 2.1, 3.0, 4.3 and 15.0 *mm*

Electrode length:  $\sim 3$  *mm*

Maximum inter-electrode gap:  $\sim 7$  *mm*

Minimum inter-electrode gap:  $\sim 0.1$  *mm* (as close as possible)

Coolant: water

The moveable anode (Fig.C.1) is on earth potential and therefore not insulated from the base body. The anode is cooled with a "pipe in pipe" cooling system. The cooling lines are fixed with thread clamps. Additional beveled teflon or ceramic (Tab.B.1) shieldings have to be put over the electrodes (Fig.C.1). These cylinders ensure well defined conditions (two parallel circular surfaces).

**Cathode** (fixed)

Electrode carrier: copper

Electrode: copper, nickel (coated) or tungsten (pin)

Electrode diameters: 2.1, 3.0, 4.3 and 15.0 *mm*

Electrode length:  $\sim 3$  *mm*

Coolant: water

The maximum potential at the cathode is 2 *kV*. Therefore the cathode (Fig.B.4) and the screws have to be insulated from the main body. (e.g. 1 *mm* POM). The cathode is cooled with a "pipe in pipe" cooling system. The cooling lines are fixed with thread clamps. Additional beveled teflon or ceramic sleeves (Tab.B.1) have to be put over the electrodes (Fig.C.1). These cylinders ensure well defined conditions (two parallel circular surfaces).

The white insulating plastic body (Fig.B.4) is moveable with three black screws. This allows a fine adjustment for the axial position of the cathode.

**Window**

Material: quartz glass SUP1

Diameter: 30 *mm*

Thickness: 5 *mm*

The window lies on an O-ring. The glass is fixed with a brass plate on the base body. A thin teflon ring prevents the glass from contact with the brass body at the sides and the brass plate at the top (Fig.C.1). The inner edge of the plate is beveled to get a better angle of view.



Figure B.1: The disassembled experiment.



Figure B.2: Water cooled moveable anode.

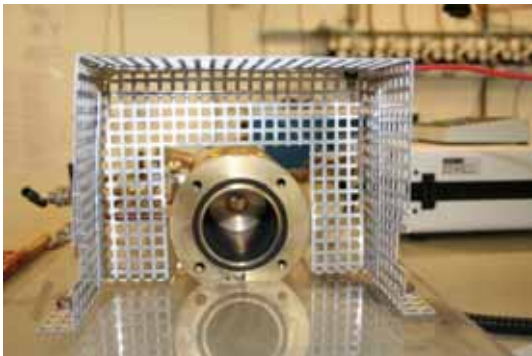


Figure B.3: The inner surface is colored with graphite to minimize reflections.



Figure B.4: Detail of the not moveable insulated water cooled cathode.

Table B.1: Specifications of the ceramic ( $Al_2O_3$ ) shielding

Rauschert Rapal 100	$Al_2O_3$ :	99.7 %
	Density:	$\geq 3.85 \frac{g}{cm^3}$
	Color:	red or white
	Heat conductivity:	$25 \frac{W}{mK}$
	Vickerts hardness:	1800-2000 HV10
	Porosity:	0 %

## B.2 Production drawings & parts list

In the beginning a 3D model with *VectorWorks 11* was created. This model helped to improve the further design. During the production state again minor changes took place (e.g. the upper surface is not flat like in Fig.B.6. These changes are documented in Sec.C.

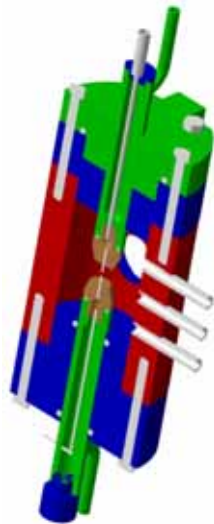


Figure B.5: Cross section of the model

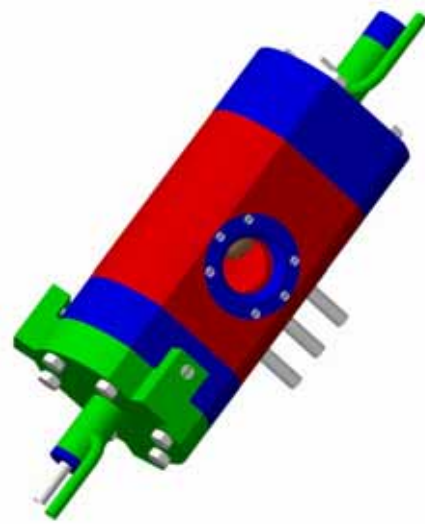


Figure B.6: 3D model of the experiment

Detailed and dimensioned production drawings of the disassembled parts can be found in Sec.C.

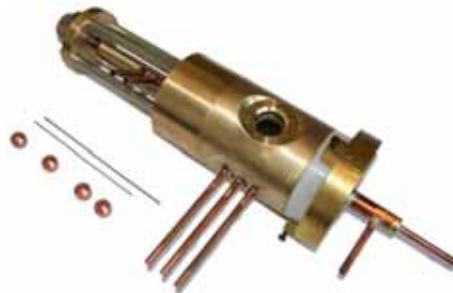


Figure B.7: The high pressure chamber

All available production drawings are listed in Tab.B.2. Note that all drawings in this  $\LaTeX$  document are scaled. The scaling factors are not "1:1" as stated. Please use the original *VectorWorks* files for further usage. Small parts like screw, sealing rings, ... are listed in Tab.B.3. Some suppliers are listed in Sec.B.3 on p.176.

Table B.2: Complete list of production drawings

Reference	Name	Chapter & page
PL1	Electrode carrier & Teflon shielding	Sec.(C.1) on p.(178)
PL2	Base body	Sec.(C.1) on p.(179)
PL3	Window frame & glass protection	Sec.(C.1) on p.(180)
PL4	Cathode & screw insulator	Sec.(C.1) on p.(181)
PL5	Guidance & distance bolt	Sec.(C.1) on p.(182)
PL6	Micrometer head & screw	Sec.(C.1) on p.(183)
PL7	Bushing & scale	Sec.(C.1) on p.(184)
PL8	Anode & inner tube	Sec.(C.1) on p.(185)
PL9	Cathode & inner tube	Sec.(C.1) on p.(186)
PL10	Cathode carrier	Sec.(C.1) on p.(187)
PL11	Torsion protection	Sec.(C.1) on p.(188)
	Assembled high pressure chamber	Sec.(C.1) on p.(189)

Table B.3: Parts list

Nr.	Name	Dimensions/type	Quantity	Reference
1	Hexagon head screw	M6x51	8	PL5, PL10
2	Hexagon head screw	M3x13	2	PL11
3	Hexagon head screw	M4x20	3	PL9
4	Counter-sunk screw	M3x11,5	6	PL3
5	Counter-sunk screw	M3x6	3	PL7
6	Hexagon set screw-headless	M3x10	1	PL6
7	Set screw-headless	M4x20	1	PL6
8	Hex nut	M4	1	PL10
9	Shim	M4	1	PL10
10	Hex nut	M5	4	PL5
11	Shim	M5	4	PL5
12	Sealing ring FPM80	50x3	3	PL2, PL10
13	Sealing ring FPM80	15x3	2	PL5
14	Sealing ring FPM80	24x2	1	PL2
15	Sealing ring FPM80	15x3	2	PL8, PL9
16	Seeger circlip ring		1	PL6
17	Ball bearing		1	PL6
18	Tungsten electrodes	1, 1.6, 2.4	1	PL1
19	Quartz glass SUP1	30x5	1	PL3

### B.3 List of suppliers



*phone* +43/1/6004102/7050

*mail* sales.austria@fronius.com

*web* www.fronius.com

*address* Daumegasse7  
1110 Wien  
Austria

Table B.4: Electrodes, welding equipment



*phone* +43/1/2593541

*mail* mail@dichtomatik.co.at

*web* www.dichtomatik.co.at

*address* Rautenweg 17  
1220 Wien  
Austria

Table B.5: Sealing rings, (O-rings)

#### Friedrich Petzolt GmbH

*phone* +43/1/5231616

*mail* verkauf@petzolt.at

*web* www.petzolt.at

*address* Burggasse 52-54  
1070 Wien  
Austria

Table B.6: Metals, ironmongery

#### Galvanische Anstalt Rudolf Fasching

*phone* +43/1/7143293

*mail* fa.fasching@aon.at

*web* www.galvanik-metallschleiferei.at

*address* Bechardgasse 3-5  
1030 Wien  
Austria

Table B.7: Galvanic

# Appendix C

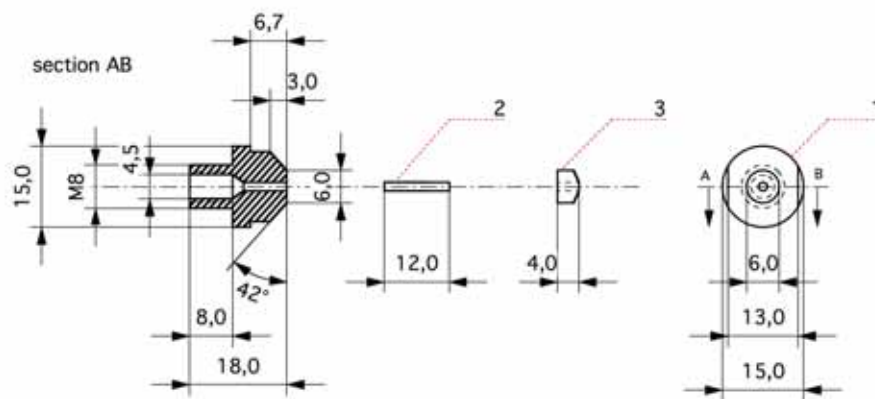
## Production drawings

### C.1 Catalogue of production drawings

All available production drawings are listed in Tab.(C.1). Note that all drawings in this L<sup>A</sup>T<sub>E</sub>X document are scaled. The scaling factors are not "1:1" as stated. Please use the original *VectorWorks* files for further usage.

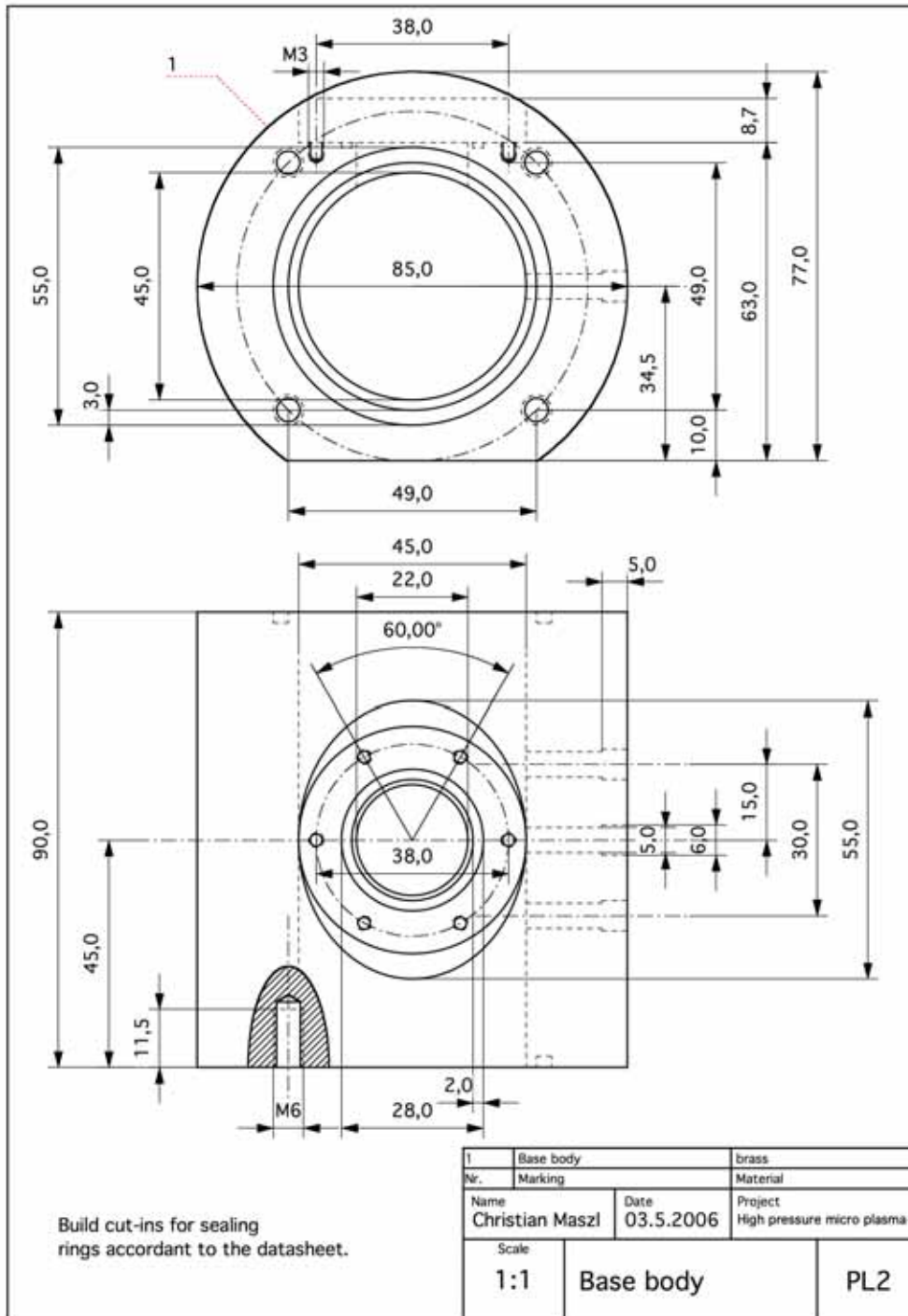
Table C.1: Complete list of production drawings

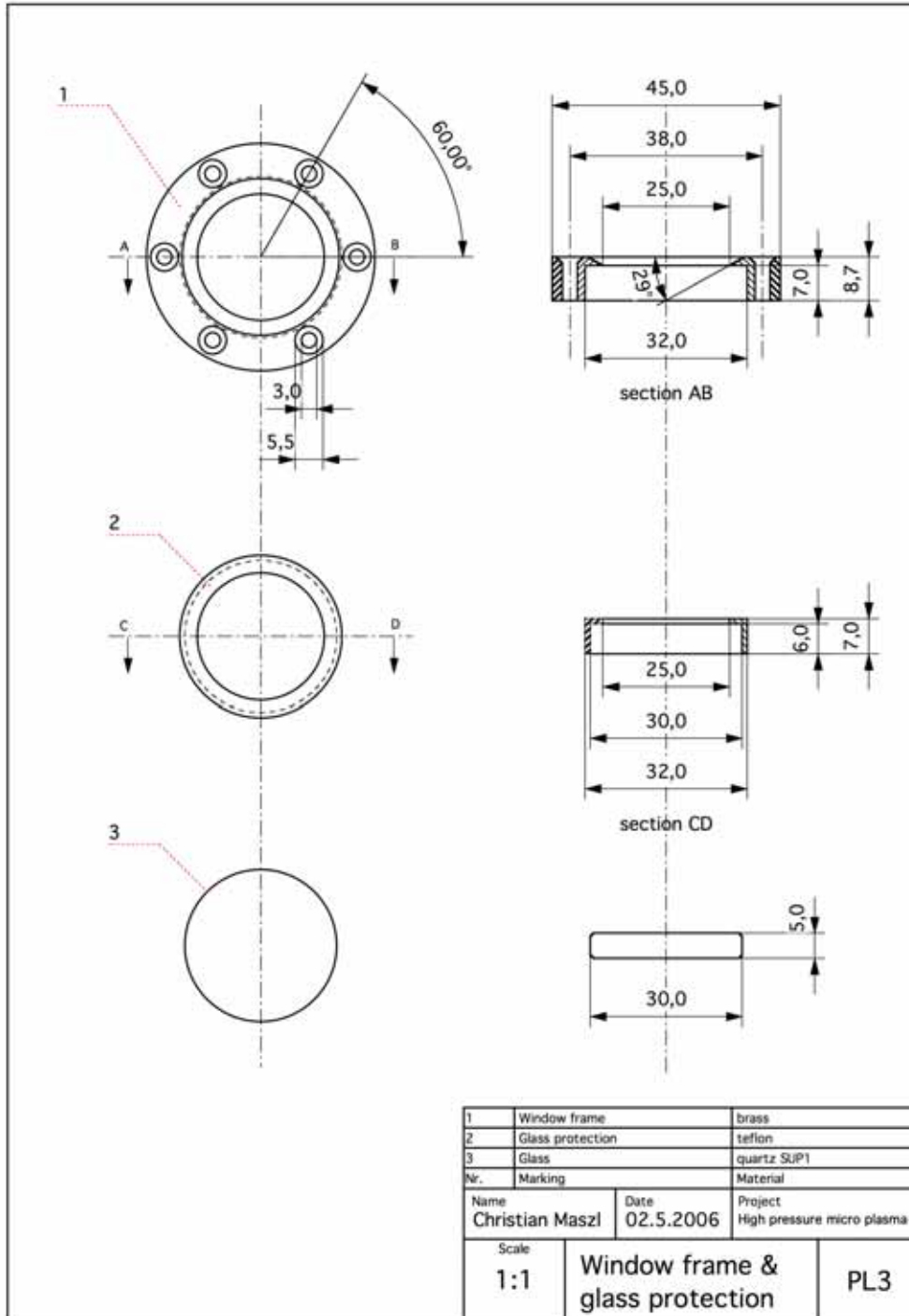
Reference	Name	Chapter & page
PL1	Electrode head & Teflon shielding	Sec.C.1 on p.178
PL2	Base body	Sec.C.1 on p.179
PL3	Window frame & glass protection	Sec.C.1 on p.180
PL4	Cathode & screw insulator	Sec.C.1 on p.181
PL5	Guidance & distance bolt	Sec.C.1 on p.182
PL6	Micrometer head & screw	Sec.C.1 on p.183
PL7	Bushing & scale	Sec.C.1 on p.184
PL8	Anode & inner tube	Sec.C.1 on p.185
PL9	Cathode & inner tube	Sec.C.1 on p.186
PL10	Cathode carrier	Sec.C.1 on p.187
PL11	Torsion protection	Sec.C.1 on p.188
	Assembled high pressure chamber	Sec.C.1 on p.189

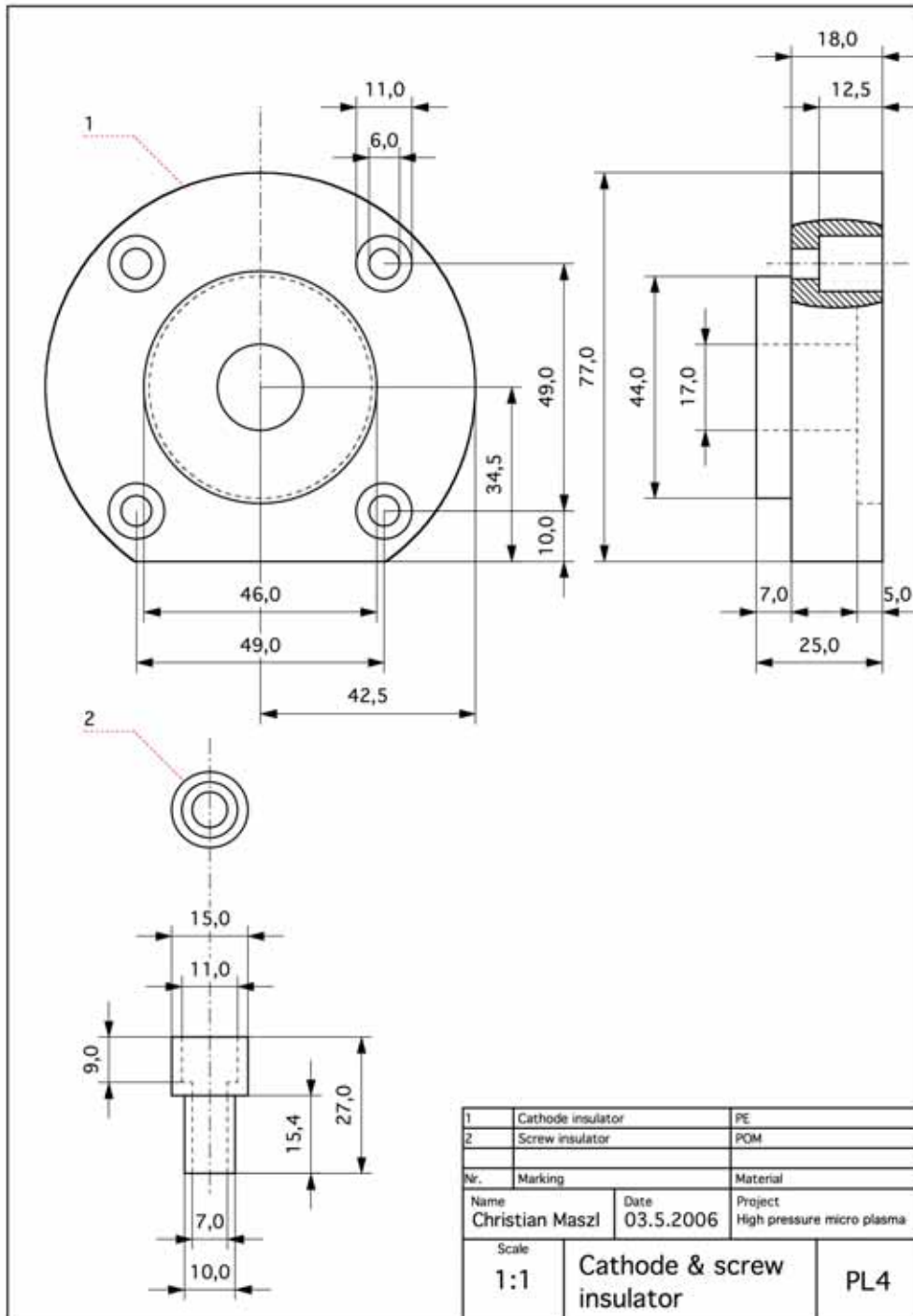


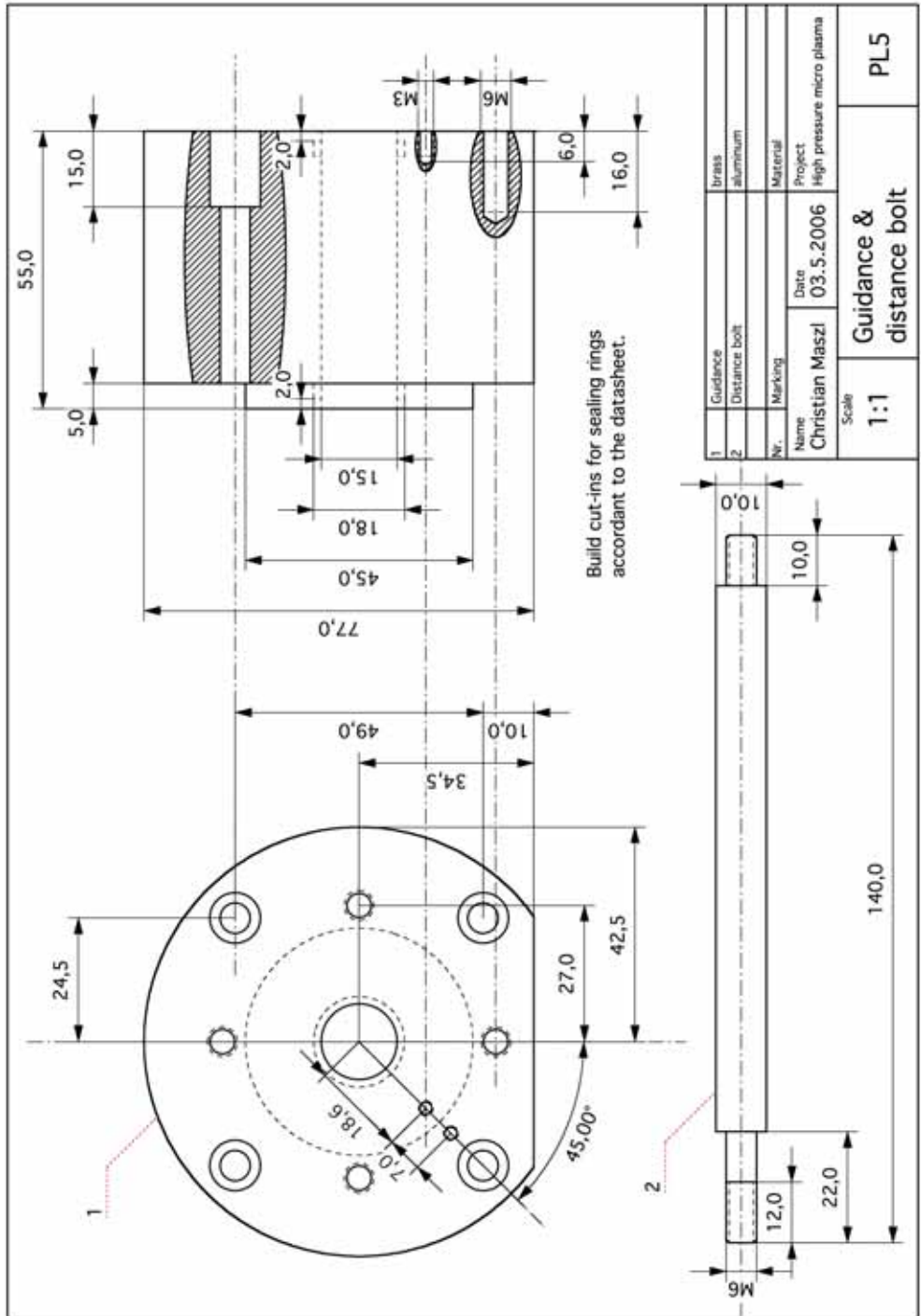
Dimensions of the teflon shielding and the drill hole for the tungsten electrode depend on the diameter of the used tungsten unit.

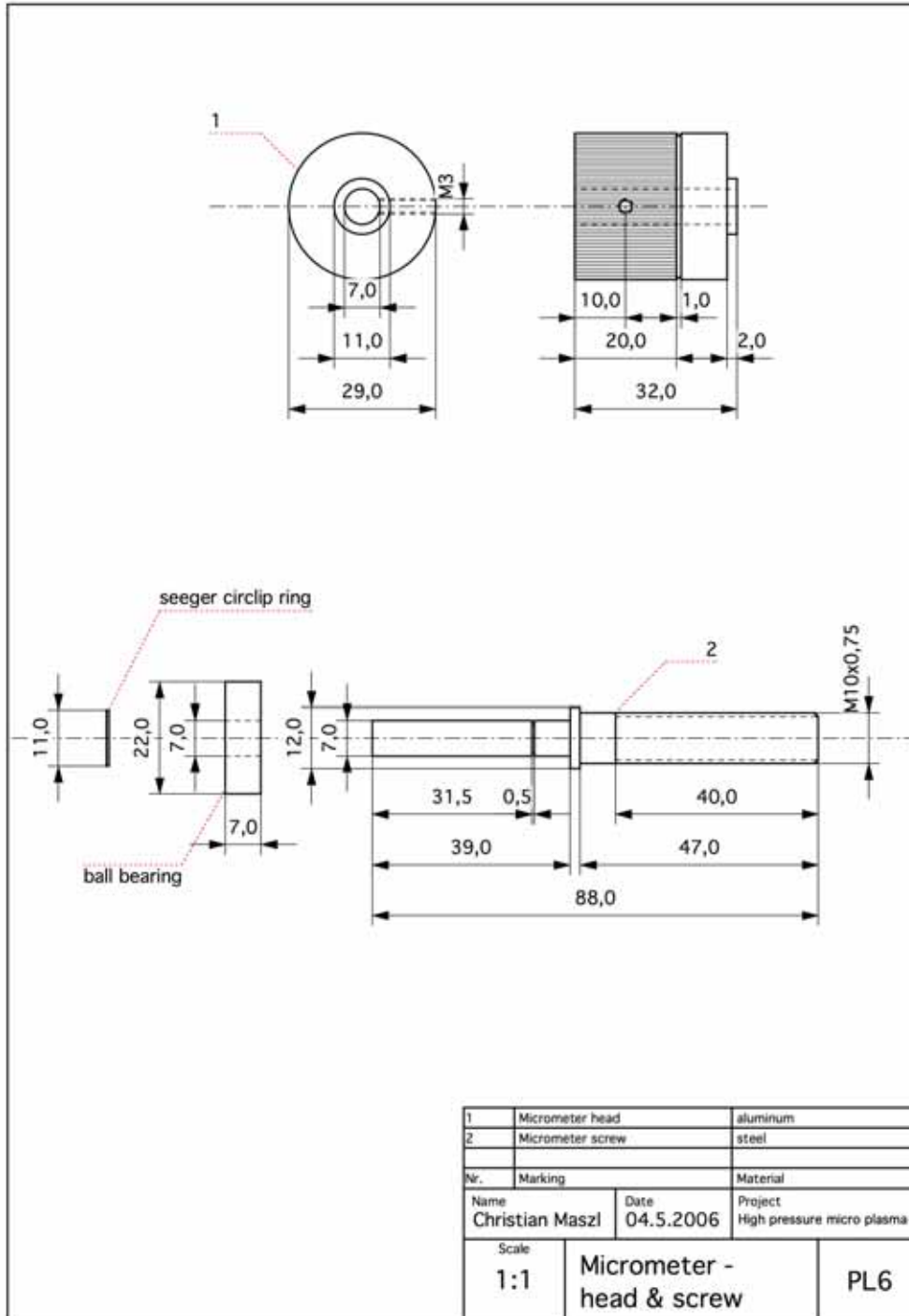
1	Electrode carrier	copper
2	Electrode	tungsten (100%)
3	Shielding	teflon
Nr.	Marking	Material
Name Christian Maszl		Date 27.4.2006
		Project High pressure micro plasma
Scale 1:1		Electrode carrier & teflon shielding
		PL1

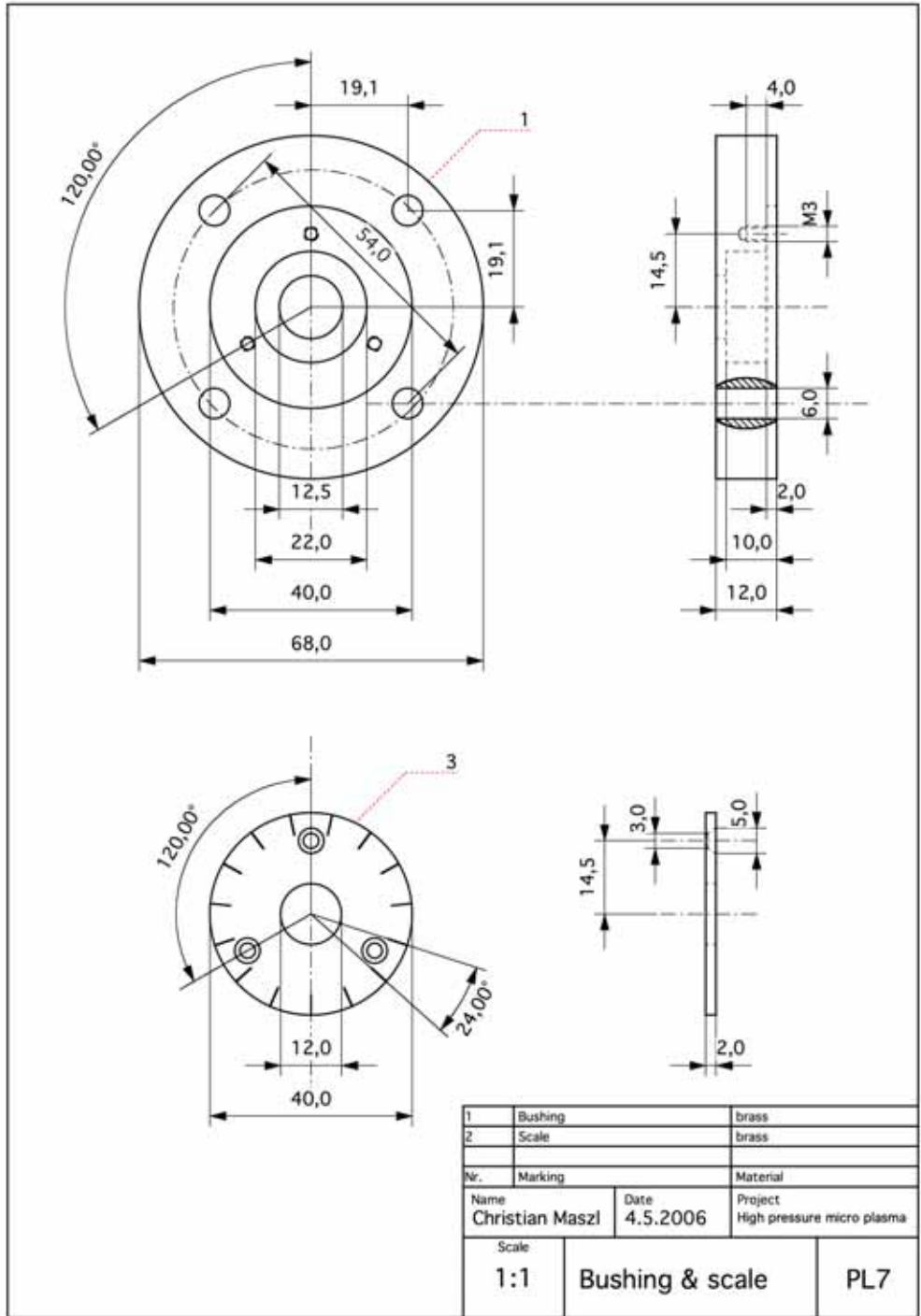


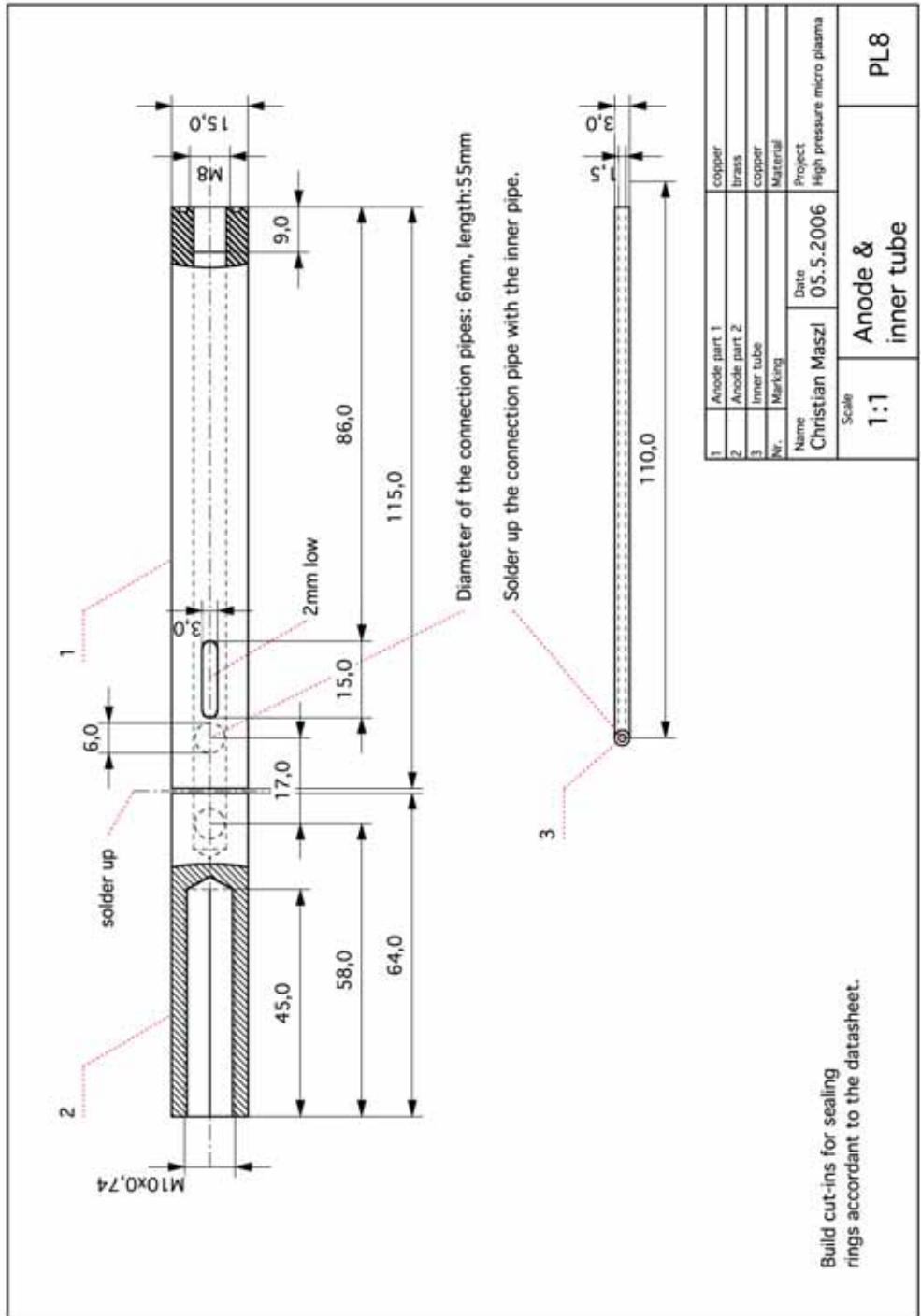


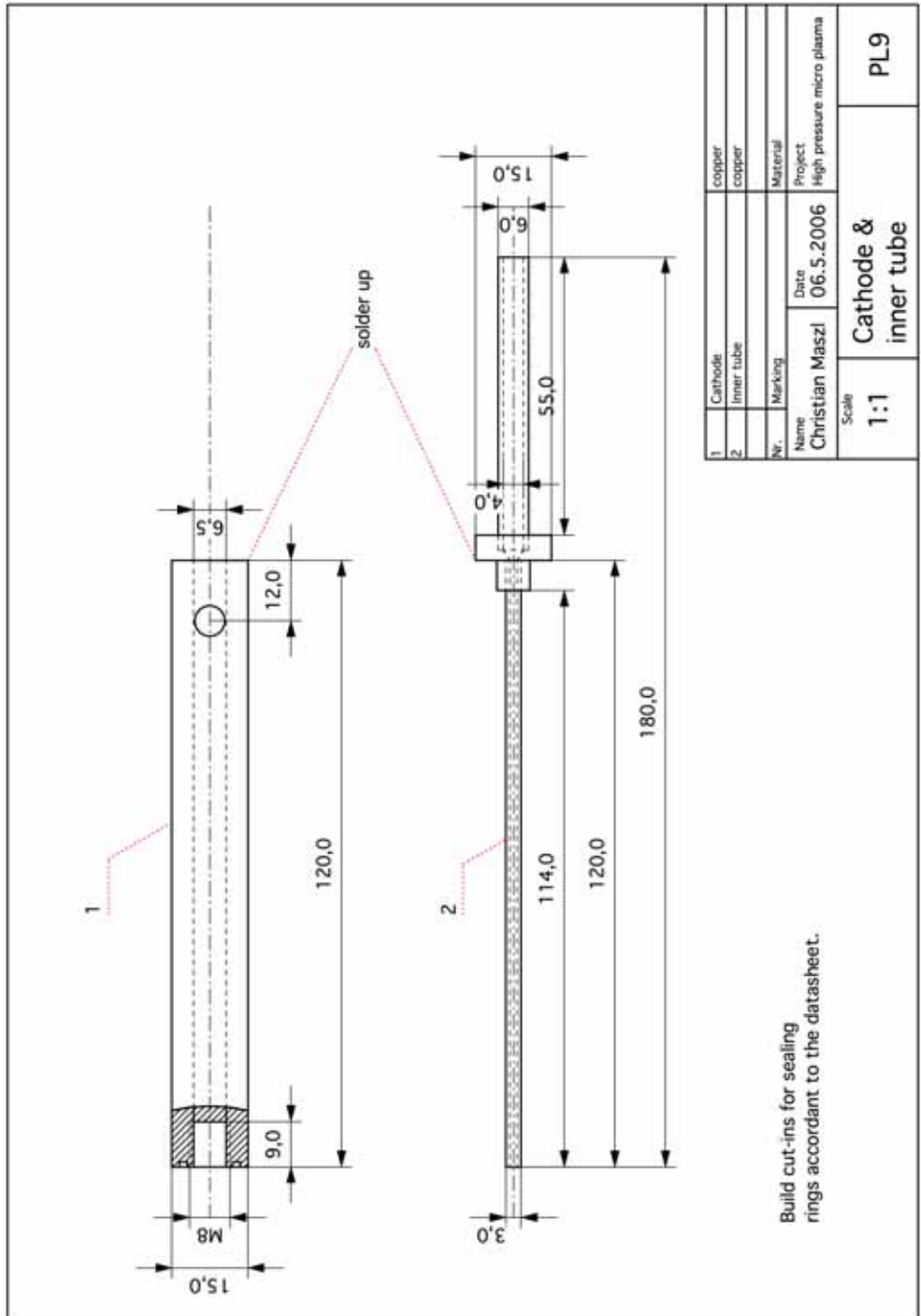


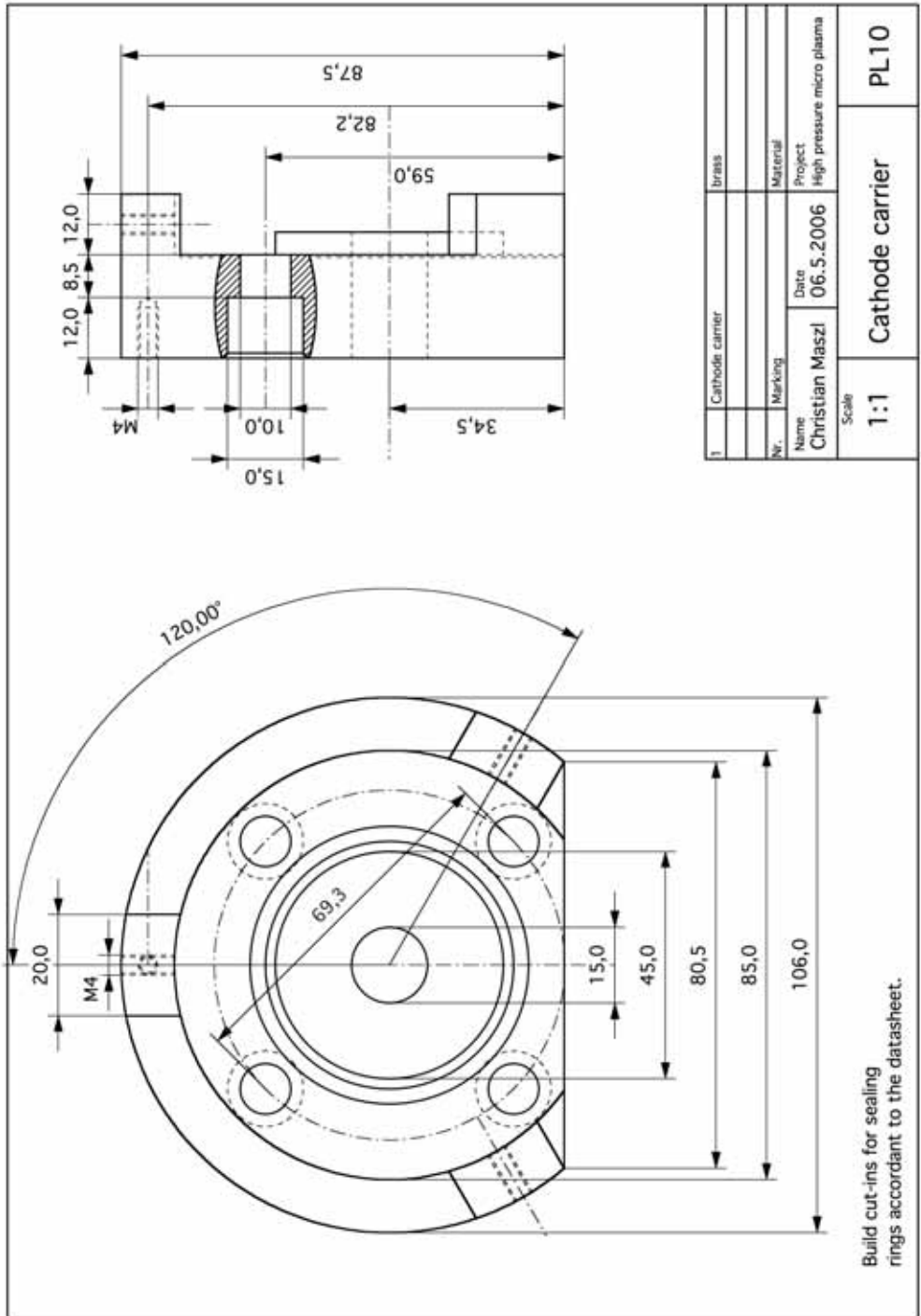


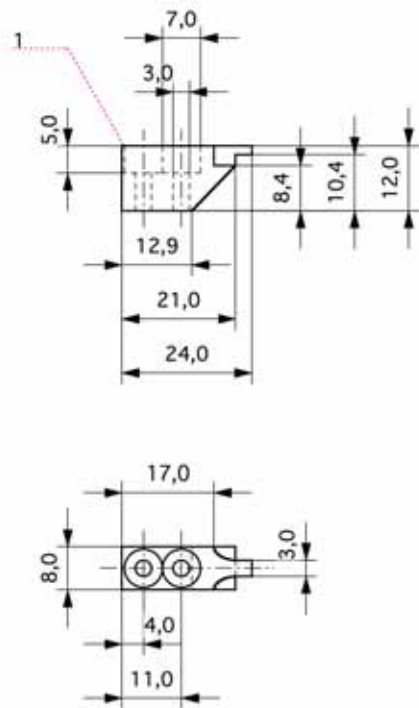












1	Torsion protection	brass
Nr.	Marking	Material
Name	Date	Project
Christian Maszl	05.5.2006	High pressure micro plasma
Scale		
1:1	Torsion protection	PL11

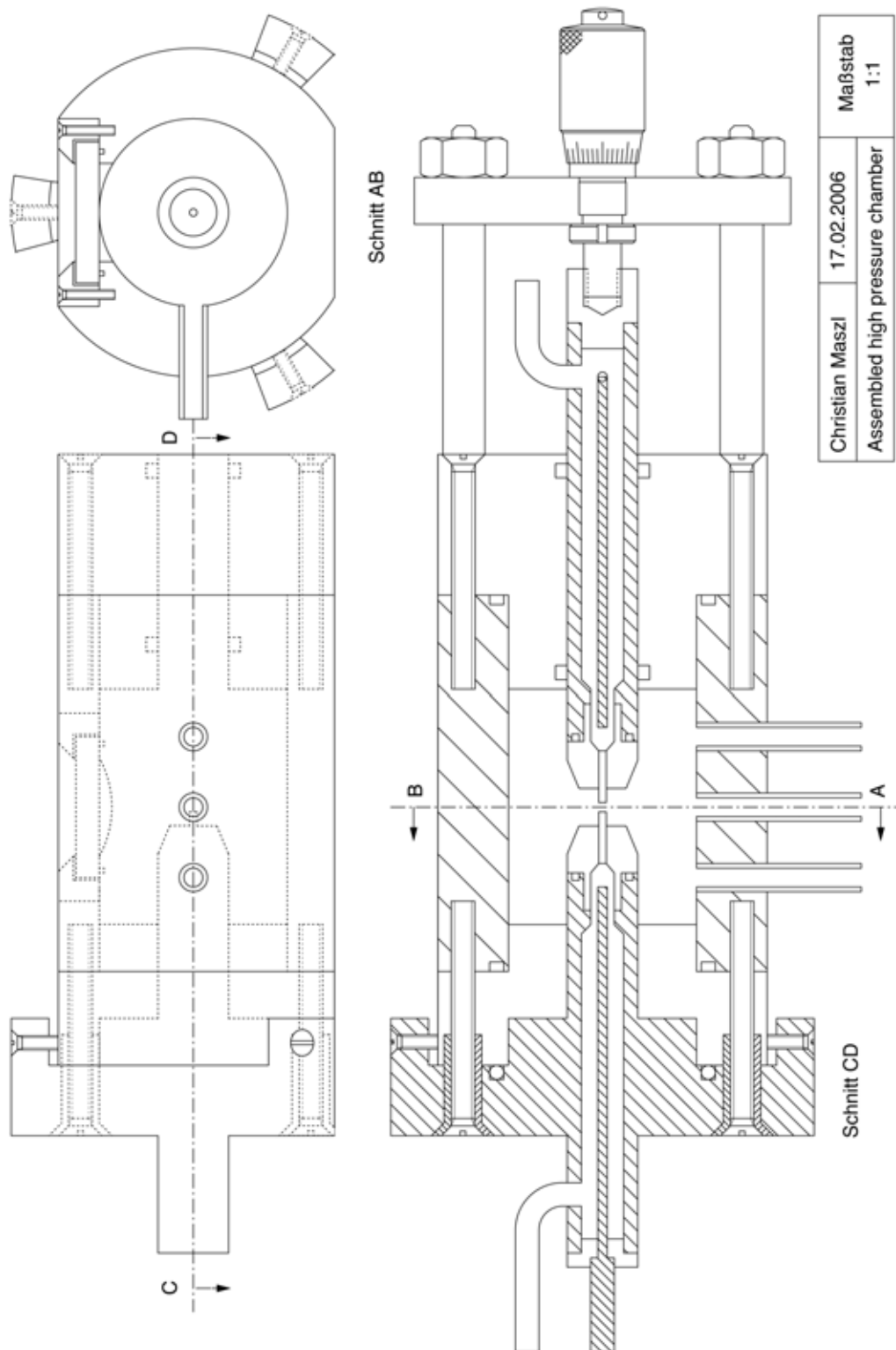


Figure C.1: Schematic of the assembled experiment



# List of figures and tables



# List of Figures

1.1	Breakdown potentials in various gases over a wide range of $pd$ values on the basis of data given in [19] (p. 134) . . . . .	4
1.2	Glow discharge in a tube . . . . .	5
1.3	$I - V$ characteristic of discharge between electrodes . . . . .	6
1.4	Similar discharges $p_1 d_1 = p_2 d_2 = const$ ( $I_1 = I_2$ ) . . . . .	7
2.1	The high pressure chamber . . . . .	13
2.2	Cross-section of the high pressure discharge chamber . . . . .	14
2.3	Equivalent circuit of the setup . . . . .	15
2.4	Gas-flow diagram of the laboratory setup . . . . .	16
2.5	Photograph of the lab setup . . . . .	17
2.6	Close view of the high pressure chamber . . . . .	17
2.7	Equivalent circuit of the voltage divider . . . . .	18
2.8	XPS of a possibly coated anode with an ESCALAB MkII, Al $K_\alpha$ 15 kV, 40 mA . . . . .	19
2.9	Chemical structure of Teflon (PTFE) . . . . .	20
2.10	VG Microlab 310F Auger-electron spectrometer . . . . .	20
2.11	Anode after $t > 5 h$ of use. . . . .	21
2.12	Cathode after $t > 5 h$ of use. . . . .	21
2.13	Influence of operation time on the discharge voltage . . . . .	22
2.14	Proposal for an improved breakdown voltage determination . . . . .	23
2.15	Flow chart for a possible breakdown voltage measurement software . . . . .	25
3.1	$OH$ -band at $p = 400 hPa$ $T = 305 K$ for $P = 2.5 W$ . . . . .	27
3.2	$OH$ -band at $p = 1200 hPa$ $T = 950 K$ for $P = 10.4 W$ . . . . .	27
3.3	Optical spectrum of the ultraviolet mercury-vapour lamp (not calibrated) . . . . .	28
3.4	Paschen curve: $d = 8.8 mm$ , $D = 15 mm$ , $p = 10 - 1600 hPa$ , Gas: helium, Electrodes: nickel . . . . .	29
3.5	Paschen curve: $d = 0.25 - 8.0 mm$ , $D = 15 mm$ , $p = 50, 200, 800, 1600 hPa$ , Gas: helium, Electrodes: nickel . . . . .	30
3.6	Paschen curve: $d = 0.1 - 7.8 mm$ , $D = 15 mm$ , $p = 200, 800, 1400, 2000, hPa$ , Gas: helium, Electrodes: copper . . . . .	30
3.7	Comparison of two methods to determine Paschen curves. . . . .	31
3.8	Fitted Paschen curve: $A_1 = 0.076 hPa^{-1} mm^{-1}$ , $B_1 = 2.26 V (mm hPa)^{-1/2}$ , $\gamma = 0.15$ . . . . .	32
3.9	Comparison of three fit-formulas for the ionisation coefficient $\alpha$ . . . . .	33
3.10	Current density $j_1$ versus pressure $p$ from 200 to 1000 hPa . . . . .	34

3.11	Current density $j_2$ versus pressure $p$ from 290 to 1430 $hPa$ . . . . .	35
3.12	Current density $j_3$ versus pressure $p$ from 400 to 1600 $hPa$ . . . . .	35
3.13	Comparison of results from [27] and the experiments in Sec.3.2 . . . . .	37
3.14	Locations of the gray value profile for Fig.3.15 . . . . .	39
3.15	Gray value profile of two selected discharges . . . . .	39
3.16	Pressure dependence of the positive column diameter 290 – 1430 $hPa$ . . . . .	40
3.17	Pressure dependence of the positive column diameter 200 – 1000 $hPa$ . . . . .	40
3.18	Pressure dependence of the temperature in the cathode fall region. . . . .	41
3.19	Comparison of three similar discharges with $p_1 = 300 hPa$ and $a = 1.4$ or $2.0$ . . . . .	44
3.20	Comparison of three similar discharges with $p_1 = 200 hPa$ and $a = 1.4$ or $2.0$ . . . . .	46
3.21	Reduced field strengths for three similar discharges . . . . .	49
3.22	Temperature-power characteristics of similar discharges . . . . .	50
3.23	The anode glow at the left-hand side has a ring-like appearance. . . . .	52
3.24	$d_C = 144 \mu m, p = 200 hPa$ . . . . .	53
3.25	$d_C = 89 \mu m, p = 300 hPa$ . . . . .	53
3.26	$d_C = 56 \mu m, p = 400 hPa$ . . . . .	53
3.27	$d_C = 44 \mu m, p = 500 hPa$ . . . . .	53
3.28	Pressure dependence of the cathode dark-space for iron and tungsten electrodes . . . . .	54
3.29	Equidistant anode spots at the anode edge . . . . .	55
3.30	Magnified anode spot at the lower edge . . . . .	56
3.31	Magnified anode spot at the upper edge . . . . .	56
3.32	Hexagonal self-organized structures at the anode's surface . . . . .	56
3.33	Equidistant spots at the anode's edge (elec.: $D = 3.0$ mm, gap: $d = 6.1$ mm) . . . . .	57
3.34	Bright centered anodic glow (elec.: $D = 3.0$ mm, gap: $d = 2.8$ mm) . . . . .	57
3.35	Glow discharge below $V_n = 177$ V (elec.: $D = 4.3$ mm, gap: $d = 1.7$ mm) . . . . .	58
3.36	Glow discharge below $V_n = 177$ V (elec.: $D = 2.1$ mm, gap: $d = 0.75$ mm) . . . . .	58
3.37	Glow discharge below $V_n = 177$ V (elec.: $D = 2.1$ mm, gap: $d = 0.5$ mm) . . . . .	59
3.38	Glow discharge above $V_n = 177$ V (elec.: $D = 2.1$ mm, gap: $d = 5.5$ mm) . . . . .	59
3.39	Time evolution from anodic glow to anodic light spots . . . . .	60
3.40	Optical spectrum of the cathode (integration time: 120 ms) . . . . .	61
3.41	Optical spectrum of the anode after ignition (integration time: 300 ms) . . . . .	62
3.42	Optical spectrum of the anode after $t = 966$ s (integration time: 300 ms) . . . . .	62
3.43	Time evolution of the spectral data from anodic glow to anodic light spots . . . . .	63
A.1	$OH$ -band at $p = 400 hPa$ $T = 305$ K for $P = 2.5$ W . . . . .	73
A.2	$OH$ -band at $p = 1200 hPa$ $T = 950$ K for $P = 10.4$ W . . . . .	73
A.3	Column gradient (Tab.A.66) and spectrum (integration time: 200 ms) . . . . .	75
A.4	Column gradient (Tab.A.67) and spectrum (integration time: 200 ms) . . . . .	76
A.5	Column gradient (Tab.A.68) and spectrum (integration time: 200 ms) . . . . .	77
A.6	Column gradient (Tab.A.69) and spectrum (integration time: 200 ms) . . . . .	78
A.7	Column gradient (Tab.A.70) and spectrum (integration time: 200 ms) . . . . .	79
A.8	Column gradient (Tab.A.71) and spectrum (integration time: 200 ms) . . . . .	80
A.9	Column gradient (Tab.A.72) and spectrum (integration time: 200 ms) . . . . .	81
A.10	Column gradient (Tab.A.73) and spectrum (integration time: 200 ms) . . . . .	82
A.11	Column gradient (Tab.A.74) and spectrum (integration time: 200 ms) . . . . .	83
A.12	Column gradient (Tab.A.75) and spectrum (integration time: 100 ms) . . . . .	84
A.13	Column gradient (Tab.A.76) and spectrum (integration time: 100 ms) . . . . .	85

A.14	Column gradient (Tab.A.75) and spectrum (integration time: 100 ms) . . . . .	86
A.15	Column gradient (Tab.A.78) and spectrum (integration time: 100 ms) . . . . .	87
A.16	Column gradient (Tab.A.79) and spectrum (integration time: 100 ms) . . . . .	88
A.17	Column gradient (Tab.A.80) and spectrum (integration time: 100 ms) . . . . .	89
A.18	Column gradient (Tab.A.81) and spectrum (integration time: 100 ms) . . . . .	90
A.19	Column gradient (Tab.A.82) and spectrum (integration time: 100 ms) . . . . .	91
A.20	Column gradient (Tab.A.83) and spectrum (integration time: 100 ms) . . . . .	92
A.21	Column gradient (Tab.A.84) and spectrum (integration time: 70 ms) . . . . .	93
A.22	Column gradient (Tab.A.85) and spectrum (integration time: 70 ms) . . . . .	94
A.23	Column gradient (Tab.A.86) and spectrum (integration time: 70 ms) . . . . .	95
A.24	Column gradient (Tab.A.87) and spectrum (integration time: 100 ms) . . . . .	96
A.25	Column gradient (Tab.A.88) and spectrum (integration time: 100 ms) . . . . .	97
A.26	Column gradient (Tab.A.89) and spectrum (integration time: 100 ms) . . . . .	98
A.27	Column gradient (Tab.A.90) and spectrum (integration time: 100 ms) . . . . .	99
A.28	Column gradient (Tab.A.91) and spectrum (integration time: 100 ms) . . . . .	100
A.29	Column gradient (Tab.A.92) and spectrum (integration time: 100 ms) . . . . .	101
A.30	I-V diagram (Tab.A.93) and spectrum (integration time: 200 ms) . . . . .	103
A.31	I-V diagram (Tab.A.94) and spectrum (integration time: 200 ms) . . . . .	104
A.32	I-V diagram (Tab.A.95) and spectrum (integration time: 120 ms) . . . . .	105
A.33	I-V diagram (Tab.A.96) and spectrum (integration time: 120 ms) . . . . .	106
A.34	I-V diagram (Tab.A.97) and spectrum (integration time: 120 ms) . . . . .	107
A.35	I-V diagram (Tab.A.98) and spectrum (integration time: 80 ms) . . . . .	108
A.36	I-V diagram (Tab.A.99) and spectrum (integration time: 60 ms) . . . . .	109
A.37	I-V diagram (Tab.A.100) and spectrum (integration time: 60 ms) . . . . .	110
A.38	I-V diagram (Tab.A.101) and spectrum (integration time: 60 ms) . . . . .	111
A.39	I-V diagram (Tab.A.102) and spectrum (integration time: 150ms) . . . . .	112
A.40	I-V diagram (Tab.A.103) and spectrum (integration time: 125ms) . . . . .	113
A.41	I-V diagram (Tab.A.104) and spectrum (integration time: 120ms) . . . . .	114
A.42	I-V diagram (Tab.A.105) and spectrum (integration time: 100ms) . . . . .	115
A.43	I-V diagram (Tab.A.106) and spectrum (integration time: 40ms) . . . . .	116
A.44	I-V diagram (Tab.A.107) and spectrum (integration time: 100ms) . . . . .	117
A.45	I-V diagram (Tab.A.108) and spectrum (integration time: 70ms) . . . . .	118
A.46	I-V diagram (Tab.A.109) and spectrum (integration time: 50ms) . . . . .	119
A.47	I-V diagram (Tab.A.110) and spectrum (integration time: 40ms) . . . . .	120
A.48	I-V diagram (Tab.A.111) and spectrum (integration time: 100ms) . . . . .	121
A.49	I-V diagram (Tab.A.112) and spectrum (integration time: 100ms) . . . . .	122
A.50	I-V diagram (Tab.A.113) and spectrum (integration time: 100ms) . . . . .	123
A.51	I-V diagram (Tab.A.114) and spectrum (integration time: 100ms) . . . . .	124
A.52	I-V diagram (Tab.A.115) and spectrum (integration time: 100ms) . . . . .	125
A.53	I-V diagram (Tab.A.116) and spectrum (integration time: 50ms) . . . . .	126
A.54	I-V diagram (Tab.A.117) and spectrum (integration time: 50ms) . . . . .	127
A.55	I-V diagram (Tab.A.118) and spectrum (integration time: 50ms) . . . . .	128
A.56	I-V diagram (Tab.A.119) and spectrum (integration time: 50ms) . . . . .	129
A.57	Comparison of three similar discharges: $p_1 = 200 \text{ hPa}$ (Fig.A.30, Fig.A.39 and Fig.A.48) . . . . .	130
A.58	Comparison of three similar discharges: $p_1 = 300 \text{ hPa}$ (Fig.A.31, Fig.A.40 and Fig.A.49) . . . . .	131

A.59 Comparison of three similar discharges: $p_1 = 400 \text{ hPa}$ (Fig.A.32, Fig.A.41 and Fig.A.50) . . . . .	131
A.60 Comparison of three similar discharges: $p_1 = 500 \text{ hPa}$ (Fig.A.33, Fig.A.42 and Fig.A.51) . . . . .	132
A.61 Comparison of three similar discharges: $p_1 = 600 \text{ hPa}$ (Fig.A.34, Fig.A.43 and Fig.A.52) . . . . .	132
A.62 Comparison of three similar discharges: $p_1 = 700 \text{ hPa}$ (Fig.A.35, Fig.A.44 and Fig.A.54) . . . . .	133
A.63 Comparison of three similar discharges: $p_1 = 800 \text{ hPa}$ (Fig.A.36, Fig.A.45 and Fig.A.56) . . . . .	133
A.64 Comparison of two similar discharges: $p_1 = 900 \text{ hPa}$ (Fig.A.37 and Fig.A.46) . . . . .	134
A.65 Comparison of two similar discharges: $p_1 = 1000 \text{ hPa}$ (Fig.A.37 and Fig.A.47) . . . . .	134
B.1 The disassembled experiment. . . . .	173
B.2 Water cooled moveable anode. . . . .	173
B.3 The inner surface is colored with graphite to minimize reflections. . . . .	173
B.4 Detail of the not moveable insulated water cooled cathode. . . . .	173
B.5 Cross section of the model . . . . .	174
B.6 3D model of the experiment . . . . .	174
B.7 The high pressure chamber . . . . .	174
C.1 Schematic of the assembled experiment . . . . .	189

# List of Tables

1.1	Constants $A_i$ and $B_i$ from Eq.[1.2], Eq.[1.3] and Eq.[1.4] for helium. . . . .	2
1.2	Validity of the similarity laws . . . . .	9
2.1	Parts list . . . . .	16
3.1	I-V characterisation for three different electrode diameters . . . . .	34
3.2	Reduced normal current densities for three different electrode diameters . . . . .	36
3.3	Reduced normal current densities $(j/p^2)_n$ [ $A/(mm^2hPa^2)$ ] at room temperature from [19] . . . . .	36
3.4	Constants for Eq.[3.9] from [19] . . . . .	42
3.5	I-V characterisation for three different electrode diameters . . . . .	44
3.6	Overview of all triples of similar discharges . . . . .	45
3.7	Raw-data for Fig.3.28 in Sec.3.6 . . . . .	53
3.8	Experimental parameters . . . . .	60
A.1	Overview of all triples of similar discharges for Sec.A.1 (Appendix) . . . . .	74
A.2	Lifbase 2.0 settings for $p_1 = 200$ hPa and $T = 375$ K ( $P_1 = 5.9$ W) . . . . .	75
A.3	Lifbase 2.0 settings for $p_1 = 300$ hPa and $T = 445$ K ( $P_1 = 6.3$ W) . . . . .	76
A.4	Lifbase 2.0 settings for $p_1 = 400$ hPa and $T = 475$ K ( $P_1 = 7.2$ W) . . . . .	77
A.5	Lifbase 2.0 settings for $p_1 = 500$ hPa and $T = 500$ K ( $P_1 = 7.2$ W) . . . . .	78
A.6	Lifbase 2.0 settings for $p_1 = 600$ hPa and $T = 800$ K ( $P_1 = 8.2$ W) . . . . .	79
A.7	Lifbase 2.0 settings for $p_1 = 700$ hPa and $T = 850$ K ( $P_1 = 8.7$ W) . . . . .	80
A.8	Lifbase 2.0 settings for $p_1 = 800$ hPa and $T = 875$ K ( $P_1 = 9.1$ W) . . . . .	81
A.9	Lifbase 2.0 settings for $p_1 = 900$ hPa and $T = 900$ K ( $P_1 = 9.5$ W) . . . . .	82
A.10	Lifbase 2.0 settings for $p_1 = 1000$ hPa and $T = 975$ K ( $P_1 = 9.9$ W) . . . . .	83
A.11	Lifbase 2.0 settings for $p_2 = 290$ hPa and $T_2 = 290$ K ( $P_2 = 6.4$ W) . . . . .	84
A.12	Lifbase 2.0 settings for $p_2 = 430$ hPa and $T_2 = 375$ K ( $P_2 = 7.1$ W) . . . . .	85
A.13	Lifbase 2.0 settings for $p_2 = 570$ hPa and $T_2 = 350$ K ( $P_2 = 8.0$ W) . . . . .	86
A.14	Lifbase 2.0 settings for $p_2 = 720$ hPa and $T_2 = 850$ K ( $P_2 = 8.8$ W) . . . . .	87
A.15	Lifbase 2.0 settings for $p_2 = 860$ hPa and $T_2 = 950$ K ( $P_2 = 9.4$ W) . . . . .	88
A.16	Lifbase 2.0 settings for $p_2 = 1000$ hPa and $T_2 = 925$ K ( $P_2 = 10.0$ W) . . . . .	89
A.17	Lifbase 2.0 settings for $p_2 = 1150$ hPa and $T_2 = 950$ K ( $P_2 = 10.5$ W) . . . . .	90
A.18	Lifbase 2.0 settings for $p_2 = 1290$ hPa and $T_2 = 950$ K ( $P_2 = 9.3$ W) . . . . .	91
A.19	Lifbase 2.0 settings for $p_2 = 1430$ hPa and $T_2 = 950$ K ( $P_2 = 9.5$ W) . . . . .	92
A.20	Lifbase 2.0 settings for $p_3 = 400$ hPa and $T_3 = 425$ K ( $P_3 = 7.3$ W) . . . . .	93
A.21	Lifbase 2.0 settings for $p_3 = 600$ hPa and $T_3 = 600$ K ( $P_3 = 8.3$ W) . . . . .	94
A.22	Lifbase 2.0 settings for $p_3 = 800$ hPa and $T_3 = 800$ K ( $P_3 = 9.3$ W) . . . . .	95

A.23	Lifbase 2.0 settings for $p_3 = 1000 \text{ hPa}$ and $T_3 = 1050 \text{ K}$ ( $P_3 = 10.2 \text{ W}$ ) . . .	96
A.24	Lifbase 2.0 settings for $p_3 = 1200 \text{ hPa}$ and $T_3 = 950 \text{ K}$ ( $P_3 = 10.4 \text{ W}$ ) . . . .	97
A.25	Lifbase 2.0 settings for $p_3 = 1300 \text{ hPa}$ and $T_3 = 950 \text{ K}$ ( $P_3 = 10.2 \text{ W}$ ) . . . .	98
A.26	Lifbase 2.0 settings for $p_3 = 1400 \text{ hPa}$ and $T_3 = 950 \text{ K}$ ( $P_3 = 10.1 \text{ W}$ ) . . . .	99
A.27	Lifbase 2.0 settings for $p_3 = 1500 \text{ hPa}$ and $T_3 = 950 \text{ K}$ ( $P_3 = 9.8 \text{ W}$ ) . . . .	100
A.28	Lifbase 2.0 settings for $p_3 = 1600 \text{ hPa}$ and $T_3 = 1000 \text{ K}$ ( $P_3 = 10.1 \text{ W}$ ) . . .	101
A.29	Overview of all triples of similar discharges for Sec.A.2 (Appendix) . . . . .	102
A.30	Lifbase 2.0 settings for $p_1 = 200 \text{ hPa}$ and $T = 475 \text{ K}$ ( $P_1 = 2.3 \text{ W}$ ) . . . . .	103
A.31	Lifbase 2.0 settings for $p_1 = 300 \text{ hPa}$ and $T = 450 \text{ K}$ ( $P_1 = 5.9 \text{ W}$ ) . . . . .	104
A.32	Lifbase 2.0 settings for $p_1 = 400 \text{ hPa}$ and $T = 300 \text{ K}$ ( $P_1 = 9.1 \text{ W}$ ) . . . . .	105
A.33	Lifbase 2.0 settings for $p_1 = 500 \text{ hPa}$ and $T = 775 \text{ K}$ ( $P_1 = 14.0 \text{ W}$ ) . . . . .	106
A.34	Lifbase 2.0 settings for $p_1 = 600 \text{ hPa}$ and $T = 875 \text{ K}$ ( $P_1 = 18.7 \text{ W}$ ) . . . . .	107
A.35	Lifbase 2.0 settings for $p_1 = 700 \text{ hPa}$ and $T = 900 \text{ K}$ ( $P_1 = 25.9 \text{ W}$ ) . . . . .	108
A.36	Lifbase 2.0 settings for $p_1 = 800 \text{ hPa}$ and $T = 1100 \text{ K}$ ( $P_1 = 32.7 \text{ W}$ ) . . . .	109
A.37	Lifbase 2.0 settings for $p_1 = 900 \text{ hPa}$ and $T = 1150 \text{ K}$ ( $P_1 = 34.2 \text{ W}$ ) . . . . .	110
A.38	Lifbase 2.0 settings for $p_1 = 1000 \text{ hPa}$ and $T = 1150 \text{ K}$ ( $P_1 = 34.8 \text{ W}$ ) . . .	111
A.39	Lifbase 2.0 settings for $p_2 = 290 \text{ hPa}$ and $T = 325 \text{ K}$ ( $P_2 = 2.2 \text{ W}$ ) . . . . .	112
A.40	Lifbase 2.0 settings for $p_2 = 430 \text{ hPa}$ and $T = 350 \text{ K}$ ( $P_2 = 5.2 \text{ W}$ ) . . . . .	113
A.41	Lifbase 2.0 settings for $p_2 = 570 \text{ hPa}$ and $T = 410 \text{ K}$ ( $P_2 = 10.5 \text{ W}$ ) . . . . .	114
A.42	Lifbase 2.0 settings for $p_2 = 720 \text{ hPa}$ and $T = 400 \text{ K}$ ( $P_2 = 12.7 \text{ W}$ ) . . . . .	115
A.43	Lifbase 2.0 settings for $p_2 = 860 \text{ hPa}$ and $T = 700 \text{ K}$ ( $P_2 = 17.4 \text{ W}$ ) . . . . .	116
A.44	Lifbase 2.0 settings for $p_2 = 1000 \text{ hPa}$ and $T = 900 \text{ K}$ ( $P_2 = 20.8 \text{ W}$ ) . . . .	117
A.45	Lifbase 2.0 settings for $p_2 = 1150 \text{ hPa}$ and $T = 1100 \text{ K}$ ( $P_2 = 32.7 \text{ W}$ ) . . .	118
A.46	Lifbase 2.0 settings for $p_2 = 1290 \text{ hPa}$ and $T = 1200 \text{ K}$ ( $P_2 = 32.0 \text{ W}$ ) . . .	119
A.47	Lifbase 2.0 settings for $p_2 = 1430 \text{ hPa}$ and $T = 1050 \text{ K}$ ( $P_2 = 32.7 \text{ W}$ ) . . .	120
A.48	Lifbase 2.0 settings for $p_3 = 400 \text{ hPa}$ and $T = 305 \text{ K}$ ( $P_3 = 2.5 \text{ W}$ ) . . . . .	121
A.49	Lifbase 2.0 settings for $p_3 = 600 \text{ hPa}$ and $T = 430 \text{ K}$ ( $P_3 = 4.6 \text{ W}$ ) . . . . .	122
A.50	Lifbase 2.0 settings for $p_3 = 800 \text{ hPa}$ and $T = 550 \text{ K}$ ( $P_3 = 6.3 \text{ W}$ ) . . . . .	123
A.51	Lifbase 2.0 settings for $p_3 = 1000 \text{ hPa}$ and $T = 650 \text{ K}$ ( $P_3 = 10.5 \text{ W}$ ) . . . .	124
A.52	Lifbase 2.0 settings for $p_3 = 1200 \text{ hPa}$ and $T = 920 \text{ K}$ ( $P_3 = 13.9 \text{ W}$ ) . . . .	125
A.53	Lifbase 2.0 settings for $p_3 = 1300 \text{ hPa}$ and $T = 750 \text{ K}$ ( $P_3 = 15.8 \text{ W}$ ) . . . .	126
A.54	Lifbase 2.0 settings for $p_3 = 1400 \text{ hPa}$ and $T = 1050 \text{ K}$ ( $P_3 = 22.0 \text{ W}$ ) . . .	127
A.55	Lifbase 2.0 settings for $p_3 = 1500 \text{ hPa}$ and $T = 1050 \text{ K}$ ( $P_3 = 29.9 \text{ W}$ ) . . .	128
A.56	Lifbase 2.0 settings for $p_3 = 1600 \text{ hPa}$ and $T = 1050 \text{ K}$ ( $P_3 = 29.9 \text{ W}$ ) . . .	129
A.57	Raw-data for Fig.3.4 in Sec.3.1.1 . . . . .	135
A.58	Raw-data for Fig.3.5 in Sec.3.1.2 ( $p = 50 \text{ hPa}$ ) . . . . .	136
A.59	Raw-data for Fig.3.5 in Sec.3.1.2 ( $p = 200 \text{ hPa}$ ) . . . . .	136
A.60	Raw-data for Fig.3.5 in Sec.3.1.2 ( $p = 800 \text{ hPa}$ ) . . . . .	137
A.61	Raw-data for Fig.3.5 in Sec.3.1.2 ( $p = 1600 \text{ hPa}$ ) . . . . .	137
A.62	Raw-data for Fig.3.6 in Sec.3.1.2 ( $p = 200 \text{ hPa}$ ) . . . . .	138
A.63	Raw-data for Fig.3.6 in Sec.3.1.2 ( $p = 800 \text{ hPa}$ ) . . . . .	139
A.64	Raw-data for Fig.3.6 in Sec.3.1.2 ( $p = 1400 \text{ hPa}$ ) . . . . .	140
A.65	Raw-data for Fig.3.6 in Sec.3.1.2 ( $p = 2000 \text{ hPa}$ ) . . . . .	141
A.66	Raw-data for Fig.A.3 in Sec.A.1.1 ( $l' \equiv 0.05 \text{ mm}$ ) . . . . .	143
A.67	Raw-data for Fig.A.4 in Sec.A.1.1 ( $l' \equiv 0.05 \text{ mm}$ ) . . . . .	143
A.68	Raw-data for Fig.A.5 in Sec.A.1.1 ( $l' \equiv 0.05 \text{ mm}$ ) . . . . .	144
A.69	Raw-data for Fig.A.6 in Sec.A.1.1 ( $l' \equiv 0.05 \text{ mm}$ ) . . . . .	144

A.70	Raw-data for Fig.A.7 in Sec.A.1.1 ( $1' \equiv 0.05 \text{ mm}$ ) . . . . .	145
A.71	Raw-data for Fig.A.8 in Sec.A.1.1 ( $1' \equiv 0.05 \text{ mm}$ ) . . . . .	145
A.72	Raw-data for Fig.A.9 in Sec.A.1.1 ( $1' \equiv 0.05 \text{ mm}$ ) . . . . .	146
A.73	Raw-data for Fig.A.10 in Sec.A.1.1 ( $1' \equiv 0.05 \text{ mm}$ ) . . . . .	146
A.74	Raw-data for Fig.A.11 in Sec.A.1.1 ( $1' \equiv 0.05 \text{ mm}$ ) . . . . .	147
A.75	Raw-data for Fig.A.12 in Sec.A.1.1 ( $1' \equiv 0.05 \text{ mm}$ ) . . . . .	147
A.76	Raw-data for Fig.A.13 in Sec.A.1.1 ( $1' \equiv 0.05 \text{ mm}$ ) . . . . .	148
A.77	Raw-data for Fig.A.14 in Sec.A.1.1 ( $1' \equiv 0.05 \text{ mm}$ ) . . . . .	148
A.78	Raw-data for Fig.A.15 in Sec.A.1.1 ( $1' \equiv 0.05 \text{ mm}$ ) . . . . .	149
A.79	Raw-data for Fig.A.16 in Sec.A.1.1 ( $1' \equiv 0.05 \text{ mm}$ ) . . . . .	149
A.80	Raw-data for Fig.A.17 in Sec.A.1.1 ( $1' \equiv 0.05 \text{ mm}$ ) . . . . .	150
A.81	Raw-data for Fig.A.18 in Sec.A.1.1 ( $1' \equiv 0.05 \text{ mm}$ ) . . . . .	150
A.82	Raw-data for Fig.A.19 in Sec.A.1.1 ( $1' \equiv 0.05 \text{ mm}$ ) . . . . .	151
A.83	Raw-data for Fig.A.20 in Sec.A.1.1 ( $1' \equiv 0.05 \text{ mm}$ ) . . . . .	151
A.84	Raw-data for Fig.A.21 in Sec.A.1.1 ( $1' \equiv 0.05 \text{ mm}$ ) . . . . .	152
A.85	Raw-data for Fig.A.22 in Sec.A.1.1 ( $1' \equiv 0.05 \text{ mm}$ ) . . . . .	152
A.86	Raw-data for Fig.A.23 in Sec.A.1.1 ( $1' \equiv 0.05 \text{ mm}$ ) . . . . .	153
A.87	Raw-data for Fig.A.24 in Sec.A.1.1 ( $1' \equiv 0.05 \text{ mm}$ ) . . . . .	153
A.88	Raw-data for Fig.A.25 in Sec.A.1.1 ( $1' \equiv 0.05 \text{ mm}$ ) . . . . .	154
A.89	Raw-data for Fig.A.26 in Sec.A.1.1 ( $1' \equiv 0.05 \text{ mm}$ ) . . . . .	154
A.90	Raw-data for Fig.A.27 in Sec.A.1.1 ( $1' \equiv 0.05 \text{ mm}$ ) . . . . .	155
A.91	Raw-data for Fig.A.28 in Sec.A.1.1 ( $1' \equiv 0.05 \text{ mm}$ ) . . . . .	155
A.92	Raw-data for Fig.A.29 in Sec.A.1.1 ( $1' \equiv 0.05 \text{ mm}$ ) . . . . .	156
A.93	Raw-data for Fig.A.30 in Sec.A.2.1 . . . . .	157
A.94	Raw-data for Fig.A.31 in Sec.A.2.1 . . . . .	158
A.95	Raw-data for Fig.A.32 in Sec.A.2.1 . . . . .	158
A.96	Raw-data for Fig.A.33 in Sec.A.2.1 . . . . .	159
A.97	Raw-data for Fig.A.34 in Sec.A.2.1 . . . . .	159
A.98	Raw-data for Fig.A.35 in Sec.A.2.1 . . . . .	160
A.99	Raw-data for Fig.A.36 in Sec.A.2.1 . . . . .	160
A.100	Raw-data for Fig.A.37 in Sec.A.2.1 . . . . .	161
A.101	Raw-data for Fig.A.38 in Sec.A.2.1 . . . . .	161
A.102	Raw-data for Fig.A.39 in Sec.A.2.1 . . . . .	162
A.103	Raw-data for Fig.A.40 in Sec.A.2.1 . . . . .	163
A.104	Raw-data for Fig.A.41 in Sec.A.2.1 . . . . .	163
A.105	Raw-data for Fig.A.42 in Sec.A.2.1 . . . . .	164
A.106	Raw-data for Fig.A.43 in Sec.A.2.1 . . . . .	164
A.107	Raw-data for Fig.A.44 in Sec.A.2.1 . . . . .	165
A.108	Raw-data for Fig.A.45 in Sec.A.2.1 . . . . .	165
A.109	Raw-data for Fig.A.46 in Sec.A.2.1 . . . . .	165
A.110	Raw-data for Fig.A.47 in Sec.A.2.1 . . . . .	166
A.111	Raw-data for Fig.A.48 in Sec.A.2.1 . . . . .	166
A.112	Raw-data for Fig.A.49 in Sec.A.2.1 . . . . .	167
A.113	Raw-data for Fig.A.50 in Sec.A.2.1 . . . . .	167
A.114	Raw-data for Fig.A.51 in Sec.A.2.1 . . . . .	168
A.115	Raw-data for Fig.A.52 in Sec.A.2.1 . . . . .	168
A.116	Raw-data for Fig.A.53 in Sec.A.2.1 . . . . .	169

A.117	Raw-data for Fig.A.54 in Sec.A.2.1 . . . . .	169
A.118	Raw-data for Fig.A.55 in Sec.A.2.1 . . . . .	169
A.119	Raw-data for Fig.A.56 in Sec.A.2.1 . . . . .	170
B.1	Specifications of the ceramic ( $Al_2O_3$ ) shielding . . . . .	173
B.2	Complete list of production drawings . . . . .	175
B.3	Parts list . . . . .	175
B.4	Electrodes, welding equipment . . . . .	176
B.5	Sealing rings, (O-rings) . . . . .	176
B.6	Metals, ironmongery . . . . .	176
B.7	Galvanic . . . . .	176
C.1	Complete list of production drawings . . . . .	177